X-ray spectral variability of disk winds in a sample of local active galactic nuclei

Michele Costa

A thesis submitted to Keele University
for the Degree of Doctor of Philosophy

Department of Physics, Keele University.

October 2019

Abstract

In this thesis I will present the culmination of my research into the phenomenon of AGN winds using several X-ray telescopes (*Suzaku*, *XMM-Newton* and *NuSTAR*); I will do this primarily through the use of radiative transfer models (Sim et al. 2010). I will be outlining, in chapter 3, the radiative transfer code which I will use to demonstrate the capabilities of the model. I will then use this to study outflows in a small sample of AGN. Firstly, with an initial deep study of PDS 456 and subsequent studies of PG1211 + 143 and 1H 0707 − 495, I will aim to provide a better understanding of the structure and variability of the disk winds in these well-known AGN. Overall, these results are consistent with the view of highly-ionised Fe K winds seen in many previous works, though this is found using a more physical model. With these new models I can probe the data in new ways, which I think represents an important addition to the currently held paradigm of AGN disk winds, and further enforces the hypothesis that they may be important for galaxy evolution.

As the out flowing material interacts with the ISM it can impart an outward pressure (through either momentum or energy transfer) clearing the inner galaxy of material, this is thought to be the cause of the relationships between the central black hole and observable galactic parameters such as the mass of the bulge (M_{buldge}) and velocity dispersion (σ^*). The requirement for feedback is also seen in cosmic simulations as without feedback there is nothing to regulate the size of galaxies so they become much more massive than what is observed (Bower et al. 2006).

Acknowledgements

I would like to extend my utmost gratitude to my stand in supervisor, Dean McLaughlin who with out him I would be completely lost and to James Reeves, I appreciate all you've both done for me. To my often roommate Gabriele Matzeu, I thank you for being there when I needed someone to listen and bounce ideas off of and for the food, the awesome food. I would like to thank the people around me who have guided and supported me through my journey: Emanuele Nardini, Valentina Braito and Andrew Lobban. A special thanks to Stuart Sim for his code and support, without which my work would not have been possible.

To the people in office who have shared many late nights Gabriele Matzeu (once again), Steve Goldman and, Ben Clark along with my friends on the outside: Nick Roberts, Micheal Greco, David Minshall, Jonathan Myerscough, James Goodman and Connor Hawkins Pinchers who, without you guys I may have gone insane. Thanks to all the people at Unipart who have supported me during my corrections.

I would like to express my deep love and gratitude to my partner in life, Pip Matthews; without her support I probably would not have finished. Lastly, and by certainly no means least, I am so grateful to my family for their love and support during my studies; in particular, my parents, Jayne and Sebastiano, along with my sisters, Giuseppa and Francesca and their respective partners Ollie and Simon. To my nephew and niece, Deacon and Rayna I look forward to watching you grow up.

I've spent a long 8 years at Keele and I've met many people along the way which have shaped my journey. Thank you, all.

Contents

List of Figures

List of Tables

1 Introduction

The nucleus of most galaxies contain a supermassive black hole (SMBH) of mass within the range of $\sim 10^6 - 10^{10}\, M_\odot$ Salpeter (1964); Lynden-Bell (1969); Kormendy & Richstone (1995); Magorrian et al. (1998); Kormendy & Ho (2013). In most, these large bodies are not observable directly; some can be observed by tracking the orbits of stars in the inner nucleus and it was through this method that the black hole Sgr A* (the black hole at the centre of our own Galaxy) was discovered. There is a subset $(10 - 20\%)$ of galaxies where the central black hole is more obvious. In these active galaxies the nucleus (an unresolved region, less than a few 100 pc in diameter) produces more electromagnetic radiation than produced by its host galaxy's stellar population – typically $\sim 10^{11}\, L_\odot$ (where $L_\odot = 3.8 \times 10^{33}$ erg s^{-1}) by a factor of ~ 100, with typical bolometric luminosity $L_{\rm bol} \sim 10^{44} - 10^{48}$ erg s^{-1} (Woo & Urry 2002; Lusso et al. 2010). These objects are known as Active Galactic Nuclei (AGN hereafter). For such a small region to produce so vast an amount of energy the energy production process must be very efficient, much more so than nuclear fusion in stars. The process thought to be powering the objects is accretion onto the supermassive black hole whereby the gravitational potential energy is released. However, as the feeding gas will likely have some amount of angular momentum, there will be a point at which the material can no longer fall in and instead this material will eventually form an accretion disk. In accretion disks angular momentum can be transported outward by viscous forces, possibly magnetic rotational instability (Balbus & Hawley 1998) whereby deformation of the elastic magnetic field line which threads the accretion disk allows angular momentum transfer from inner to outer radii allowing material to fall deeper into the gravitational potential. Much of the energy released by this process is radiated away producing the AGN.

There is evidence that the AGN and their host galaxies co-evolve, due to the several correlations in observable parameters (Ferrarese & Merritt 2000; Gebhardt et al. 2000) which will be mentioned later on in subsection 1.4.1. These correlations demonstrate some

self-regulating (feedback) mechanism which communicates between AGN and the host galaxies. The $M_{\rm BH} - \sigma_*$ relation is a correlation between the mass of the central black hole and the velocity dispersion of the stars within the bulge of the host galaxy – where σ_* effectively measures the potential well of the bulge. The sphere of influence (within which the gravity of the central black hole has an appreciable effect) of the black hole is $\sim 100 - 1000$ times smaller than the galactic bulge. Therefore connection between the size scales is required to cause this correlation. Mechanical feedback in the form of AGN winds could link the black hole and the host galaxy, as it is efficient when compared to radiative feedback where only a small fraction of the energy is relinquished to the host unless the host is optically thick.

This research is focused on the spectroscopy of this unresolved region. Using the X-ray regime allows observers to penetrate to the smallest scales of the AGN. During this chapter I will explain the radiative processes and the information which the observed radiation carries. This information can enlighten the observer to how the properties of the AGN and how it interacts with the host environment. Observation and modelling of the features imprinted on the spectrum (via emission and absorption) allow the properties of the outflows to be quantified; leading to a better understanding of the phenomenon.

1.1 Observational overview of active galaxies

In this section I will discuss the classifications of active galaxies using observed features, such as the presence (or lack thereof) of radio jets, Doppler broadened optical emission lines and bolometric luminosity. The initial broad classification is radio loudness. Kellermann et al. (1989) defines radio loudness as the ratio of the luminosities in the 5 GHz band and the optical B band $\left(R = \frac{L_\nu(5\,\mathrm{GHz})}{L_\nu(\mathrm{B-band})}\right)$, and that an object is "radio-loud" (as opposed to "radio-quiet") when $R > 10$. Luminosity separates AGN into Quasars and Seyferts (Seyfert 1943). Schmidt & Green (1983) used the B-band magnitude to define to a separation between

the classifications as $M_B = -23$ mag with less luminous $M_B > -23$ mag being Seyferts.

The final sub-classification based on the presence (or absence) of broad optical emission features such as Balmer lines (i.e. Hα and Hβ) and are called type 1 (or type 2) Seyferts. Fig. 1.1 shows differences between the optical spectra of various types of AGN and for comparison a normal galaxy. The normal galaxy can be seen to fall off at shorter wavelengths and lacks forbidden lines such as [O III] (at 5007 Å) which can be seen in most AGN spectra, with the exception of the example jet dominated BL Lac object (0814+425) and a low-ionisation nuclear emission-line region (LINER; NGC 4579). The radio-loud BL Lac object has a featureless optical spectrum, while the LINER looks similar to the normal galaxy with a stronger Hα (6563 Å). The mean quasar is a composite spectrum generated by Francis et al. (1991). The Broad Line Radio Galaxy (BLRG; 3C 390.3) and Seyfert 1 (NGC 4151) are both type 1 AGN with broad (~ 3000 km s^{-1}) lines such as Hα and narrow (~ 300 km s^{-1}) [O III] forbidden lines where as the type 2s Narrow Line Radio Galaxy (NLRG; Cygnus A) and Seyfert 2 (NGC 4941) lack the broad lines. Tadhunter (2008) uses these classifications as the axes of the scheme shown in Fig. 1.2.

1.1.1 Seyfert galaxies

The most commonly observed AGN class in the local universe ($z < 0.3$; Schmidt & Green 1983) is Seyfert galaxies. Seyferts lie at the lower end of the AGN luminosity range with $L_{\rm bol} \approx 10^{43} - 10^{45}$ erg s^{-1}. The breadth of the Balmer lines (Hα, Hβ) and C IV are generally used to define the classification of Seyferts; these broad optical lines typically have full width at half maximums (FWHM) of $\approx 1000 - 10,000$ km s^{-1} for type 1 Seyfert. The intermediate classifications Sy1.5–1.9 (Osterbrock 1981) show progressively thinner permitted lines as the number increases. These lines are doppler broadened by the orbital motion around the black hole.

The region where these lines originate is called the Broad Line Region (BLR). The BLR is located between $\approx 2 - 30$ light days from the SMBH. There appears to be stratification

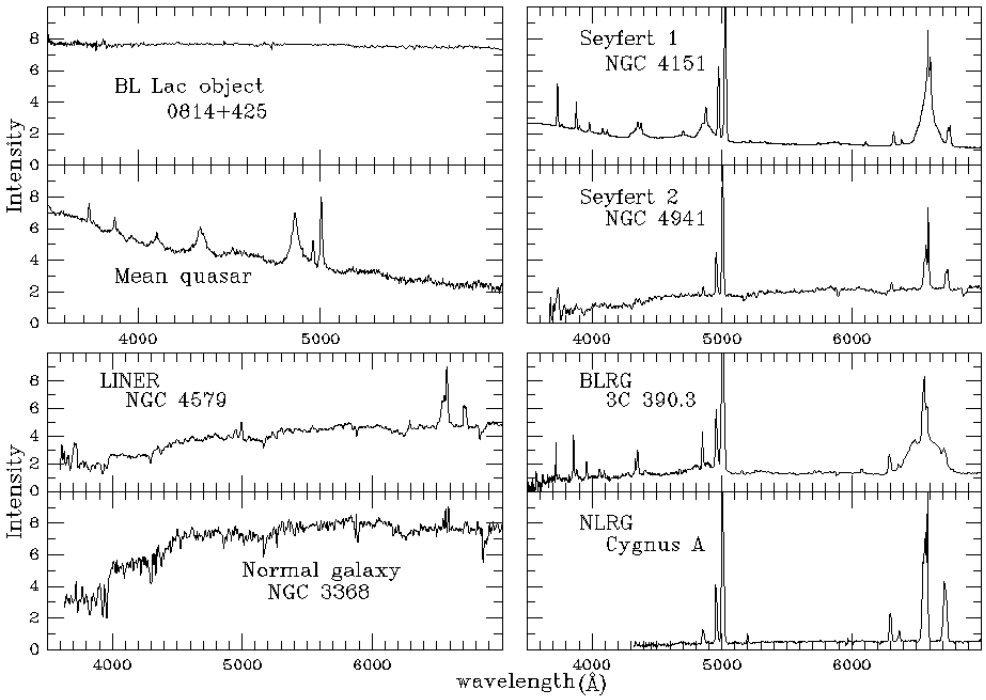

Figure 1.1: The normalised spectra of the different classifications of AGN and for comparison a normal galaxy.
The spectra of 0814+425 and 3C 390.3 are from Lawrence et al. (1996).
The composite "mean quasar" spectrum was generated by Francis et al. (1991).
NGC 4579 and NGC 4941 (Keel 1983).
Cygnus A (Owen et al. 1990).
The normal-galaxy spectrum (NGC 3368; Kennicutt 1992). Taken from http://pages.astronomy.ua.edu/keel/agn/spectra.html

as highly ionised lines such as C IV emission is typically seen at distances ~ 10 light days from the black hole. While lower ionisation lines such as Hβ originate from further away, ~ 26 light days away from the black hole (Kollatschny & Zetzl 2013).

Alongside the broad optical emission present in type 1s, all Seyferts have narrow (FWHM $\approx 300 - 450$ km s^{-1}) forbidden lines (such as [O III] and [N II]); originating from the Narrow Line Region (NLR). As the NLR contains forbidden lines the gas must have

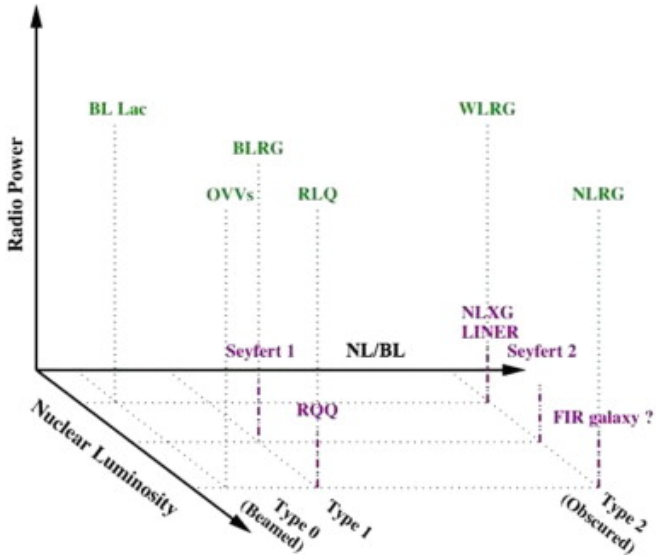

Figure 1.2: The classifications scheme taken from Tadhunter (2008), where each axis corresponds to an observed property of AGN (radio loudness, luminosity and presence of broad optical lines). The acronyms used in the figure are RLQ - Radio Loud Quasar; BL Lac - BL Lacertae Blazar; OVV - Optical Violent Variables; BLRG - Broad Line Radio Galaxy; WLRG - Weak Line Radio Galaxy; RQQ - Radio Quiet Quasar; NLRG - Narrow Line Radio Galaxy; FIR - Ultra Luminous infra-red Galaxy; LINER - Low ionisation Nuclear Emission-line Region

moderately low density at least for AGN ($n_e \sim 10^3 - 10^6\,\mathrm{cm}^{-3}$) to avoid being collisionally suppressed. Whereas the lack of broad forbidden lines means that the density must be higher ($n_e \sim 10^9\,\mathrm{cm}^{-3}$) in the BLR. The narrow permitted and forbidden (such as [O III]) lines, must come from regions further from the SMBH, but within $\leq 10 - 20\,\mathrm{pc}$ (Peterson 1997; Beckmann & Shrader 2012).

Narrow-line Seyfert 1 galaxies

A subset of Seyfert galaxies is narrow-line Seyfert 1 galaxies (NLS1; Osterbrock & Pogge 1985) which as the name suggests are similar to Sy1s, however the Hα line widths are much

lower than regular Sy1s (FWHM $\lesssim 2000\ \mathrm{km\,s^{-1}}$). Another peculiarity is that NLS1s also have a lower black hole mass ($M_{\mathrm{BH}} \sim 10^5 - 10^7\ M_\odot$) as evidenced by there comparatively rapid temporal X-ray variability (Vaughan et al. 1999, 2011; Lobban et al. 2011; Legg et al. 2012; Giustini et al. 2015). As their bolometric luminosities are still comparable to Seyferts (Collin & Kawaguchi 2004) they must be accreting at appreciable fractions of their Eddington rates (the effective pseudo-maximum accretion rate – see section 1.2.1.1). Due to their low mass (and therefor smaller accretion disks; see section 1.2.1.2) they also tend to have a strong excess in soft X-ray (0.1–2 kev) part of there spectrum (Laor et al. 1994; Boller et al. 1996; Nardini et al. 2012). Finally they are generally radio quiet with only 7% (Komossa et al. 2006) of NLS1s being radio-loud.

1.1.2 Quasars

Quasars are similar to Seyferts but with a larger luminosity ($L_{\mathrm{bol}} \simeq 10^{45} - 10^{47}\ \mathrm{erg\,s^{-1}}$) making them the most luminous sub-class. They are point-like, as they outshine their host galaxies by a factor of $10^2 - 10^3$. When combing appearance with their high redshift, caused them to initially be classified as Quasi-Stellar Objects (QSOs). The Quasar number density peaks at cosmological redshift $z \approx 2 - 3$ (Schmidt 1963) meaning that luminous Quasars were more common. This can be thought of as a fixed population which is becoming less luminous over time (Warren et al. 1994; Croom et al. 2004). Or it could also mean that more massive AGN accreted first, with the lower mass black holes having started accreting in the relatively recent past (Cowie et al. 2003; Merloni 2004; Heckman et al. 2004). At $z \approx 2 - 3$ about 10% are radio-loud (Kellermann et al. 1989) producing strong radio emission, powered by a collimated relativistic jet. Quasars are generally type 1 analogously to Seyferts. Type 2s only being found relatively recently (Stern et al. 2002; Norman et al. 2002; Martínez-Sansigre et al. 2006; Severgnini et al. 2006)). Despite the terms QSO and Quasar originally being reserved for radio-quiet and radio-loud objects respectively, they are now both used interchangeably. In this thesis I will only be covering radio-quiet objects.

1.1.2.1 Broad Absorption Line Quasars

Broad Absorption Line Quasars (BALQSOs; Hamann & Sabra see 2004, for a detailed review) are Quasars characterised by broad (FWHM $\sim 10^4$ $\mathrm{km\,s^{-1}}$) absorption line (BAL) troughs imprinted on the optical spectra due to resonant transitions of ionised metals e.g., $\mathrm{C_{iv}}$, $\mathrm{N_v}$, $\mathrm{O_{vi}}$, $\mathrm{Si_{iv}}$, observed in the UV spectrum. These broad features are seen to be outflow velocities $v_{\mathrm{out}} \sim 1000 - 10,000$ $\mathrm{km\,s^{-1}}$.

1.1.3 Unified models

Antonucci (1993) noted that broad lines have been detected in the polarised spectra of some Sy2 objects. The BLR photons must have been scattered back into the line of sight. This suggests that at least in some objects the broad line regions are present but are obscured by Compton-thick ($N_{\mathrm{H}} \gtrsim 1.5 \times 10^{24}\,\mathrm{cm^{-2}}$) material. The proposed source of this obscuration is a dusty molecular torus which lies along the plane of the accretion disk, located at the dust sublimation radius ($\sim 1\,\mathrm{pc}$) with scale height large enough that it would obscure the BLR when viewed at inclinations close to the disk plane. As photons emitted close to the disk plane would be absorbed (and reprocessed into infra-red radiation), this will inherently lead to anisotropic emission. This inclination-dependent obscuration could explain the observed difference between type 1 and 2 AGN. There is mounting evidence that the structure of the molecular torus is likely to be clumpy (Elitzur 2012) so as to explain the so-called 'changing-look' AGN which show a rapid and repeated transitions from an un-obscured to obscured state as per NGC 1365 (Risaliti et al. 2005) which were interperated as Compton-thick clouds crossing the line of sight.

The overall unification scheme is presented in Fig. 1.3 indicating that the type of object that is observed depends on the extent to which the nuclear region is visible. In the case where the viewing angle is such that the nuclear region (together with the BLR) can be directly seen, it follows that the observed object can be classified as type 1 source

(or Sy1). On the other hand, if the viewing angle is such that the nucleus, including the BLR, is obscured by an absorber, then it is only possible to detect the reprocessed emissions (i.e. absorbed, scattered and reflected) coming from the dusty torus and/or the NLR. The resulting optical spectrum will then be dominated by narrow emission lines and hence the object is classified as a type 2 AGN (or Sy2). The unification scheme can provide at present, a first order understanding of the AGN phenomenon, predicting differences in appearance based only on the orientation angles relative to the observer, assuming no differences in the intrinsic physical properties of the AGN.

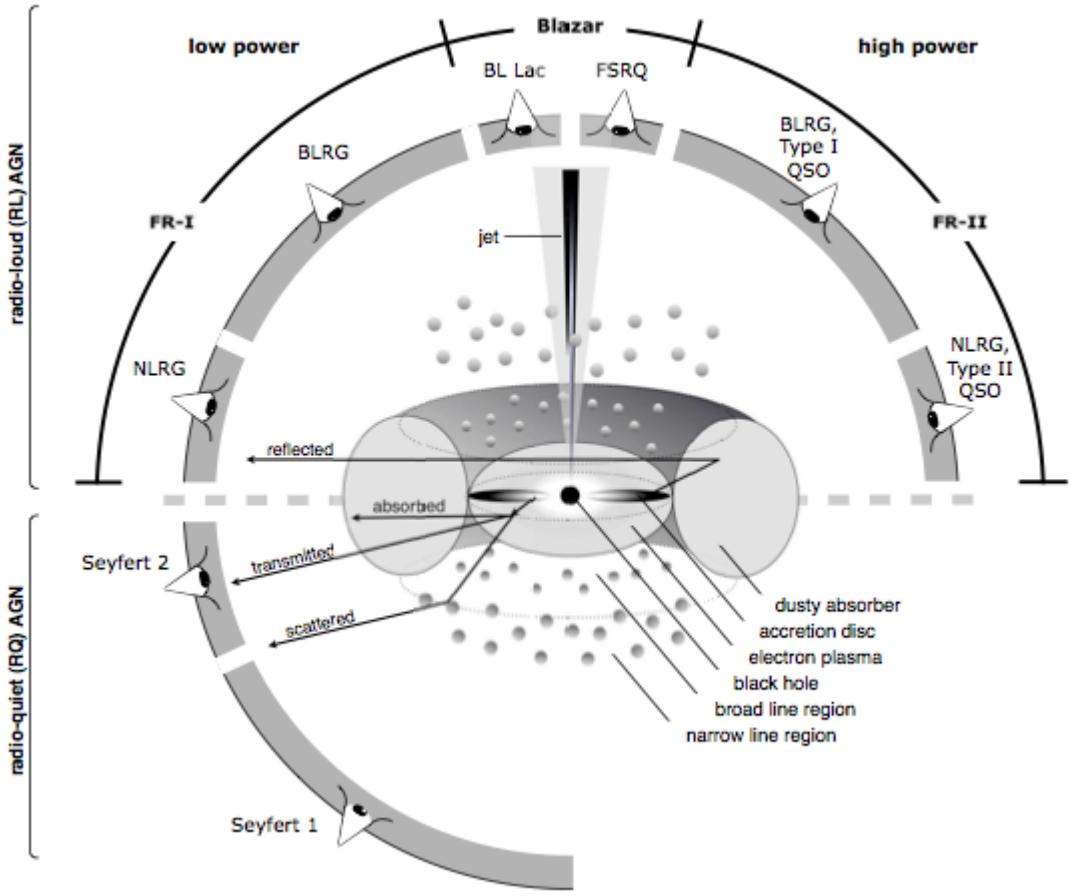

Figure 1.3: Schematic illustration of the current understanding of the AGNs in the unified scheme. The central engine is mainly composed of a SMBH that is accreting matter forming an accretion disk and a region of relativistic electrons defined as corona; however, the location and geometry of the latter is still under debate. The nuclear region is surrounded by a dusty medium of absorbing material of toroidal geometry and the observer's line of sight with respect to it determines if the object is observed as a type 1 or type 2 AGN. The broad line region (BLR) is observed through broad permitted emission lines and is located at sub-parsec scales. The narrow line region (NLR) is located further out from the SMBH at kpc scales and its responsible for the observed narrow forbidden and permitted lines. The analogous viewing angle principle can be applied for the radio-loud sources where a collimated relativistic jet emission is present. The FR-I and FR-II correspond to Fanaroff Riley class I and II galaxy respectively, where FSRQ and BL Lac are Flat Spectrum Radio Quasar and BL Lacertae respectively. Figure taken from Beckmann & Shrader (2012)

1.2 Physical processes

The physical processes which are involved in shaping AGN spectra are emission powered by accretion onto a black hole (Salpeter 1964; Rees 1984) and absorption. In this section I will explain the various manifestations of these processes.

1.2.1 Accretion

Mass accretion (hereafter accretion) is an efficient mechanism for releasing gravitational potential energy. As matter falls from a mass reservoir onto the central object of mass $M_{\rm BH}$, if its angular momentum J exceeds a critical value it can no longer continue to fall and will instead fall into a Keplerian orbit around the central object. Assuming the accretion rate is high enough this material then flattens out to form a disk structure known as an accretion disk. The radius ($R_{\rm k}$) at which the material starts to orbit instead of falling in is given by:

$$J_k = \sqrt{GM_{\rm BH}R_k}. \tag{1.1}$$

As angular momentum must be conserved, it must be transported outward to allow material to continue to move inwards, so it can continue to release gravitational potential energy ($E_{\rm GPE}$). The amount of potential energy liberated from moving a test mass m into the gravitational potential of the central object from infinity to a radius r is given by:

$$\Delta E_{\rm GPE} = -\frac{GM_{\rm BH}m}{r}. \tag{1.2}$$

If instead of a test mass we consider the mass accretion rate ($\dot{M} = \frac{dm}{dt}$) we get the rate of change of $E_{\rm GPE}$ within accretion disk. The virial theorem states ($2\Delta E_{\rm kin} + \Delta E_{\rm GPE} = 0$) so only half of the potential energy released will go into increasing the orbital velocity whilst the other half must be radiated away (via viscous forces in the disk). Assuming the disk extends to an inner orbit of $R_{\rm in}$ the energy released by the accretion process is given by:

$$L_{\rm acc} = -\frac{1}{2}\frac{dE_{\rm GPE}}{dt} = \frac{GM_{\rm BH}\dot{M}}{2R_{\rm in}} \equiv \eta \dot{M} c^2, \tag{1.3}$$

where η is the efficiency of the accretion process. By rearranging equation 1.3 we get that the efficiency is dependent on $R_{\rm in}$ ($\eta = \frac{GM_{\rm BH}}{2R_{\rm in}c^2}$). Redefining $R_{\rm in}$ to be $R_{\rm ISCO}$ which is the radius of the innermost stable circular orbit (ISCO) for a non-rotating (Schwarzschild) black hole $R_{\rm ISCO} = 6\frac{GM_{\rm BH}}{c^2}$ this yields $\eta = 1/12$.

As the ISCO is linked to the spin of a rotating black hole in the Kerr metric, it moves inwards to $1.235\,R_{\rm g}$ at maximal spin – because the spin causes space time to become twisted. This means that accretion onto a Kerr black hole will be more efficient ($\eta = 0.40$). However when taking into account other general relativistic effects such as photon capture and energy losses from escaping the potential well, the maximum "radiative" efficiency is reduced to $\eta = 0.057$ for a Schwarzschild black hole (Salpeter 1964) and $\eta = 0.32$ for a maximally spinning Kerr black hole (Thorne 1974).

1.2.1.1 The Eddington Limit

As the radiation field interacts with the in-falling matter via scattering/absorption, momentum can be transferred. The point at which this outward radiation pressure overcomes the gravitational pull is known as the Eddington limit. Equating the two forces gives

$$F_{\rm rad} = \frac{\sigma_T L}{4\pi r^2 c} = F_{\rm grav} = \frac{GM_{\rm BH}m_p}{r^2}, \tag{1.4}$$

where $F_{\rm rad}$ is the outward force due to radiation pressure, $F_{\rm grav}$ is the force of gravity, m_p is the proton mass and σ_T is the cross section of Thompson scattering. Rearranging equation 1.4 gives the luminosity at which the forces are balanced, known as the Eddington luminosity:

$$L_{\rm edd} = \frac{4\pi G m_p c}{\sigma_T} M_{\rm BH} \simeq 1.3 \times 10^{38} \frac{M_{\rm BH}}{M_\odot}\,{\rm erg\,s^{-1}}. \tag{1.5}$$

The accretion rate required to power the Eddington luminosity can be found by combining Eqs. 1.3 and 1.5 to be

$$\dot{M}_{\rm edd} = \frac{L_{\rm edd}}{\eta c^2}. \tag{1.6}$$

$\dot{M}_{\rm edd}$ gives a pseudo-maximum accretion rate because at higher rates the photon momentum flux will overcome the gravitational potential of the central object, driving off material lowering the accretion rate.

1.2.1.2 The structure of an accretion disk

An optically thick, geometrically thin disk was proposed by Shakura & Sunyaev (1973a). Then the spectrum of an annulus of thickness Δr with an area of $2 \times 2\pi r \Delta r$ (with an extra factor of 2 as there is a top and bottom to the disk) is given by a black body of temperature $T(r)$. Thus, equating the Stefan-Boltzmann Law and the GPE released within that annulus we obtain:

$$L_{disk} = 2 \times 2\pi r \, \Delta r \, \sigma_{SB} \, T^4 = \frac{G M_{\rm BH} \dot{M}}{\Delta r} 2r^2. \tag{1.7}$$

The term $\sigma_{\rm SB} T^4$ is the flux (luminosity per radiated area). The temperature profile is then found by rearranging equation 1.7 to give

$$T(r) = \left(\frac{G M_{\rm BH} \dot{M}}{8\pi \sigma_{SB} r^3} \right)^{\frac{1}{4}}. \tag{1.8}$$

A proper treatment of the viscosity modifies this to become

$$T(r) = \left(\frac{3 G M_{\rm BH} \dot{M}}{8\pi \sigma_{SB} r^3} \right)^{\frac{1}{4}}. \tag{1.9}$$

We can once again the use mass-dependent units, this yields:

$$T(r) = 4.4 \times 10^7 \eta^{-\frac{1}{4}} \left(\frac{\dot{M}}{\dot{M}_{\rm edd}} \right)^{\frac{1}{4}} \left(\frac{M_{\rm BH}}{M_\odot} \right)^{-\frac{1}{4}} \left(\frac{r}{R_{\rm g}} \right)^{-\frac{3}{4}} {\rm K}. \tag{1.10}$$

It can easily be seen from equation 1.10 that the temperature quickly increases moving radially inwards as $T \propto r^{-\frac{3}{4}}$. From this we can take multiple annuli each with their own

characteristic temperature given by equation 1.10 and integrate their contributions to form the total disk spectrum. This is the called the multicolour black body.

For a Schwarzschild black hole of mass $10^6\,M_\odot$, accreting at the Eddington rate ($\dot{M}_{\rm edd}$) the inner temperature (T at $6\,R_{\rm g}$) would peak at $k_bT \simeq 64\,{\rm eV}$ whereas for a black hole mass of $10^9\,M_\odot$ the disk peak would be at $k_bT \simeq 11\,{\rm eV}$. This decrease in the inner disk temperature with growing black hole is because the area over which the energy is radiated increases faster than the extra energy released from having a larger potential well. This means for AGN the disk peaks in the UV part of the electro-magnetic spectrum, however the Wien tail may extend into the soft X-rays in lower mass AGN such as NLS1s.

1.2.2 Comptonisation

Compton scattering is the interaction of a high energy photon and a non-relativistic ($v_e \ll c$) free electron. In this process energy from the photon is given to the electron which then recoils carrying away energy and momentum from the collision. As momentum must also be conserved the amount of energy transferred to the electron can be seen from the change in photon wavelength given by:

$$\lambda' - \lambda = \Delta\lambda = \frac{h}{m_e c}(1 - cos\theta). \tag{1.11}$$

Here λ is the incident wavelength, λ' its the scattered wavelength and θ gives the deviation of the outward photon from is incident trajectory.

If the electron is moving relativistically ($v_e \lesssim c$) and its kinetic energy is greater than the photon energy then the photons can gain energy. This process is known as inverse Compton scattering or Comptonisation. This means that a lower frequency photon can gain a substantial amount of energy, $E' \propto \gamma^2 E$ where E and E' are the initial and final energies respectively. γ and γ' is the Lorentz factor of the electron before and after the interaction. Therefore electrons with large inital Lorentz factors the photon energy can be significantly boosted to an energy of $E' = E + (\gamma - \gamma')m_e c^2$.

This is a likely mechanism for X-rays to be produced in AGN where the optical/UV photons radiated from the accretion disk are up-scattered by a reservoir of hot electrons (known as the corona). The process of Comptonisation removes energy from the electrons, cooling them. The corona will eventually reach an equilibrium, balancing the electron heating process with the Compton cooling from up-scattering seed photons.

1.2.3 Photoelectric effect

Absorption is an important phenomenon in observing AGN. The presence of an absorber along the line of sight to the X-ray source modifies the intrinsic spectrum, imprinting information about itself. In the X-ray regime the most common interaction of photons with matter is the photoelectric effect because X-ray photons exceed the binding energy of the most populous atoms (H, He). Hence an X-ray interaction will liberate an electron from the innermost K (n=1) shell resulting in ionisation of the atom (this is known as bound–free absorption). However, when the binding energy is not exceeded by the absorbed photon, the electron instead transitions to a higher energy level and not ejected (this is called a bound–bound transition); the atom remains in an excited state until it decays (by either emission or charge exchange). In both, absorption features (such a curvature, edges and/or lines) are imprinted on the intrinsic spectrum as photons are removed from the observer's line of sight.

1.2.3.1 Bound–free absorption

The amount of photoelectric absorption is defined by the amount of atoms/ions in the line of sight; this gives the optical depth of a species i, defined as:

$$\tau_i = \sigma(E)_i N_i \tag{1.12}$$

Where $\sigma(E)_i$ and N_i are the energy-dependent photoelectric cross section and the column

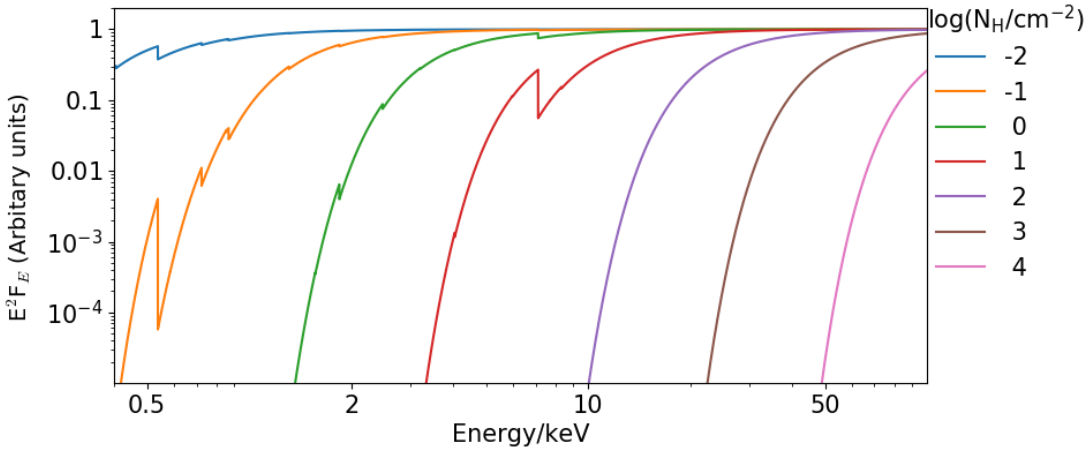

Figure 1.4: Variation of observed spectrum with increasing column density of a neutral absorber. The y-axis is the flux density multiplied by energy squared this is so that power laws with a photon index of two are flat.

density along the line of sight. A simple approximation for a given energy is $\sigma(E) \propto (E/E_{\rm edge})^{-3}$ (where $E_{\rm edge}$ is the energy of the K edge, for example $E_{\rm edge}$ of hydrogen is 13.6 eV). The total cross section would be the abundance-weighted sum of σ_i over all species. The observed modification to the intrinsic spectrum is

$$F_{\rm obs}(E) = F_{\rm src}(E) \times \sum_i e^{-\sigma(E)_i N_i}. \tag{1.13}$$

The energy of the edge increases with proton number due to the stronger nuclear bonding ($E_{\rm edge} \sim 0.5\,$keV for O and $E_{\rm edge} \sim 7\,$keV for Fe). Fig. 1.4 shows as the column increases the weaker edges of heavier elements become visible at increasingly higher energies, until the column density becomes sufficiently large to remove all flux at that energy.

1.2.3.2 Bound–bound absorption & spectral lines

As described earlier, when a photon below the ionisation threshold is absorbed (assuming a valid transition can occur at that energy) the atom/ion enters an excited state. This removes photons from the input spectrum. The energy of this absorption feature is characteristic of the transition and the atom/ion. When the atom/ion returns to the ground state one or more photons are emitted with the total energy emitted equal to that of the original exciting electron. The energy of the outgoing photons is dependent on the element and the charge. This provides an important diagnostic tool; giving information about the ionisation, optical depth and relative abundances of the material observed. The strength of the absorption/emission feature relative to the continuum is the equivalent width (EW) and is defined as:

$$EW = \int_{E_1}^{E_2} \frac{f(E) - f_c}{f_c} dE, \tag{1.14}$$

where $f(E)$ the flux is the continuum + line and f_c is the expected continuum flux. This is a useful diagnostic tool as lines are reprocessed; they respond to the flux they observe (after a delay for light travel time and recombination). This delay can be used to effectively measure distances between the source and the reprocessing material. This is called reverberation mapping and can be used to test the overall structure of the AGN.

1.2.3.3 photo-ionised absorption

When the rate of photo-ionisation is comparable to the recombination rate (the rate which electrons are captured by ions) – which is likely to be the case when there is a significant X-ray flux – ions can have a large contribution to the overall absorption cross-section. The ionisation state of a gas cloud can be defined as (Tarter & Salpeter 1969):

$$\xi = \frac{L_{\rm ion}}{n_{\rm H} R^2} \tag{1.15}$$

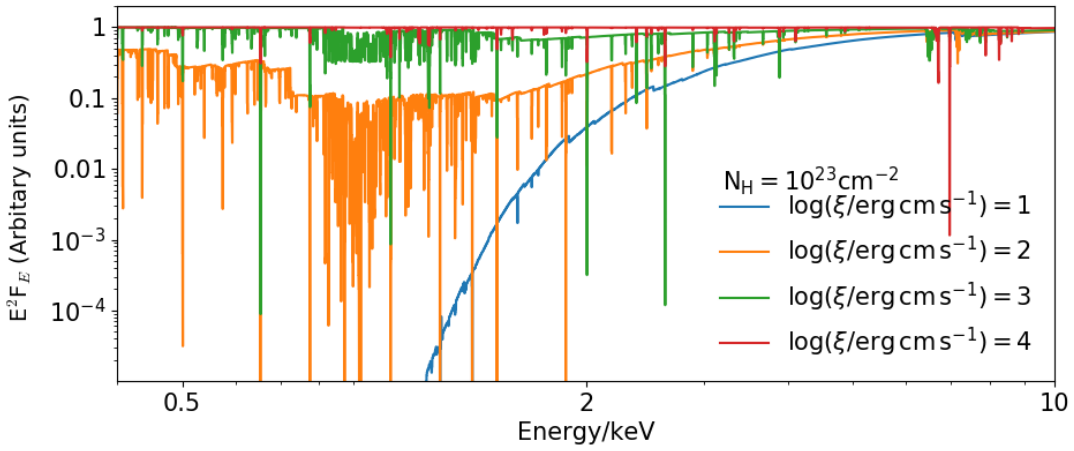

Figure 1.5: The spectrum of photo-ionised gas under increasing illumination

where $L_{\rm ion}$ is the luminosity of the ionising continuum from 1–1000 Rydberg (a range covering the ionisation potential of most cosmically abundant elements); $n_{\rm H}$ is the number density of hydrogen; and R is the distance between the absorbing cloud and the X-ray source. Fig. 1.5, shows the spectrum of a shell of gas ($N_{\rm H} = 10^{23}\,{\rm cm}^{-2}$) with increasing ionisation $\log \xi = 1$ to 4. The soft flux increases as the shell becomes more transparent, as atoms/ions are stripped of there outer electrons. At first, more features can be seen between 0.5–2 keV as the electrons have more allowed transitions. However, as the ionisation becomes larger there are less bound electrons and so the continuum becomes comparatively featureless again. This can also be seen around 6 keV, where some absorption features become stronger as the population of He-like Fe increases.

1.2.3.4 Fluorescence

Fluorescence occurs when a high-energy photon interacts with an atom and causes an electron from the inner shell (for example the K-shell in Fe) to be ejected. This leaves a hole which is filled by an electron from a higher shell; this causes the hole to move outwards as

electrons cascade inwards. During this cascade the electrons emit photons as they move to lower energy orbitals. In the case where an emitted fluorescence photon has an energy which overcomes the binding energy of the outer electrons, such as a photon emitted from an L-shell to K-shell transition interacting with an M-shell (or L-Shell) electron, then the outer electron is ejected (therefore no photon is emitted) this process is known as auto-ionisation or the "Auger" effect. The relative probability between these two processes (fluorescence vs auto-ionisation) is given by the fluorescence yield, which varies as $\alpha \propto\sim Z^3$ (Krause 1979) where Z is the proton number. This strong dependence on atomic number means that heavier elements should have a larger fluorescence yield and therefore produce much stronger fluorescence emission lines.

1.3 The complex X-ray spectrum

The X-ray spectrum of an AGN is often complex and modelling them requires many distinct components; these can be seen in the schematic Fig. 1.6. Not all of these components are observed in every AGN and the origin of these components is still not fully understood. In Fig. 1.6 the green line is the primary continuum which is modified by absorption. The soft excess is in purple and is a component whose origins are still unknown. The narrow and broad Fe lines are in brown and red respectively. The orange line is the reflection component peaking around $\sim 30\,\mathrm{keV}$ – the so called "Compton Hump". The hard excess can be caused by Compton thick obscuration (Tatum et al. 2012, 2016).

1.3.1 Producing the X-ray continuum

As mentioned before, the temperature of an AGN accretion disk ranges between $k_bT \sim 10 - 100\,\mathrm{eV}$ (Shakura & Sunyaev 1973b). This means that the majority of disk emission will be in the EUV (Extreme Ultra Violet). Therefore we still require some form of X-ray

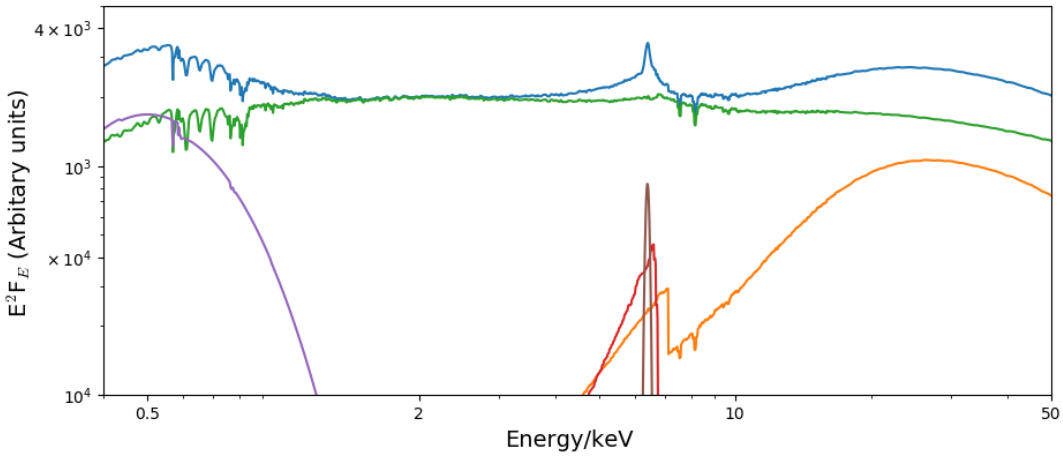

Figure 1.6: A decomposition of spectral components: the primary continuum in green, the soft excess in purple, neutral reflection in orange, then in brown and red are the narrow and broad Fe Kα; the total spectrum also includes absorption features. The characteristic Compton Hump peaking around ~ 30 keV is shown in orange. The absorption features between 0.5–1 keV show the warm absorber where as the absorber between 7–10 keV is referred to as the highly ionised outflow due to velocity shift required to produce these features. The blue line is the superposition of all the components.

source. The accepted method of X-ray production is (multiple) inverse Compton scattering events of the disk photons in a putative "corona" of hot (relativistic) electrons at a typical temperature k_bT of a few hundred keV (Haardt & Maraschi 1991, 1993). Over a narrow enough range the continuum can be approximated as a power law:

$$F(E) = kE^{-\Gamma}. \tag{1.16}$$

Typical values of Γ are between 1.7–2.5 (Nandra & Pounds 1994; Reeves & Turner 2000; Porquet et al. 2004; Scott & Stewart 2014). At higher energies there may be a "roll over" set by the temperature of the hot corona (Marinucci et al. 2016). The exact geometry of the corona is unknown, however two scenarios have been proposed. It can be either a vertical structure above the rotational axis of the black hole (the so called lamp-post; Dauser et al.

2014) or a structure above the disk such as a hot atmosphere such as the one presented in Done et al. (2012).

Dovčiak & Done (2016) showed that to produce the observed flux of 1H 0707 − 495 requires a minimum size of a lamp-post corona which extends $20\,R_{\rm g}$ in the axial direction to intercept enough of the disk photons to produce the observed X-ray flux. Matzeu et al. (2016) found that the maximum size of the corona in PDS 456 is $\sim 20\,R_{\rm g}$, as a cloud with a radius of $\sim 20\,R_{\rm g}$ fully eclipses the corona. Finally Chartas et al. (2016) showed that in several high redshift (z = 0.66 − 2.32) lensed AGN the radius of the corona is $< 30\,R_{\rm g}$ from the light curve variability. All of these measurements point towards an extended source of $\sim 20\,R_{\rm g}$.

1.3.2 The reflection component

The reflection component comes in two flavours narrow distant and blurred. Both are used to explain an excess in the hard X-rays around $E \simeq 30\,\mathrm{keV}$.

First I will explain the distance which probably arises where the primary continuum illuminates cold ($T < 10^6\,\mathrm{K}$, $k_bT \sim 85\,\mathrm{eV}$) Compton-thick circumnuclear material (Guilbert & Rees 1988; Ferland & Rees 1988; Lightman & White 1988). One of two geometries are modelled: a slab (Magdziarz & Zdziarski 1995; George & Fabian 1991; García & Kallman 2010) or torus (Murphy & Yaqoob 2009). Both geometries produce spectra with narrow Fe florescence lines (Kα and Kβ) superimposed on a scattered continuum which has broad emission peaking at 30 keV (this can be seen in Fig. 1.7).

This hump like feature is caused by a combination of two factors. The decrease in the photo-electric cross section (above 10 keV) and the Klein–Nishijima scattering cross section (above 30 keV) cause the initial rise. The down turn of the hump is caused by the Compton scattering of higher energy photons down to $\sim 30\,\mathrm{keV}$. Some hard excess can not be purely reflection and must be enhanced by a Compton-thick absorber (e.g., Tatum et al. 2016).

While a neutral reflector will not produce strong features below 2 keV, an ionised

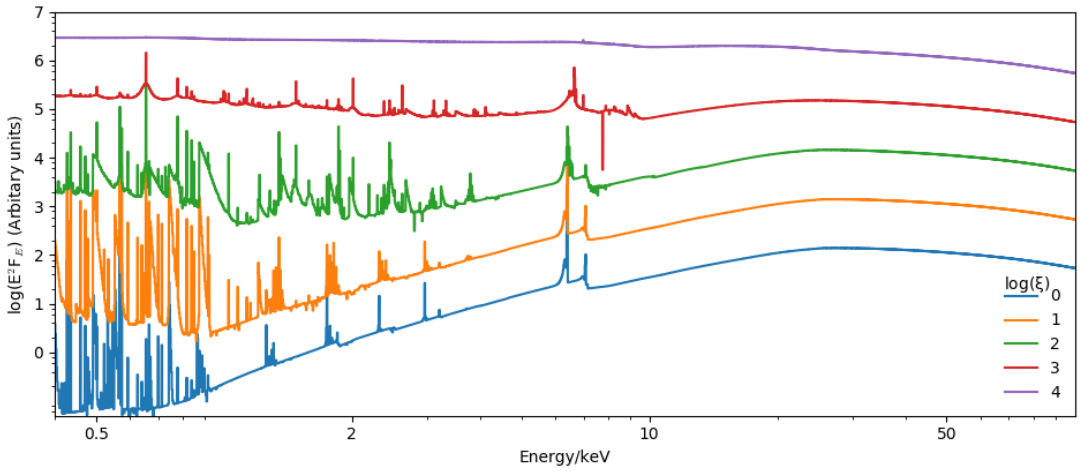

Figure 1.7: Increasing ionisation of disk shows how the reflection spectrum becomes increasingly more featureless.

reflector will produce soft lines while the corresponding ionic species is present. Fig. 1.7 demonstrates how the ionisation of the reflector affects the reflection spectrum, which becomes increasingly more featureless as the ions become stripped of more electrons and Compton scattering begins to dominate over the atomic processes.

Reflection off the disk causes Keplerian velocities to Doppler broaden the observed features. At smaller radii within the disk the orbital velocities can become large (0.2c at 25 R_g). This means that special relativity will boost emission from the advancing side of the wind whilst suppressing the receding side. Finally as the disk extends far into the gravitational well general relativistic effects will redshift the spectrum. These effects are stronger at smaller radii due to being deeper in the potential well.

Fig. 1.8 shows the spectrum after these effects have been applied to the spectra presented in Fig. 1.7 (using relxill; García et al. 2014); this is done for a Schwartzschild (solid) and maximally spinning Kerr (dashed) black hole.

In the lower ionisation cases it is easy to see that the maximal spin distributes more flux to lower energies. The Kerr black hole has a stronger effect due to the increased gravitational

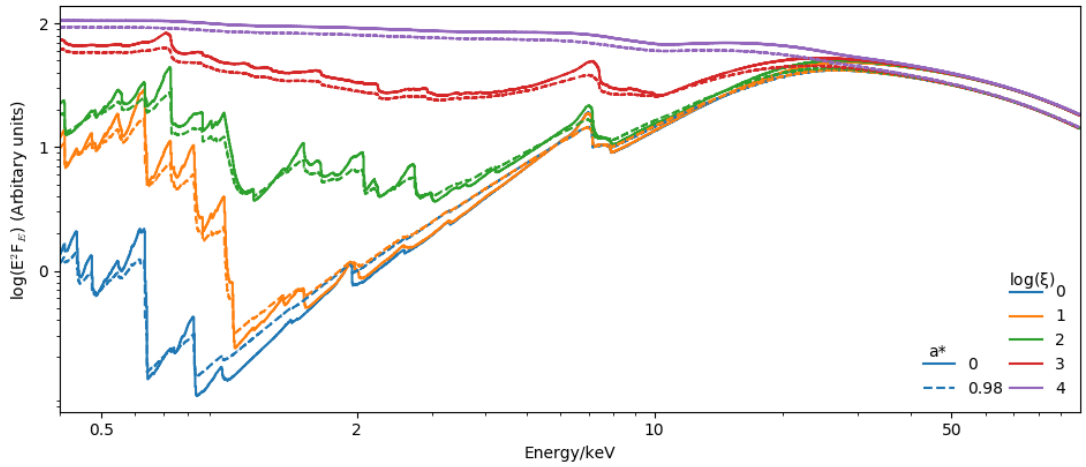

Figure 1.8: The effect of blurring on the reflection spectrum.

redshift as the accretion disk moves deeper into the gravitational well.

1.3.3 The soft excess

Many unobscured AGN show an excess in emission relative to the continuum below $\sim 2\,\mathrm{keV}$ (Singh et al. 1985; Turner & Pounds 1988; Porquet et al. 2004; Nardini et al. 2011, 2012). The origin of this so called "soft excess" is still an open issue. Gierliński & Done (2004); Czerny et al. (2003); Walter & Fink (1993) have shown that the peak energy of the soft excess is almost constant 0.1–0.2 keV over several decades in black hole mass and also does not correlate with measured disk temperature. Therefore it cannot be the direct Wien tail (i.e. hard tail) of the accretion disk, as this would require disk temperatures to exceed expected values, except in perhaps the lowest mass AGN. Instead, Done et al. (2012) proposed that an atmosphere of "warm" electrons could up-scatter the photons from the disk but to a lesser degree than the hot corona which produces the X-rays above 2 keV. Gierliński & Done (2004) noted that this quasi-constant temperature suggests atomic processes. Perhaps

absorption of partially ionised O and Fe which introduce an increase in opacity between 0.7 and 2 keV (seen in the green line in Fig. 1.5) however, the smoothness of the soft excess observed in some AGN (Ark 120 for instance; Reeves et al. 2016) requires an implausible large velocity shear.

Another way of producing the soft excess is through the general relativistic blurring of the disk reflection spectrum (Fabian et al. 2002; Crummy et al. 2006), as shown in Fig. 1.8; where the narrow emission features blend into a quasi-smooth component. This has the added bonus of using the same phenomenon to explain the soft excess, broad iron line and hard excess. However, Boissay et al. (2016) show evidence that the strength of the soft and hard excess does not correlate, suggesting that these would arise from separate components. Once again, the smoothness of Ark 120 poses for this interpretation of the soft excess.

1.3.4 X-ray absorption and spectral signatures of winds

The ionisation potential of hydrogen is 13.6 eV; this means that even the low column of the inter-stellar medium is enough to remove all photons, as disk emission peaks in the EUV (10–70 eV). Therefore AGN can not be studied in one of the most important parts of the spectrum.

The most common intrinsic absorption is the warm absorbers found in $> 60\%$ of AGN (Blustin et al. 2005; McKernan et al. 2007; Tombesi et al. 2013). They are mildly ionised ($\log \xi \sim 0.5 - 1.5$), with columns of $\sim 10^{22}\,\mathrm{cm}^{-2}$ (Tombesi et al. 2013). The ionisation leads to them to appear between 0.5–2 keV, seen in lines such as O VII, O VIII, Fe L-shell. Blustin et al. (2005) estimated that the warm absorbers are observed at distances $\sim$ 1pc away from the black hole. High resolution observations of "warm absorbers" have measured a shift to higher energies of the absorption features, showing these absorbers to be outflowing (e.g. Kaastra et al. 2000; Longinotti et al. 2013; Gupta et al. 2013; Reeves et al. 2016). Outflow velocities (v_{out}) of $\sim 100 - 1,000\ \mathrm{km\,s^{-1}}$ appear to be typical (Tombesi et al. 2013). Even in Ark 120, a so-called "bare" AGN, Reeves et al. (2016) show evidence of a warm absorber in

emission, meaning it is still present in the AGN but lies out of the line of sight.

Fig. 1.9 shows five synthetic spectra produced using the Sim et al. (2010) code (which will be presented in chapter 3). These five spectra show the effects of ionisation on the disk wind with the top spectrum showing absorption features throughout the band pass. Whereas in the bottom spectra blue-shifted Fe XXV Heα and Fe XXVI Lyα absorption lines can be seen in absorption between 7–10 keV. The rest frame energy of the Fe XXV Heα and Fe XXVI Lyα is shown at two black vertical lines so the shift in energy is apparent. The lines can be identified as Fe XXV Heα and Fe XXVI Lyα because Fe is the last cosmically abundant element within that energy range.

These features are found in $30-40\%$ of AGN (Tombesi et al. 2010; Gofford et al. 2013), with $v_{\rm out} \sim 0.05 - 0.35$c they are referred to as ultra-fast outflows (UFOs). The column densities range between $N_{\rm H} = 10^{21}$–$10^{24}\,{\rm cm}^{-2}$ and ionisation ranges between $\log \xi = 2.5$–6 (Gofford et al. 2013). These UFOs can carry mass outflow rates of $\dot{M} \sim 2$ and $\sim 10\,M_{\odot}$ yr^{-1} with $v_{\rm out}$ of 0.15c and 0.3c in PG1211 + 143 (Pounds & Reeves 2009) and PDS 456 (Hagino et al. 2015; Reeves et al. 2016). These features can be variable in both EW and velocity (Gofford et al. 2013); this variability can be a useful tool understand the nature of the outflow this will be demonstrated later in section 4.7.

Along with the highly ionised ultra fast outflows in PG1211 + 143 and PDS 456, we also observed warm absorbers. However, they have much broader profiles ($\sigma \sim 10,000$ km s^{-1}) with outflow velocities faster than what is measured in typical warm absorbers with velocities comparable to the Fe Kα outflows (Reeves et al. 2016; Pounds et al. 2016).

1.3.5 Powering the wind

Winds must be launched in some way. The characteristics of these flows allow a determination of their origin in some cases, but this has long been a contentious issue as in many cases a solution for more than one driving mechanism can be found. However, I will demonstrate later (see section 4.7) how variability of the outflow might allow for a better understanding

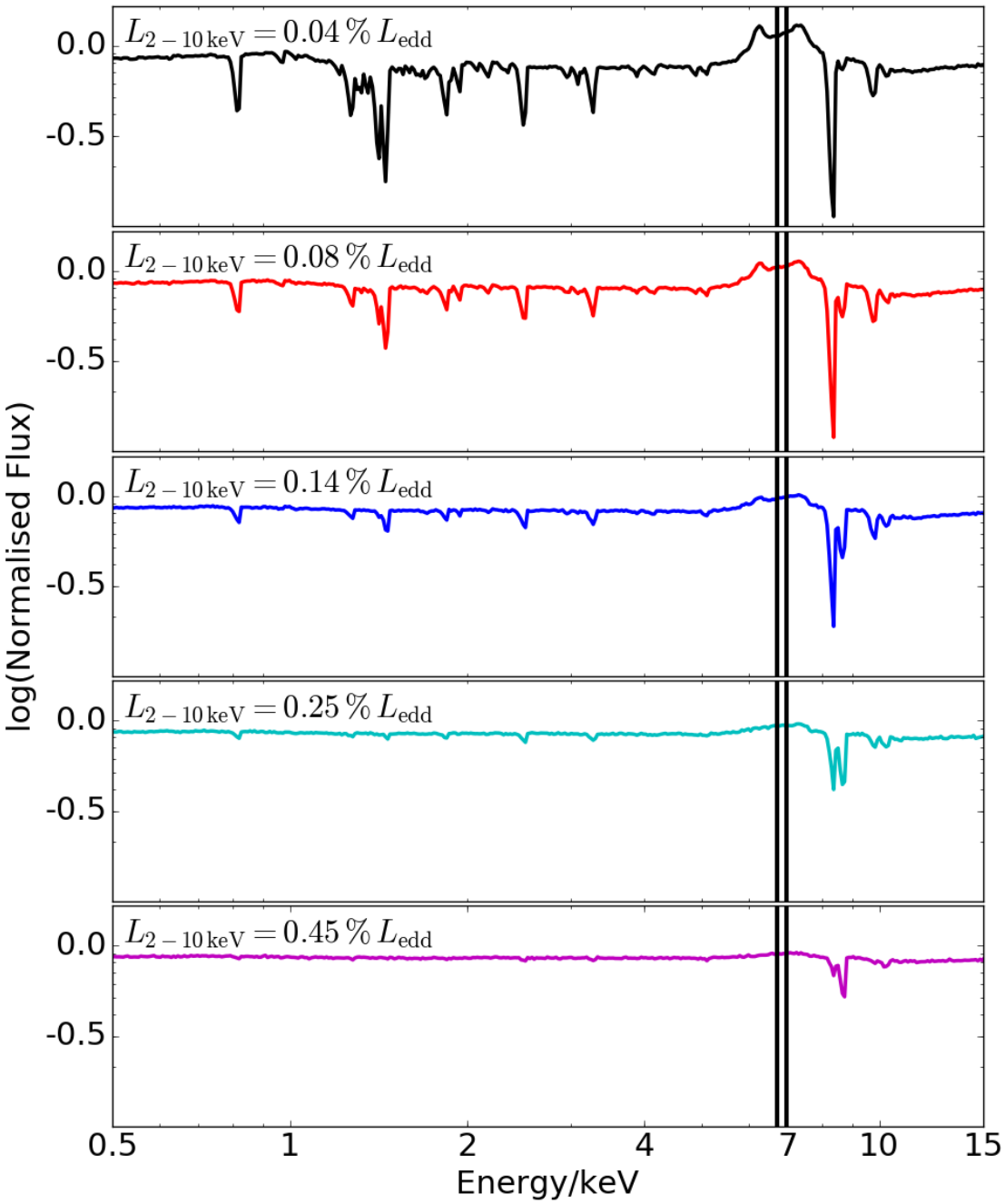

Figure 1.9: Five output spectra from the Sim et al. (2010) disk wind model (which will be presented in chapter 3) showing a disk wind with a mass outflow rate of $5.0\,M_{\odot}$ yr^{-1} illuminated with increasing luminosity. The black lines show the rest frame energies for the He-like Fe Heα and H-like Fe Lyα absorption lines which have been shifted by an observed outflow velocity (v_{out}) $\sim$ 0.2c.

of the physics at work.

Driving mechanisms fall into roughly three categories:

1. Thermal driving: produced by the kinetic motions within the disk as it is heated by the illuminating spectrum.

2. Radiative driving: when momentum is transferred from the radiation field illuminating the wind.

3. Magnetic driving: occurs when charged particles interact with the local magnetic field.

I will now go into the various driving mechanisms in greater detail, but generally winds will only be launched when the driving mechanism allows the material to gain sufficient velocity to overcome the local gravitational potential. This means that the faster winds, which come from the inner disk, will require stronger driving to launch a wind as the gravitational potential becomes larger.

Thermal pressure can drive a wind when the kinetic energy of the atoms in the gas exceed the local escape velocity ($k_b T/m_p \gtrsim v_{\rm esc}^2$). This can occur when the disk surface is irradiated. This is only possible for large radii where the escape velocity is small. This means that thermal winds can reach a maximum velocity of the order $\sim 10,000$ km s^{-1}

Radiative driving occurs when photons transfer momentum to material, which requires high photon flux with a significant cross section. The wind's opacity defines how efficiently momentum transfers from the radiation field. The radiative driving falls into two categories: line and continuum driving.

Line driving occurs when the dominant source of opacity comes from bound–bound absorption. As resonance lines have a large cross section ($10 - 1000\,\sigma_T$), act as "force multipliers" (Castor et al. 1975), if the ionisation is low enough that there are sufficient lines available. This is an efficient way to accelerate material, since the velocity of the atom increases as the continuum is redshifted (with respect to the atom/ion's rest frame) by

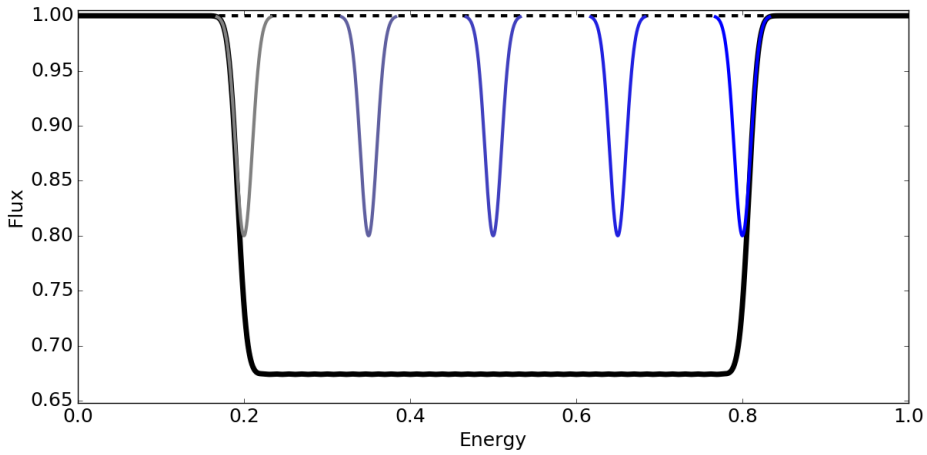

Figure 1.10: Flux (and therefore momentum) absorbed by an accelerating atom/ion from its rest frame (gray Gaussian) to a final velocity (blue Gaussian), with the total absorbed flux shown in black. An accelerating atom can absorb a large amount of flux carving a trough into the observed spectra; these can been seen in BALQSOs.

the relative motion of the atom; this allows the material to absorb more flux which was previously at a higher energy. Fig. 1.10 shows the absorption feature as the ion accelerated. The 5 Gaussians show the absorption feature as it accelerates, with the total absorption trough shown in black.

When the wind is highly ionised, absorption lines do not offer the opacity to drive the outflow. However, the derivation of the Eddington limit shows that outflows will be driven by Compton/Thomson scattering when $L_{\rm bol} \gtrsim L_{\rm edd}$ (King & Pounds 2003; King 2005, 2010). For this to occur the optical depth must be high ($\tau \gtrsim 1$).

Magnetic driving is the coupling of charged particles within the disk and the magnetic field which threads the accretion disk. The theory behind this is encoded into the structure of the magnetic field (Blandford & Payne 1982; Emmering et al. 1992; Contopoulos & Lovelace 1994; Bottorff et al. 1997). The magnetic field accelerates material, channelling it along the field lines and away from the disk. Prescriptions of the outflows have been produced by Konigl & Kartje (1994); Everett (2005); Ohsuga et al. (2009); Ohsuga & Mineshige (2011);

Kazanas et al. (2012); Fukumura et al. (2015). Magneto-centrifugally driven winds differ in overall velocity structure compared to the radiative driven winds. Magnetic winds should have fast orbital velocities due to the material being connected to the field lines, which as previously stated threads the disk, meaning that as material flows outwards it will maintain its velocity, removing angular momentum (Crenshaw & Kraemer 2007).

1.4 The connection between the AGN and its host galaxy

The mass of the SMBH is correlated with properties of the host galaxy's bulge. This shows that the AGN must have an important role in the evolution of the host (or visa versa). Some properties that show tight correlations with black hole mass ($M_{\rm BH}$) are:

- The stellar velocity dispersion ($\sigma_* = \sigma_v/\bar{v}$; Ferrarese & Merritt 2000; Gebhardt et al. 2000; Merritt & Ferrarese 2001; Ferrarese & Ford 2005; Gültekin et al. 2009; Larkin & McLaughlin 2016) which is the dispersion of the stellar velocities; the correlation is known as the $M_{\rm BH} - \sigma_*$ relation and is shown in Fig. 1.11.
- The bulge binding energy (Aller & Richstone 2007).
- The mass of stellar material ($M_{\rm BH} - M_{\rm bulge}$; Marconi & Hunt 2003; Häring & Rix 2004; Reines & Volonteri 2015).
- The luminosity of bulge component ($M_{\rm BH} - L_{\rm bulge}$; Kormendy & Ho 2013).

As the virial theorem links the velocity to the system's potential energy, it therefore provides an indirect estimate of the depth of the gravitational potential well linking the first item to the others.

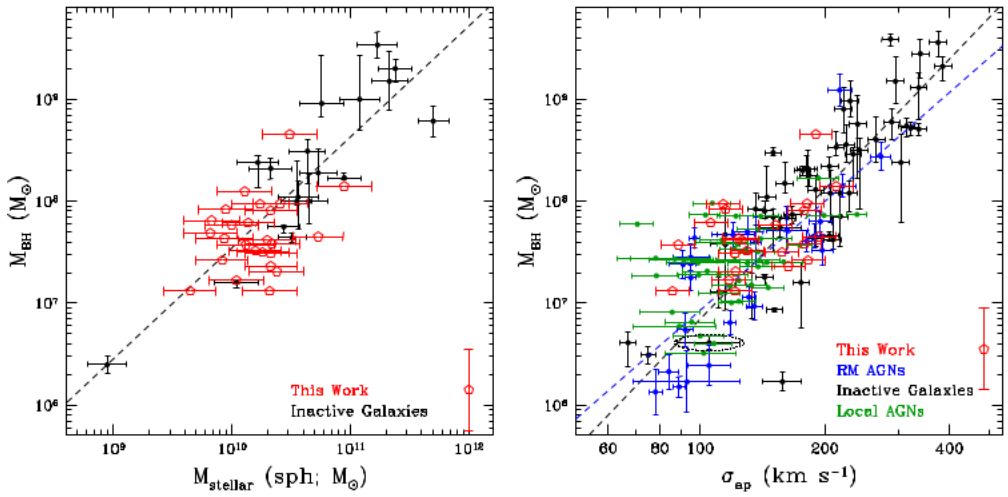

Figure 1.11: The observed correlations of $M_{\rm BH} - M_{\rm stellar}$ (left panel) and $M_{\rm BH} - \sigma_*$ (right panel). 'RM AGNs' refers to AGN with reverberation mapped black hole masses available in literature. 'This Work' refers to the results of Bennert et al. (2011) where these plots were taken from. Note the Milky Way has a $M_{\rm BH} \sim 4 \times 10^6\, M_\odot$ (Gillessen et al. 2009) and is outlined by an ellipse in lower left of the right hand side plot.

1.4.1 The role of feedback

King (2003) and King & Pounds (2003) have shown that disk winds can liberate enough energy produced by the accretion process to unbind the bulge of the host galaxy. As mentioned before these outflows have large mass outflow rates and high velocities, therefore are able to transport large amounts of energy/momentum. For instance the mass outflow rate in PDS 456 is $\sim 10\, M_\odot$ yr^{-1} (Nardini et al. 2015); when combined with a velocity of 0.25c (note $v_{\rm out}$ is variable between 0.25–0.3c in PDS 456 Matzeu et al. 2017) we can calculate the kinetic luminosity ($L_{\rm kin}$):

$$L_{\rm kin} = \frac{1}{2}\dot{M}_{out}\, v_{\rm out}^2 = 1.1 \times 10^{46}\, {\rm ergs\, s^{-1}}. \tag{1.17}$$

If we then integrate the energy over the AGN life time ($\sim 10^8$ yrs) and duty cycle of

an outflow of 0.3 (based on the fraction of AGN with winds) this gives $E_{\rm wind} = 6 \times 10^{53}$ ergs. Assuming that the mass of the bulge $M_{\rm bulge} \sim 10^3 M_{\rm BH} \sim 10^{12}\, M_\odot$ and $\sigma_* \sim 300$ km s^{-1} this makes the binding energy of the bulge: $M_{\rm bulge}\, \sigma_*^2 = 3 \times 10^{52}$ ergs. Even a conservative estimate of the wind's energy output exceeds the binding energy of the bulge by an order of magnitude.

Di Matteo et al. (2005); Hopkins & Elvis (2010) showed that the kinetic luminosity is required to be $L_{\rm kin} \sim 0.5 - 5\%\, L_{\rm bol}$ for the wind to interact with ISM and sweep up star forming material – driving it out from the bulge, and so quenching star formation. The requirement for AGN feedback is also seen in cosmic simulations as without feedback there is nothing to regulate the size of galaxies so they become much more massive than what is observed (Bower et al. 2006). As previously explained outflows can provide a source of feedback. Particularly UFOs, due to their high mass outflow rates and outflow velocity will be the dominant component of AGN feedback in objects in which they are observed. Gofford et al. (2015) found that 85–45% of the 20 AGN with winds exceeded the 0.5–5% $L_{\rm bol}$ threshold.

Warm absorbers, however, are not likely to provide a sufficient source of feedback. This is due to their low mass outflow rates and slow outflow velocity. In objects like PG1211 + 143 and PDS 456 the soft X-ray absorbers are not typical warm absorbers (Reeves et al. 2016, 2018) and have $v_{\rm out}$ comparable to the highly ionised parts of the flow. Whether these absorbers are significant will depend on measuring their filling factor which will require more detailed study.

UFOs and molecular outflows have been discovered in IRAS F11119+3257 (Tombesi et al. 2015), Mrk 231 (Feruglio et al. 2015) and APM 08279+5255 (Feruglio et al. 2017). A connection between the highly ionised outflows observed in the X-rays and the molecular outflow is important as this is likely the same outflow at different size scales and understanding this connection will allow the study of how feedback propagates though the bulge. The bulge being the part of the galaxy with the largest solid angle will be most affected by AGN disk winds.

1.5 Aims of this thesis

Throughout this thesis I will attempt to model the outflows of three well known AGN. I will use a comparison of high and low flux states as an attempt to understand the parameters which drive the observed changes as this allows for a better understanding of the outflows themselves.

Chapter 2 details the observatories used (*Suzaku*, *XMM-Newton*, *NuSTAR*) and fitting techniques that I have used to carry out my research. I also present some background knowledge of some of the models used within this thesis.

Chapter 3 presents the current state of the radiative transfer (Sim et al. 2010) model used throughout my work. I show how the input parameters affect the observed spectra and how this can be used to fit observed spectra.

Chapter 4 introduces Quasar PDS 456, showing a study of the several data sets available from historical *XMM-Newton* observations; a large dataset spanning from 2007 to 2013 with *Suzaku*; and a long campaign of utilising both *XMM-Newton* and *NuSTAR*.

Chapter 5 follows on from Chapter 4 where I apply the (Sim et al. 2010) disk wind model to the PDS 456 datasets, confirming much of the previous work on PDS 456 with a more physically realistic model.

Chapter 6 continues from Chapter 5 and I apply the (Sim et al. 2010) disk wind model to two well studied AGN (PG1211 + 143 and 1H 0707 − 495).

Chapter 7 summarises the major conclusions that I draw from my work and discusses future prospects, presenting a sample of objects to study and possible advancements to the radiative transfer model.

In this thesis three objects will be studied PDS 456, PG1211 + 143 and 1H 0707 − 495. PDS 456 is the most luminous Quasars ($L_{\rm bol} \sim 10^{47}$ erg s^{-1}; Simpson et al. 1999) in the local universe (z < 0.3) and is known to host a powerful outflow ($L_{\rm kin} \sim 15\% \, L_{\rm bol}$; Nardini et al. 2015). The first detection of a UFO outside of BAL QSOs was in the Quasar PG1211 + 143 ($L_{\rm bol} \sim 4 \times 10^{45}$ erg s^{-1}; Pounds et al. 2003). There is evidence that PG1211 + 143 has multiple velocity streams: $v_{\rm out,1} = 0.06 \pm 0.001$ c and $v_{\rm out,2} = 0.188 \pm 0.002$ c (Pounds et al. 2016a). 1H 0707 − 495 is an NLS1 which is likely to be accreting at a super-Eddington rate ($L_{\rm bol} \sim 10^{45}$ erg s^{-1}; Done & Jin 2016) meaning that a powerful disk wind (Hagino et al. 2016) is unsurprising as the derivation of the Eddington limit predicts such an outflow. These objects provide a small sample which covers the full range in $M_{\rm BH} = 10^6$–$10^9 \, M_\odot$.

2 Instrumentation, data analysis and statistical methods

2.1 The current generation of X-ray telescopes

2.1.1 *Suzaku*

The X-ray telescope *Suzaku* was a Japanese Aerospace eXploration Agency (JAXA) mission in collaboration with National Aeronautics and Space Administration (NASA). *Suzaku* was the fifth Japanese mission developed by the Institute of Space and Astronautical Science (ISAS) at JAXA in collaboration with the NASA facility Goddard Space Flight Center (GSFC). *Suzaku* was launched on 10^{th} July 2005 from Uchinoura Space Center in Japan into an almost circular low-Earth orbit at an altitude of ~ 550 km with an inclination of 31.9° and a orbital period of ~ 96 minutes. The payload consisted of two main instrument sets, the first of which comprised of five grazing incidence (Wolter type 1) telescopes (XRT; Serlemitsos et al. 2007) leading to four imaging detectors (and a micro-calorimeter) and the second a non-imaging, collimated Hard X-ray Detector (HXD; Takahashi et al. 2007). The XRT's led to four silicon-based charge coupled devices (CCDs) called the X-ray Imaging Spectrometers (XIS; Koyama et al. 2007) and the X-ray micro-calorimeter (XRS; Kelley et al. 2007) all of which were positioned in the focal plane of the XRT. The XRS was lost shortly after launch when it lost its coolant[1] while the XIS and HXD continued to function until the project's termination on 26^{th} August 2015 by JAXA[2] (two years after the intended lifetime of the experiment), citing battery and communication problems as the root cause.

[1] NASA XRS Press release: http://heasarc.gsfc.nasa.gov/docs/astroe/news/xrsend.html
[2] JAXA Termination Press release: http://global.jaxa.jp/press/2015/08/20150826_suzaku.html

The X-ray Imaging Spectrometer (XIS)

The XIS CCD detectors are the primary *Suzaku* instruments used throughout my work. The detectors are sensitive in the 0.2–12.0 keV range with a spectral resolution of ~ 130 eV at 6 keV, with a field of view (FOV) of $17'.8 \times 17'.8$. The X-ray CCDs come in two types: front and back illuminated (FI and BI respectively). The FI detectors (XIS 0, 2 and 3) are more sensitive to harder X-rays due to the larger penetration depth, whereas the BI XIS 1 is more sensitive to soft X-rays. Unfortunately XIS 2 became inoperable[3] due to a suspected micrometeorite impact on 9$^{\text{th}}$ November 2006.

CCDs convert photons into electron clouds, with electrical charge trapped in potential wells within the detector. The charge is transferred from pixel to pixel on read-out, until it finally reaches the read-out amplifier and is digitised (a PHA event). X-ray CCDs are generally set to photon-counting mode whereby the position and energy of each photon can be found. This requires that only one photon interacts with a given pixel in between read-outs. If more than one photon is detected (for instance in a high count rate source), then the charge produced will be the sum of the charge produced from the single events. Therefore multiple lower energy photons can be mistaken for a single higher energy photon; this is known as "pile-up". This causes a lower recorded count rate and spectral hardening.

2.1.2 *XMM-Newton*

XMM-Newton (Jansen et al. 2001) is a mission by the European Space Agency, launched on 10$^{\text{th}}$ December 1999 into an elliptical orbit (with an apogee of $\sim 1.1 \times 10^5$ km and a perigee of $\sim 1 \times 10^4$ km with an eccentricity of ~ 0.8 at an inclination of $\sim 66°$). This allows for long periods of uninterrupted observations. However, leaving the protection from Earth's magnetosphere means that *XMM-Newton* suffers from a high background during parts of the observations; these are removed during data reduction.

[3]XIS anomaly: ftp://legacy.gsfc.nasa.gov/suzaku/doc/xis/suzakumemo-2007-08.pdf

XMM-Newton's payload consists of three sets of detectors: the European Photon Imaging Camera (EPIC), the *XMM-Newton* RGS and the *XMM-Newton* OM. *XMM-Newton*'s EPIC consists of three detectors, the first of which is the PN CCD array (Strüder et al. 2001) with a FOV of $27'.5 \times 27'.5$ and a spatial resolution of $61''$ FWHM. This has a band pass of 0.1–15 keV with a spectral resolution $E/\Delta E \approx$20–50. The PN is FI in contrast to the second detector, the Metal Oxide Semi-conductor (MOS; Turner et al. 2001) detectors which are BI CCDs. They have a FOV of $33' \times 33'$, cover the same band pass as the PN and have nominally the same spectral resolution. However the MOS detectors only receive $\sim 44\%$ of the flux as the rest is redirected to the Reflection Grating Spectrometer (*XMM-Newton* RGS; den Herder et al. 2001). The grating spreads the incoming spectrum over the CCD array, removing one of the spatial axes by exchanging it for energy. This gives much higher spectral resolution ($E/\Delta E \approx 200 - 800$) but greatly reduces the throughput of the optics. Finally *XMM-Newton* has an optical/UV telescope known as the optical monitor (OM; Mason et al. 2001). This has a FOV of $\sim 17'$ and spatial resolution of $\sim 1''$ with 6 band filters: V (580–510 nm), B (490–390 nm), U (390–300 nm), UVW1 (345–320 nm), UVM2 (245–205 nm) and UVW2 (225–180 nm).

2.1.3 *NuSTAR*

The Nuclear Spectroscopic Telescope ARray (*NuSTAR*; Harrison et al. 2013) is the most modern X-ray telescope used in this work and it was the first focusing high-energy X-ray telescope when launched (13^{th} June 2012) into its elliptical (650 km apogee and 610 km perigee) orbit (with a 6° inclination). Focusing hard X-rays requires for low scattering angles, therefore a long focal length, so *NuSTAR* has a long mast of 10 m. *NuSTAR* covers a FOV of $12' \times 12'$ and operates in the band from 3 to 79 keV with a spectral resolution of 0.4 keV at 6 keV and 0.9 keV at 60 keV (FWHM). The ability to focus photons has the benefit of a low background, in *NuSTAR*'s case, $1.1 \times 10^3\,\text{cts}\,\text{s}^{-1}\,\text{arcmin}^{-2}$ between 10–30 keV, making it at least two orders of magnitude more sensitive than the *Suzaku* HXD (above 10 keV). The

lower background in turn lowers the 3σ detection limit to $1 \times 10^{-14}\,\mathrm{erg\,s^{-1}\,cm^{-2}}$ (over the same band pass) for 1 Ms exposure.

2.2 Software

These tasks often are sometimes contained specific to the mission and are contained within mission-speific software suites (*NuSTAR*: nutardis; *XMM-Newton*: XMM-SAS). Telescopes produce tools for reduction of their data such as event selection and producing response files. Other tools are more generic such as FTOOLS which provide generic functionality for manipulating fits files. An important collection of software is *HEASoft* which is combination packages for analysis (such as XSPEC) and data reduction (such as XSELECT). It also includes XSTAR a code for producing spectra of photo-ionised gas (Bautista & Kallman 2001). XSELECT[4] is particularly useful as it acts standard interface to other tools with some sane defaults which simplifies the data reduction process. Once the data are in a usable form (generally spectra in this work) the higher level analysis tools are used. There are many X-ray spectral fitting packages that apply theoretical X-ray models to the data through the use of fitting algorithms and allow the construction of complex models. XSPEC is the software used throughout this work, as it has a simple command driven interface (with good documentation) and contains a large catalogue of X-ray models. Another strong point of XSPEC it that is allows users to provide their own models; this means there is some important suite of community built models.

[4] XSELECT User guide: https://heasarc.gsfc.nasa.gov/ftools/xselect/xselect.html

2.3 Data reduction

Analysis of the raw data received from the telescopes mentioned above requires many pieces of software. An overview is given of the software used for many data reduction and analysis tasks and the methods they employ. The focus will be on the data reduction steps for *Suzaku*'s XIS, but the general steps are the same for each telescope. The reduction and analysis of data from any given telescope is usually done using some form of software, which generally perform one or more steps in the following tasks:

- screening: filtering of photon detections (events) such as removing dead/hot pixels and "grading" events (explained below) and removing periods of high background;
- region selection: filtering of events based on the area of the detector done to produce source and background data sets;
- event selection: filtering for investigation purposes such as splitting up a longer observation into parts;
- producing data products: such as images, spectra and/or light curves for analysis;
- generation of response files which are used to account for the detector.

2.3.1 *Suzaku* data reduction

The data used in the subsequent chapters comes from a variety of telescopes. The steps taken in the reduction of XIS data are reasonably representative of all X-ray observatories used in this work – depending on the source/telescope there may be some subtle differences.

On completion of an observation, the PHA events and any relevant meta-data are output into a multi-layered FITS (Flexible Image Transport System) file, these event files are then processed via the telescope's pipeline and made available to the researcher and

after a period of time (depending on the telescope) is then made available to the public via on-line archives (such as heasarc). Before these "raw" event files can be useful for analysis they must first undergo several steps of screening which be presented next.

2.3.1.1 Screening

Raw data need to be screened to remove contaminants from the data. Contaminants come in many forms, from dead/hot pixels to charged particles and cosmic rays. Screening is done to remove contamination form the events. The *Suzaku* team present a list of criteria for science data which are followed to remove most "bad" data; these vary from pointing/orbiting information to instrumental information. A detector-level constraint comes from events being spatially resolved over the CCD; this allows events to be "graded"[5] (which is the spatial distribution of charge) as photons will distribute charge differently to charged particles for instance.

One of the orbital constraints is due to the South Atlantic Anomaly (SAA) which is a region of the atmosphere where the Van Allen radiation belts extend closer to the Earth's surface. As this contains high energy particles no useful data can be obtained by the low Earth telescopes (such as *Suzaku* and *NuSTAR*); this can be seen in table 2.1 with "SAA_HXD==0" and "T_SAA_HXD>436", the second of which gives time for radioactive products of the particle bombardment to decay. Other obvious constrains on the telescope pointing are making sure the telescope pointing is with a small angular distance of the source. Also the pointing must not be too close to bright pollutants such as the Sun, along with the Earth and Moon which can scatter some solar X-rays.

[5]ASCA Grades: http://www2.astro.psu.edu/xray/docs/TARA/TARA_users_guide/node12.html

Criterion	Comments
GRADE=0, 2, 3, 4, 6	ASCA grades indicating X-ray events
STATUS=0:524287	Bad columns, charge injection rows removed
cleansis	Flickering pixels are removed
ANG_DIST<1.5	Instantaneous pointing within 1.5 arcmin of mean
Sn_DRATE<3	Telemetry rate SuperHigh, High, or Medium
SAA_HXD==0	Satellite is outside SAA
T_SAA_HXD>436	Time since SAA passage >436 sec
ELV>5	Pointing direction >5 deg above Earth
DYE_ELV>20	Pointing direction >20 deg above sunlit limb of Earth

Table 2.1: Screening criteria of events for the XIS. SAA: South Atlantic anomaly

2.3.1.2 High-level data products

This is done as a part of the initial pipeline so that clean event files can be downloaded from archives such as heasarc. These event files can be used for producing scientific products. To produce high-level scientific products a series of event selection steps take place, these steps are carried out using XSELECT. The first of which is spatial event selection, this is done by producing an image of the events and selecting regions for the source (typically a circle with a radius $\sim 1.5'$) and background (typically one or more circles with an equal or greater area). For each of these regions light curves can be extracted, these can be investigated on their own or used to select periods of interesting behaviour or high background count rate. After any time filtering spectra are also extracted for each region.

Before spectra can be analysed, two response files are generated, these are: the *Redistribution Matrix File* (RMF) and the *Ancilliary Response File* (ARF) and are generated by using XISRMFGEN[6] and XISSIMARFGEN[7] respectively (which are packaged within *HEAsoft*).

[6]NASA's help page for XISRMFGEN: http://heasarc.gsfc.nasa.gov/ftools/fhelp/xisrmfgen.txt
[7]NASA's help page for XISSIMARFGEN: http://heasarc.gsfc.nasa.gov/ftools/fhelp/xissimarfgen.txt

The RMF is used to define the probability of a photon of given energy being detected by a particular channel, hence it encodes the energy resolution and mapping of the channels into energy. The ARF is defined as the energy-dependent effective area of the telescope and detector system (in cm^2). Both RMF and ARF are indispensable components in the overall instrument response and therefore required to produce the flux spectrum.

Channels can then be grouped to increase signal to noise within a bin, this is performed using the GRPPHA tool. Another use of GRPPHA is to set headers in the FITS file of the source pointing to the background and response files, this is done so that XSPEC can import them together.

2.4 Outline of X-ray spectral analysis

Once the spectra and response files have been generated, they are then loaded into a spectra fitting package (nominally XSPEC), these fitting packages define convenient subroutines for loading data, applying models and optimising their parameters.

2.4.1 The 'forward-fitting' technique

To optimise the models the "forward-fitting" technique is employed. In this method the user provides a physically motivated model which is then calculated over the energy range and convolved with the detector response functions. This is then compared to the observational data. The model parameters are then adjusted to reduce the fit statistic (see section 2.4.2). This is repeated until the change in fit statistic drops below a tolerance (or a maximum number of iterations). This is illustrated in the flow chart in figure 2.1. Note this method is employed as deconvolution is less stable than convolution, especially due to the non-Gaussian distributions within the RMF.

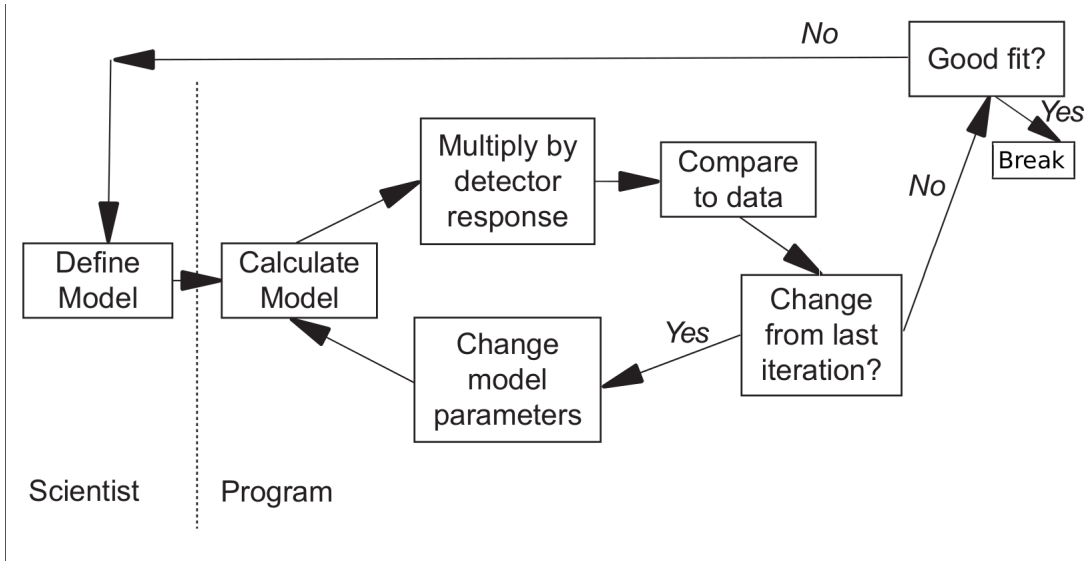

Figure 2.1: The forward-fitting technique used in X-ray astronomy is performed by calculating the result of the model parameters convolving with the detector response functions then comparing with observed values. This is applied iteratively, with changes in the parameters applied based on an optimising function, until a break condition is met (typically a maximum number of iterations or minimum change in fit static).

2.4.2 Fit statistics

Fit statistics are used by optimisation algorithms to assess how well a model with a given set of parameters represents the data. There are many possible statistics which can be used depending on the properties of the data.

In the Gaussian limit the probability of observing D_i events in bin i of data set D, given a predicted count rate M_i is:

$$P(D_i) = P(D_i|M_i\sigma_i) = \frac{1}{\sigma_i\sqrt{2\pi}} \exp\left[\frac{(D_i - M_i)^2}{2\sigma_i^2}\right], \tag{2.1}$$

where σ_i is the standard deviation (or error) in each count per channel i (thus σ_i^2 is the variance) and is usually estimated as $\sqrt{D_i}$ by X-ray data analysis packages.

The χ^2 distribution assume that the data are distributed as a Gaussian, therefore

data are nominally grouped into $\gtrsim 20$ counts per bin, to produce this via the central limit theorem. The χ^2 distribution is given by:

$$\chi^2 \equiv S^2 = \sum_{n=i}^{N} \frac{(D_i - M_i)^2}{\sigma_i^2}. \tag{2.2}$$

The Chi-Squared (χ^2) is used throughout this thesis as it has some convenient features. For instance, the 90% interval for a given parameter can be found by varying the parameter until a change of $\Delta\chi^2 = 2.71$ from a minimised value of χ^2. For multiple free parameters this value increases, the change required can be found in using the cumulative probability function for the required confidence interval. Another useful feature of the χ^2 statistic is that it is easy to modify to include background data, by making $D_i = D_{\mathrm{src,i}} - D_{\mathrm{bkg,i}}$ and $\sigma_i^2 = \sigma_{\mathrm{src,i}}^2 - \sigma_{\mathrm{bkg,i}}^2$, making it convenient for use with dealing with spectra.

As with any fit statistic, local minima occur in χ^2 space for complex models. This causes models to become stuck in parts of the parameter space where moving in any direction produces an increase in the fit statistic, this can be seen schematically in Fig. 2.2. Features such as this often occur when fitting absorbers, as two features with different parameter space can fit the same observed line. This is mitigated by searches of the parameter space during error calculations.

χ^2 has an easy goodness of fit statistic known as the reduced χ^2, which is given by χ^2/ν (where ν is the degrees of freedom, which is the number of data points minus the number of free parameters). Reduced χ^2 allows the assessment of the validity of a model. For instance a $\chi^2/\nu = 1$ means that the data are on average distributed 1σ away from the model and hence they are consistent. When $\chi^2/\nu \gg 1$ then it is unlikely that the data are drawn from the model and if $\chi^2/\nu < 1$ then the model is too complex or the error bars of the data have been overestimated.

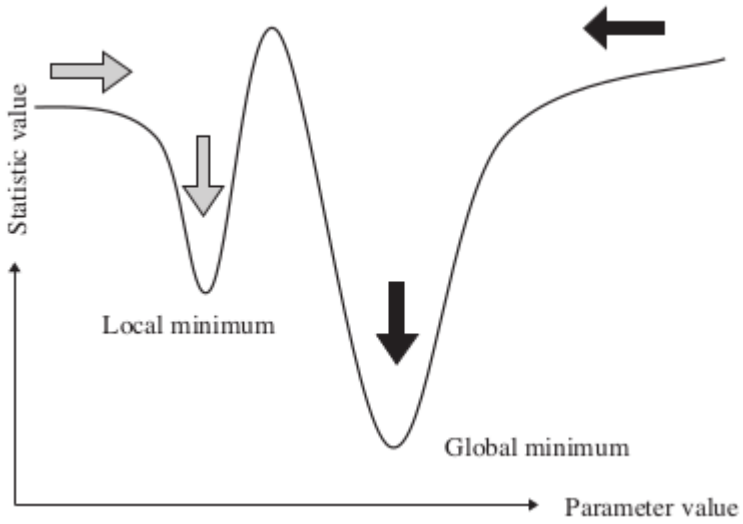

Figure 2.2: A representation of local minima when compared to global minima.

2.5 Models

This section will describe the models which are used in the analysis of objects in chapters 4, 5 and 6. Models can be separated into two categories: primary emission and reprocessing models. These models can provide a means of understanding the physical processes that produce the observed spectra. These models can be either ad hoc (e.g. a Gaussian line or power law) or more representative of the underlying physical processes which may be occurring (e.g. a photo-ionisation model). In chapter 3, a disk wind model will be introduced, which will be used in the later chapters 5 and 6.

Within XSPEC, models are provided in two flavours, ones prefixed with "z" allow the output to be redshifted, these are often used to shift output spectra to the rest frame of the source.

2.5.1 Primary emission

A common initial phenomenological step used in the literature is to parameterise the X-ray continuum by a combination of a power law and black body, usually modelled in XSPEC as (`powerlaw` + `bbody`). A more realistic model would be that of a self-consistent Comptonisation model such as `optxagnf` (Done et al. 2012) which should yield a better representation of some key X-ray features. The equation for a power law is:

$$F(E) = kE^{-\Gamma}. \tag{2.3}$$

A simple power law approximates the hard X-ray continuum above 1 keV (over a narrow enough range), below the high energy cut-off. The roll-over occurs at energies three times that of the "hot" coronal electrons, which is a feature in Comptonisation models. However, a power law is often sufficient.

The soft excess — the spectral region which often shows an excess when compared to the power law of the continuum — is often fitted with a black body, although once again it is probably produced by Comptonisation in some form of "warm" corona. The equation for a black body is described by:

$$B(E,T) = \frac{K8.0525E^2dE}{(k_bT)^4[\exp(E/k_bT) - 1]} \tag{2.4}$$

where $K8.0525$ [8] is a normalisation factor, k_b is the Boltzmann constant and T is the temperature of the black body emitter. Finally Gaussian profiles are generally used as an ad hoc probe of individual emission and absorption lines.

[8] See: https://heasarc.gsfc.nasa.gov/xanadu/xspec/manual/node137.html

2.5.2 Absorption

2.5.2.1 Neutral absorption

The attenuated flux through an absorber is:

$$F(E) = F_0 \exp[-N_{\rm H}\sigma E(1+z)], \tag{2.5}$$

where $N_{\rm H}$ is the integrated line of sight column density and σ is the energy-dependent photon scattering cross section. A neutral absorption model used in this work is `Tbabs` (Wilms et al. 2000). If not all sight-lines to the source intercept the absorber then some of the primary continuum leaks through. This can be represented as:

$$F(E) = [f_{\rm cov}\texttt{absorber}(\texttt{E}[\texttt{z}+\texttt{1}]) + (\texttt{1}-\texttt{f}_{\rm cov})] \times \texttt{continuum}(\texttt{E}[\texttt{z}+\texttt{1}]), \tag{2.6}$$

where $f_{\rm cov}$ is the fraction of the source covered by the absorber, thus $1 - f_{\rm cov}$ gives the fraction of the primary continuum observed directly.

2.5.2.2 XSTAR

XSTAR calculates the absorption and emission spectra of photo-ionised gas for a spherical shell of gas for a given set of input conditions, such as the density, ionising luminosity, continuum shape and velocity turbulence. The *xstar2xspec* script is used to generate a grid model for a range of input parameters by combining the spectra output from individual XSTAR runs.

Although absorbers (especially outflows) are thought to have complex geometries (Proga et al. 2000; Nomura et al. 2016), it provides a detailed database of atomic transitions observed in the X-ray energy range. Therefore XSTAR is often used as an initial probe of the wind conditions (Reeves et al. 2003, 2009; Nardini et al. 2015; Hagino et al. 2015, 2016,

2017). A more realistic geometry is employed by the Sim et al. (2008) and Sim et al. (2010) model which will be presented in detail in the next chapter.

3 Production of synthetic spectra

3.1 Radiative transfer

To understand the effects of winds the parameter space they occupy must first be discerned. As mentioned in section 1.3.4, this has been done using statistical methods on samples of high quality archival data by Tombesi et al. (2010, 2011) and Gofford et al. (2013, 2015) using *XMM-Newton* and *Suzaku* data respectively. Instead I attempt to construct synthetic spectra in an attempt to reproduce the observed datasets so the conditions of the outflows can be inferred. To produce these spectra I use a 3D radiative transfer code in order to explore the observational effects of the parameters and the conditions in which the signature absorption features of outflows could be expected.

Sim et al. (2008) performed 3D radiative transfer on a bi-conical wind structure in order to produce predicted broad-band spectra, which they then compared to the NLS1 Mrk 766, showing the blue-shifted absorption feature which has already been discussed, as well as the broad Fe Kα emission features often observed in AGN. Sim et al. (2010) improved the code with an extended atomic database which defines more atomic transitions, making the resultant spectra more accurate over a larger range of photon energies. This then allows the treatment of ionisation and radiative heating by self-consistently calculating the heating and cooling of the electrons based on the "photon packets" (the computational structure used in the simulations) passing through the wind structure. This allows temperature gradients to be calculated, therefore providing a more physical representation of the ionisation structure of the wind. The process is repeated to define the heating and cooling rates for the wind. After the heating and cooling rates have stabilised, the photon packets are collected, then grouped into bins based on their angle from the Z axis. Inclination bins are defined so that each bin has the same solid angle. Sim et al. (2010) is version of the code that will be used throughout the rest of this work.

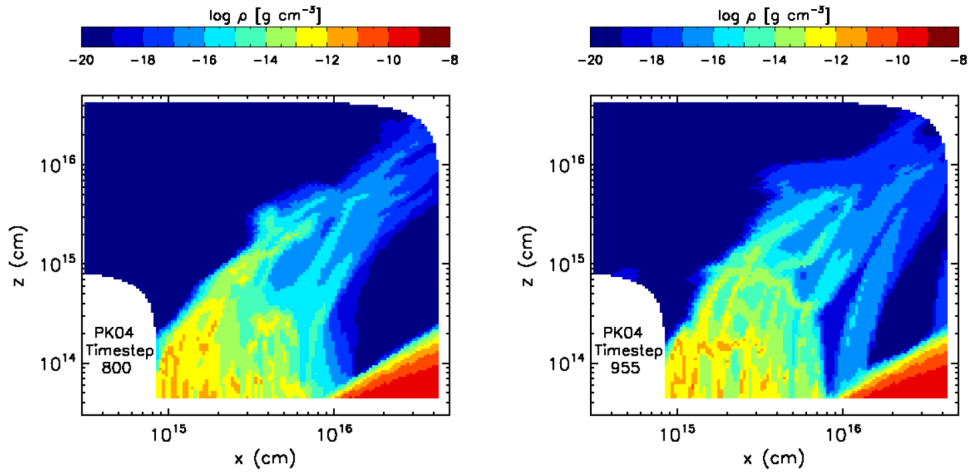

Figure 3.1: The density structure of the Proga & Kallman (2004) disk wind of two time steps separated by 5 years, taken from Sim et al. (2010), showing the inhomogeneous nature of the radiatively driven disk wind.

In Sim et al. (2010), the radiative transfer of complex geometries were studied. These geometries are the results of hydrodynamical simulations of a radiatively driven disk wind presented in Proga & Kallman (2004). These simulations provide time-dependent density and velocity structures, which were then used as input to the radiative transfer code. Two time steps (separated by 5 years) were selected to be studied. The density maps of these time steps can be seen in Fig. 3.1, showing the filaments and small scale structure within the flow. Fig. 3.2 shows the charge of iron in these time steps, where it can be seen that the denser filaments shield the less dense parts — allowing for a lower ionisation than might be expected for the low densities in Fig. 3.1. This leads to the comparative smoothness of the wind ionisation in Fig. 3.2.

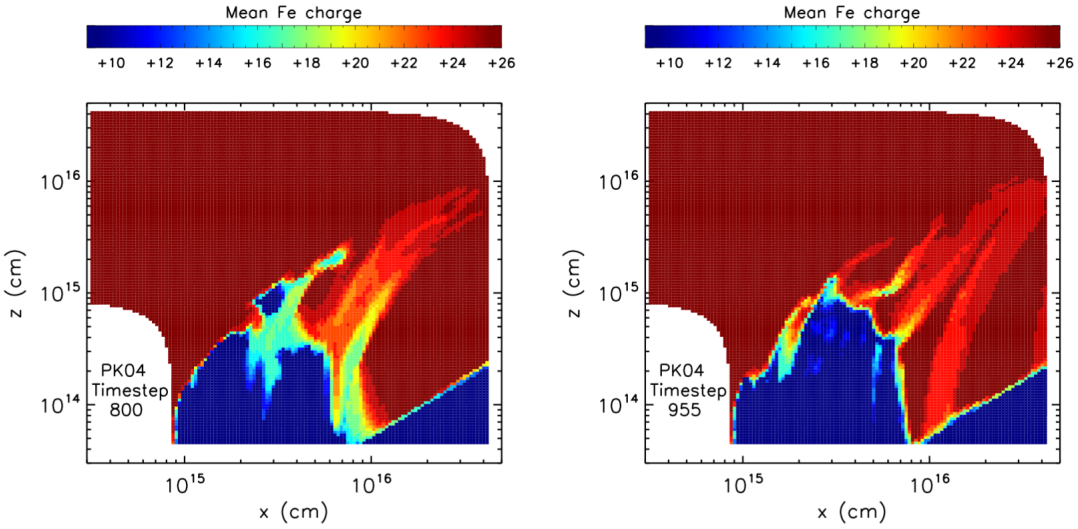

Figure 3.2: The ionisation structure of the Proga & Kallman (2004) time steps. The effects of shielding can be seen where the less dense parts have lower ionisation than might be expected. The denser areas (e.g. $x < 10^{16}$ and $z < 10^{15}$ cm) shield the lower-density gas filament at $x \sim 10^{16}$ cm preventing it from becoming fully ionised. Figure taken directly from Sim et al. (2010).

Fig. 3.3 shows that the emergent spectra from the two time steps are vastly different. The left panel shows a narrow feature associated with Fe XXVI Lyα absorption at ~ 7 keV, which increases in velocity, depth and breadth at larger inclinations, whereas the right panel shows weaker, broader features. This disparity between spectra poses problems as having no direct control on the flow parameters means fitting over multiple time steps which could have vastly differing spectra.

The inhomogeneities, while more realistic, may pose problems fitting the parameters which I can control. As differing sight lines can have similar column densities because of intercepting local clumps within the flow, this can produce minimisation problems (e.g. local minima in χ^2 space), leading to solution which is not unique with this set up. This aspect could be investigated in the future in terms of the partial covering of the X-ray source by clumps within the flow. To avoid these problems in this work I have adopted a

simple homogeneous bi-conical structure as presented in Sim et al. (2008) and subsequently expanded on in Sec. 3.2.

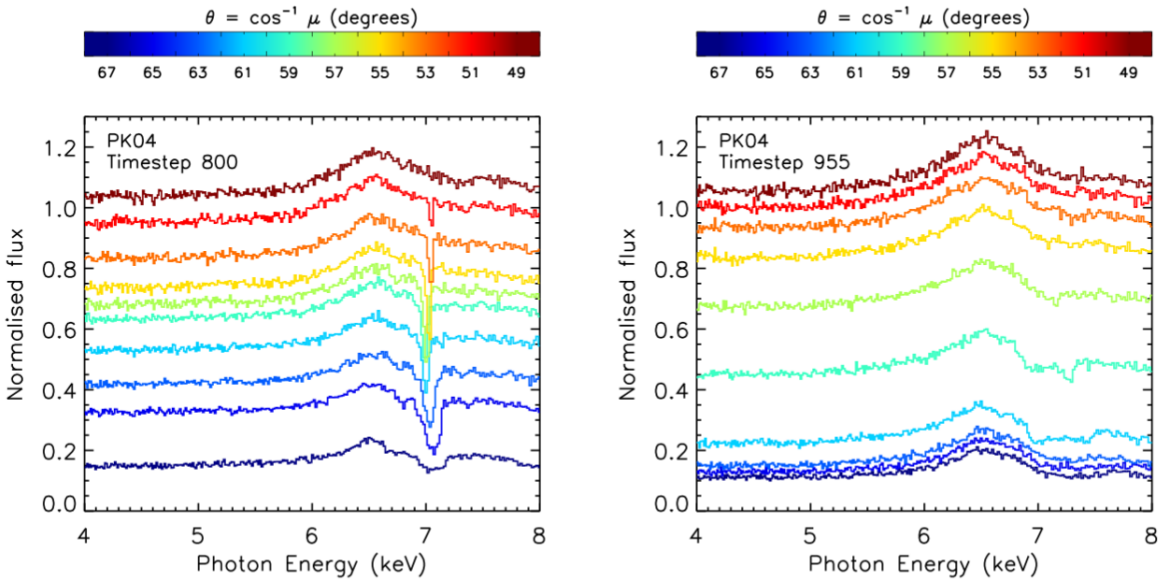

Figure 3.3: The spectra of each inclination of the Proga & Kallman (2004) two time steps showing that each time step has vastly different spectra showing the specificity of the more complex structures. Figure taken directly from Sim et al. (2010).

3.1.1 Other models

A model similar to the Sim et al. (2008) is defined and used in Hagino et al. (2015) (MONACO: MONte Carlo simulation for Astrophysics and COsmology), which is then subsequently used in Hagino et al. (2016, 2017) to fit the disk winds in PDS 456, 1H 0707 − 495 and APM 08279+5255 . The same bi-conical structure is used although the formation of the structure is slightly different (see fig. 3 in Hagino et al. 2015). MONACO separates the wind structure into shells and then performs a series of XSTAR runs to ascertain the ionisation balance and the luminosity leaving and entering each cell. The radiative transfer is then performed using the He-like and H-like iron and nickel transitions along with Compton scattering. This

has the benefit of being less computationally expensive than the Sim et al. (2010) code as the higher the number of lines which are tracked, the more computationally intensive the simulation. Therefore, the limited number of transitions allows quicker exploration of the parameter space. The argument for only tracking the highly ionised species is that the high-velocity winds that are typically highly ionised. However lower ionisation species can survive in thicker winds requiring them to considered. These lower ionisation species may be observed at lower energies such as the lower ionisation lines, observed in *XMM-Newton* RGS spectra of many AGN. In PG1211 + 143 (Pounds et al. 2016a) and PDS 456 (Reeves et al. 2016) these soft features have been strongly linked with the highly ionised outflow. These features may be studied in more detail in the future by lowering the ionisation in runs. This can be done by either lowering the source luminosity or increasing density through clumps within the streamlines.

3.1.2 Physical processes

The predictive power of radiative transfer comes from modelling how photons interact with matter as they move through a simulated wind. The physical processes governing the propagation of the photon packets through the material of the wind are: (i) bound–bound (line) transitions, (ii) bound–free absorption (photo-electric effect, absorption edges and the Auger process) including subsequent recombination, and (iii) free–free processes (e.g. Compton scattering), as described in chapter 1. The dominant form of reprocessing within the wind is Compton scattering by free electrons due to the highly ionised nature of the flow. This means that He, H and many of the lighter elements (up to N) will be fully ionised even in the "low" ionisation runs (see Fig. 3.11 below). The heavier elements (limited at Ni in "low" ionisation simulations) will be at least partially ionised, resulting in free electrons. Within the model I assume the electron temperature (typically $\sim 8 \times 10^6$ K, equivalent to a photon energy of ~ 0.7 keV) is low enough such that inverse Compton scattering can be ignored. The emission from excited states, following photo-absorption or bound–bound

absorption, is calculated using the macro-atom scheme devised by Lucy (2002, 2003).

3.2 Input parameters

3.2.1 Geometry

As discussed earlier, a simple geometry allows fitting with a small set of defined parameters. For instance the bi-conical structure (see Fig. 3.4) requires only three geometric values to construct, reducing the number of parameters which need to be inferred. $R_{\rm in}$ is the distance from the origin to the inner edge of the wind in the equatorial (xy) plane. $R_{\rm out}$ is the distance from the origin to where the outer edge of the wind intercepts the xy-plane. The third parameter is the distance to the focal point of the wind below the origin. This is called d and is typically set to the same value as $R_{\rm in}$. Lines extending from d intercepting $R_{\rm in}$ and $R_{\rm out}$ produces a quarter of the bi-conical wind, which is then made symmetric under rotation in the azimuthal direction (around the z axis) and reflected in the xy-plane. To define the X-ray source the centre point of a sphere is placed at the origin, with a radius $R_{\rm src}$. $R_{\rm src}$ is set to $6\,R_{\rm g}$, which was inferred from the hard X-ray flares in PDS 456 and is assumed to be a reasonable size for the X-ray source by Matzeu et al. (2016).

In an object such as PDS 456 with a black hole mass $\sim 10^9\,M_\odot$ $6R_{\rm g}$ comes to $\sim 9 \times 10^{14}$ cm. Assuming the outflow velocity is close to the escape velocity of material within the disk this means that $R_{\rm in}$ must lay between 10s to 100s of $R_{\rm g}$ to match the observed velocities in UFOs (see section 3.2.9) with the faster outflows having a smaller $R_{\rm in}$. $R_{\rm out}$ will likely be of the same order of magnitude as $R_{\rm in}$. So $R_{\rm in}$ and $R_{\rm out}$ will likely be in the range of a few 10^{15}–10^{16} cm.

It is assumed that the source is far enough from the black hole that photon trajectories are not significantly altered by the effects of general relativity. This means the photon packets distributed over the surface are initially radiated isotropically. While photons propagate through the wind, photons which intercept the x–y plane are considered to be lost – rather

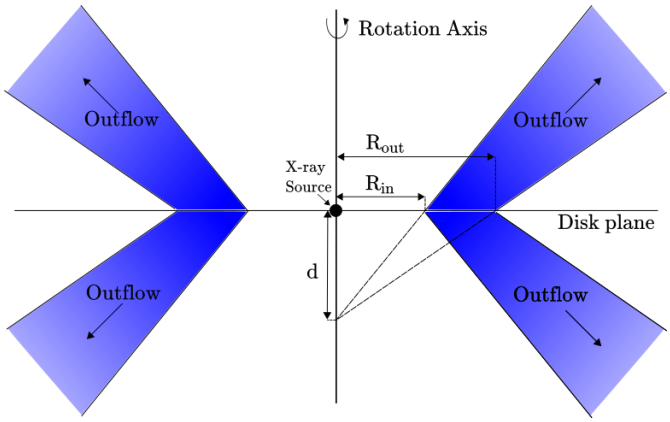

Figure 3.4: The bi-conical shape adopted for the wind model. The 2D geometry is defined with three parameters: $R_{\rm in}$, $R_{\rm out}$ and d. $R_{\rm in}$ and $R_{\rm out}$ represent the radii at which the inner and outer edges of the wind intercept the disk plane respectively, and d defines the focus of the wind below the disk plane, which controls the degree of collimation and opening angle of the wind and is generally set to be equal to $R_{\rm in}$. This structure is then rotated around the z axis and mirrored in the disk plane to produce the structure.

than scattered/reflected. A full treatment of disk reflection is currently being worked on, however it is not touched on in this work and the effect on the results would be minimal over 0.5–10 keV band pass as only a small number of photons are lost to the disk. However, it may be a factor observing at higher energies around the Compton hump (~ 30 keV).

3.2.2 The computational grid

The computational grid as defined in Sim et al. (2008) is made of two domains. The first is a 2D grid typically constructed out of $100 \times 100 + 1$ cells, which store the information used to contains the information about the cells within the wind such as electron temperature, density, velocity and local radiation field. The additional cell is used to define empty cells which lie outside of the wind. These cells are then linked into a 3D domain (typically $100 \times 100 \times 100$) where the 2D grid is placed in cells to provide the 3D structure. This is done by assuming

rotational symmetry and reflection in the x–y plane. Cells are spaced logarithmically to allow reasonable spatial resolution at inner radii whilst being computationally efficient (over several decades) at larger radii where the higher resolution is not required. However, as a logarithm cannot go to 0 innermost cell is set to be 10% of $R_{\rm in}$.

3.2.3 Velocity

The wind is assumed to be driven away from point defined by d so the rotational velocity within the wind is assumed to be the Keplerian velocity at the base of a streamline where it crosses the x–y plane, and therefore dependent on geometry and the black hole mass. Angular momentum is then conserved to define the rotational velocity at each point along the streamline. The outflow's radial velocity points away from the focus point of the wind, d (as in Fig. 3.4). Its magnitude is given by:

$$v_l = v_0 + (v_\infty - v_0)\left(1 - \frac{R_v}{R_v + l}\right)^\beta \tag{3.1}$$

where l is the distance along the streamline, R_v is the acceleration length (typically = $R_{\rm out}$) which defines the midpoint of the acceleration (which acts as a scale length) and β sets the rate of acceleration – β is generally set to 1 as current X-ray data are not able to constrain it.

The initial velocity v_0 is set to 0 as it is assumed that $v_0 \ll v_\infty$. The terminal velocity as $v_\infty = f_v\sqrt{\frac{2GM_{\rm BH}}{R}}$, where f_v is the scaling factor of v_∞ with respect to the escape velocity at the launch radius R. R_v and β could in principle change the breadth of the observed profile. For instance, reducing β would increase the red wing of the absorption feature as material would take longer to accelerate to v_∞. Reducing R_v would mean that matter would travel less distance through the wind before reaching v_∞, which would reduce the red wing. A change in the red wing is due to the change in the probability of observing material at lower velocities along a given streamline.

3.2.4 Mass density

The wind is assumed to be smooth and steady state, meaning it can be defined by a mass loss rate $\dot{M}$, which gives the total mass within the flow. The mass loading is the local mass loss rate per area as a function of R, $d\dot{m}/dA \propto R^k$. The mass loading parameter (k) is normally set to -1. The integral of $d\dot{m}/dA$ has to equal the total mass loss rate, such that $\dot{M} = 4\pi \int_{R_{\rm min}}^{R_{\rm max}} (d\dot{m}/dA) R d(R)$. Thus,

$$\frac{d\dot{m}}{dA} = \frac{\dot{M}(k+2)}{4\pi[R_{\rm max}^{k+2} - R_{\rm min}^{k+2}]} R^k \tag{3.2}$$

This shows that decreasing the mass loading parameter has the effect of making the mass within the flow more centrally concentrated. Taking the definition of mass density for a given cell as $\rho = dm/dV$. Defining $dV = v_l dA dt$, where $v_l dt$ is the distance an element travels in the time dt. This is illustrated in Fig. 3.5. This means that the unit of volume is found by combining these equations to get:

$$\rho = \frac{1}{v_l} \frac{d\dot{m}}{dA}. \tag{3.3}$$

As v_l is the velocity along the wind this means that a conversion factor must be used to put a more natural wind reference frame. This means that the mass density falls off faster than would be expected from equation 3.2 as the wind accelerates up to v_∞. This can be seen in Fig. 3.6 where the mass density at R= $10^3\,R_{\rm g}$ and $10^4\,R_{\rm g}$ is -17.6 and -20.1 respectively, therefore $\Delta \log(\rho/{\rm g\,cm^{-3}}) = -2.5$ than expected from expected from mass loading parameter $k = -1$.

I will be using a grid originally produced to investigate the disk wind of PDS 456 (see chapter 5) as an example in many cases during this chapter. The grid parameters are listed in table 3.1 and, unless otherwise stated, will be used for subsequent illustrations in this chapter. The parameters are defined in cgs units within the radiative transfer code. When generating the models, the mass outflow rate and 2–10 keV luminosity are converted into

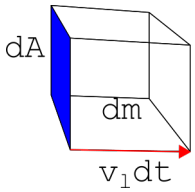

Figure 3.5: A volume unit defined by the depth a unit of material, dm, spread over a unit of area, dA, moves in a time step, dt. This is used to define the mass density within a cell.

Eddington units and gravitational radii for distances, respectively. This means that the parameters are independent of the black hole mass.

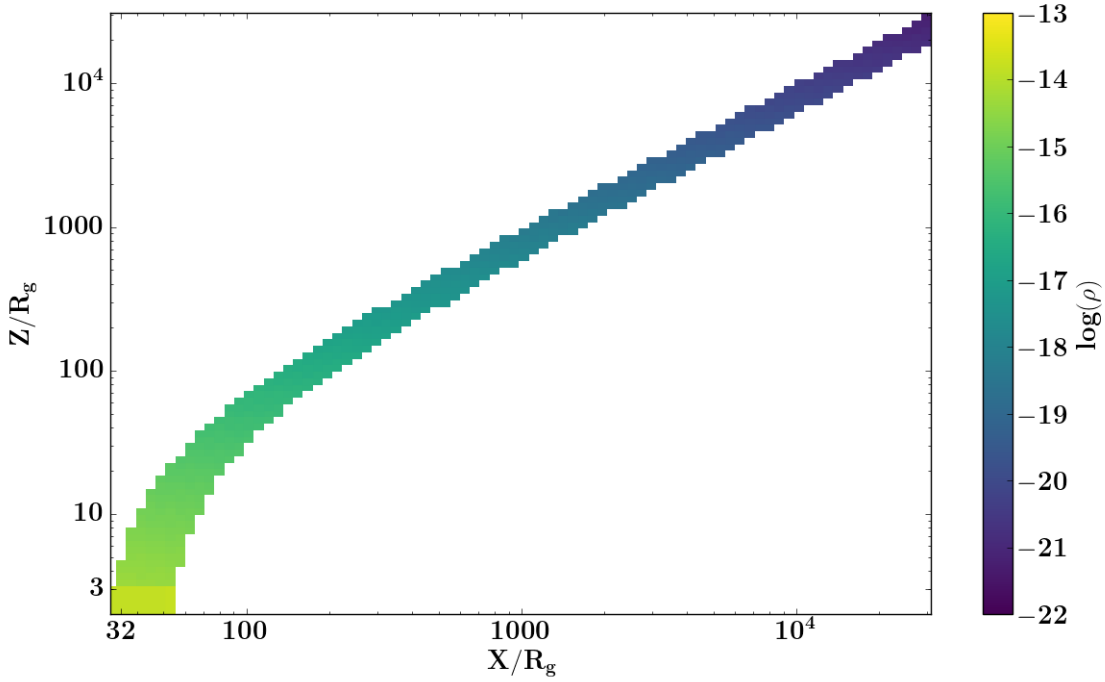

Figure 3.6: A colour map showing the log of the mass density of material in the disk wind cells in units of $\mathrm{g\,cm^{-3}}$. The x axis represents the disk plane while the z axis is along the rotational axis. Both axes are in units of gravitational radii. These "typical" parameters for this work can be found in table 3.1

.

Parameter	Value
$R_{\rm in}/R_{\rm g}$	32
$R_{\rm out}/R_{\rm in}$	1.5
$\dot{M}/\dot{M}_{\rm edd}$	0.68
$L_{2-10\,{\rm keV}}/L_{\rm edd}$	0.25–0.80%
Γ	2.4
f_v	1
$d/R_{\rm in}$	1
k	-1
v_0	0
β	1
$R_{\rm v}$	$R_{\rm out}$
[Fe/H]/[Fe/H]$_\odot$	1
$R_{\rm src}/R_{\rm g}$	6
$R_{\rm outer}/R_{\rm g}$	3.4×10^4
Black hole mass/$M_\odot$	10^9

Unit	Value
$\dot{M}_{\rm edd}/M_\odot$ yr^{-1}	37
$L_{\rm edd}/$ erg s^{-1}	1.3×10^{47}
$R_{\rm g}/$cm	1.5×10^{14}

Table 3.1: The parameters of the grid used throughout this section; these values are based on values I use for the PDS 456 grid model. The total mass outflow rate and the 2–10 keV luminosity are normalised to the values at Eddington rate and all distances are in units of gravitational radii, such that these parameters are independent of black hole mass. The effects of these parameters will be explained throughout this chapter. The lower table shows the values of the mass dependent units for a mass of $10^9\,M_\odot$ (consistent with PDS 456).

3.2.5 Inclination

As mentioned earlier, photon packets are collected into inclination bins (parameterised with respect to the z-axis), which are then processed into energy bins forming spectra. The output spectra are then normalised to the input spectra. This leaves the deviations from the

input spectra to be fitted via the use of a multiplicative model, which modifies a continuum spectrum as $fit\_continuum \times (output\_spectrum/input\_spectrum)$. It is important to note (as discussed later) that the input spectrum has an effect on the ionisation state of the wind which is not removed by this treatment; if possible the photon index should vary with that of the fit continuum. Failing that, the photon index of the fit continuum should be fixed or limited to be close to the photon index of the simulations.

The Monte Carlo method used to produce the output spectra causes high frequency noise, which can be seen in the thickness of the Compton hump around 30 keV in the (green) reflection spectrum in panels (b) to (d) of Fig. 3.8. This means that normalising the output to input spectrum can also sometimes be misleading as signal to noise (S/N) will fall off towards higher energies. Therefore, a Savitzky-Golay filter is used for plotting; this is a method for reducing the high frequency noise by fitting a low order polynomial to a moving window of points. However, this causes some highly blended features to appear as a single feature, but this is purely for plotting purposes as the data quality of X-ray spectra does not require smoothing of the output spectra.

Inclination is measured as the angle with respect to the polar (z) axis. The different sight lines from each inclination bin intercept increasing column densities with increasing polar angle. Fig. 3.7 shows that the column quickly increases into the optically thick regime. The d parameter controls the degree of collimation — this sets the lowest inclination at which the wind will intercept the line of sight (LOS), which is $\sim 45^\circ$ for the standard geometric values in table 3.1. These inclinations can be split into three categories: low inclinations (polar), intermediate (along the wind) and high (edge on). The "typical" spectra for these categories are shown in Fig. 3.8 in the top-right-hand plot. A zoom-in on the Fe K region is shown in Fig. 3.9.

At close to polar inclinations the LOS does not intercept the wind, meaning that there is no modification to the directly observed spectrum. This can be seen in plot (b) in Fig. 3.8, which in this case is at an inclination of 32° (blue solid line). The deviations observed from the input spectra come from the reflection spectrum of the wind (green line of plot b) that

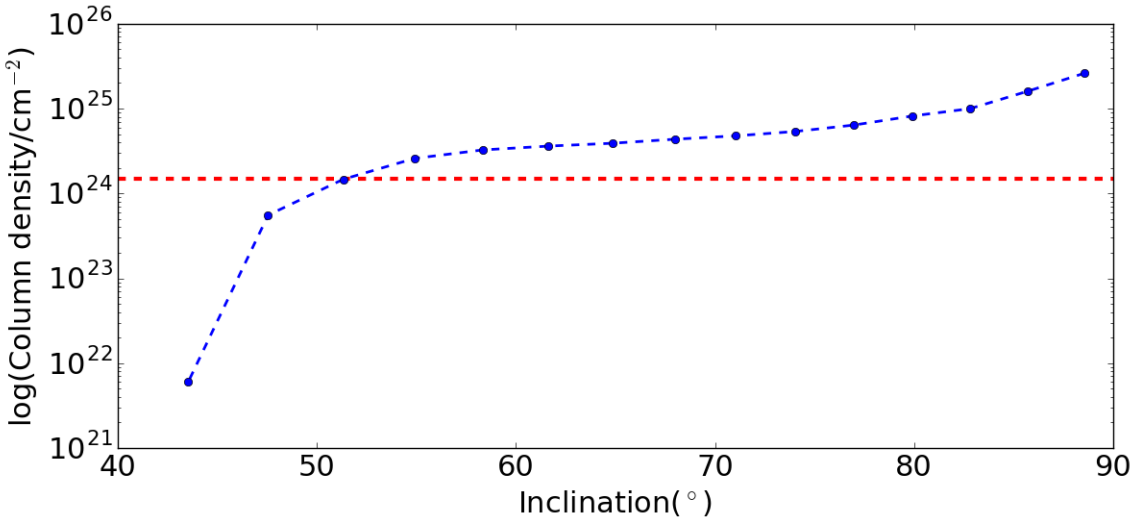

Figure 3.7: Angular dependence of the column density. Along a line of sight below 40° the wind does not intercept the line of sight to the X-ray source so the column density is 0, although the observed spectrum is modified by photons scattered into the line of sight. The column density increases from 44–90° as the line of sight becomes more edge on. The dashed red line represents one Compton depth where $N_{\rm H}= 1/\sigma_T = 1.5\times10^{24}\,{\rm cm}^{-2}$ where the flux is suppressed to 38% of the unattenuated flux.

encompasses the Fe Kα emission seen at 6.4 keV which is blurred due to the Doppler shifts within the flow and a weak Compton hump (as described in section 1.3.2) produced in the scattered spectrum above 10 keV. The resultant spectrum (black line) is the superposition of the direct and scattered components.

In principle the broad Fe Kα emission lines seen in many type 1 Seyfert galaxies could be fitted with the Fe K emission line of the disk wind model such as the ones seen in panel (b) of Fig. 3.8 and panel (a) of Fig. 3.9. Indeed, Tatum et al. (2012) found acceptable fits for several bare Seyferts with relatively face-on inclinations. These objects are normally fit with the reflection spectrum blurred by transverse Doppler and gravitational redshift (as discussed in the previous chapter), and could in principle be fit with the reflection spectrum of a wind which is located out of the direct LOS of the observer (i.e. an angle $\lesssim 40\,^\circ$) such

as the blue line in panel (a) of Fig. 3.8.

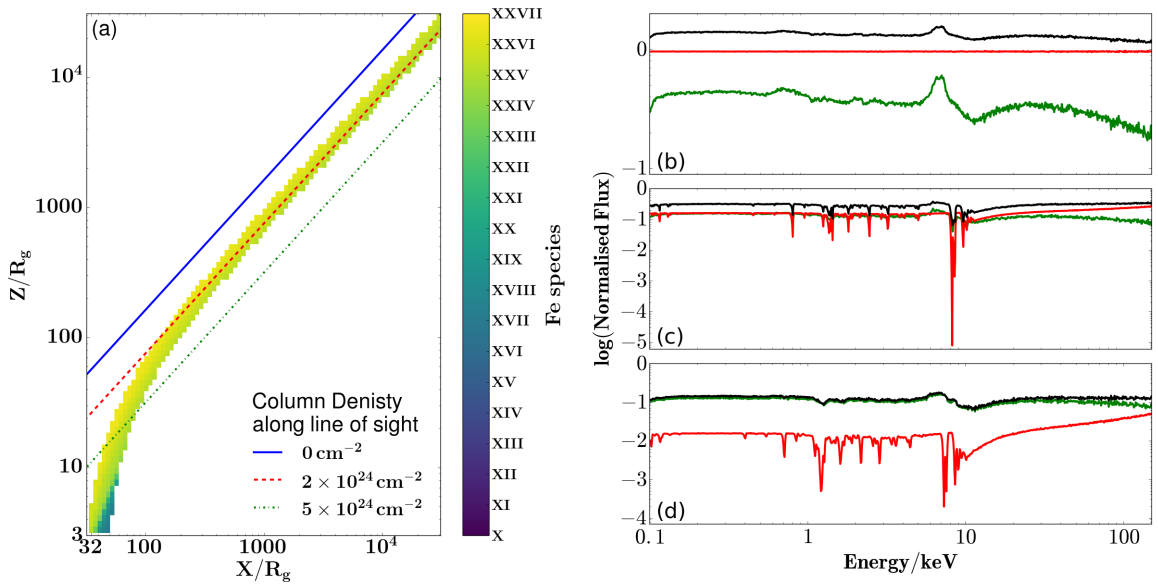

Figure 3.8: The effects on the observed spectra when intercepting the wind at different inclinations. The plot on the left is a colour map of the average charge of iron within each cell. Three lines corresponding to different lines of sight through the wind are overlaid. From top to bottom the inclinations (measured with respect to the z-axis) are 32° (blue solid line and panel b), 51° (red dashed line and panel c) and 73° (green dash-dot line and panel d). These sight lines intercept different column densities. The spectra in the right-hand panels show the deviations from the input continuum for each of the aforementioned inclinations. Along with the total spectrum (black). The direct (red) and scattered (green) spectra are also shown for each of the aforementioned inclinations. The direct spectrum shows the absorption due to the wind in the line of sight whereas the scattered spectrum primarily shows the emission/reflection from the wind.

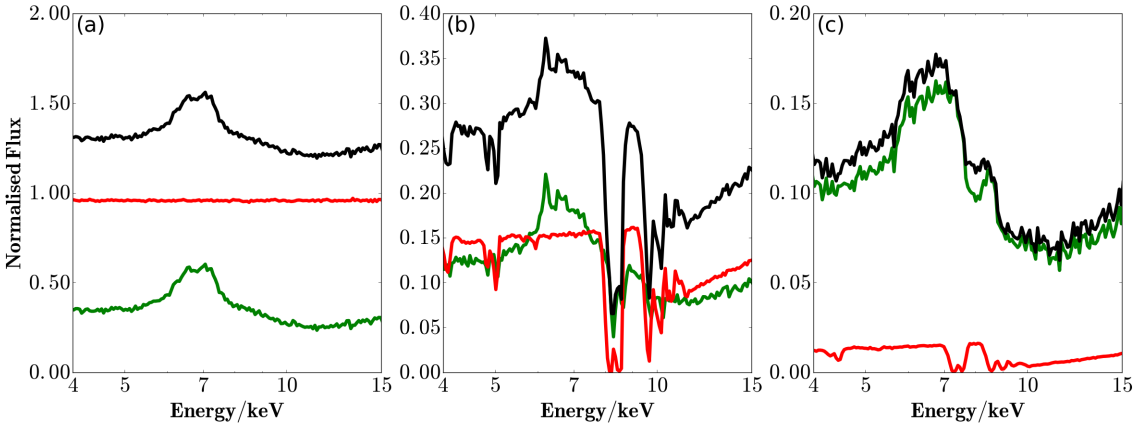

Figure 3.9: Plot of the Fe Kα region of the output spectra. As in Fig. 3.8 the spectra show the deviations from the input. Along with the total spectrum (black) I also show the direct (red) and scattered (green) spectra for each aforementioned inclinations. The direct spectrum shows the absorption due to the wind in the line of sight whereas the scattered spectrum primarily shows the emission/reflection from the wind. The line of sight (an inclination of 32°) for panel does (a)not intercept the wind so is dominated by the photons scattered off the inner edge of the wind and thus demonstrates the broad Fe Kα emission feature. Panel (b) shows the 51° inclination angle which shows modification from both emission and absorption with deep absorption troughs due to He-like and H-like iron. Finally, panel (c) shows the heavily absorbed equatorial inclination of 73°, where the direct continuum is heavily suppressed by the large column and so is dominated by the scattered spectrum, showing a broad shallow absorption feature.

At intermediate inclinations (such as 51°, red dashed line in Fig. 3.8 panel a) seen in panel (c) of Fig. 3.8 intercepting a column density of $2 \times 10^{24}\,\mathrm{cm}^{-2}$, the observed spectra will have emission and scattering into the LOS as before. However, now that the wind is intercepting the LOS to the X-ray source, it modifies the direct continuum (red line) by suppressing it. This can be seen in the reduced magnitude of the direct continuum (20% of the unattenuated direct component), and by imprinting absorption features at this ionisation where the 2–10 keV luminosity has been set to 0.8% of the Eddington luminosity (see Sec. 3.2.6).The strongest features are from He-like and H-like Fe, as illustrated in panel (b) of Fig. 3.9, where strong absorption lines from Fe XXV/XXVI are seen imprinted on

both the transmitted (direct) and reflected spectra. The lines are blueshifted with respect to the laboratory frame energies (6.7/6.97 keV). Higher-order (1s–3p) absorption features (Fe XXV Heβ and Fe XXVI Lyβ) are also seen at energies ~ 10 keV in Fig. 3.9.

At an inclination of 73° (the green dash-dot line in panel (a) in Fig. 3.8), the scattered emission dominates over the direct continuum. This can be seen in panel (d) in Fig. 3.8. The column intercepting the LOS is $\sim 5 \times 10^{24}\,\mathrm{cm}^{-2}$, corresponding to an optical depth (τ) of 3.3, meaning the direct continuum (in red) should be suppressed to $\sim 3\%$ of the unattenuated flux in panel (d) of Fig. 3.8.

It can also be seen that the Compton hump is much weaker at 53° and 73° despite the reflection component being stronger compared to the direct continuum, due to the angular dependence of Compton scattering. It is also important to note that the observed velocity shift is dependent on the inclination. This can be seen when comparing direct spectra of the panels (b)–(d) in Fig. 3.8. In panel (b) in Fig. 3.9, the absorption line observed in the direct (red) spectrum is at 8.2 keV which corresponds to an outflow velocity (v_{out}) of $-0.16\,\mathrm{c}$, associated with Fe XXVI (H-like) Lyα. At the higher inclination in panel (c) the absorption line is seen at the lower energy of 7.2 keV, thus the resultant v_{out} is $-0.03\,\mathrm{c}$. Thus along the direct line of sight through the wind the observed velocity shift will be higher than for high inclination, due to shifting to slower streamlines. Along with this the observed width of the line will be larger at high inclinations when compared to lower inclinations due to the divergence of velocity streamlines.

3.2.6 Ionising luminosity

As photon packets propagate through the wind they interact with the material, heating and cooling of the cells as the go this sets the ionisation state of the wind. The packets are drawn from the input spectrum, allowing any spectral input to be adapted. The input spectrum is then scaled to the model parameter $L_{2-10\,\mathrm{keV}}$ (the luminosity between 2 and 10 keV) by integrating the input spectrum over this energy range. This energy band is

used as it is covered by most X-ray detectors so is obtainable from the observed spectrum. As it sets the amplitude of the ionising continuum, this parameter acts as a proxy for the ionisation state of the wind. To explore the effect of the ionisation state of the wind on the observed spectrum I collect the output spectrum with increasing 2–10 keV luminosity, ranging from 0.03% to 0.8% $L_{\rm edd}$. These can be seen in Fig. 3.10 which shows the spectra from an intermediate inclination angle of $\sim 51°$. I note that $L_{2-10\,\rm keV}$ is normalised to $L_{\rm edd}$ as it makes it essentially independent of black hole mass.

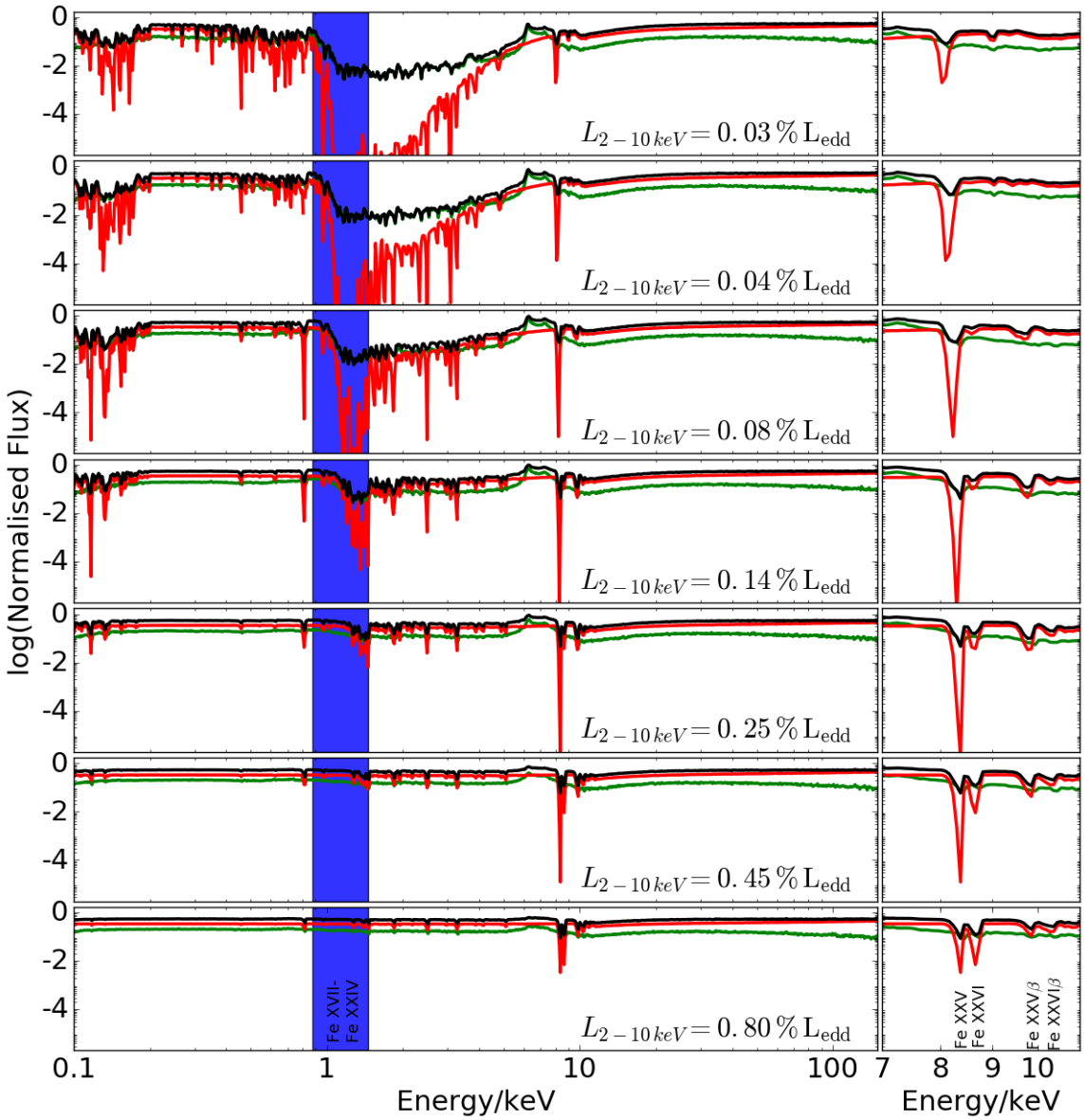

Figure 3.10: Spectral changes with increasing luminosity from 2–10 keV with $\dot{M} = 0.68\,\dot{M}_{\rm edd}$. As ionising luminosity increases more elements become more highly ionised. This causes a reduction in the line strengths of these ions as their population becomes smaller; this can be seen between 1 and 2 keV. It is interesting to note that the top panel corresponds to Fig. 3.11 while the bottom panel corresponds to Fig. 3.12. The change in wind ionisation can also be seen in the absorption feature around 8 keV in the reduction of the depth of the line and profile (of He-like Fe) and the development of a second line (H-like Fe). This ionisation change can be seen in the profile of the Fe Kα emission as a reduction in the emission line strength.

Moving to higher luminosities (top to bottom in Fig. 3.10) the atoms are stripped of their electrons making the wind more transparent. This is seen in the reduction of the (bound–free) curvature in the direct spectra – specifically between 1–5 keV. The shaded range in Fig. 3.10, which shows the energy range where the Fe L absorption from mildly ionised iron ($\mathrm{Fe_{XVII-XXIV}}$) would be expected after applying the velocity shift due to the winds motion. The top panel will also have contributions from the K-shell absorption of lighter elements such as (Mg,Si,Ne,S,Ca) which introduces much of the opacity along the wind above 1 keV. Fig. 3.11 shows the spatial distribution of the ions of each element. For the lowest ionisation ($0.03\%\, L_{\mathrm{edd}}$) simulation it can be seen that most elements are only partially ionised except for the lightest elements C and N, which have already been fully ionised except at the very base of the wind.

As the $L_{2-10\,\mathrm{keV}}$ increases further, moving to lower panels in Fig. 3.10 the outer electrons of most elements are stripped meaning that the lighter elements become over-ionised. In Fig. 3.12 it can be seen that all atoms below iron are fully ionised except at the base of the wind. This is seen in the corresponding spectrum in the bottom panel of Fig. 3.10 where only He-like and H-like iron absorption remains.

This change in ionisation can also be seen in the equivalent width of Fe XXV Heα and Fe XXVI Lyα absorption features. As the luminosity increases, the mildly ionised iron ions move into a more highly ionised population (as is seen by comparing Fig. 3.11 to Fig. 3.12), so the equivalent width of He-like Fe increases as is seen in table 3.2. The Heα absorption from the H-like iron is not detected until $L_{2-10\,\mathrm{keV}} = 0.08\%\, L_{\mathrm{edd}}$ when the population of Fe XXVI becomes large enough to produce a measurable feature. As the luminosity increases further so does the average ionisation state of iron; this can be seen in the decrease of the ratio ($\mathrm{Fe_{XXV}/Fe_{XXVI}}$) and therefore the relative strength of the H-like line increases with $L_{2-10\,\mathrm{keV}}$. Another effect is the weakening of the Fe Kα emission feature in the scattered spectrum, as the scattering medium becomes more highly ionised and therefore becomes closer to full transparency.

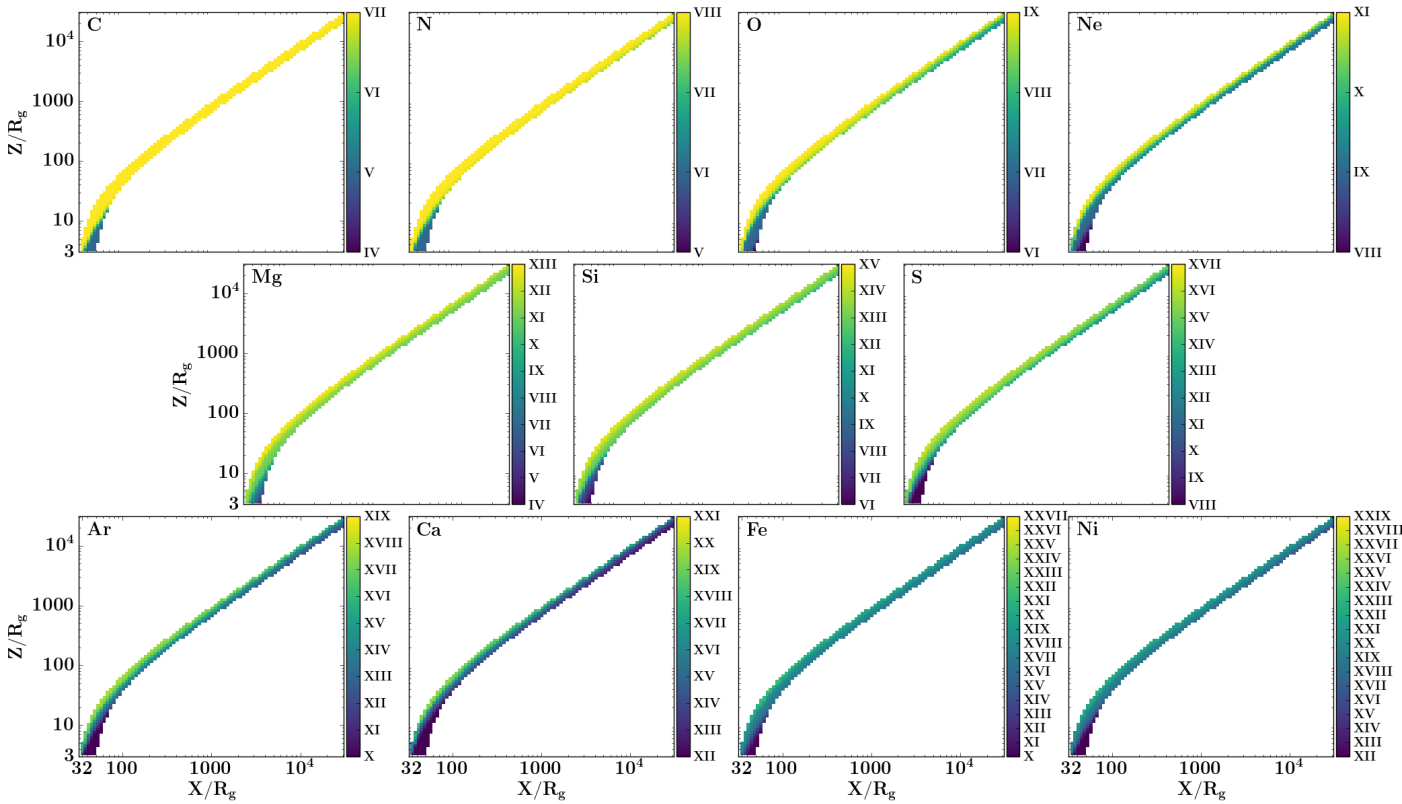

Figure 3.11: The ionisation colour maps of average ionisation state (right hand side scale) within each cell for different elements within the outflow. This shows that the ionisation structure is the same for all elements. This is a low ionisation example with $L_{2-10\,\mathrm{keV}} = 10^{43.5}\,\mathrm{erg\,s^{-1}}$ ($0.03\%\,L_{\mathrm{edd}}$) and $\dot{M} = 25\,\dot{M}\ \mathrm{yr}^{-1}$ ($68\%\,\dot{M}_{\mathrm{edd}}$). It can be seen that the base is of lower ionisation. This is due to the wind being denser at the base but also the side of the wind which faces the source acts to shield the far side of the wind from much of the intrinsic luminosity, allowing lower ionisation species to survive.

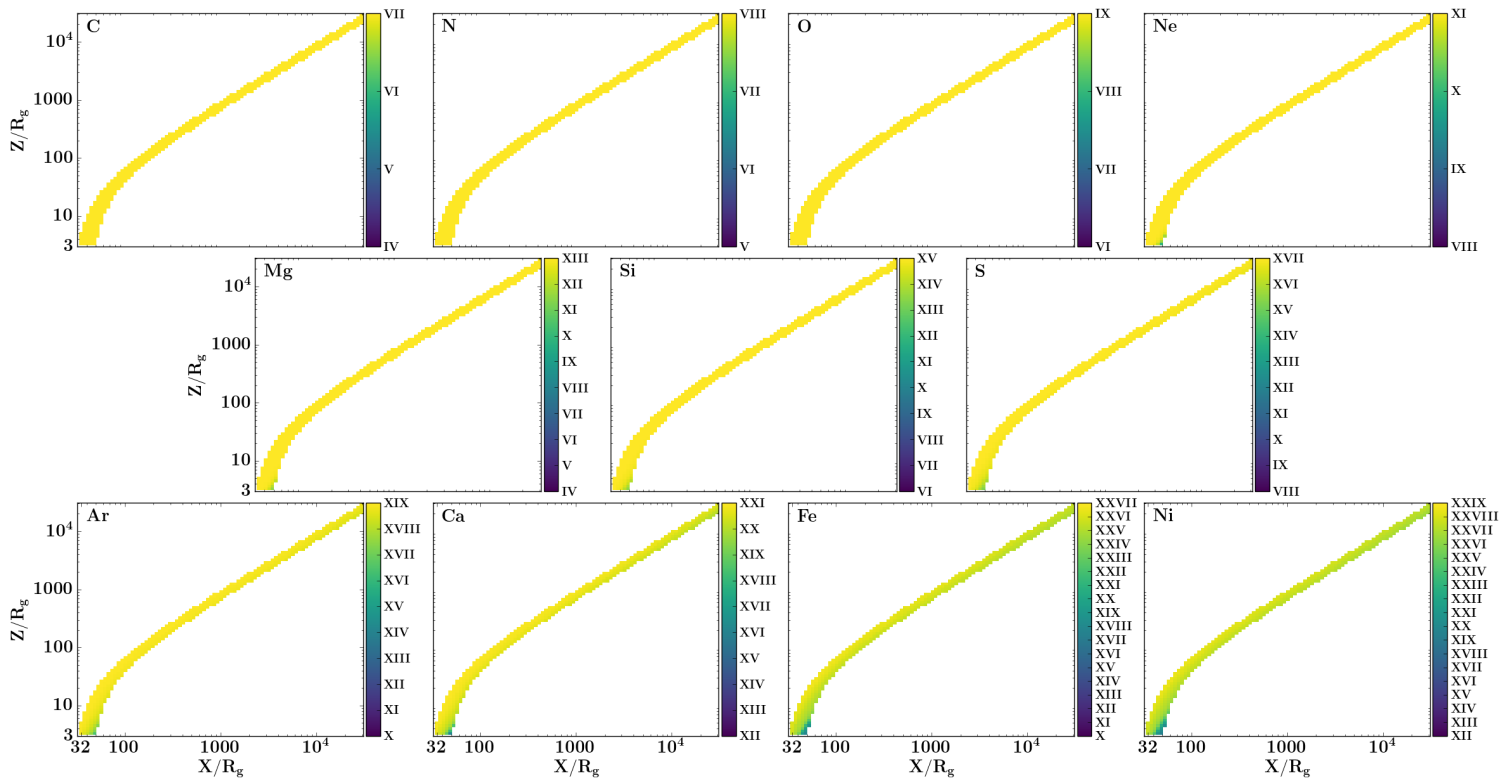

Figure 3.12: High ionisation example of Fig. 3.11 with $L_{2-10\,\mathrm{keV}} = 10^{45.0}\,\mathrm{erg\,s^{-1}}$ ($0.8\%\,L_{\mathrm{edd}}$) and $\dot{M} = 25\,\dot{M}$ $\mathrm{yr^{-1}}$ ($68\%\,\dot{M}_{\mathrm{edd}}$). It can be seen that all elements below iron are completely ionised everywhere but at the base of the wind. This means that most of the lines observed in Fig. 3.10's top panel are lost, as observed in the bottom panel.

$\%\ L_{2-10\,\mathrm{keV}}/L_{\mathrm{edd}}$	Equivalent width of features/eV		Fe XXV/Fe XXVI
	Fe XXV Heα	Fe XXVI Lyα	
0.03	−199	–	–
0.04	−237	–	–
0.08	−260	−064	4.04
0.14	−274	−167	1.65
0.25	−268	−238	1.13
0.45	−265	−264	1.00
0.80	−228	−253	0.90
1.40	−149	−220	0.68
2.40	−061	−169	0.36
4.10	−018	−107	0.17
7.10	−002	−060	0.03

Table 3.2: The equivalent width of the absorption features with varying 2–10 keV luminosity; this can be seen from the ratio of Fe XXV to Fe XXVI. Initially as the ionisation increases, the mildly ionised iron becomes He-like as can be seen by the increase in equivalent width. However as the ionisation increases further, the H-like line first appears and then growths in depth. These values are based on simulations with a mass outflow rate of 68% $\dot{M}_{\mathrm{edd}}$.

It is important to note that moving from $L_{2-10\,\mathrm{keV}} = 0.03\%$ to $7.1\%\, L_{\mathrm{edd}}$ in table 3.2 decreases the equivalent width of both the He-like and H-like iron lines as the wind becomes more transparent. However the former decreases more rapidly leading to a change in the observed change in the Fe XXV/Fe XXVI ratio, which is a sensitive measure of the wind's overall ionisation.

As mentioned earlier this grid was built based upon the parameters of PDS 456. The observed $L_{2-10\,\mathrm{keV}}$ range is from 0.11 to $0.54\,\%\, L_{\mathrm{edd}}$. I can compare this to the expected intrinsic value for $L_{2-10\,\mathrm{keV}}$ using the 2–10 keV to L_{bol} correction factors of Marconi et al. (2004). This paper compiles the $L_{2-10\,\mathrm{keV}}/L_{\mathrm{bol}}$ ratios for a sample of AGN at different luminosities. For the luminosity of $L_{\mathrm{bol}} = 10^{47}\ \mathrm{erg\,s^{-1}} \sim L_{\mathrm{edd}}$ Reeves et al. (2000) give a correction factor $L_{\mathrm{bol}}/L_{2-10\,\mathrm{keV}} = 79$. Therefore an expected $L_{2-10\,\mathrm{keV}}/L_{\mathrm{bol}}$ for PDS 456 is $\sim 1.2\%$. I cover the range in expected and observed values for PDS 456 within the spectra

in Fig. 3.10.

From Fig. 3.11 and Fig. 3.12 it can be seen once again that inclination is important, as the inner edge of the wind has the highest ionisation because it sees the full unattenuated flux of the X-ray continuum. So inclinations which intercept more of the inner edge of the wind will not only be faster but will also have a higher ionisation state and therefore a reduced opacity. For larger inclinations we see through larger optical depths through the wind, therefore I will see lower ionisation gas due to shielding of the layers at lower physical depths.

This means that larger depths see a reduced flux. This effect is strongest at the base of the wind where the increased column density increases the scattering so lower ionisation species can survive at the larger optical depths. Even with the self shielding an ionising luminosity of $0.8\%\, L_{\rm edd}$ is enough to over-ionise all atoms below iron except at the base of the wind. It can also be seen that the ionisation decreases further out showing that the flux is falling off quicker than the density, once again due to the self shielding.

3.2.7 Effect of changing the mass outflow rate

As discussed earlier, the mass within the flow is controlled by the mass outflow rate ($\dot{M}$); increasing $\dot{M}$ scales the mass density in each cell. Fig. 3.13 shows the output spectra of several runs with increasing $\dot{M}$ (from 14 to 115% $\dot{M}_{\rm edd}$) with a constant 2–10 keV luminosity of $0.8\%\, L_{\rm edd}$ at an inclination of $\sim 51^{\circ}$.

The increase in mass outflow rate has the effect of increasing the optical depth directly; this can be seen as the flux becomes suppressed. As interactions (scatterings) change the direction of photons into different lines of sight, the relative strength of the reflection component increases proportionally to $\dot{M}$, which can also be seen in (green spectra) Fig. 3.13.

As $\dot{M}$ increases the column density intercepted goes from $3.1 \times 10^{23}\,{\rm cm}^{-2}$ in the top panel to $2.5 \times 10^{24}\,{\rm cm}^{-2}$ in the bottom panel, corresponding to an increase in the attenuation of the direct power law of 18% and 81% respectively.

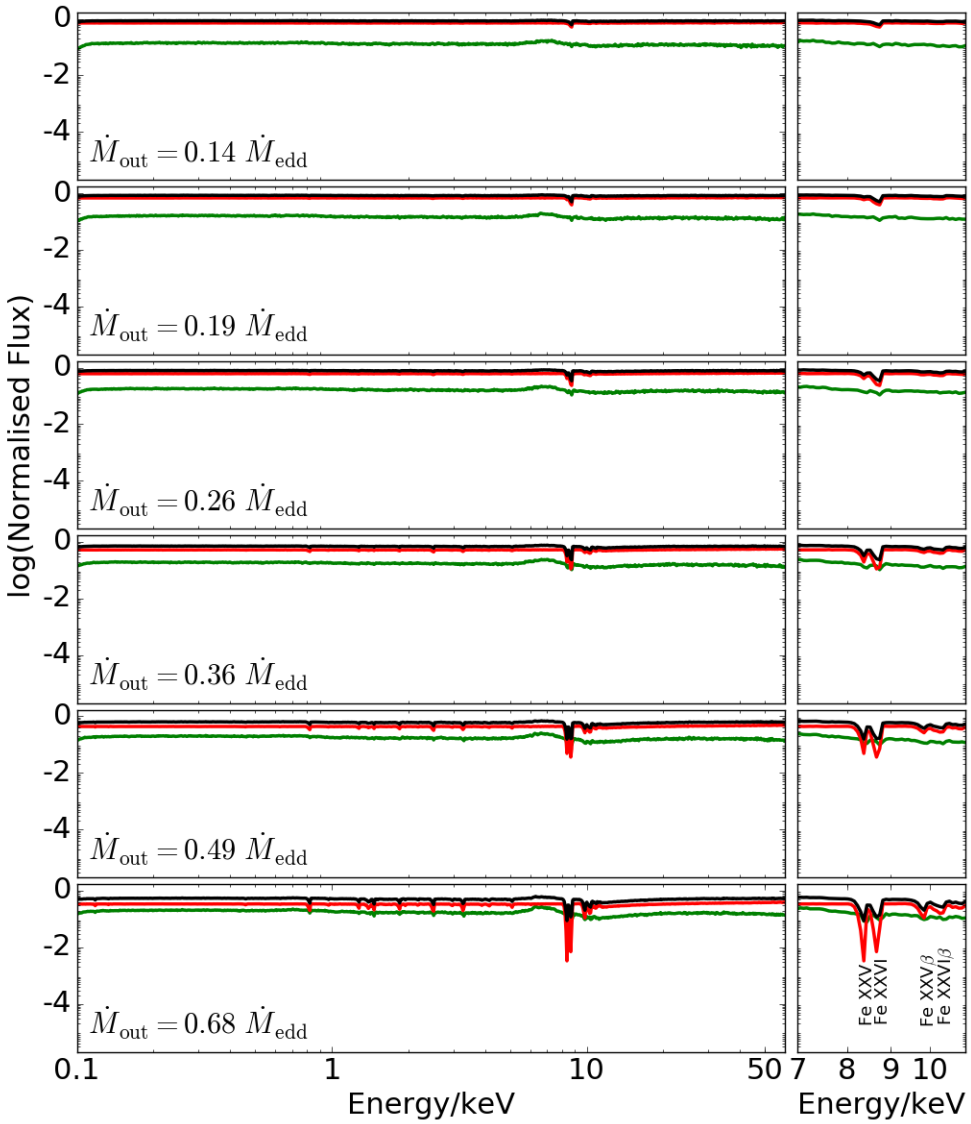

Figure 3.13: The spectra of six runs which have increasing mass outflow rates from top to bottom in units of Eddington mass loss rate $\dot{M}$. Moving from top to bottom there is an increase in the strength of the 8.7 keV absorption feature along with the emergence of the 8.3 keV feature. Here the ionising luminosity is constant at $0.8\%\ L_{\rm edd}$. Note the relative increase in strength in the lower ionisation species, this is due to the increase of density, which in turn decreases the ionisation of the wind. The increase in density also serves to suppress the overall continuum whilst also increasing the strength of the Fe Kα emission. The inclination for all spectra is 51°.

$\dot{M}/\dot{M}_{\rm edd}$	Equivalent width of features/eV Fe XXV Heα	Fe XXVI Lyα	Fe XXV/Fe XXVI
0.14	−008	−063	0.13
0.19	−019	−094	0.21
0.26	−056	−145	0.38
0.36	−117	−195	0.60
0.49	−181	−233	0.78
0.68	−228	−253	0.90
0.88	−247	−258	0.96
1.20	−253	−250	1.01

Table 3.3: The equivalent widths of the He and H-like Fe absorption features with varying mass outflow rates showing that while the depth of the features increase, the ionisation state of the wind decreases. This is shown in the fourth column where the Fe XXV line becomes stronger relative to the Fe XXVI line with increasing outflow rate as the $L_{2-10\,\rm keV}$ is kept constant at 0.8% $L_{\rm edd}$ (and thus equivalent to the bottom panel of Fig. 3.10) as well as the geometry with the values in table 3.1.

The depth of the 8.7 keV absorption line also increases as seen in the right hand side panel of Fig. 3.13; this line corresponds to the H-like Fe Lyα line. This can also be seen in table 3.3. Where the column density increases, so does the equivalent width. An interesting side effect of increasing $\dot{M}$ is that the ionisation state of the wind decreases. This can be seen in the right hand side panel of Fig. 3.13, as indicated by the increase in depth of the lower ionisation line at ~ 8.4 keV (corresponding to the He-like iron line). This is also seen in the ratio between the two lines in table 3.3, where the ratio of Fe XXV to Fe XXVI increases with $\dot{M}$. The relative strength of the Fe XXV Heα line increases, because there are fewer photons compared to the number of atoms due to the increase in density of the wind as $\dot{M}$ becomes larger — whereas the 2–10 keV luminosity remains constant causing the ionisation to fall.

$L_{2-10\,\rm keV}$ and $\dot{M}$ have similar effects yet opposite on the spectra. While larger $L_{2-10\,\rm keV}$ increases the ionisation, larger $\dot{M}$ decreases it (whilst also suppressing the observed flux). Therefore it is combination of $\dot{M}$ and $L_{2-10\,\rm keV}$ that sets the ionsiation state of the elements within the wind (and therefore the opacity of the wind at any given energy). This in turn

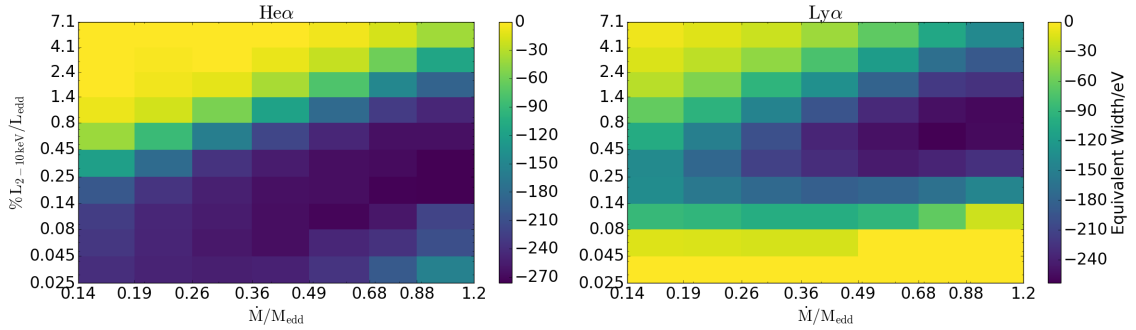

Figure 3.14: The distribution of equivalent widths over different $\dot{M}$ and $L_{2-10\,\mathrm{keV}}$ values for both Fe XXV Heα and Fe XXVI Lyα lines showing the interplay between the two parameters.

sets the species observed and the observable depth of the lines. In Fig 3.14, the equivalent width (EW) of the Fe XXV Heα and Fe XXVI Lyα in the left and right hand side panels respectively is shown in $\dot{M}$ vs $L_{2-10\,\mathrm{keV}}$. At low $\dot{M}$ and high $L_{2-10\,\mathrm{keV}}$ neither line is visible (as the wind is over-ionised), whereas at low ionisation and high mass outflow rate the line strength (largest absolute EW) is still not maximised as there are not enough atoms in the He/H-like state (i.e. the wind is under-ionised). This is most apparent in the H-like Lyα line, which is not visible at the lower ionisations.

The relative strengths of the Heα and Lyα lines can be seen in Fig. 3.15, which presents the ratio between the EWs of the two lines. This shows the shift from He-like iron to H-like and then to completely ionised iron as both lines become very weak as $L_{2-10\,\mathrm{keV}}$ increases and $\dot{M}$ decreases (upper left of Fig. 3.15). Conversely the white region of Fig. 3.15 is due to the wind being under-ionised with a lack of Fe ions in the H-like state. As $L_{2-10\,\mathrm{keV}}$ increases more, similar values for EW (and ratios of Heα and Lyα lines) can be produced by increasing $\dot{M}$ to compensate. This can be seen both in Fig. 3.14 and Fig. 3.15 in the diagonal bands. This was alluded to in section 3.2.6. The degeneracy between these parameters is important as discussed in section 1.4.1: the mass outflow rate (alongside the outflow velocity) is important for determining the kinetic luminosity of the wind. The kinetic luminosity is a

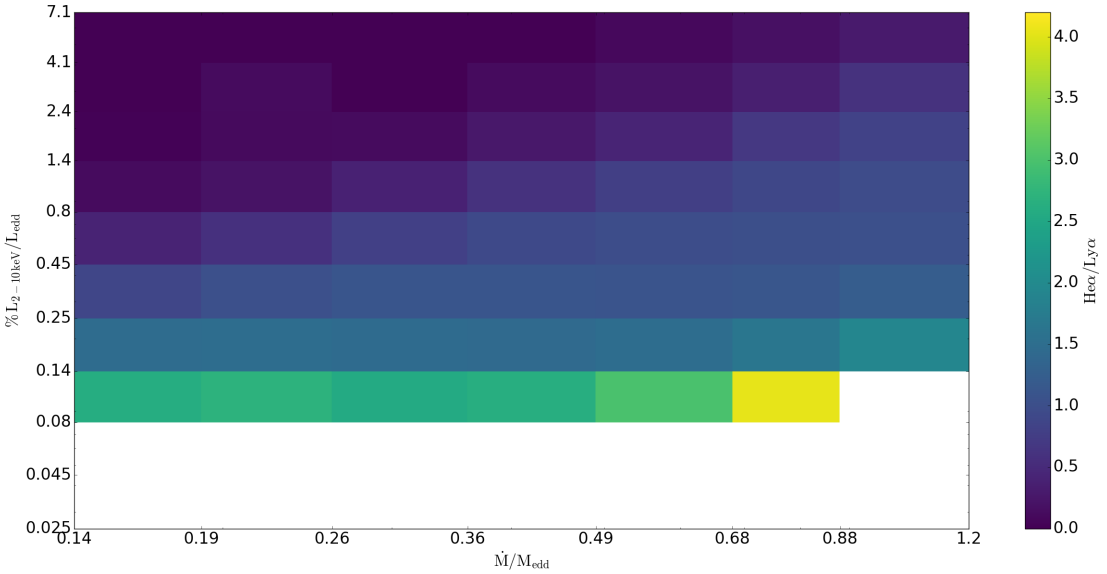

Figure 3.15: The distribution of the comparative line strengths based on the ratio of the Fe XXV Heα and Fe XXVI Lyα lines. This shows the interplay between the $L_{2-10\,\mathrm{keV}}$ and $\dot{M}$ parameters. The white region is where the Lyα line is too weak to be detected (Heα/Lyα) > 4.2.

diagnostic parameter if the wind plays a role in feedback.

However, as the 2–10 keV luminosity is directly observed or can at least be constrained by the observed spectra, this is a relatively easy degeneracy to break – or at least limit its effect. Disentangling the effects changing ionising luminosity and changing mass outflow rate is important for parameters such as the amount of mass carried by a flow over its lifetime, which is used to infer the influence on the host galaxy. Therefore a physically meaningful anchor for $L_{2-10\,\mathrm{keV}}$ or $\dot{M}$ is required to limit the effect of the degeneracy. This is discussed in section 3.3.

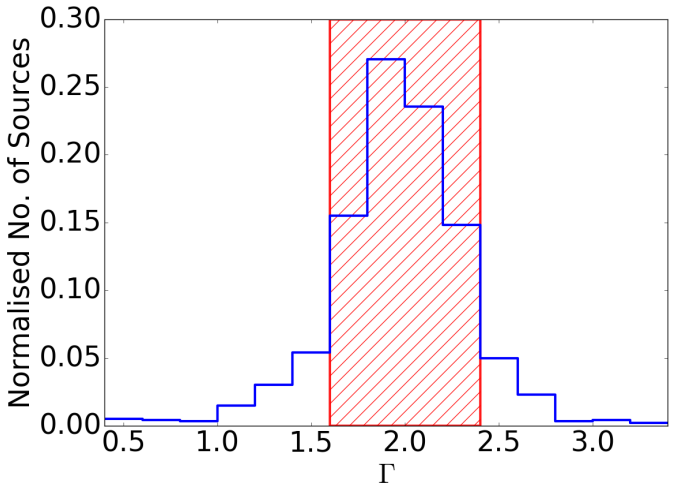

Figure 3.16: The distribution of photon indices from Fig. 1 in Scott & Stewart (2014) of 761 type 1 AGN. The shaded area ($\Gamma = 1.6$ to 2.4) corresponds to $\sim 80\%$ of the sources within the sample.

3.2.8 The Input Spectrum

It is known that AGN have diverse intrinsic spectra. A key question is how the intrinsic spectrum affects the wind's observable parameters. I use the distribution of X-ray photon indices (see Fig. 3.16) measured by Scott & Stewart (2014) from fitting 761 type 1 sources in the *XMM-Newton* serendipitous catalogue (2XMMi; Watson et al. 2009). As type 1 objects are generally less obscured, they should be a more reliable measure of the intrinsic distribution of photon indices. Also, the sources studied throughout this thesis are type 1 AGN. The range $\Gamma = 1.6$ to 2.4 is chosen. This corresponds to $\sim 80\%$ of the sources, as seen in the shaded area in Fig. 3.16.

A power law is assumed to be a reasonable first order approximation of the intrinsic X-ray continuum of AGN. However, as already discussed (in section 1.3.1), it is likely to be much more complex. Fig. 3.17 presents five power laws with increasing photon index from 1.6 to 2.4.

Parameter	Values	Description
$\log(L/L_{\rm edd})$	-0.08	The Eddington ratio used to define the accretion energy provided
$R_{\rm cor}/R_{\rm g}$	41	The radius at which black body transitions to the Comptonised spectrum
kT/eV	468	The temperature of the soft X-ray component
τ	10	The optical depth of the soft X-ray component
Γ	2.4	The photon index of the hard X-ray power law
F_{pl}	0.09	The fraction of accretion energy emitted in the power law component

Table 3.4: The parameters of the `optxagnf` model which was used to define the `optxagnf` input spectrum. These parameters are taken from the fit of Matzeu et al. (2016) to one of the low-state 2013 *Suzaku* spectra which is modified by cold absorption. However, these values are comparatively equivalent for its purpose here to fits found for the high state in Matzeu et al. (2017).

Alongside the power laws there are two more complex models: a simple broken power law SED and `optxagnf` (Done et al. 2012), a Comptonised disk model. Both models are taken from Matzeu et al. (2016), who fit PDS 456 using photometric data from the *XMM-Newton* Optical Monitor along with X-ray spectra from *Suzaku* and *NuSTAR*. The use of these detectors provides data from ∼2 eV to 50 keV, allowing for a realistic input spectrum over a wide energy range. The broken power law has a fixed break energy of 0.5 keV, which is the lowest energy of the *Suzaku* spectrum used. The broken power law model has a steep photon index of Γ=3.3 between the UV and the soft X-ray and a harder Γ=2.4 above a fixed break of 0.5 keV. The input parameters for the `optxagnf` disk–corona model are listed in table 3.4, presented in Matzeu et al. (2016). In both models the hard X-ray component is a power law with a photon index of 2.4 – however `optxagnf` adds a high energy cut-off (100 keV) which causes a roll over at higher energies.

In Fig. 3.17 the integrated $2-10$ keV fluxes of the input spectra are normalised to unity. The fraction of luminosity radiated above 9.28 keV compared to the hardest ($\Gamma = 1.6$) power law is then calculated for each of the input continua in Fig. 3.17. This can be used to understand the expected ionisation state of the wind, although rather simplistically. Harder spectra have a higher luminosity above the ionisation potential of H-like iron relative to the softer photon indices. The subsequent effects of the harder spectral energy distribution on

the disk wind model can be seen in the top panel of Fig. 3.18, where the power law input spectrum with a Γ of 1.6 produces a very weak absorption feature from H-like Fe with an equivalent width EW$= -18$ eV, as most of the iron becomes fully ionised and therefore does not produce any opacity. As the distribution softens there are fewer ionising photons and therefore the population of fully ionised Fe XXVII is reduced in favour of lower ionisation states such as He-like and H-like iron. In Fig. 3.18 it is shown that as the photon index increases the softer input spectrum produces a stronger lower energy feature, as the average Fe ionisation state changes from fully ionised to H-like, and subsequently to He-like. A similar effect can be seen in the strength of the broad emission feature, which is barely visible in the top panel but grows in strength as the input spectrum becomes softer – a similar effect is seen in Fig. 3.10. The increase in strength of the absorption can be seen in the corresponding equivalent widths presented in table 3.5, particularity when looking at the correlation of the ratio of the line strengths to the photon index.

It is important to note that the absolute values of the equivalent width vary strongly with other parameters (notably the mass outflow rate). The observed values from the AGN outflow samples in Tombesi et al. (2010) and Gofford et al. (2013) vary typically from -10 to -90 eV for Fe XXV and from -10 to -150 eV for Fe XXVI. Whilst the mass outflow rate could be scaled to match these, as shown in Fig. 3.14, a more detailed object by object approach is favourable. A large equivalent width feature has been observed in the PDS 456 low flux state 2013 observation which will discuss in the next chapter has a equivalent width of ~ 500 eV; the fitting of this feature will be explored in later chapters.

A key result from the dependence of the absorption line strength with the photon index is that soft X-ray continuum sources such as in PDS 456 and the NLS1 1H 0707 $-$ 495 are prime candidates for finding disk winds. They are indeed sources accreting at least close to the Eddington limit (Reeves et al. 2009; Done & Jin 2016) therefore have the physical requirements for launching a wind, and are X-ray weak meaning they have a relatively low 2–10 keV luminosity compared to the UV (Reeves et al. 2009). They have a steep soft X-ray spectrum meaning that any wind launched would not be over-ionised and therefore

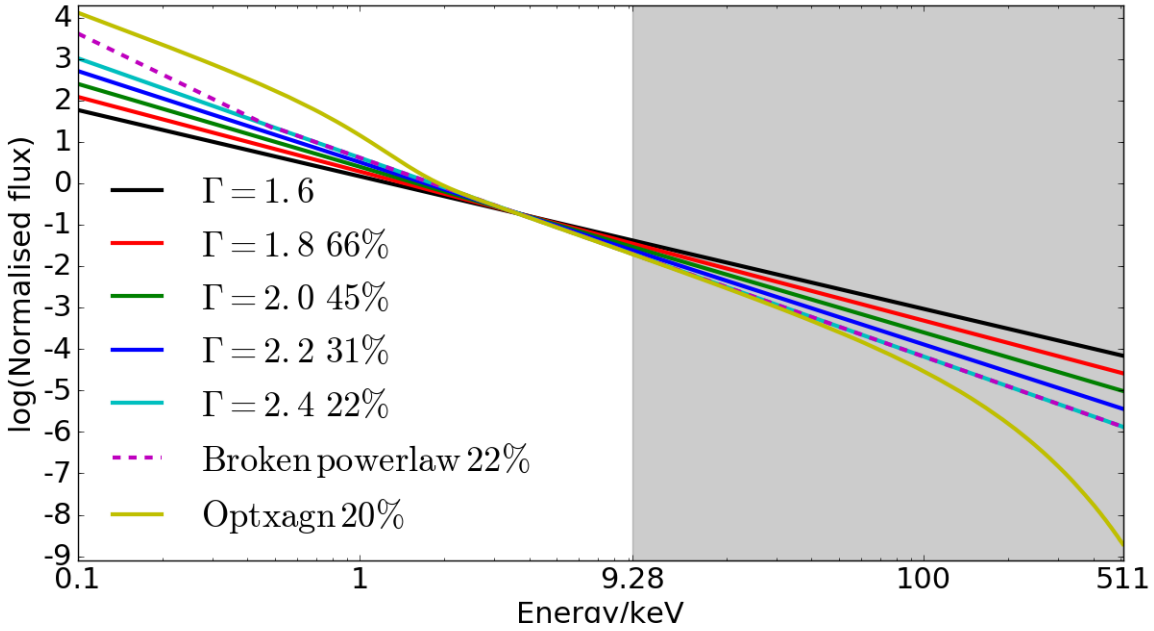

Figure 3.17: The illuminating continuum represented as five power laws with increasing photon indices from 1.6 to 2.4, alongside the more realistic input spectra, the first of which is a broken power law and the second is a disk corona Comptonisation model (`optxagnf`). The spectra have been normalised to 1 in the 2–10 keV band for comparison. Note that as the input spectrum becomes steeper, the number of photons above the threshold of ionisation for iron decreases therefore, lowering average charge of iron within the outflow. The labels provide the percentage of integrated flux above H-like iron's K edge (9.28 keV) relative to the power law with $\Gamma = 1.6$ - as photons are required to be above this energy to ionise iron, it is this band which will have the largest effect on the populations of iron species.

more visible. So it may not be surprising that they may be expected to produce strong observable wind features over the X-ray band. Moving to more realistic spectra such as the `optxagnf` model does not lead to a large modification to the observed Fe Kα line profile when compared to the equivalent hard X-ray spectrum ($\Gamma = 2.4$) in Fig. 3.18. This is because of the similarities in flux above 9 keV, which is identical in the case of the broken power law and only lower by 2% in the case of the `optxagnf` model.

Input Spectrum	Equivalent width of features/eV Fe XXV Heα	Fe XXVI Lyα	Fe XXV/Fe XXVI
$\Gamma = 1.6$	–	−112	–
$\Gamma = 1.8$	–	−201	–
$\Gamma = 2.0$	−071	−304	0.23
$\Gamma = 2.2$	−199	−389	0.51
$\Gamma = 2.4$	−395	−423	0.93
Broken power law	−337	−476	0.71
`optxagnf`	−387	−486	0.79

Table 3.5: The equivalent width of the absorption feature with varying photon index (Γ). This shows how the distribution of photons to higher energies decreases the ratio of the absorption features.

However, the increased soft flux from the SED fitting will be important for the presence of lower ionisation lines as observed in the *XMM-Newton* RGS for both PDS 456 (Reeves et al. 2016) and PG1211 + 143 (Pounds et al. 2016a). The presence of soft X-ray absorption features in the model was first noted in Sim et al. (2010) in relation to PG1211 + 143, who attempted a simple comparison between the wind spectra and the observed soft X-ray absorption features.

3.2.9 Effects of varying the launch radius

As explained earlier the terminal velocity is set by its launch radius:

$$v_\infty = f_v \sqrt{2R_\mathrm{g}/R}\, c. \tag{3.4}$$

The top panel in Fig. 3.19 shows the density colour maps of three winds with inner radii of 32, 48 and 64 R_g, and the outer radii is set to be $R_\mathrm{out} = R_\mathrm{in} + 20\,R_\mathrm{g}$ to keep physical depth of the wind constant. The effect of setting f_v is that the effective launch radius R_eff moves inwards by a factor of ${f_v}^2$, so I keep f_v fixed at 1 for clarity.

The spectra of the three winds are shown in bottom panels in Fig. 3.19, with an inclination of $\sim 47°$. The left hand side panel shows the broad band spectra, whilst the right hand side shows a zoom in on the Fe K region with the spectra shifted along the y axis so that the continua overlap. The velocity shift is seen in the centroid energy of all spectral features where the larger inner radii (red) have the smallest velocity shift while the smaller R_in has the higher centroid energy.

A difference in velocities of the stream-lines can be seen in the width of the absorption lines; this is because v_∞ is non-linear with respect to launch radius as shown in equation 3.4. This means there is a larger difference in the velocity launched from R_in vs R_out for the smaller radii as seen in the wind where $R_\mathrm{in} = 32\,R_\mathrm{g}$ (black), while the resultant terminal velocities are $0.25 - 0.20\,\mathrm{c}$ compared to $0.20 - 0.17\,\mathrm{c}$ and $0.18 - 0.15\,\mathrm{c}$ when $R_\mathrm{in} = 48$ (blue) and $64\,R_\mathrm{g}$ (red) respectively. Fig. 3.19 also shows that the faster winds are launched from the inner radii. The innermost winds have a greater column as the density is relatively higher (and therefore the line depth is relatively stronger) for similar $\dot{M}$ due increase the in the volume with increasing R_in.

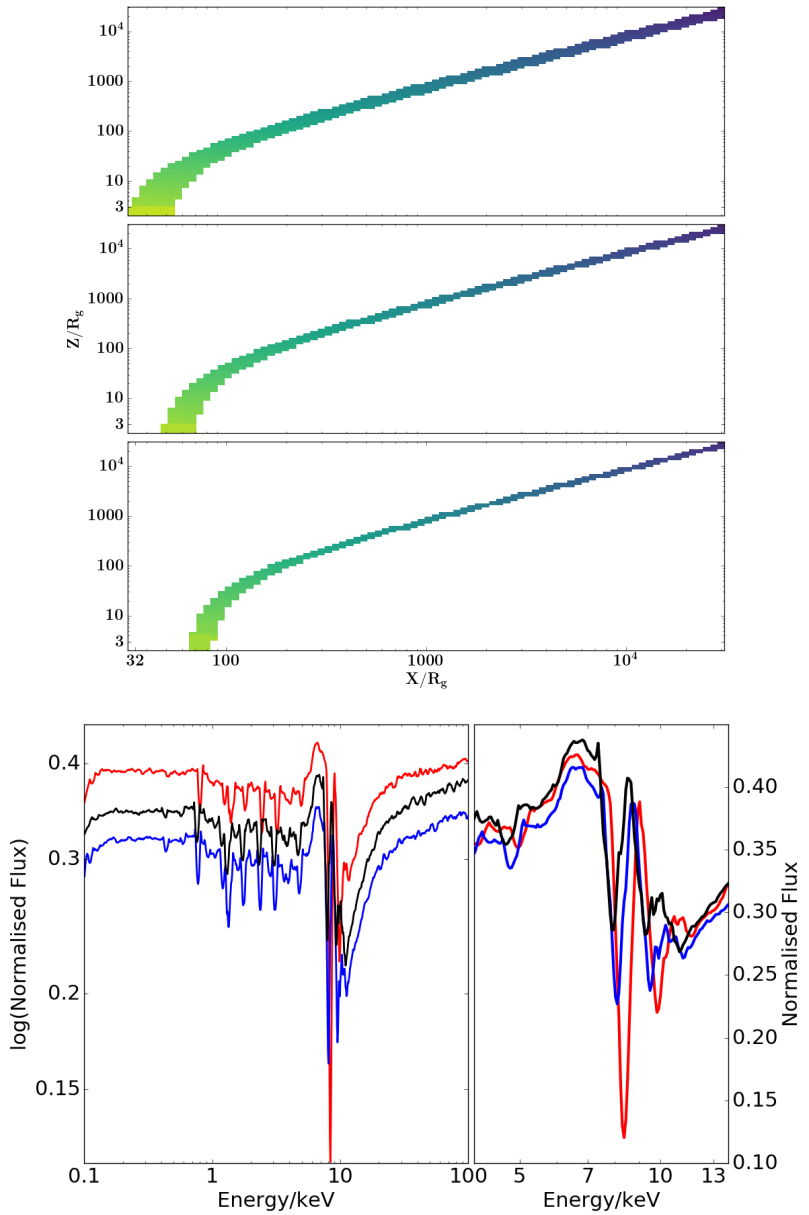

Figure 3.19: The upper plot is a set of density colour maps for three values of $R_{\rm in}$ of 32, 48 and 64 R_g going from top to bottom; to keep the wind width the same I set $R_{\rm out} = R_{\rm in}$ $+20\,R_{\rm g}$. The lower plot contains the total output spectrum from the three runs. The left hand side shows the total spectrum, whilst the right hand side shows a zoom in on the Fe Kα region where the spectra have been adjusted to overlap.It can be seen there appears to be a velocity shift with the black ($R_{\rm in} = 32\,R_{\rm g}$) being the fastest and red ($R_{\rm in} = 64\,R_{\rm g}$) being the slowest. This is because the velocity along the streamline directly scales with the escape velocity at the launch radius, so the largest velocity shift occurs at smaller radii where the escape velocity is larger. In these simulations $f_v = 2$.

Another way to increase the line width is to simply increase the depth of the wind as a larger depth means more velocity streams as v is dependent on radius. This is achieved by moving $R_{\rm out}$ to larger radii while keeping the inner radius constant (at $R_{\rm in} = 32\,R_{\rm g}$). For a flow with $f_v = 2$ and the standard ratio ($R_{\rm out}/R_{\rm in}$) of 1.5 ($48\,R_{\rm g}/32\,R_{\rm g}$), the velocity at the inner and outer radii corresponds to 0.5 c and 0.4 c respectively. Fig. 3.20 shows flows with a ratio ($R_{\rm out}/R_{\rm in}$) of 3, 5 and 8 moving from the top to bottom panel. As each stream absorbs in its own rest frame it removes photons at different energies in the observer frame; this leads to a broader profile. For the same inner velocity (0.5 c) and the ratios of $R_{\rm out}/R_{\rm in}$ above, this gives outer velocities of 0.29 c, 0.22 c and 0.18 c, thus producing larger Δv values of 0.21 c, 0.28 c and 0.32 c.

The increased volume means that the mass within the flow must also be increased to keep the density the similar so that $L_{2-10\,\rm keV}$ does not over-ionise the wind. By using the column density corresponding to the $\sim 75^\circ$ inclination (so that the outer face of the wind is intercepted in all simulations) the mass outflow rates ($\dot{M}$) are set to 19, 28 and 48% of $\dot{M}_{\rm edd}$. As seen in Fig. 3.20, the winds are self similar where the larger radii streamlines have a lower ionisation but the inner ones remain the same, showing that the mass outflow rate was increased sufficiently. As inclination angle affects the observed line width, this means that changes in the structure which affect the line of sight through the wind may cause similar changes in the observed profile. The spread of angles of the velocity vectors which causes this is a function of the distance between the inner and outer radii, so this effect will be stronger in thicker winds. Thus, thicker winds produce broader absorption line profiles due to increased number of steam lines which are intercept the LOS.

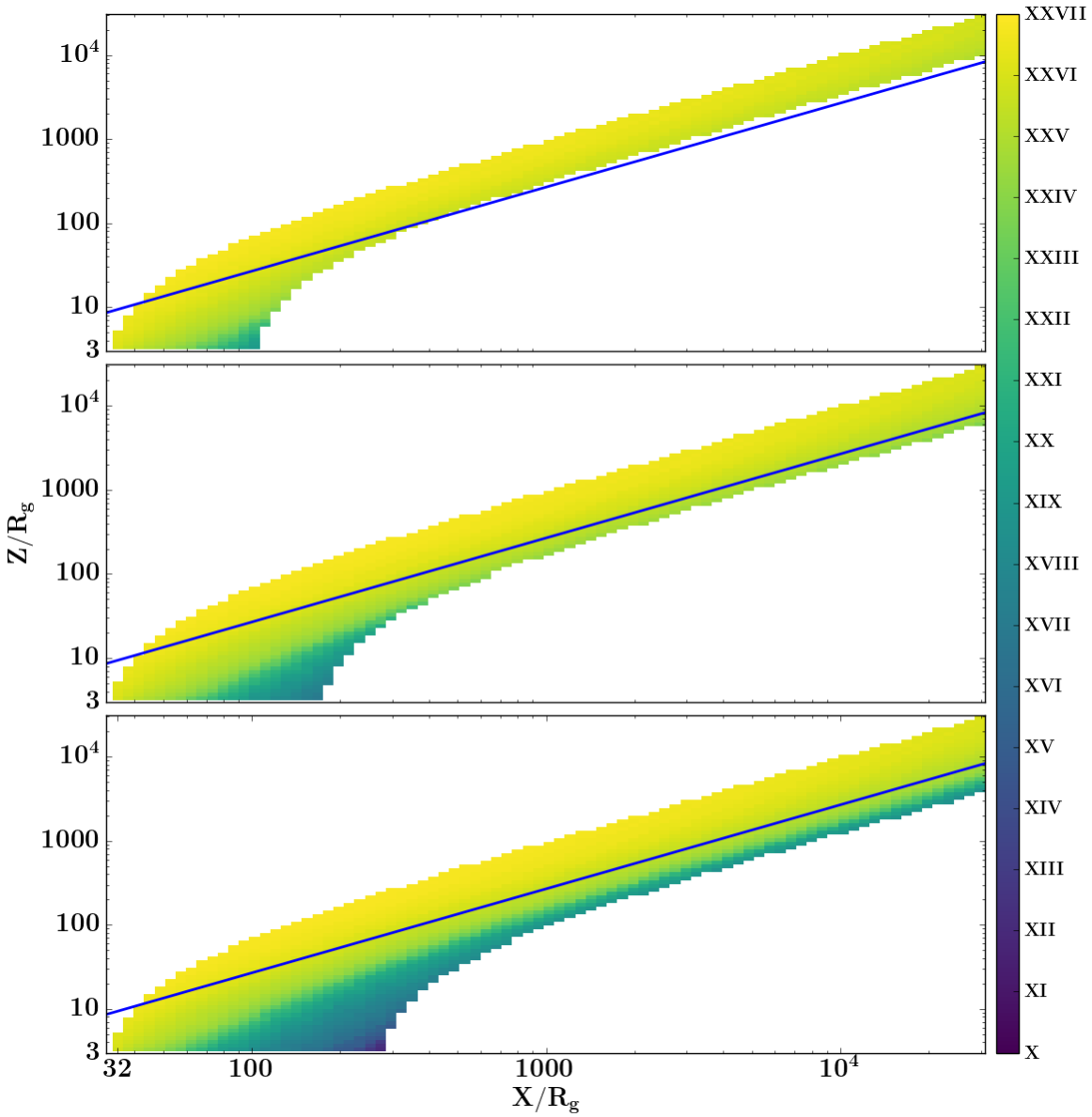

Figure 3.20: Average charge of iron within three flows of varying thickness. By changing the outer radius but keeping the inner radius fixed (at $32\,R_g$), I increase the thickness of the wind. Here I have three examples of thicker winds with $R_{out}/R_{in} = 3$, 5 and 8, with an $L_{2-10\,keV}/\,L_{edd}$ of 0.25% and a mass outflow rate of 19, 28 and 48% $\dot{M}_{edd}$. These were selected as they gave similar column densities at an inclination of $\sim 75°$.

The resultant spectra of the three thickness ratios ($R_{\rm out}/R_{\rm in}$) along the $\sim 75°$ inclination (the blue line in Fig. 3.20) are seen in Fig. 3.21, where the top panel shows the components and total spectrum with increasing ratio $R_{\rm out}/R_{\rm in}$ from top to bottom. The blue (high velocity) part of the absorption line profile occurs at the same energy (defined by $R_{\rm in}$). The increase of $R_{\rm out}$ means that the red wing shifts to lower energies (as the escape velocity is lower) increasing the width of the features.

It can be seen that the increased geometric thickness of the wind causes broader absorption features. In addition to the increase in breadth, the lower ionisation species are present on the slower streamlines due to the wind self shielding, causing the observed difference to be even larger than would be expected from velocity differences alone. The lower panel in Fig. 3.21 contains the overlay of the Fe K region of the aforementioned spectra. The higher velocity occurs at the same energy, whereas the absorption feature extends to lower energies and a He-like line at lower velocity shows a double pronged. This may account for some objects which seem to have multiple velocity components such as in PG1211 + 143 or broad absorption troughs such as those seen in 1H 0707 − 495. This is due to the LOS intercepting the outer, slower streamlines in the wind, which will also have a lower ionisation (i.e. Fe XXV). This means that wind features will be separated by both ionisation (and therefore emission energy) as well as velocity (observed energy), which can produce a larger than expected difference in the observed centroid energies.

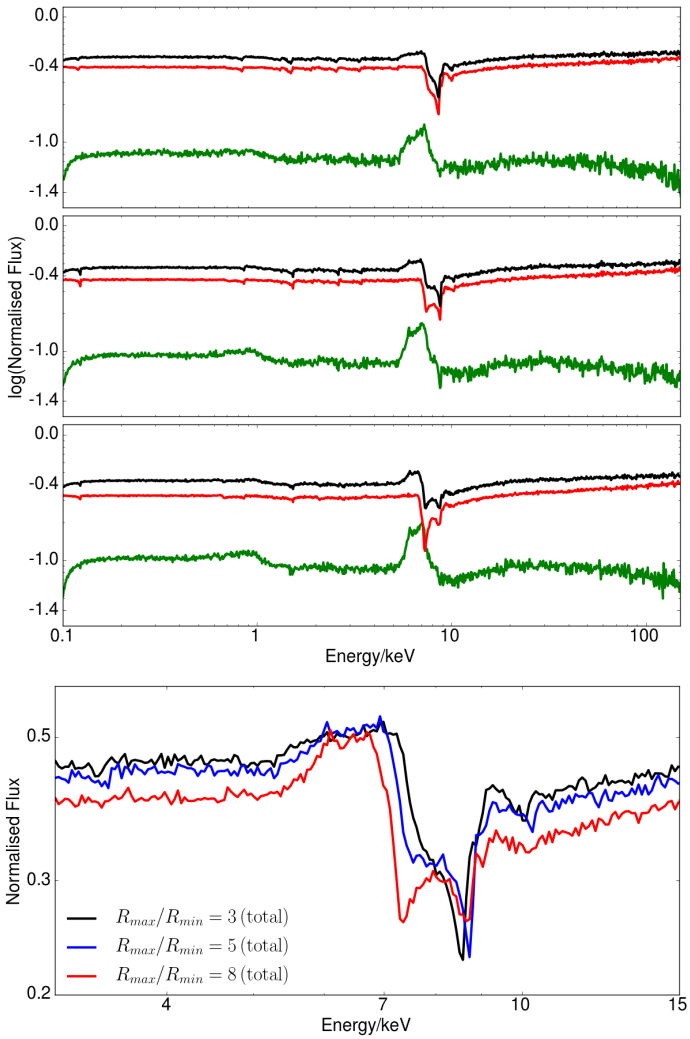

Figure 3.21: The output spectra for the three thicknesses shown in Fig. 3.20. The top, middle and bottom panel of the top plot correspond to an $R_{\rm out}/R_{\rm in}$ ratio of 3, 5 and 8 respectively. These spectra are at an inclination of $\sim 75°$ (shown by the blue line on each plot) which has a column density of $\sim 8 \times 10^{23}\,{\rm cm}^{-2}$. The terminal velocity of a wind with $f_v = 2$ where innermost steam line is launched from $32R_{\rm g}$ will have a terminal velocity of 0.5 c. The top plot shows the total (black) and the decomposed direct (red) and scattered (green) components, while the lower plot shows a zoom-in on the iron K region. It can be seen in thicker winds that the absorption features are much broader. This is a two-fold effect: the thicker winds observe multiple steam lines as different launch radii will have different velocities, so a broad profile is observed. As is a larger range in ionisation states within the wind; this is shown by the double trough in the $R_{\rm out}/R_{\rm in} = 8$ (red) spectra in the lower plot: the slower streamlines are further out, they have a lower ionisation so this will have the effect of increasing the observed spread of velocities.

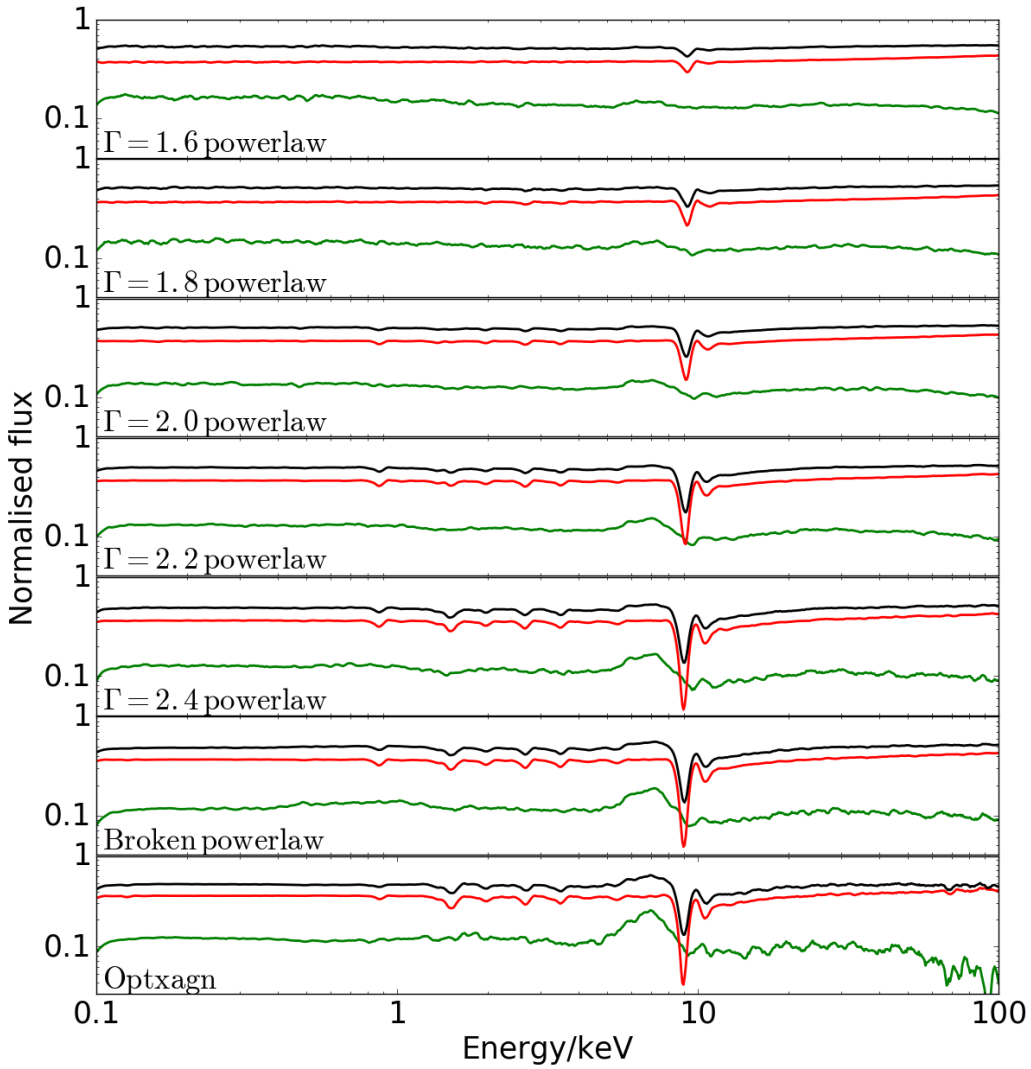

Figure 3.18: The total (black), direct (red) and scattered (green) spectra normalised to their input spectrum. The observed changes are due to different input spectra which can be seen in Fig. 3.17. The absorption feature around 9 keV deepens and shifts to lower energies as gamma becomes larger. Because there are fewer high energy photons, the ionisation of the wind is reduced. The last three spectra are very similar, particularly around ~ 8 keV, where it is the high energy flux that the He/H-like Fe atoms are responding to. All the spectra were simulated with a 2–10 keV luminosity of 1.24% $L_{\rm edd}$, an outflow rate of 15 $M_\odot$ yr^{-1} and $f_v = 2$.

3.3 Requirements for fitting

I have demonstrated throughout this chapter the effect of changing various parameters of the radiative transfer code which I will be using for the rest of this thesis. Parameters can be constrained based on observed features of the spectra or the object. Along with reasonable model construction these can mitigate many of the degeneracies. For instance the $L_{2-10\,\mathrm{keV}}$ parameter can be found from the fit continuum. Another parameter linked with $L_{2-10\,\mathrm{keV}}$ is the shape of the input spectrum, as they both modify the ionisation state of the wind. The shape of the fit continuum also can give the shape of the input spectrum allowing better constraints on $L_{2-10\,\mathrm{keV}}$. Sometimes the intrinsic continuum is modified heavily by absorption: by modelling the absorption, often a reasonable approximation of the intrinsic spectra can be found.

The velocity can be measured from the energy shift of the absorption features. The velocity shift within the model can be changed as demonstrated earlier by modifying R_{in} or f_v. f_v often used as this is to keep the geometric structure the same for simplicity (as you do not have to change LOS through the wind). The width of the absorption feature can be used to define the thickness of the wind; although the inclination does affect the observed widths it is also dependent on the energy shift and the depth of the feature, all of which are also constrained by other parameters. $R_{\mathrm{out}}/R_{\mathrm{in}} = 1.5$ is generally sufficient to model the width of most absorption troughs, except for particularly broad features such as those observed in 1H 0707 − 495 which has a broad and deep profile.

The following chapters will show how to use reasonable parameter choices and model construction to limit the degeneracies within the model. This allows the use of these models to gain a better understanding of the disk winds in the objects PDS 456, PG1211 + 143 and 1H 0707 − 495.

4 PDS 456: The Rosetta stone of disk winds

4.1 Introduction to PDS 456

The radio-quiet quasar PDS 456 is located relatively close ($z = 0.184$) and its high bolometric luminosity ($L_{\rm bol} \sim 10^{47}$ erg s^{-1}; Simpson et al. 1999) makes it the most luminous quasar in the local universe ($z < 0.3$). Such high luminosity is more reminiscent of objects at redshift 2–3 when high luminosity quasars were more common. The combination of its high luminosity and proximity allows for high quality spectra, and hence detailed study of PDS 456. Even with its large black hole ($M_{\rm BH} \sim 10^9\,M_\odot$ Simpson et al. 1999; Reeves et al. 2000) it is still accreting at a substantial fraction of $\dot{M}_{\rm edd}$ ($L_{\rm bol}/L_{\rm edd} \sim 1$). This allows it to power a substantial wind ($L_{\rm kin}/L_{\rm bol}$ = 15–20%; Nardini et al. 2015), which, as mentioned in chapter 1.3.4, well exceeds the theoretically predicted value of $L_{\rm kin}/L_{\rm bol} \sim 0.5$–5% for feedback to unbind the host galaxy's bulge (Di Matteo et al. 2005; Hopkins & Elvis 2010). For these reasons the quasar PDS 456 can be considered to be hosting the prototype powerful disk-wind, allowing us to decipher the complexities of similar objects at larger redshifts.

Little is known about the host galaxy of PDS 456. However, K-band imaging obtained with *Keck* observatory revealed three faint ($M_K \sim -21$ mag) compact companions (within ~ 10 kpc) which could suggest that PDS 456 has recently interacted or undergone a merger. Moreover, the host galaxy's morphology is not known due to the brightness of the nucleus which dominates at most wavelengths (Yun et al. 2004).

4.2 Observations

PDS 456 has been the subject of intense studies between 2001–2014, with over 1.5 Ms (in duration) of observations carried out with *Suzaku*, *XMM-Newton* and *NuSTAR* X-ray observatories. The details of these observations are listed in table 4.1. Overall, PDS 456

shows two distinct spectral states: low-hard (refering to flux–slope) and high-soft with intermediate states between the extremes.

Thus in this chapter will be presented three overall sets of observations: the *Suzaku* data (i), which are comprised of spectra from 2007, 2011, along with three from the 2013 campaign (2013a–c); the *XMM-Newton–NuSTAR* campaign (ii) which contains 5 spectra (labelled A–E) all of which were taken simultaneously with *XMM-Newton* and *NuSTAR* between 2013 and 2014; finally the archival *XMM-Newton* observations (iii) comprised of one from 2001 and two from 2007 (2007a–b).

Observation	Satellite	Start Date	End Date	Exposure/ks[1]	Flux[2]	Obs. ID
2001	*XMM-Newton*	2001-02-26	2001-02-26	36	10.88 (3.83/2.95)	0041160101
2007a	*XMM-Newton*	2007-09-12	2007-09-13	77	10.23 (4.22/2.42)	0501580101
2007b	*XMM-Newton*	2007-09-14	2007-09-15	74	5.72 (2.50/1.26)	0501580201
2007	*Suzaku*	2007-02-24	2007-03-01	191	6.86 (3.54/1.32)	701056010
2011	*Suzaku*	2011-03-16	2011-03-19	126	4.10 (1.45/1.14)	705041010
2013a	*Suzaku*	2013-02-21	2013-02-26	182	2.63 (0.57/1.02)	707035010
2013b	*Suzaku*	2013-03-03	2013-03-08	165	1.80 (0.30/0.79)	707035020
2013c	*Suzaku*	2013-03-08	2013-03-11	108	1.93 (0.44/0.69)	707035030
A	*XMM-Newton*	2013-08-27	2013-08-28	96	10.37 (3.79/2.83)	0721010201
	NuSTAR	-	-	44	11.19 (5.08/4.89)	60002032002
B	*XMM-Newton*	2013-09-06	2013-09-07	92	5.36 (2.59/1.04)	0721010301
	NuSTAR	-	-	43	3.77 (2.02/1.47)	60002032004
C	*XMM-Newton*	2013-09-15	2013-09-17	102	5.80 (2.32/1.44)	0721010401
	NuSTAR	-	-	44	6.03 (2.79/2.57)	60002032006
D	*XMM-Newton*	2013-09-20	2013-09-21	93	6.10 (2.25/1.60)	0721010501
	NuSTAR	-	-	59	6.39 (2.94/2.73)	60002032008
E	*XMM-Newton*	2014-02-26	2014-02-27	100	4.27 (1.62/1.09)	0721010601
	NuSTAR	-	-	110	3.76 (1.98/1.45)	60002032010

Table 4.1: Summary of the five observations with *Suzaku* and five *XMM-Newton* observations with simultaneous *NuSTAR*. [1] Net exposure time, after screening and dead-time correction. [2] Observed flux in 0.5–10 (0.5–2/5–10) keV band for *Suzaku* and *XMM-Newton* but 3–60 (3–10/10–40) keV, units $\times 10^{-12}$ erg s^{-1} cm^{-2}. All fluxes were detected by xis 0 and xis 3 (*Suzaku*), PN (*XMM-Newton*) and FPMA (*NuSTAR*).

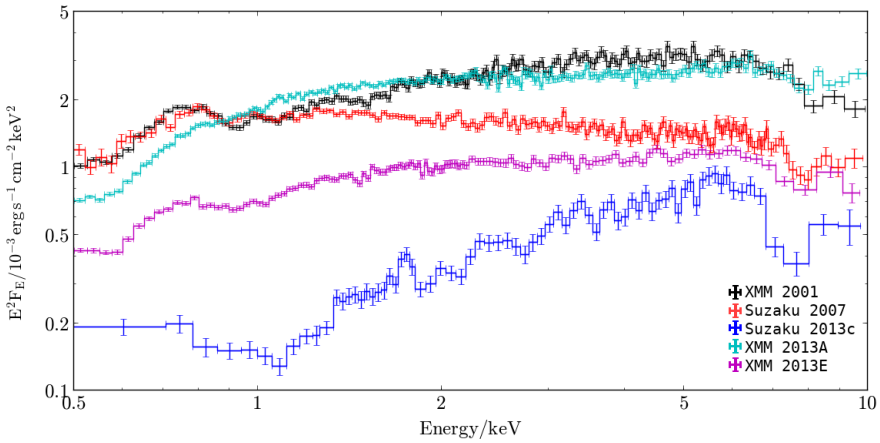

Figure 4.1: Representative selected sample of spectra showing the extremes of shape for PDS 456 over the time period from *XMM-Newton* 2001 to *XMM-Newton–NuSTAR* campaign in 2014.

PDS 456 shows a wide range of broadband variability in both flux and spectral shape as well as a remarkable variability in the Fe Kα absorption feature. This profile is at it deepest in the *Suzaku* observation 2013c but very weak in observation A in the *XMM-Newton–NuSTAR* campaign — which are separated by just over five months.

The remarkable variations between the extremes of the observation campaigns, along with some observed intermediate states, can be seen in Fig. 4.1. The high flux spectra in Fig. 4.1 were both observed with *XMM-Newton* in 2001 (black) and 2013 (teal; specifically observation A). While both are in a high flux state, the 2001 observation is significantly more absorbed. The *Suzaku* 2007 observation is comparable to *XMM-Newton* 2001 below 1 keV, however the *Suzaku* 2007 observation has a much steeper photon index causing the hard X-ray flux to drop by a factor of ~ 2.

The lowest observed flux state occurred in the *XMM-Newton–NuSTAR* campaign (observation E, magenta) showing an intermediate state with some hardening compared to the higher flux observations but not as extreme as the lower flux observations seen in the

2013 *Suzaku* campaign. The faintest spectrum of the *Suzaku* campaign can be seen as the blue spectrum in Fig. 4.1. It is characterised by the hardest observed slope (as mentioned previously) and strong absorption across the spectrum, which is particularly noticeable in the Fe K band. Furthermore, the general trend is that the observable parameters (centroid energy and depth) of the Fe K absorption correlate with the decreasing flux (directly for velocity, inverse for the absorption depth).

The behaviour of PDS 456 can generally be split up into two states: the high-soft state where intra-observation variability is dominated by continuum variations (Matzeu et al. 2017), and the low-hard state where absorption is dominating the spectra and the variability follows suit (Matzeu et al. 2016). The 2013 *XMM-Newton–NuSTAR* observations, which started only 6 months after the *Suzaku* observations, occur in the high state where the spectral variations are dominated by the power law photon index.

4.3 Fitting *Suzaku* spectra

To gain a simple understanding of the spectral changes between *Suzaku* observations 2007 and 2013c, I first use the partial covering model presented in Matzeu et al. (2016) as a baseline, where I allow two layers of neutral partial covering gas (Wilms et al. 2000) which partially cover the primary power law continuum only. The high column (zone 1; $\texttt{zTBabs}_1$) primarily adds curvature above 2 keV whereas the low column (zone 2; $\texttt{zTBabs}_2$) is a soft X-ray absorber. Along with a full covering absorber ($\texttt{TBabs}_{\texttt{gal}}$), this accounts for absorbers between PDS 456 and the observer. An additional soft excess emission component is required; for this I use a black body (`zbbody`). I also have included two Gaussian lines ($\texttt{zgauss}_{\rm em}$ and $\texttt{zgauss}_{\rm abs}$) at iron K corresponding to the emission and absorption due to the wind, and an additional soft Gaussian ($\texttt{zgauss}_{\rm soft}$) ~ 0.9 keV emission line as per Reeves et al. (2009, 2014); Matzeu et al. (2016, 2017). The construction of the model is:

$$F_E = \texttt{TBabs}_{\texttt{gal}} \times (\\ [(1 - \texttt{C}_2 - \texttt{C}_1) + \texttt{C}_2 \times \texttt{zTBabs}_2 + \texttt{C}_1 \times \texttt{zTBabs}_1] \times \texttt{po} \\ + \texttt{zgauss}_{\text{soft}} + \texttt{zbbody} + \texttt{zgauss}_{\text{em}} + \texttt{zgauss}_{\text{abs}}), \quad (4.1)$$

where $\texttt{C}_1$ and $\texttt{C}_2$ are constants that multiply the intrinsic continuum and relevant absorption model. They can be directly interpreted as covering fractions because the $(1 - \texttt{C}_2 - \texttt{C}_1)$ term forces the sum of the constants to equal one. $\texttt{C}_2^*$ is defined as the flux absorbed by the low column zone (C_2) to the ratio of the radiation transmitted through $\texttt{C}_1$ (as its high column zone (C_1) will remove much of the flux below 2 keV), mathematically defined as $\texttt{C}_2^* = \frac{\texttt{C}_2}{1-\texttt{C}_1}$.

The column densities are kept fixed across the observations as it is degenerate with the covering fraction. It is likely that both are varying at the same time. However, a pragmatic decision must be made as both cannot be constrained independently with the current spectral quality. Furthermore, changes in covering fraction are easier to model and when ionised absorbers are used later a more constrained column density will be beneficial. Therefore, the changes in spectral shape are reproduced by varying the covering fractions between observations.

The primary continuum is modelled using a power law. The photon index is tied over all observations as it is degenerate with the column density due to the lack of higher energy data. However the normalisation of the power law is free to vary. The normalisation of the soft excess black body component varies between observations whereas the model's temperature is kept the same for all observations. The normalisation of the $\texttt{zgauss}_{\text{soft}}$ emission line is also fixed between observations. This feature is also observed in Reeves et al. (2014) and Matzeu et al. (2016) while the line energy ($0.92^{+0.01}_{-0.02}$ keV) and σ width (37^{+30}_{-20} eV) is allowed to vary but is fixed between observations. The $\texttt{zgauss}_{\text{em}}$ and $\texttt{zgauss}_{\text{abs}}$, which could be interpreted as the Fe K emission and absorption of the wind, are seen in the form of the strong and variable absorption feature between 8.5–9 keV in the quasar rest frame, as well as the subsequent re-emission observed around ~ 7 keV in the quasar rest frame

(Nardini et al. 2015) where a P-Cygni like profile is observed. Both the absorption and emission features are allowed to vary in normalisation with the absorption feature also being allowed to vary in energy to account for the observed changes in the outflow velocity.

Component	Parameter	2007	2011	2013a	2013b	2013c
zTBabs$_1$	$N_{\rm H}/10^{22}\,{\rm cm}^{-2}$	$13.9^{+2.0}_{-2.4}$	13.9^{t}	13.9^{t}	13.9^{t}	13.9^{t}
	$v_{\rm out}/{\rm c}$	$-0.25^{+0.10}_{-0.04}$	-0.25^{t}	-0.25^{t}	-0.25^{t}	-0.25^{t}
zTBabs$_2$	$N_{\rm H}/10^{22}\,{\rm cm}^{-2}$	$1.4^{+0.2}_{-0.4}$	1.4^{t}	1.4^{t}	1.4^{t}	1.4^{t}
	$v_{\rm out}/{\rm c}$	-0.25^{tPC1}	-0.25^{t}	-0.25^{t}	-0.25^{t}	-0.25^{t}
C$_3$	%	$82.8^{+8.8}_{-7.5}$	$37.9^{+1.6}_{-1.2}$	$22.5^{+0.1}_{-8.9}$	$15.7^{+1.0}_{-14.2}$	< 13.4
C$_2^*$	%	$17.2^{+7.5}_{-8.8}$	$62.1^{+1.2}_{-1.6}$	$77.5^{+8.9}_{-0.1}$	$84.3^{+14.2}_{-1.0}$	> 86.6
C$_1$	%	$24.0^{+4.9}_{-6.8}$	$43.2^{+3.6}_{-2.7}$	$66.7^{+0.1}_{-1.1}$	$75.8^{+2.6}_{-0.1}$	$61.7^{+0.6}_{-0.2}$
po	Γ	$2.5^{ug}_{-0.10}$	2.5^{t}	2.5^{t}	2.5^{t}	2.5^{t}
	norm$/10^{-3}$	$3.6^{+2.7}_{-2.2}$	$3.4^{+2.5}_{-1.6}$	$2.9^{+2.5}_{-1.7}$	$2.4^{+2.2}_{-1.5}$	$2.2^{+1.9}_{-1.2}$
zbbody	kT/keV	$0.13^{+0.03}_{-0.02}$	0.13^{t}	0.13^{t}	0.13^{t}	0.13^{t}
	norm$/10^{-5}$	$1.96^{+1.10}_{-0.95}$	< 1.28	$0.52^{+0.75}_{-0.43}$	$0.47^{+0.55}_{-0.48}$	$1.52^{+0.70}_{-0.50}$
zgauss$_{\rm soft}$	Energy/keV	$0.92^{+0.01}_{-0.02}$	0.92^{t}	0.92^{t}	0.92^{t}	0.92^{t}
	σ/eV	37^{+30}_{-20}	37^{t}	37^{t}	37^{t}	37^{t}
	norm$/10^{-5}$	$9.9^{+5.7}_{-3.5}$	$5.3^{+2.6}_{-2.2}$	$1.8^{+1.8}_{-1.2}$	< 0.1	< 1.4
	EW/eV	18^{+6}_{-5}	32^{+11}_{-16}	24^{+23}_{-15}	< 46	< 35
zgauss$_{\rm em}$	Energy/keV	7.0 ± 0.1	7.0^{t}	7.0^{t}	7.0^{t}	7.0^{t}
	σ/eV	300^{f}	300^{f}	300^{f}	300^{f}	300^{f}
	norm$/10^{-5}$	0.44 ± 0.18	0.23 ± 0.21	0.38 ± 0.17	0.47 ± 0.16	0.40 ± 0.20
	EW/eV	98^{+50}_{-41}	96^{+11}_{-85}	81^{+101}_{-24}	199^{+54}_{-89}	123^{+133}_{-40}
zgauss$_{\rm abs}$	Energy/keV	$9.23^{+0.18}_{-0.22}$	$8.92^{+0.17}_{-0.13}$	$8.46^{+0.11}_{-0.09}$	$8.84^{+0.09}_{-0.08}$	8.68 ± 0.06
	σ/eV	< 422	396^{+186}_{-133}	< 200	247^{+86}_{-71}	221^{+90}_{-75}
	norm $/10^{-5}$	$-0.40^{+0.16}_{-0.19}$	$-0.79^{+0.24}_{-0.29}$	$-0.17^{+0.08}_{-0.05}$	$-0.52^{+0.13}_{-0.15}$	$-0.70^{+0.15}_{-0.18}$
	EW/eV	-180^{+91}_{-91}	-241^{+14}_{-212}	-52^{+21}_{-77}	-276^{+36}_{-150}	-539^{+193}_{-16}

Table 4.2: The best fit Gaussian model used for parameterisation. ^{ug} - the Γ parameter has the upper bound set to 2.6 to stop the model from going to extreme parts of the parameter space. ^{t} - parameter is tied to the value of 2007. ^{tPC1} - parameter is tied to the complementary value in $PC1$. ^{f} - parameter is fixed at this value. The high column covering fraction is C_3 of the zTBabs$_1$, the high column absorber. I then define C$_2^*$ as the covering fraction of the low column absorber of the flux transmitted through the high column, this is mathematically represented as C$_2^*$ = C$_2$/(C$_1$ + C$_2$). Finally I define transmitted flux as C$_3$ = 1 − (C$_2$ + C$_3$)

.

This model yields a fit statistic of $\chi^2/\nu = 758/725$ the parameters for which can be seen in table 4.2. Large changes in covering fractions are observed for the low ($\texttt{zTBabs}_2$, $N_{\rm H}= 1.4^{+0.2}_{-0.4} \times 10^{22}\,{\rm cm}^{-2}$) and high ($\texttt{zTBabs}_1$, $N_{\rm H}= 13.9^{+2.0}_{-2.4} \times 10^{22}\,{\rm cm}^{-2}$ column partial coverers, ranging from $24.0^{+4.9}_{-6.8}\%$ in 2007 to $75.8^{+2.6}_{-0.1}\%$ in 2013b and from $17.2^{+7.5}_{-8.8}\%$ in 2007 to $> 86.6\%$ in 2013c for the low and high column zone respectively. These changes in the neutral partial covering zones shows there has been an increase in the extent of the obscuring material.

The velocity of the partial covering gas is found to be comparable to values reported for the velocity of the ionised wind (Reeves et al. 2009, 2014; Nardini et al. 2015; Matzeu et al. 2016, 2017).

When using the 2013 data, Matzeu et al. (2016) found that when setting the velocity of the partial coverer to that of highly ionised outflow the fit was improved ($> 99.99\%$ confidence level). This suggests that the partial covering zones are part of the same or similar flow as the Fe Kα absorption feature.

This suggests a link between the partial covering gas and the wind. The partial covering could stem from the inhomogenous phase of the wind, as this will be less ionised due to a higher density resulting from clumping. This will be investigated further later on in this section. It can also be seen that the centroid energy of the Fe K absorption feature ($\texttt{zgauss}_{\rm abs}$) decreases from $9.23^{+0.18}_{-0.22}\,{\rm keV}$ in 2007 to $8.68 \pm 0.06\,{\rm keV}$ in 2013c, this can be interpreted as changes in outflow velocity — which was investigated in Matzeu et al. (2017) and will be discussed in section 4.7. The mechanism behind both of these changes is important as it provides crucial information about the physical properties of the wind.

In general (excluding 2013a) the magnitude of the equivalent of the Fe K absorption feature increases with decreasing flux, changing from -180^{+91}_{-91} to -539^{+193}_{-16} eV in 2007 and 2013c respectively. In contrast the Fe Kα emission feature ($\texttt{zgauss}_{\rm em}$) constant in flux across all of the five observations. The presence of these two spectral signatures gives an insight into the physical structure of the wind as the absorption feature is caused by the material that intercepts the line of sight (LOS), while the emission profile (and its broadness) is

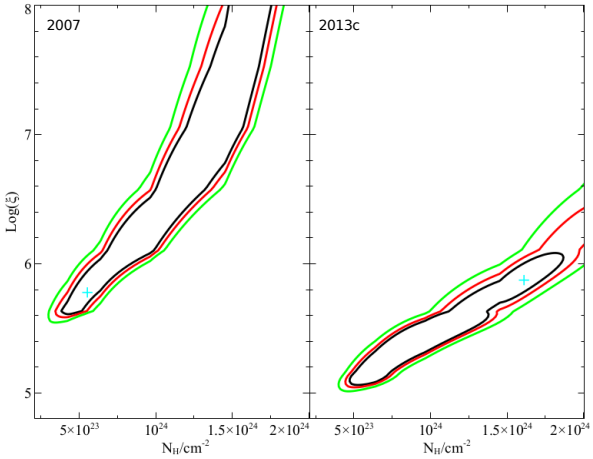

Figure 4.2: Contour plots of column density against the log of ionisation for 2007 (left) and 2013c (right). It shows the degeneracy between these parameters such that the two parameters can not be independently found from these spectra. Instead I have taken two simplistic models where ionisation or column density varies while keeping the other fixed.

characteristic the overall amount of reprocessing material (as line emission is isotropic) that covers the sky. Thus the observed behaviour may be due to variation of material that crosses the LOS and not the amount of absorbing gas as a whole; therefore the wind is inhomogeneous in structure but globally self-similar.

The changes of the soft ($\sim 0.9\,\mathrm{keV}$) emission feature ($\texttt{zgauss}_{\mathrm{soft}}$) seem to correlate with the covering fraction of the lower column partial coverer. This can be explained in two ways: either (a) the emission region is located within the partial covering zone, so the increased absorption attenuates the observed flux; or (b) the emission feature is located outside the partial covering complex and is instead responding to the observed soft flux.

To gain a better understanding of the broadband effects imparted by the highly ionised wind component on the spectra, I replace the adhoc $\texttt{zgauss}_{\mathrm{em}}$ and $\texttt{zgauss}_{\mathrm{abs}}$ with XSTAR emission/absorption grids with a velocity width of $10,000\ \mathrm{km\,s^{-1}}$ in order to account for the broad profiles observed. The 2007 observation shows two separate absorption lines for

H-like and He-like iron, each with a velocity width of $\sim 5,000$ km s^{-1} (Reeves et al. 2009). However, the same broadening in maintained for all the observations as the focus of this chapter is the broadband spectral variability not the precise line profile. To model the Fe K absorption and emission self-consistently I link the $N_{\rm H}$ and ionisation parameters between the grids. The outflow velocity is fixed between 2013a and 2013b to constrain the former as it has the weakest line profile observed (table 4.2). It is kept free for all other observations.

Shifting the velocity from the quasar rest frame to that of the outflow produces a $\Delta\chi^2 = -62$ for no change in the degrees of freedom in the previous section. This, as already mentioned, provides the evidence that they are part of the same flow. In order to better represent this scenario in the model, I use the same grid for both partial covering zones and Fe K absorption. This of course leads to more complexities within the model such as the additional ionisation parameter. In a highly ionised regime, an increase in the ionisation will cause the H-like ions to become fully ionised, reducing the effective absorbing column so that the value of $N_{\rm H}$ will increase to compensate. This leads to the degeneracy discussed already in Matzeu et al. (2016) and also shown in the contour plots in Fig. 4.2 between $N_{\rm H}$ and $\log \xi$). For this reason only one of these two parameters is allowed to vary between the observations.

Allowing $\log \xi$ to vary gives statistically a better fit ($\Delta\chi^2/\Delta\nu = 12/0$) compared to varying $N_{\rm H}$ which yielded $\chi^2/\nu = 714/707$. However, I opt for a model in which the column density varies, as it is hard to reconcile a factor of 6 change in the ionisation state against the hard band flux change of only a factor of 2 (see table 2.1). Note that only the 5–10 keV hard band flux is considered here as it would have the largest influence on the ionisation state of the highly ionised parts of the outflow. Ideally it would be appropriate to scale the ionisation with the power-law normalisation, however as there is evidence that there might be a delay in the wind's response to intrinsic flux variations (Matzeu et al. 2016) This is not possible without knowing the wind's response function. Finally, having the `zbbody` located outside of the partial covering is nonphysical, as both the soft excess and power law continuum originate from similar regions closer to the SMBH than the partially covering

structure so the soft excess component is moved within the partial covering zones.

The black body normalisation and power law normalisation are kept at the same ratio (black body/power law) for all observations. This link between the two components may or may not be valid depending on the nature of the soft excess, however it also serves as an attempt to break the degeneracy between the covering fractions and the black body normalisation.

The combination of the above modifications produces a model of the form:

$$F = \texttt{Tbabs} \times ([(1 - \texttt{C}_2 - \texttt{C}_1) + \texttt{C}_2 \times \texttt{wind\_pc}_2 + \texttt{C}_1 \times \texttt{wind\_pc}_1] \times (\texttt{po} + \texttt{zbbody}) + \texttt{zgauss}_{\rm soft} + \texttt{wind\_Fe}_{\rm em}) \times \texttt{wind\_Fe}_{\rm abs} \quad (4.2)$$

Here the constants ($\texttt{C}_{1-3}$) have the same meaning as in the previous model. The $\texttt{wind\_pc}_{1-2}$ are the two zones (high and low $N_{\rm H}$) of the partially ionised partial coverers. Whereas $\texttt{wind\_Fe}_{\rm abs/em}$ correspond the highly ionised absorption and emission components. The partial covering and highly ionised components occupy different parts of the parameter space within the same XSTAR grid. I find that $\texttt{wind\_pc}_1$ and $\texttt{wind\_pc}_2$ have lower ionisation ($\log \xi = 2.62^{+0.25}_{-0.24}$ and $0.89^{+0.20}_{-0.02}$) compared to $\texttt{wind\_Fe}_{\rm abs}$ ($\log \xi = 5.8^{+0.2}_{-0.3}$). The absorbing column densities of the partially covering zones are $1.5^{+0.1}_{-0.2} \times 10^{23}\,{\rm cm}^{-2}$ and $1.73^{+0.27}_{-0.12} \times 10^{22}\,{\rm cm}^{-2}$ for zone 1 and 2 respectively, while for $\texttt{wind\_Fe}_{\rm abs}$ component the $N_{\rm H}$ ranges between $4.6^{+1.6}_{-2.0} \times 10^{23}\,{\rm cm}^{-2}$ (in 2013a) and $1.56^{+0.21}_{-0.44} \times 10^{24}\,{\rm cm}^{-2}$ (in 2013c).

A plot of the data-to-model ratio of the resultant fit can be seen in Fig. 4.3. While the absorption feature in some of the spectra is not perfectly fit, in general the model parameterises the absorption lines sufficiently.

I find a ratio of black body to power law of $0.017^{+0.069}_{-0.008}$; this presents problems in the strength of the soft component in the highly absorbed observation 2013c which produces large residuals; in principle this can be rectified by removing this constraint for that dataset, however for a consistent analysis between datasets the constraint is kept.

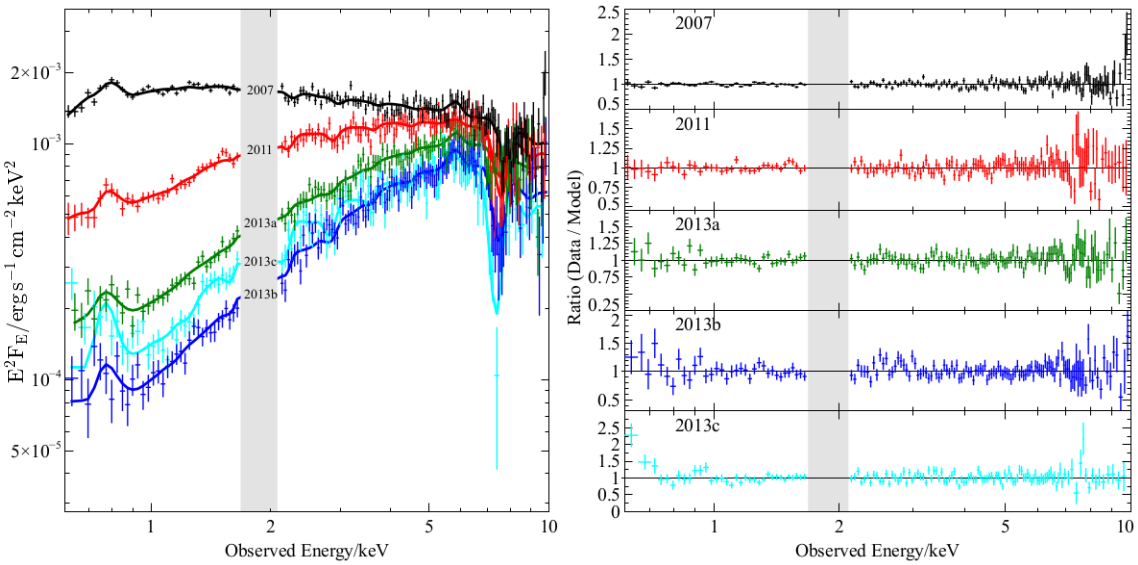

Figure 4.3: Ratios of the data to the best fit partial covering model for all *Suzaku* observations.

Overall the same trends or equivalent values are seen in the analogous components in the more physical model - except for where this was impossible due to modelling constraints namely the black body normalisation.

The flux of the wind emission is once again consistent with being constant as seen in table 4.3. The trend (with the exception of 2013a) for increasing covering fractions and increased Fe K shell absorption are consistent with the previous model. While columns of the partial covering absorbers are slightly larger being mildly ionised this is to be expected as ionisation will reduce the effect of the overall absorbing column.

Therefore this more physically accurate model (equation 4.2) agrees with the phenomenological model (equation 4.1) in showing that in PDS 456 the spectra become harder due to covering fraction changes in the low ionisation part of the wind. The strength of the absorption trough imprinted by the high ionisation phase of the wind increases as the observed flux decreases.

Component	Parameter	2007	2011	2013a	2013b	2013c
$\texttt{wind\_Fe}_{\rm abs}$	$N_{\rm H}/10^{22}\,{\rm cm}^{-2}$	$57.9^{+15.7}_{-12.9}$	$83.2^{+23.0}_{-16.2}$	$45.7^{+16.3}_{-20.2}$	$96.8^{+22.5}_{-17.0}$	$155.5^{+20.6}_{-43.6}$
	$\log\xi$	$5.8^{+0.2}_{-0.3}$	5.8^{t}	5.8^{t}	5.8^{t}	5.8^{t}
	outflow velocity/c	$-0.295^{+0.010}_{-0.009}$	$-0.265^{+0.009}_{-0.010}$	$-0.254^{+0.009}_{-0.008}$	-0.254^{ta}	-0.242 ± 0.007
$\texttt{wind\_Fe}_{\rm abs}$	$\log(F/\,{\rm erg\,s^{-1}\,cm^{-2}}\,)$	$-13.4^{+0.2}_{-0.3}$	< -13.1	$-13.2^{+0.2}_{-0.5}$	$-13.2^{+0.2}_{-0.3}$	$-13.2^{+0.2}_{-0.6}$
$\texttt{zgauss}_{\rm soft}$	Energy/keV	$0.89^{+0.02}_{-0.01}$	0.89^{t}	0.89^{t}	0.89^{t}	0.89^{t}
	σ/eV	50^{f}	50^{f}	50^{f}	50^{f}	50^{f}
	norm $/10^{-5\,g}$	$14.1^{+3.5}_{-4.1}$	$4.7^{+2.4}_{-2.3}$	$2.3^{+1.3}_{-1.2}$	$1.2^{+0.5}_{-1.0}$	$4.5^{+1.7}_{-1.8}$
C_3	%	62.5 ± 7.8	22.5 ± 3.6	8.3 ± 1.6	4.3 ± 0.9	6.8 ± 1.1
C_2^*	%	18.3 ± 3.6	64.4 ± 4.2	75.1 ± 4.6	81.1 ± 3.8	82.1 ± 3.0
C_1	%	23.5 ± 8.3	36.8 ± 5.2	66.7 ± 4.1	77.1 ± 2.7	62.1 ± 4.1
$\texttt{wind\_pc}_1$	$N_{\rm H}/10^{22}\,{\rm cm}^{-2}$	$15.4^{+1.2}_{-1.6}$	15.4^{t}	15.4^{t}	15.4^{t}	15.4^{t}
	$\log\xi$	$2.62^{+0.25}_{-0.24}$	2.62^{t}	2.62^{t}	2.62^{t}	2.62^{t}
$\texttt{wind\_pc}_2$	$N_{\rm H}/10^{22}\,{\rm cm}^{-2}$	$1.73^{+0.27}_{-0.12}$	1.73^{t}	1.73^{t}	1.73^{t}	1.73^{t}
	$\log\xi$	$0.89^{+0.20}_{-0.02}$	0.89^{t}	0.89^{t}	0.89^{t}	0.89^{t}
zbbody	kT/keV	$0.11^{+0.02}_{-0.03}$	0.11^{t}	0.11^{t}	0.11^{t}	0.11^{t}
	norm$/10^{-5} L_{39} D_{10}^{-2}$	6.2^{+16}_{-3}	5.8^{r}	5.2^{r}	4.4^{r}	4.0^{r}
po	Γ	$2.53^{+0.03}_{-0.06}$	2.53^{t}	2.53^{t}	2.53^{t}	2.53^{t}
	norm$/10^{-3\,p}$	$3.7^{+0.1}_{-0.5}$	3.5 ± 0.2	$3.1^{+0.1}_{-0.2}$	$2.6^{+0.1}_{-0.2}$	2.4 ± 0.1

Table 4.3: The parameters of the best fit model showing an increase in covering fraction. L_{39} is source luminosity in units of $10^{39}\,{\rm erg\,s^{-1}}$ and D_{10} is the distance to the source in units of 10 kpc. The redshift of Fe Kα $_{\rm em}$ is consistent with the quasar rest frame. ^{f}: parameter is fixed that value. ^{t}: parameter is tied to the value of parameter in 2007. ^{ta}: parameter is tied to the value of observation 2013a. ^{r}: parameter is fixed to the ratio of normalisations such that $\texttt{zbbody}_{\rm b} = \texttt{po}_{\rm b}(\texttt{zbbody}_{\rm a}/\texttt{po}_{\rm a})$ ^{p}: photons keV^{-1}cm^{-2} s^{-1}
^{g}: photons cm^{-2} s^{-1}

4.4 Fitting *XMM-Newton–NuSTAR* data

A series of five observations were taken simultaneously with *XMM-Newton* and *NuSTAR*. The first four observations were separated by roughly a week starting on 27/08/2013 and the last observation 6 months later. Further details can be found in table 4.1.

Fig. 4.4 shows large continuum variability. The majority of the flux variably can be seen in the hard X-rays between 10–20 keV. The most extreme change coming between observation A (black spectrum) and B (red spectrum) with the continuum becoming much softer.

To fit these spectral changes a similar model to equation 4.2 is used with a few distinctions. The *NuSTAR* bandpass extends to much higher energies than the XIS detectors.

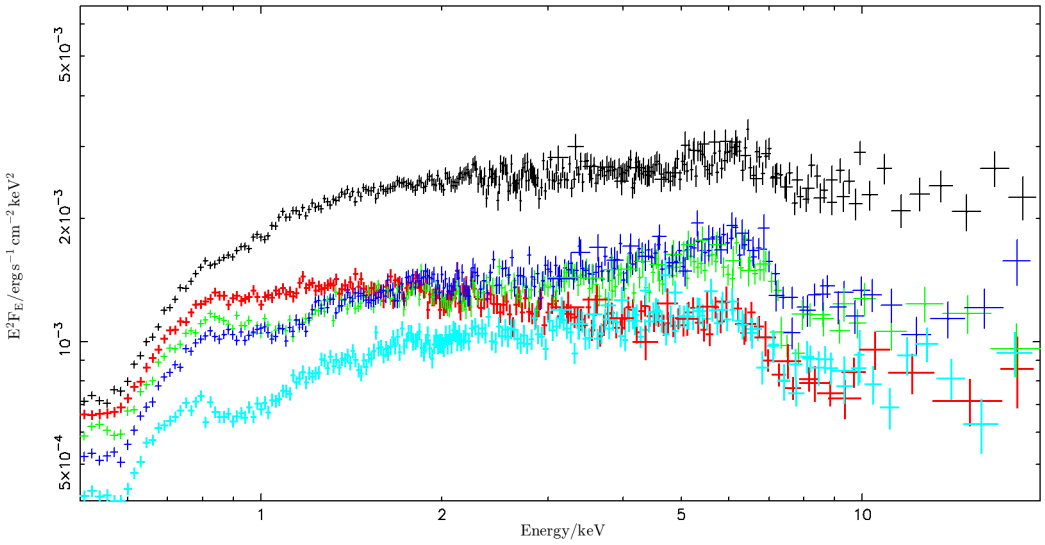

Figure 4.4: A plot of the *XMM-Newton–NuSTAR* spectra observations A (black), B (red), C (green), D (blue), and E (cyan). The large continuum variations can be seen in the comparison between the spectra of observations A, B and D — observation A being comparatively flat between 2–5 keV to observation B being very soft then finally in observation D becoming harder.

This allowed, for the first time, to obtain high quality spectra above 10 keV and hence provide a better understanding of the broadband X-ray continuum (0.3–50 keV), which resulted in a better constraint on the wind profile (Nardini et al. 2015).

However a multiplicative offset is required to account for the cross calibration in flux between the *XMM-Newton* PN and *NuSTAR* FPMA and FPMB detectors. The data *NuSTAR* provides above 10 kev means it is possible to allow the photon index of the primary continuum to vary between the observations. While it should be noted that in some very high quality spectra there seems to be a problem with the cross calibration of the photon index, the data used here is not of sufficient quality to notice (Porquet et al. 2018).

Finally as per Nardini et al. (2015), the ionisation of the low column partial covering zone to change between observations (giving a $\Delta\chi^2/\Delta\nu = 290/4$) and swap the highly ionised absorption grid for one with a larger velocity width ($v_{\rm width} = 15,000$ km s^{-1}; `wind-Fe-v15k`).

This is done because the breadth of the profile has increased between the observing campaigns showing that the outflow has changed. The new grid is generated for this as it is not feasible produce a grid allowing $v_{\rm width}$ to vary. The partial covering grids are still $v_{\rm width} = 10,000$ km s^{-1} (`wind-pc-v10k`). All other symbols retain the meaning. After the changes above the resulting model is:

$$\begin{aligned} F = \texttt{offset} \times \texttt{Tbabs} \times (\texttt{zgauss}_{\rm soft} + \\ [(1 - \texttt{C}_2 - \texttt{C}_1) + \texttt{C}_2 \times \texttt{wind-pc-v10k}_2 + \texttt{C}_1 \times \texttt{wind-pc-v10k}_1] \times (\texttt{po} + \texttt{zbbody}) \\ + \texttt{wind-Fe-v15k}_{\rm em}) \times \texttt{wind-Fe-v15k}_{\rm abs} \end{aligned} \quad (4.3)$$

This produces an overall fit of $\chi^2/\nu = 4301/4038$; the parameters of this fit can be seen in table 4.4; the ratio to the best fit model can be seen in Fig. 4.5. The photon index of the primary continuum: 2.10 ± 0.03 to 2.43 ± 0.04 between observations A and B which are only separated by a week are the two extremes in photon index.

Compared to this the changes in the partial covering fraction are comparatively small ($1 - (\texttt{C}_2 + \texttt{C}_1)$ varying from 34 ± 6 in observation A to $< 17\%$ in observation C before

returning back to 30^{+4}_{-3} in observation E). For all but observation E (the last and lowest in flux) the covering fraction of the high column zone is unconstrained giving only an upper limit. The low column partial covering zone's ionisation does not track with any of the flux measurements. Observation E has the highest ionisation ($L_{\rm ion} = 1.64^{+0.46}_{-0.25}$) while having almost the lowest flux level in all bands.

It is interesting to note that the wind's emission is found to be outflowing at $5700 \pm 2400\,{\rm km\,s^{-1}}$; this can not be constrained on a per observation basis so it is kept consistent between observations. However it does show that the broad emission assumed to be part of the outflow is in fact moving towards the observer. Once again the emission component is consistent with being constant in flux with the larger variations observed in the LOS absorber, even with the larger range in hard X-ray flux observed. Overall it seems that the higher flux *XMM-Newton–NuSTAR* campaign is dominated by intrinsic variability as observed by Matzeu et al. (2017) within the 2007 *Suzaku* observation. So the longer timescale variations while larger in magnitude are similar in characteristics.

Component	Parameter	A	B	C	D	E
wind-Fe-v15k$_{\rm abs}$	$N_{\rm H}/10^{22}\,{\rm cm}^{-2}$	$12.7^{+3.0}_{-2.3}$	$24.0^{+6.2}_{-6.4}$	$35.2^{+4.6}_{-4.0}$	$31.6^{+4.0}_{-3.6}$	$29.5^{+4.2}_{-6.5}$
	$\log\xi$	4.68 ± 0.04	4.68^{t}	4.68^{t}	4.68^{t}	4.68^{t}
	outflow velocity/c	-0.30 ± 0.01	-0.30 ± 0.01	-0.31 ± 0.01	-0.31 ± 0.01	-0.28 ± 0.01
wind-Fe-v15k$_{\rm em}$	outflow velocity/c	-0.019 ± 0.008	-0.019^{t}	-0.019^{t}	-0.019^{t}	-0.019^{t}
	$\log({\rm Flux}/\,{\rm erg\,s^{-1}\,cm^{-2}}\,)$	$-12.71^{+0.12}_{-0.21}$	$-12.84^{+0.11}_{-0.18}$	$-12.74^{+0.09}_{-0.14}$	$-12.61^{+0.08}_{-0.12}$	$-12.91^{+1.11}_{-0.19}$
zgauss	Energy/keV	0.87 ± 0.01	0.87^{t}	0.87^{t}	0.87^{t}	0.87^{t}
	σ/eV	50^{b}_{-10}	50^{t}	50^{t}	50^{t}	50^{t}
	norm$/10^{-4\,g}$	$1.08^{+0.17}_{0.17}$	$1.01^{+0.18}_{-0.17}$	1.58 ± 0.16	1.41 ± 0.15	$1.06^{+0.16}_{-0.17}$
$1-(\mathtt{C_2}+\mathtt{C_1})$	%	34 ± 6	< 36	< 17	< 19	30^{+4}_{-3}
$\mathtt{C_2}$	%	55 ± 5	57^{+20}_{-17}	48^{+4}_{-14}	47 ± 10	39 ± 4
$\mathtt{C_1}$	%	< 22	< 63	< 56	< 43	31 ± 7
wind-pc-v10k$_2$	$N_{\rm H}/10^{22}\,{\rm cm}^{-2}$	$0.89^{+0.17}_{-0.15}$	0.89^{t}	0.89^{t}	0.89^{t}	0.89^{t}
	$\log\xi$	0.10 ± 0.09	-0.42 ± 0.36	$-0.44^{+0.29}_{-0.13}$	$-0.22^{+0.22}_{-0.19}$	$1.64^{+0.46}_{-0.25}$
wind-pc-v10k$_1$	$N_{\rm H}/10^{22}\,{\rm cm}^{-2}$	$9.04^{+0.82}_{-0.80}$	9.04^{t}	9.04^{t}	9.04^{t}	9.04^{t}
	$\log\xi$	3.41 ± 0.02	3.41^{t}	3.41^{t}	3.41^{t}	3.41^{t}
zbbody	kT/keV	0.20 ± 0.01	0.20^{t}	0.20^{t}	0.20^{t}	0.20^{t}
	norm$/10^{-5\,bb}$	$4.39^{+1.32}_{-1.03}$	3.11^{r}	3.81^{r}	3.62^{r}	2.60^{r}
po	Γ	2.10 ± 0.03	2.43 ± 0.04	2.33 ± 0.04	2.25 ± 0.04	2.31 ± 0.03
	norm$/10^{-3\,p}$	3.2 ± 0.2	2.3 ± 0.2	2.8 ± 0.2	2.6 ± 0.2	1.9 ± 0.1
nustar offset	FPMA	1.02 ± 0.02	1.03 ± 0.04	1.07 ± 0.03	1.00 ± 0.03	1.00 ± 0.03
	FPMB	$1.01^{+0.03}_{-0.02}$	1.04 ± 0.04	1.05 ± 0.04	1.00 ± 0.03	1.07 ± 0.03
	χ^2/ν	971/877	747/644	926/760	724/747	744/667
	H_0	0.01	3×10^{-3}	3×10^{-5}	0.72	0.02

Table 4.4: The parameters of the best fit model (equation 4.3) showing an increase in covering fraction. ^{bb}: $L_{39}D_{10}^{-2}$ where L_{39} is source luminosity in units of $10^{39}\,{\rm erg\,s^{-1}}$ and D_{10} is the distance to the source in units of 10 kpc. ^{f}: parameter is fixed that value. ^{t}: parameter is tied to the value of parameter in 2007. ^{ta}: parameter is tied to the value of observation 2013a. ^{r}: parameter is fixed to the ratio of normalisations such that $\mathtt{bbody_b} = \mathtt{po_b}(\mathtt{bbody_a}/\mathtt{po_a})$
^{p}: photons keV^{-1}cm^{-2} s^{-1}
^{b}: The parameter hits the upper bound 50 eV
^{g}: photons cm^{-2} s^{-1}

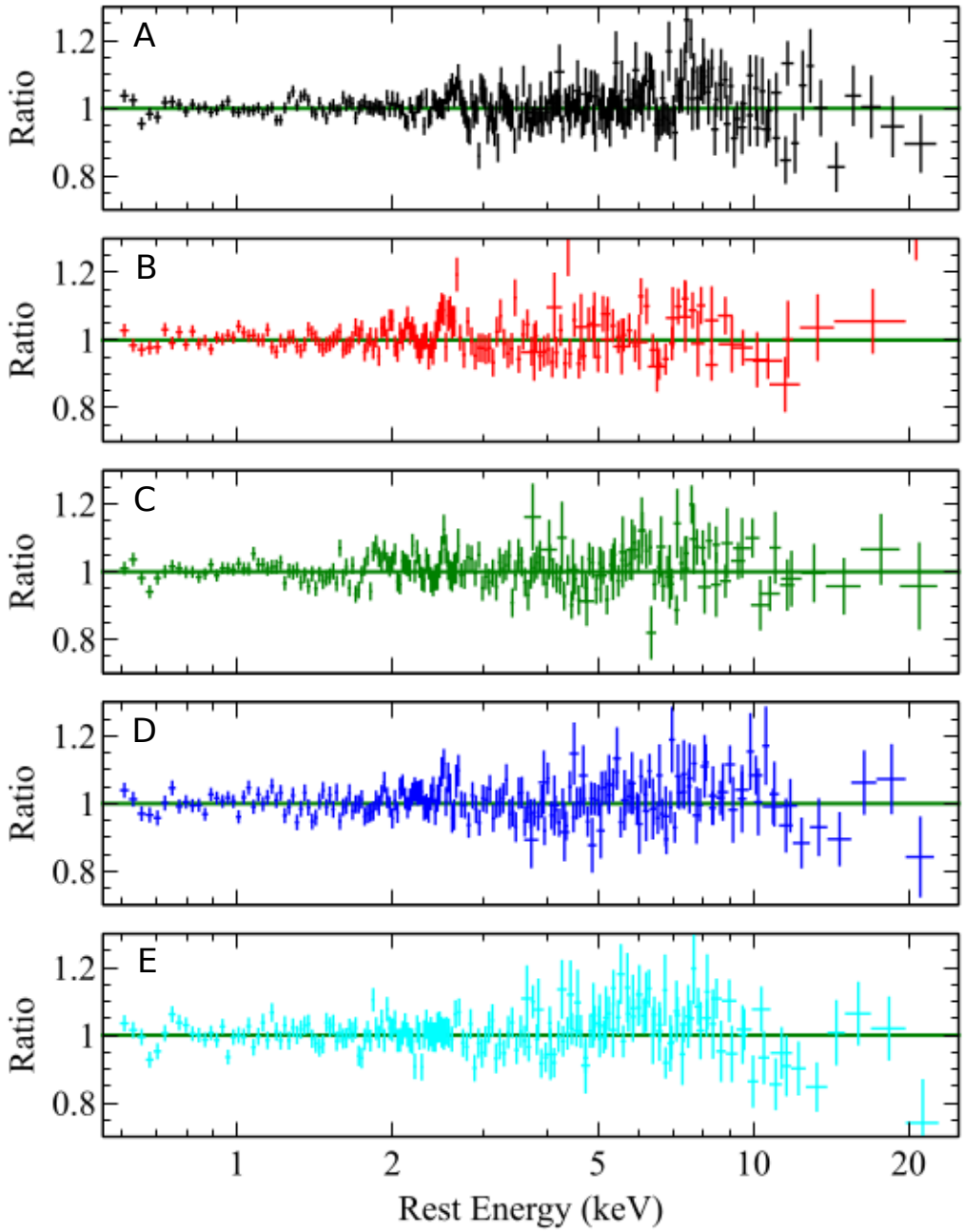

Figure 4.5: The ratios of the data to the best fit model (equation 4.3). While some of the spectra still show residuals around 10 keV, the continuum curvature is generally well fit.

4.5 Fitting archival *XMM-Newton* data

The first observation of PDS 456 performed by *XMM-Newton* in 2001 shows PDS 456 in the high flux ($F_{0.5-10\,\mathrm{keV}} = 10.88 \times 10^{-12}\,\mathrm{erg\,s^{-1}\,cm^{-2}}$) state. However, despite its high flux the spectra have strong absorption both at Fe K ($E_{\mathrm{obs}} = 7 - 10\,\mathrm{keV}$) band (EW $= -350^{209}_{-91}\,\mathrm{eV}$) and in the soft X-ray band (below 2 keV); this will be shown later in the RGS section (4.6). Then two further observations were taken in 2007(a–b); while lower in flux $F_{0.5-10\,\mathrm{keV}} = 10.23 \times 10^{-12}$ and $5.72 \times 10^{-12}\,\mathrm{erg\,s^{-1}\,cm^{-2}}$) the spectra are overall less obscured.

The previous model (equation 4.3) is applied to the archival *XMM-Newton* data. Because of the lack of contemporaneous hard X-ray data, the cross calibration offset is removed from the model and the photon index of the primary continuum is kept constant. The ionisation and column density of the partial coverer is allowed to vary freely for 2001 but is kept fixed between 2007a and 2007b.

$$\begin{aligned} F = \mathtt{Tbabs} \times (&\mathtt{zgauss}_{\mathrm{soft}} + \\ &[(1 - \mathtt{C}_2 - \mathtt{C}_1) + \mathtt{C}_2 \times \mathtt{wind\text{-}pc\text{-}v10k}_2 + \mathtt{C}_1 \times \mathtt{wind\text{-}pc\text{-}v10k}_1] \times (\mathtt{po} + \mathtt{zbbody}) \\ &+ \mathtt{wind\text{-}Fe\text{-}v15k}_{\mathrm{em}}) \times \mathtt{wind\text{-}Fe\text{-}v15k}_{\mathrm{abs}} \end{aligned} \tag{4.4}$$

The resulting best fit is $\chi^2/\nu = 2701/2490$ for the parameter values given in table 4.5. The ratios of the data to the best fit model can be seen in figure 4.7. Once again the variations of the wind emission is not significant. The highly ionised wind absorption $\mathtt{wind\text{-}Fe\text{-}v15k}_{\mathrm{abs}}$ is relatively unconstrained with 2001 and 2007b hitting the upper bound of the grid, as the upper limit of the column density ($2 \times 10^{24}\,\mathrm{cm^{-2}}$) is already Compton thick so not much will be gained from extending the grid further so it is not extended. Oddly the two partial covering zones in 2001 seem to converge to similar columns but with different

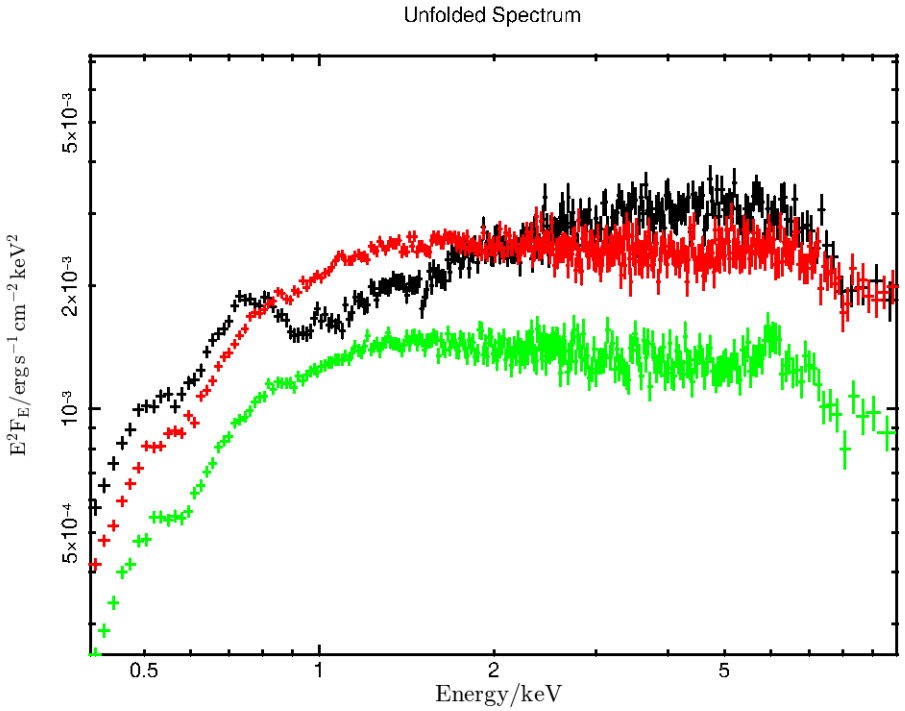

Figure 4.6: The unfolded spectra of the archival *XMM-Newton* observations: 2001 (black), 2007a (red) and 2007b (green). The 2001 spectrum is more heavily absorbed showing stronger curvature and some clear absorption troughs between 0.8–1.2 keV (observed). Compared to 2001 the 2007 observations are comparatively bare although they still show absorption in the Fe K region ($E_{\rm obs} = 7 - 10\,{\rm keV}$). The variation between the two 2007 observations is mainly in flux.

ionisation states. The higher column has the lower ionisation, which has not occurred in fits of the other observations.

It is also interesting to note that the soft Gaussian emission appears to track the normalisation of the intrinsic continuum (decreasing from 2001 to 2007b), while the percentage of unattenuated flux stays relatively constant.

Component	Parameter	2001	2007a	2007b
wind-Fe-v15k$_{\rm abs}$	$N_{\rm H}/10^{23}\,{\rm cm}^{-2}$	$9.4^{b}_{-2.7}$	$3.0^{+7.2}_{-1.0}$	$8.2^{b}_{-3.0}$
	$\log\xi$	$5.35^{+0.48}_{-0.13}$	5.35^{t}	5.35^{t}
	outflow velocity/c	-0.33 ± 0.01	-0.33^{t}	-0.33^{t}
wind-Fe-v15k$_{\rm em}$	$\log({\rm Flux}/\,{\rm erg\,s^{-1}\,cm^{-2}}\,)$	$-13.2^{+0.5}_{-1.0}$	$-12.7^{+0.1}_{-0.4}$	$-12.8^{+0.1}_{-0.3}$
zgauss$_{\rm soft}$	Energy/keV	0.87 ± 0.01	0.87^{t}	0.87^{t}
	σ/eV	50^{c}_{-10}	50^{t}	50^{t}
	norm/$10^{-4\,g}$	3.6 ± 0.3	1.4 ± 0.2	0.8 ± 0.1
$1-(C_2+C_1)$	%	24 ± 3	21^{+3}_{-4}	29^{+4}_{-5}
C_2	%	25 ± 14	63^{+4}_{-6}	58^{+4}_{-5}
C_1	%	51^{+11}_{-7}	16 ± 10	13 ± 1
wind-pc-v10k$_2$	$N_{\rm H}/10^{22}\,{\rm cm}^{-2}$	$1.70^{+0.64}_{-0.45}$	2.62 ± 2	2.62^{t}
	$\log\xi$	2.91 ± 0.05	$0.21^{+0.09}_{-0.05}$	0.21^{t}
wind-pc-v10k$_1$	$N_{\rm H}/10^{22}\,{\rm cm}^{-2}$	$2.59^{+0.21}_{-0.44}$	$42.11^{+1.69}_{-6.12}$	42.11^{t}
	$\log\xi$	$1.32^{+0.16}_{-0.50}$	$3.92^{+0.19}_{-0.07}$	3.92^{t}
zbbody	kT/keV	0.20 ± 0.01	0.20^{t}	0.20^{t}
	norm/$10^{-5\,bb}$	$12.11^{+2.38}_{-3.78}$	9.81^{r}	5.24^{r}
po	Γ	$2.28^{+0.02}_{-0.03}$	2.28^{t}	2.28^{t}
	norm/$10^{-3\,p}$	5.0 ± 0.2	$4.1^{+0.3}_{-0.2}$	2.2 ± 0.1
	χ^2/ν	837/749	1111/952	754/763
	H_0	0.01	2×10^{-4}	0.60

Table 4.5: The parameters of the best fit model showing an increase in covering fraction.
Key:
^{bb}: $L_{39}D_{10}^{-2}$ where L_{39} is source luminosity in units of $10^{39}\,{\rm erg\,s^{-1}}$ and D_{10} is the distance to the source in units of 10 kpc.
^{f}: parameter is fixed that value. ^{t}: parameter is tied to the value of parameter in 2007.
^{r}: parameter is fixed to the ratio of normalisations such that zbbody$_{\rm b}$ = po$_{\rm b}$(zbbody$_{\rm a}$/po$_{\rm a}$)
^{p}: photons keV^{-1}cm^{-2} s^{-1}
^{b}: The parameter hits the upper bound $2\times10^{24}\,{\rm cm}^{-2}$
^{c}: The parameter hits the upper bound 50 eV
^{g}: photons cm^{-2} s^{-1}

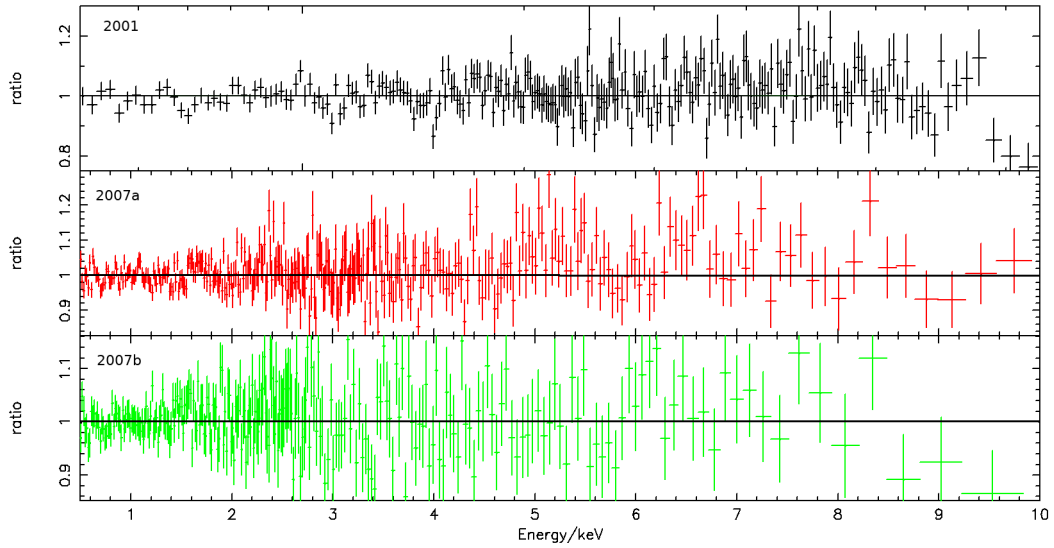

Figure 4.7: The ratios of the *XMM-Newton* archival spectra to the best fit model. While the model struggles to completely fit the absorption from the diskwind the overall shape of the spectra is captured.

4.6 *XMM-Newton* RGS

As I have already demonstrated outflows are observed through highly ionised iron at $\sim 9\,\mathrm{keV}$, but as suggested by the outflowing partial covering in the aforementioned models for all datasets, outflows are also seen in the soft band ($\sim 1\,\mathrm{keV}$). Reeves et al. (2016) analysed the *XMM-Newton* RGS spectra from all *XMM-Newton* (2001–2014) observations. The residuals to a black body continuum for the *XMM-Newton* observations are shown in Fig. 4.8. A single broad absorption trough is seen in the 2001 spectra labelled as ABS1. While two absorption features (labelled ABS1 and ABS2) can be seen in the co-added observations C and D, in *XMM-Newton* RGS observation E two absorption features are again presented with the addition of an emission feature, while no absorption features are found in observations A, B or the two 2007 spectra. These low ionisation lines are observed with outflow velocities of -0.17c to -0.3c, which is comparable to the highly ionised flow, and therefore are further

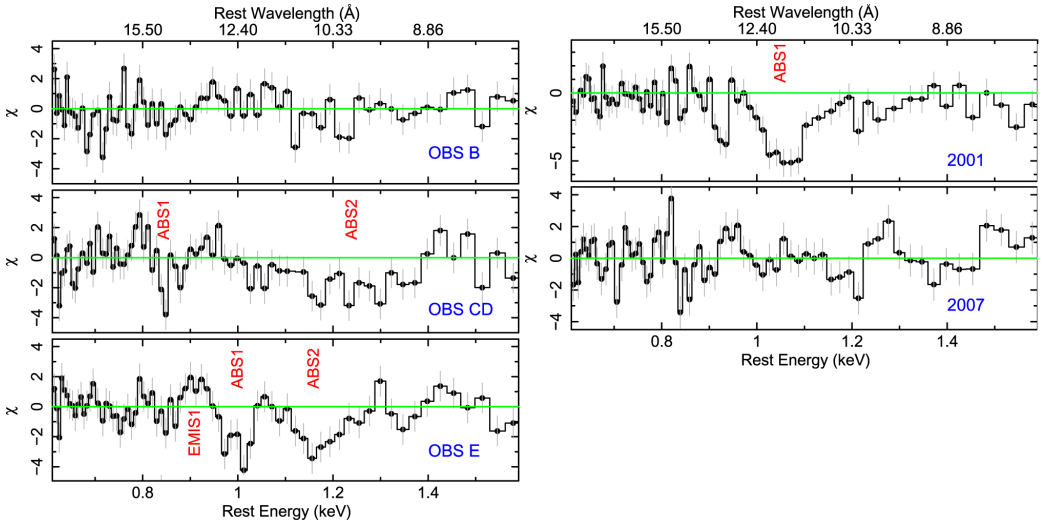

Figure 4.8: Taken from Reeves et al. (2016). The residuals to a continuum (plotted as χ, the square root of the χ^2 fit statistic) for the RGS data of PDS 456, for all *XMM-Newton* RGS spectra (excluding observation A). For the 2014 campaign observations C and D are combined; as are 2007a and 2007b. They are plotted as residuals instead of a ratio as the absorption features can be lost when compared to the continuum.

evidence they are linked.

4.7 Evidence for a radiative outflow

The variability of the outflow is a powerful tool for better understanding of the physics producing outflow. Matzeu et al. (2017) found a correlation (shown in Fig. 4.9) between the intrinsic luminosity (L_{7-30}) and the outflow velocity via two proxies: centroid of a Gaussian fitted to the absorption profile and the outflow velocity inferred from fitting a photo-ionised model (XSTAR). Both produce comparable slopes and agree with a radiatively driven flow which observed velocity is mediated by ionisation, where the radiative driving increases the

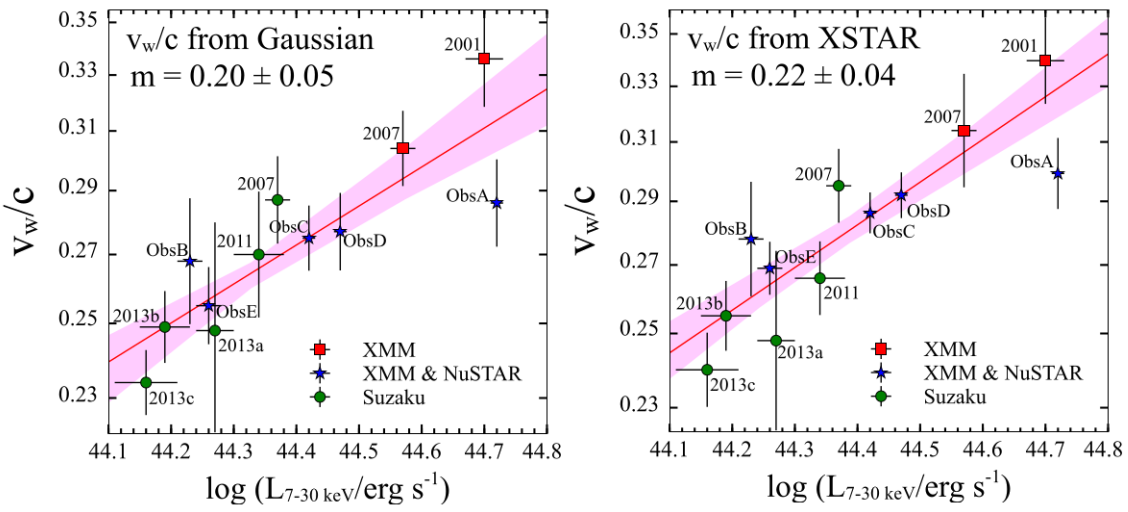

Figure 4.9: The regression taken from the Matzeu et al. (2017) between the intrinsic luminosity ($L_{7-30\,\mathrm{keV}}$) and the outflow velocity via two proxies centroid of a Gaussian fitted to the absorption profile and the redshift of an XSTAR grid.

outflow velocity while the over-ionisation causes the fastest parts of the wind to become transparent in the X-rays.

Assuming the wind is accelerated through line driving (where UV/optical lines produce a large opacity) then the UV flux (which is an appreciable fraction of L_{edd}) is the important factor, not the X-ray flux (which are very sub-Eddington). Therefore it could be assumed that the variability X-ray band is acting as a proxy for variability in the Optical-EUV, however, the UV flux has shown to be relatively stable in the *XMM-Newton* OM (Matzeu et al. 2017) (although force multipliers could accentuate any variability) so unlikely to be the cause of this correlation.

Another driving mechanism could be Compton scattering, if σ/σ_T approaches or exceeds unity, then more energetic but (sub-Eddington) X-ray flux would be significant in driving the wind, as they could transfer more of their energy to the wind. Compton thick clouds are not observed in PDS 456. However, Waters et al. (2017) showed how illuminating

clouds would cause them to disintegrate due to the momentum they receive. This could result in a resulting in a fast wind with a lower column density. Matzeu et al. (2016) found that the flaring events observed in PDS 456 do not have the energy required to trigger mass ejections. Therefore, the launching mechanism cannot be purely due to the flux in the X-ray band. This does not disclude the X-ray flux from being an additional driving force to the wind, once it has been launched. Therefore the X-ray flux could dictate the upper velocity but not the low one.

The outflow's momentum transport, compared to the momentum transfer of the radiation field is:

$$\dot{p}_{\rm out} = \dot{M}_{\rm out}\, v_{\rm out} \sim \tau\, L_{\rm AGN}/c. \tag{4.5}$$

Taking the definition of mass outflow rate as:

$$\dot{M}_{\rm out} = \Omega\, \mu\, m_p\, N_{\rm H}\, v_{\rm out}\, R, \tag{4.6}$$

where Ω is the solid angle of the outflow, $\mu(\sim 1.2)$ is average atomic mass and R is the launch radius of the wind. Substituting equation 4.6 into equation 4.5 yields:

$$v_{\rm out} \sim \left(\frac{L_{\rm AGN}}{R} \frac{\tau}{\Omega\, \mu\, m_p,\, N_{\rm H}\, c} \right)^{0.5}. \tag{4.7}$$

However, the radius (R) at which the line is produced is dependent on the ionisation. Therefore this must be taken into account as it affects the launch velocity. The radius at which the observed ionisation state exists for a given luminosity is:

$$R = \left(\frac{L_{\rm AGN}}{n\, \xi} \right)^{0.5}. \tag{4.8}$$

Feeding this back into equation 4.7 gives:

$$v_{\rm out} \sim \left(\frac{L_{\rm AGN}}{L_{\rm AGN}^{0.5}} \right)^{0.5} \left(\frac{\tau (n\xi)^{0.5}}{\Omega\, \mu\, m_p\, N_{\rm H}\, c} \right)^{0.5} \propto L_{\rm AGN}^{0.25} \tag{4.9}$$

This is a simplified scenario approximation as the other parameters — such as $N_{\rm H}$ and ionisation ξ — along with the bolometric correlation which links $L_{7-10\,\rm keV}$ to $L_{\rm bol}$— could also change which will affect this slope. Also note as well this derivation assumes a uniform density. However to a first order this is what appears to be found in Matzeu et al. (2016).

4.8 Conclusions

The broadband spectral variability in the *Suzaku* observations of PDS 456 clearly in showing that the transition to the low-hard state is dominated by an increase in the partial covering fractions, coupled with an increase in the opacity of the highly ionised wind. The model constructed shows the data can be explained with a physically motivated model where the `zbbody` located within the partial covering and having a fixed ratio with power law continuum.

The *XMM-Newton–NuSTAR* observations show dramatic changes in the slope of the intrinsic power law and is therefore dominated by the intrinsic variability. It is interesting to note that the *NuSTAR* spectrum appears to be a continuation of the power law. Therefore, there is no requirement for a strong reflection component.

The archival *XMM-Newton* observations show a high-absorbed state in 2001 as seen in both the PN at Fe Kα and in the RGS. Both the 2007 *XMM-Newton* observations occur at a similar flux level and while still requiring a partial covering they are relatively bare in the RGS.

Note over all observation the wind emission is consistent while there is a lot of change in LOS absorption; on a large scale the wind is self-consistent. As the emission does not seem to respond to the flux variability, it must spread over an extended region. Clumps within the flow are the likely cause of the LOS changes; these density perturbations are predicted for a time varying source (Dyda & Proga 2018b).

The absorption features in RGS data show outflow velocities of 0.17–0.27c. Therefore,

the soft absorber is not the typical warm absorber and instead is likely linked with the highly ionised outflow.

The correlation is evidence for radiation driving of the wind which is moderated by the ionisation. However it is not conclusive as the X-ray luminosity is sub-Eddington so cannot power the wind by itself. It could provide an extra driving force to accelerate the wind to higher velocities causing this correlation with X-ray luminosity. This would require the wind to have a high optical depth which is not observed in the LOS.

5 Fitting a disk wind to PDS 456

In this chapter I will explore the implementation of the disk wind code presented in chapter 3. The disk wind code allows for self-consistent calculation of both the emission and absorption arising from the presence of the disk wind with a more realistic geometry. Therefore a more accurate model of the disk wind is produced. Applying this model to all PDS 456 observations will allow for a better constraint on the wind parameters and therefore $L_{\rm kin}$.

The results of the previous chapter are used to provide the information required to specify the input parameter space for the radiative transfer code. The absorption features of all the datasets are presented in Fig. 5.1 which shows the 2–10 keV spectra as a ratio to a power law continuum for *XMM-Newton* and *Suzaku* spectra in table 4.1. Note that in Fig. 5.1 the range of the y axis is fixed. Therefore, due to the very strong features in *Suzaku* 2013 b and c, some weaker features look less significant. Moving down columns the flux generally reduces (and absorption increases); the 2001 *XMM-Newton* and the 2013a *Suzaku* observations being two exceptions.

The 2001 observation (top panel of the first column) shows a broad ($\sigma = 0.5$ keV; the maximum value allowed in the Gaussian fit) and deep (EW $= -310 \pm 90$ eV) absorption trough at a high flux (11×10^{-12} erg s^{-1} cm^{-2}; between 2–10 keV) whereas the 2013a *Suzaku* observation (middle panel of the middle column) shows only a weak feature (EW $= -57^{+21}_{-77}$ eV) at a low flux (1.93×10^{-12} erg s^{-1} cm^{-2}; over the same energy range). A disk wind model is produced to explain the observed variability from the weak feature observed in *XMM-Newton–NuSTAR* observation A (top panel of the right hand side column) to the stronger feature seen in *Suzaku* 2013c (bottom panel of the middle column).

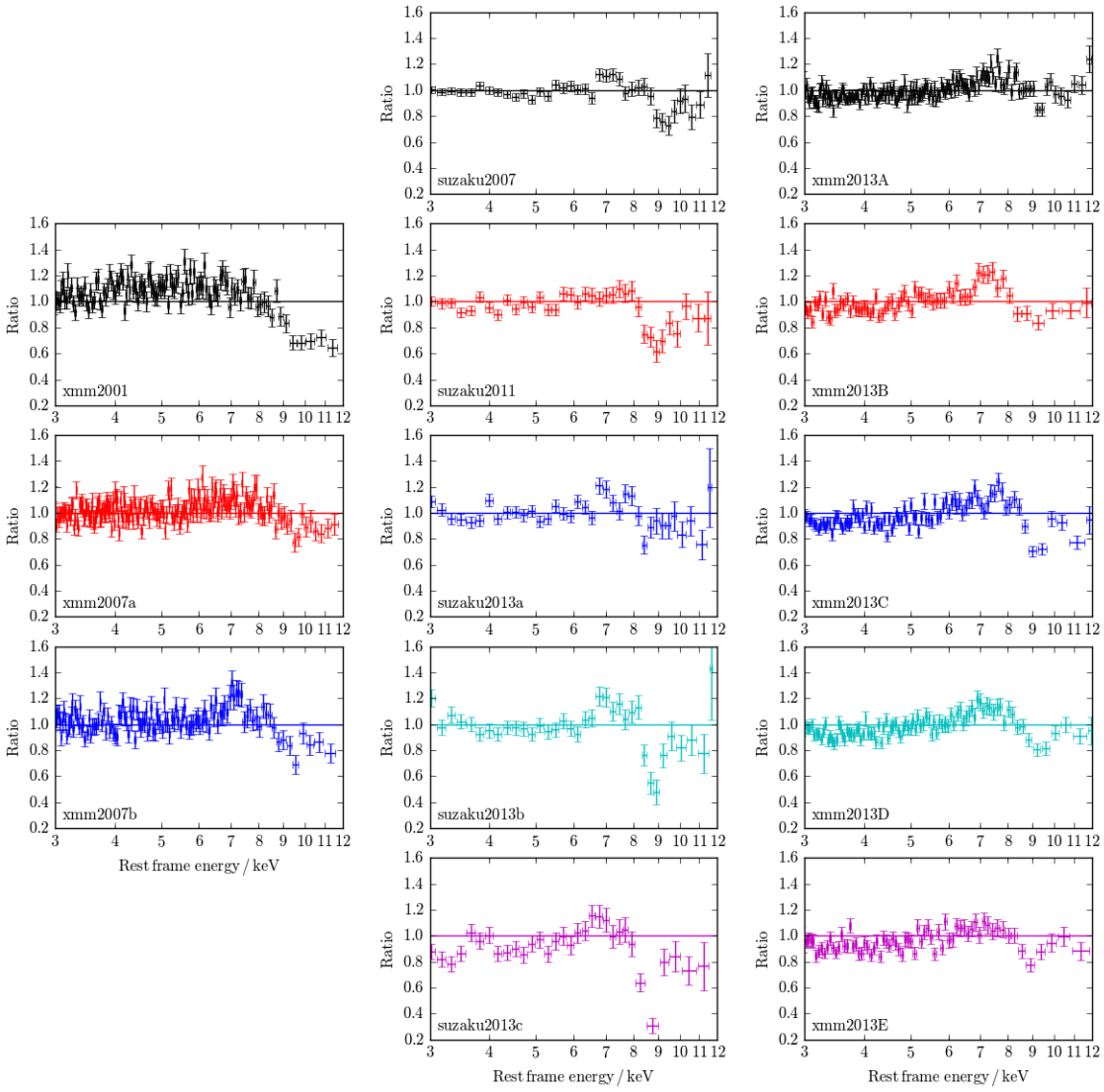

Figure 5.1: Ratios of the spectra (of PDS 456 from 2001 to 2014) to a power law; this shows the profile of the disk wind, which shows remarkable variability. Luminosity decreases down the columns along with a general increase in absorption. The two notable exceptions to this are *XMM-Newton* 2001, which is high in flux whilst also absorbed, and *Suzaku* 2013a, which is low in flux with weak absorption. The depth of the features is highly variable as seen when comparing the weak features of *XMM-Newton* 2013A (top panel of the right hand side column) and strong features in *Suzaku* 2013c (bottom panel of the middle column). The velocity shift is also apparent when comparing *XMM-Newton* 2013D and *XMM-Newton* 2013E. The range of the y axis is fixed, so some features may appear weak when compared to the strong feature of *Suzaku* 2013c.

5.1 *Suzaku* data

The *Suzaku* datasets are initially fit as they show the largest variations in the absorption feature. Hagino et al. (2015) show a good fit to the data using the `monaco` disk wind model (described in section 3.1.1). However, the model construction has been improved upon to place tighter constraints on the parameters; as well as using the Sim et al. (2010) disk wind code which has a larger atomic database. The disk wind model was constructed to fit the 2–10 keV spectrum based on the ionised partial covering model as shown in chapter 4. The low column zone and black body were removed as the features they imprint are below 2 keV and therefore are not required. The high ionisation wind absorption and emission grids are replaced with the disk wind model. As such, the mathematical representation of the model is as follows:

$$F = \texttt{DW} \times [(\texttt{1} - \texttt{CF}) + \texttt{CF} \times \texttt{PC}] \times \texttt{po} \tag{5.1}$$

Where model components are described as follows:

- The fully covering `DW` is the model component of the Sim et al. (2010) radiative transfer code which imprints the emission and absorption from the disk wind.
- `CF` is the fraction of the power law which the `PC` covers.
- `PC` is the ionised partial covering absorber; this is the same model ($\texttt{wind} - \texttt{pc}$) as in the previous chapter.
- `po` is the intrinsic power law continuum, the photon index of which is bound to the input spectrum of the disk wind (`DW`) model.

The disk wind parameters can be found in table 5.1. The terminal velocity (f_v) of the wind can vary between 0.125c and 0.5c. The mass outflow rates used span from 0.7 to 25.0 $M_\odot$ yr^{-1} and $L_{2-10\,\mathrm{keV}}$ varies from 3×10^{43} to 1×10^{45} erg s^{-1}.

Parameter	Value
$R_{\rm in}/R_{\rm g}$	32
$R_{\rm out}/R_{\rm in}$	1.5
$\dot{M}$ $\dot{M}_{\rm edd}$	0.020–0.676
$L_{2-10\,{\rm keV}}/L_{\rm edd}$	0.025–0.796%
Γ	2.0–2.4
f_v	0.5–2.0
${\rm d}/R_{\rm in}$	1
k	-1
v_0	0
β	1
$R_{\rm v}$	$R_{\rm out}$
[Fe/H]	1
Black hole mass/$M_\odot$	10^9

Table 5.1: The input parameters of the `DW`. $R_{\rm min}/R_{\rm g} = 32$ therefore the launch velocity of the innermost stream line is 0.25c. table 3.1 contains pre-calculated values for $\dot{M}_{\rm edd}$, $L_{\rm edd}$ and $R_{\rm g}$ in physical units.

Due to the lack of high-quality hard X-ray data and strong absorption in the *Suzaku* datasets, the power law slope cannot be determined independently for each observation, so it is allowed to vary but kept the same for each observation. Due to the lack of a simple dependence of velocity on inclination (μ) the outflow velocity of the partial cover cannot be tied directly to the wind's outflow velocity and so instead it is kept the same for each observation.

Fig. 5.2 shows the confidence contours (of 68%, 90% and 99%) in the χ^2 space between $\dot{M}$ and $L_{2-10\,{\rm keV}}$, for the disk wind model fit to the 2013c spectrum. The constrained model (solid lines) is where the observed flux is calculated from the $L_{2-10\,{\rm keV}}$ parameter and unconstrained model (dashed lines) where the observed flux and intrinsic $L_{2-10\,{\rm keV}}$ is free to vary. Both models display a degeneracy, with the strong departure from a circular shape. The constraint makes the parameters more degenerate, as seen by the narrowness of the solid contours. This is because an increase in scattering caused by an increase in $\dot{M}$ will decrease the observed flux (assuming the line of sight intercepts the wind), and therefore requires a comparative increase in the intrinsic luminosity to match the observed flux. This

of course can cause a run-away completion between these parameters, if a solution cannot be found in the narrower valid parameter space. However, the parameters are much better constrained by calculating the observed flux from the intrinsic luminosity This can be seen from the much smaller area of the constrained contours compared to the unconstrained contours. Therefore the ionising luminosity is used to set the normalisation for the intrinsic spectrum (`po`).

The photon index of the wind model is set to match the continuum. Constraining both Γ and $L_{2-10\,\mathrm{keV}}$, will allow for better parameterisation of the wind's ionisation, as the photon index plays an important role in setting the ionisation state — as shown in section 3.2.8. This is required as it is clear from the correlations of Matzeu et al. (2017) presented in section 4.9 and Parker et al. (2017) that ionising luminosity plays a key role in the variability of disk winds. Therefore, a good measure of the ionisation state of the wind is required to understand the variability in other parameters and determine the mechanism for these changes (i.e. ionisation, structure or mass outflow rate).

Initially only $L_{2-10\,\mathrm{keV}}$ is allowed to vary between observations. This produces a fit of $\chi^2/\nu = 603/559$ and the ratios to the fit are shown in Fig. 5.3. All observations show strong residuals between 8–10 keV. In particular the Fe K absorption is over-predicted in the 2013a observation and under-predicted in the 2013c observation. This suggests that the outflow itself is variable – not just the X-ray source illuminating it. This is investigateds below in terms of variations in the sight-line through the wind (μ) or mass outflow rate ($\dot{M}$).

To understand the observed variability of the wind (in the middle column of Fig. 5.1) and therefore which parameters to vary must be considered. The variations between the wind profiles show fluctuations in the strength of the profile and observed energy. The fastest profiles (with the exception of 2013a) appear to have lower equivalent widths (2007) and the profile with the smallest velocity shift are the deepest (2013c). This seems to match the expected variation from changes in the observer's inclination μ ($\cos\theta$ where θ is measured with respect to the polar axis) as noted by Hagino et al. (2015). These variations to the wind profile can be inferred from Fig. 5.4, which shows the structural differences which

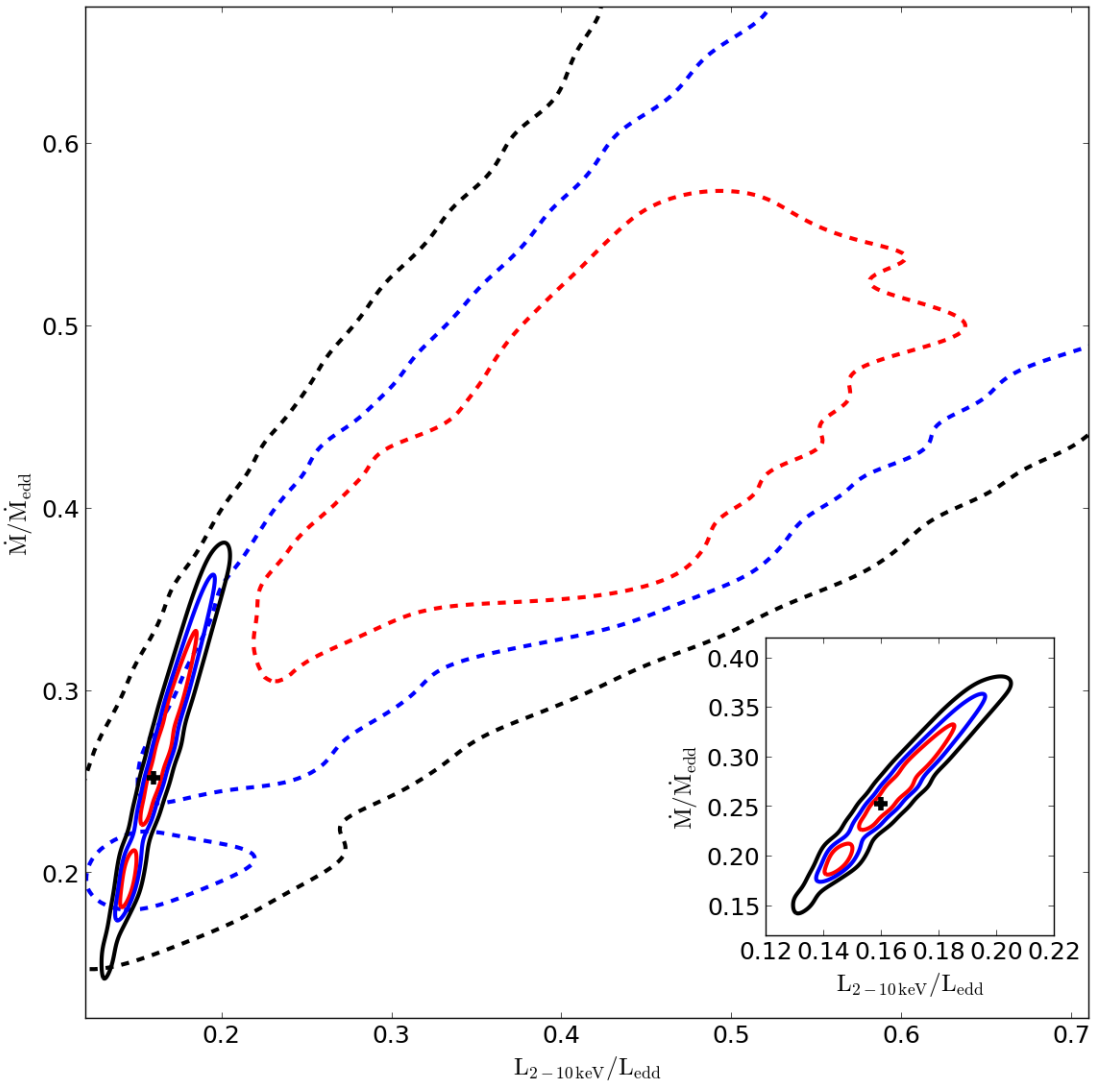

Figure 5.2: The contours for 69%, 90% and 99% confidence intervals between $L_{2-10\,\mathrm{keV}}$ and $\dot{M}$ for the 2013c spectrum. The dashed and solid contours show the unconstrained and constrained model respectively. From these contours it is obvious that these parameters are degenerate as an increase in $\dot{M}$ can be compensated by an increase in the luminosity; this is exaggerated in the constrained model which is also presented in the inner plot.

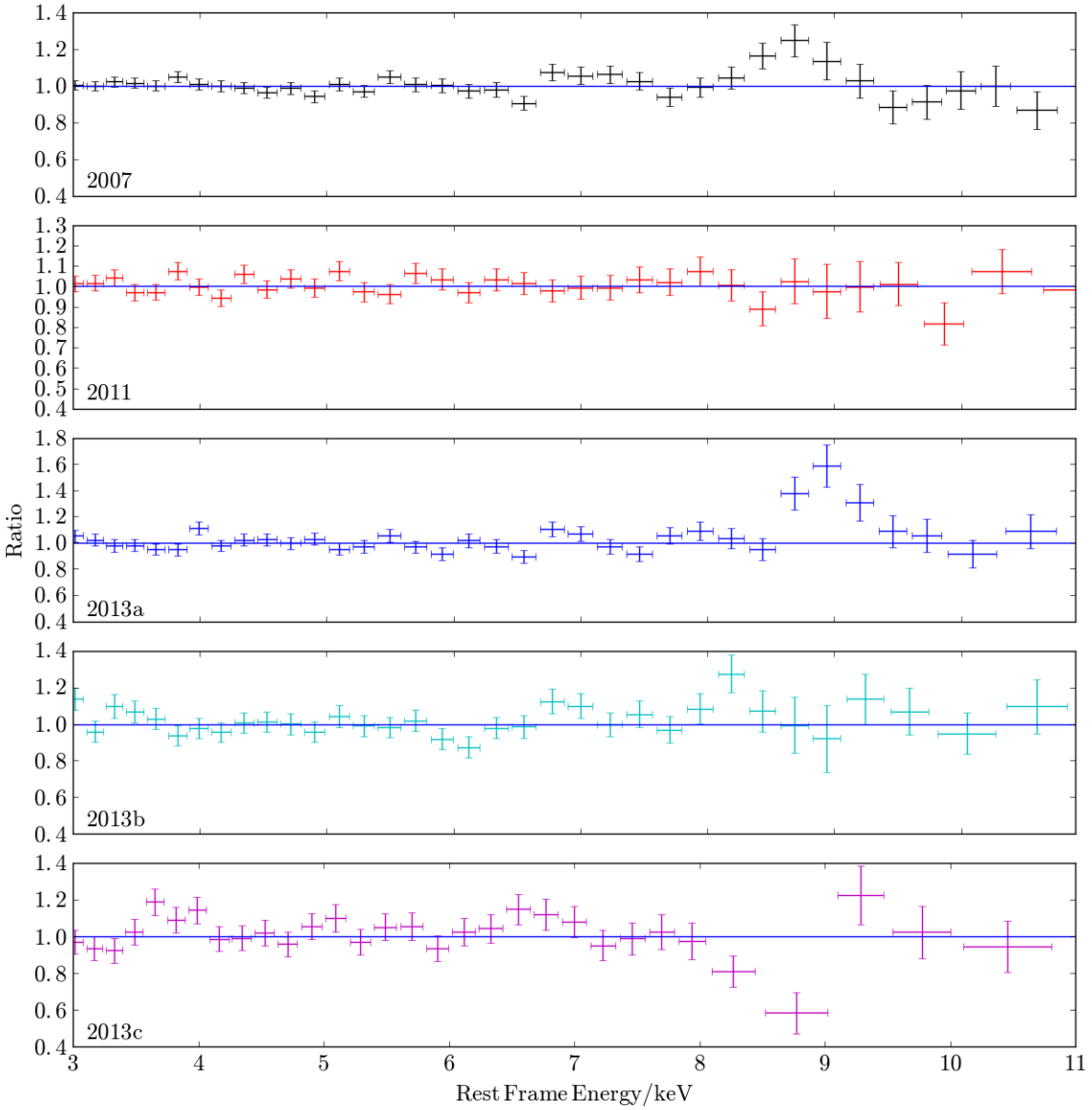

Figure 5.3: The ratios of the five *Suzaku* datasets to the disk wind model when only $L_{2-10\,\mathrm{keV}}$ is allowed to vary between observations. The residuals between 8 and 10 keV show the need for more free parameters.

could be inferred from variable μ with a constant LOS super-imposed (black line). Panel (a) of Fig. 5.4 shows the wind structure from lower μ values, meaning that the wind is more polar relative to the LOS. Therefore, the LOS goes through a thicker (geometrically and optically) part of the wind. This produces a high column density, a broad profile and a lower centroid energy — as the direction of propagation (red arrow) is more polar; so velocity projected along the LOS is slower than the more equatorial flow in panel (b). In panel (b) by comparison, the outflow is more equatorial (representing smaller values of μ). The LOS is mainly intercepting the fastest inner stream lines and the projection angle is smaller, as your are looking down the wind not across it. This means that the observed velocity shift will be higher than in panel (a). The absorption feature is also weaker as the inner streamlines have a comparatively lower opacity due to their high ionisation, along with the generally lower column density. In summary, a low value of μ (or equivalent a more polar outflow for a fixed line of sight) intercepts a higher column density and more stream lines (although they have a lower projected velocity) producing a broader, deeper and slower profile – reminiscent to that of 2013c. The opposite is the case for a large value of μ which would be equivalent to observing a more equatorial flow, with a narrower, shallower and faster profile (similar to *Suzaku* 2007).

Structural changes similar to Fig. 5.4 are seen in the simulation of Proga et al. (2000). It should be noted that these changes are on much longer timescales than the observed changes in PDS 456. However, the wind is are only moving radially in Proga et al. (2000). These observed changes could be due to parts of the wind which rotate in/out of view. Therefore, the wind structure itself is not required to change, but the part of the wind we are viewing could be structurally different.

When allowing μ and $L_{2-10\,\mathrm{keV}}$ to vary the fit improves by $\Delta\chi^2/\Delta\nu = 41/4$ compared to only $L_{2-10\,\mathrm{keV}}$ variations and is therefore preferred at $> 99.999\%$ confidence. The first column in figure 5.5 shows the ratios to the μ and $L_{2-10\,\mathrm{keV}}$ fit and shows residuals in the range 8–9 keV where the absorption features are observed. Table 5.2 presents the parameters of the minimised model, from which it can be seen that the photon index ($\Gamma = 2.28^{+0.06}_{-0.03}$) is

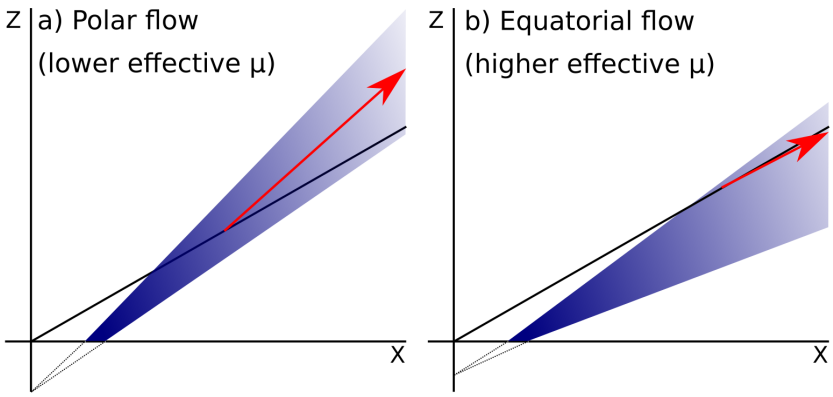

Figure 5.4: The structural changes which can be understood from changing μ. As the inclination to the object does not change the line of sight (black line) is fixed. The blue gradient shows the wind and the red arrow represents the direction of propagation. The dashed lines show the projection to the focus below the disk plane which lies along the x-axis. The cosine of the angle between arrow and LOS represents the magnitude of the component along the LOS and therefore the obscured energy shift. In panel (a) this will be small compared to panel (b). As panel (a) looks through more of the wind the observed column will be larger. Both of these observable parameters are affected by the streamlines being observed as inner streamlines will be faster and have a lower opacity.

within the typical range for this object as seen in the previous chapter. The parameters of the partial covering are similar to the expected from the previous chapter. With covering fraction (CF) increasing from < 0.09 (2007) to > 0.81 (2013b) before decreasing slightly in 2013c ($\mathtt{CF} = 0.80^{+0.08}_{-0.12}$). The fit also shows moderate values of $N_{\rm H}= 6.8^{+1.9}_{-0.8} \times 10^{22}\,{\rm cm}^{-2}$ and ionisation ($\log \xi = 2.5^{+0.4}_{-0.6}$) all of which are comparable with the values obtained for the high column partial coverer in the previous chapter. The partial coverer is also outflowing with a velocity ($v_{\rm pc}$) of $-0.33^{+0.17}_{-0.12}$c which although on the fast end of the velocities observed is not alarmingly high – it is also highly uncertain as it lacks a strong feature to constrain its velocity. Let us now consider the variable wind parameters ($L_{2-10\,{\rm keV}}$ and μ). As mentioned before $L_{2-10\,{\rm keV}}$ is used to set the normalisation of spectrum, therefore, it is not surprising that the highest $L_{2-10\,{\rm keV}}$ value is observed in 2007 ($0.243^{+0.017}_{-0.021}\,L_{\rm edd}$) and then decreases to $0.119^{+0.010}_{-0.008}\,L_{\rm edd}$ in 2013b, before recovering to $0.137^{+0.005}_{-0.007}\,L_{\rm edd}$ in 2013c. The value of μ does not seem to follow the expected behaviour, however the observed depth of the profile could be influencing this heavily.

As noted before, 2013a does not fit the shallow-when-fast trend; this can be seen in the residuals of the 2013a observation in Fig. 5.5, which shows the ratio of the data to the variable μ fit in the first column. The 2013a feature is clearly still present and the excess shows the absorption feature to be too high in energy ($\sim 9\,{\rm keV}$ as opposed to $\sim 8.3\,{\rm keV}$). This is confirmed in Fig. 5.6 which shows the unfolded (against a $\Gamma = 2$ power law) data and model fits, where the red line is the $L_{2-10\,{\rm keV}}$ & μ variable model.

In an attempt to relax the constraints on the model the mass outflow rate is allowed to vary freely between observations; this can mitigate some of the column density variations expected from changes in inclination, by reducing the amount of material in the flow. Variations in $\dot{M}$ are to be expected in a radiatively driven flow (Dyda & Proga 2018b).

This improves the fit by $\Delta\chi^2/\Delta\nu = 15/4$ and is therefore preferred at 99.5% confidence. This is partly due to μ being allowed to reduce from 0.65 ± 0.02 to $0.49^{+0.02}_{-0.03}$ in observation 2013a as $\dot{M}$ compensate, where $\dot{M}$ reduces from $0.18^{+0.02}_{-0.03}\,\dot{M}_{\rm edd}$ when varying only $L_{2-10\,{\rm keV}}$ and μ to $0.09 \pm 0.03\,\dot{M}_{\rm edd}$ as presented in table 5.3.

Obs	2007	2011	2013a	2013b	2013c
Γ	$2.28^{+0.06}_{-0.03}$	2.28^{t}	2.28^{t}	2.28^{t}	2.28^{t}
$\dot{M}/\dot{M}_{\rm edd}$	$0.18^{+0.02}_{-0.03}$	0.18^{t}	0.18^{t}	0.18^{t}	0.18^{t}
$\%L_{2-10\,\rm keV}/L_{\rm edd}$	$0.243^{+0.017}_{-0.024}$	$0.224^{+0.012}_{-0.013}$	$0.125^{+0.009}_{-0.008}$	$0.119^{+0.010}_{-0.008}$	$0.137^{+0.005}_{-0.007}$
f_v	$1.37^{+0.06}_{-0.03}$	1.37^{t}	1.37^{t}	1.37^{t}	1.37^{t}
μ	0.62 ± 0.03	$0.57^{+0.02}_{-0.03}$	0.65 ± 0.02	$0.58^{+0.02}_{-0.04}$	$0.52^{+0.01}_{-0.02}$
`CF`	< 0.09	$0.44^{+0.06}_{-0.07}$	$0.83^{+0.07}_{-0.12}$	> 0.81	$0.80^{+0.08}_{-0.12}$
$N_{\rm H}/10^{22}\,{\rm cm}^{-2}$	$6.77^{+1.94}_{-0.80}$	6.77^{t}	6.77^{t}	6.77^{t}	6.77^{t}
$\log \xi$	$2.5^{+0.4}_{-0.6}$	2.5^{t}	2.5^{t}	2.5^{t}	2.5^{t}
$\rm v_{pc}/c$	$-0.33^{+0.17}_{-0.12}$	-0.33^{t}	-0.33^{t}	-0.33^{t}	-0.33^{t}
χ^2/ν	136/114	90/105	117/107	110/104	107/93
$\rm H_0$	0.08	0.85	0.24	0.33	0.12

Table 5.2: The parameters of the best fit model when $L_{2-10\,\rm keV}$ and μ vary between observations for the *Suzaku* datasets. μ generally decreases from 2007 to 2013c excluding 2013a. χ^2/ν and Null probability is shown for each observation individually therefore parameters tied between observations are treated as free. The total χ^2/ν is 562/555 and the Null probability is 0.41.
Key:
^{t}: tied to the previous 2007 observation.
$\rm H_0$ refers to the Null probability.

Obs	2007	2011	2013a	2013b	2013c
Γ	$2.27^{b}_{-0.03}$	2.27^{t}	2.27^{t}	2.27^{t}	2.27^{t}
$\dot{M}/\dot{M}_{\rm edd}$	$0.15^{+0.03}_{-0.04}$	0.19 ± 0.05	0.09 ± 0.03	0.15 ± 0.04	$0.25^{+0.05}_{-0.08}$
$\%L_{2-10\,\rm keV}/L_{\rm edd}$	$0.267^{+0.014}_{-0.015}$	$0.246^{+0.022}_{-0.018}$	$0.157^{+0.009}_{-0.007}$	0.126 ± 0.009	$0.160^{+0.016}_{-0.022}$
f_v	1.57 ± 0.04	1.57^{t}	1.57^{t}	1.57^{t}	1.57^{t}
μ	0.56 ± 0.02	0.50 ± 0.02	$0.49^{+0.02}_{-0.03}$	0.51 ± 0.02	0.48 ± 0.01
CF	< 0.16	$0.40^{+0.08}_{-0.06}$	$0.76^{+0.07}_{-0.08}$	0.86 ± 0.08	0.67 ± 0.08
$N_{\rm H}/10^{22}\,{\rm cm}^{-2}$	9^{+2}_{-1}	9^{t}	9^{t}	9^{t}	9^{t}
$\log \xi$	$2.6^{+0.4}_{-1.1}$	2.6^{t}	2.6^{t}	2.6^{t}	2.6^{t}
$v_{\rm out}/{\rm c}$	$-0.33^{+0.18}_{-0.10}$	-0.33^{t}	-0.33^{t}	-0.33^{t}	-0.33^{t}
χ^2/ν	131.63/114	91/105	112/107	106/104	107/93
H_0	0.12	0.84	0.34	0.44	0.15

Table 5.3: Best fit model $L_{2-10\,\rm keV}$, μ and $\dot{M}$ variations in the *Suzaku* datasets. The total χ^2/ν is 547/551 and the Null probability is 0.54.
Key:
^{t}: tied to the previous 2007 observation.
^{b}: the parameter hits the edge of the grid.
H_0 refers to the Null probability.

The variations in $\dot{M}$ range from low rates of $0.15^{+0.03}_{-0.04}\,\dot{M}_{\rm edd}$ and $0.09 \pm 0.03\,\dot{M}_{\rm edd}$ in 2007 and 2013a respectively, to $0.25^{+0.06}_{-0.08}$ in 2013c which has the deepest absorption feature, while f_v shifts from $1.33^{+0.04}_{-0.03}$ to 1.57 ± 0.04 compensating for changes to lower values in μ. The 2013a ratio in the middle column of Fig. 5.5 shows some improvement however as the line energy shifts (see Fig. 5.6).

Variations in μ can by mimicked by variations in both mass outflow rate and the velocity scaling factor (f_v) which, as previously described, modifies the velocity shift in the observed spectra. Varying both $\dot{M}$ and f_v instead of μ decouples the velocity, observed column and the width of the absorption feature allowing for greater freedom. This improves the fit by $\Delta\chi^2/\Delta\nu = 17/4$ compared to the fit where μ varies and $\dot{M}$ is fixed; this is preferred at 99.8% confidence with the resulting $\chi^2/\nu = 545/551$ producing a slight over-fit, as with the $L_{2-10\,\rm keV}$, μ and $\dot{M}$ variable fit. The best-fit values can be found in table 5.4. It can be

Obs	2007	2011	2013a	2013b	2013c
Γ	$2.29^{b}_{-0.05}$	2.29^{t}	2.29^{t}	2.29^{t}	2.29^{t}
$\dot{M}/\dot{M}_{\rm edd}$	$0.14^{+0.03}_{-0.04}$	0.18 ± 0.05	0.09 ± 0.03	0.13 ± 0.04	$0.19^{+0.06}_{-0.05}$
$\%L_{2-10\,\rm keV}/L_{\rm edd}$	$0.261^{+0.012}_{-0.013}$	$0.224^{+0.020}_{-0.016}$	$0.145^{+0.006}_{-0.007}$	$0.116^{+0.008}_{-0.007}$	$0.131^{+0.016}_{-0.010}$
f_v	$1.54^{+0.06}_{-0.11}$	1.37 ± 0.05	$1.35^{+0.07}_{-0.08}$	1.35 ± 0.06	1.25 ± 0.03
μ	0.57 ± 0.01	0.57^{t}	0.57^{t}	0.57^{t}	0.57^{t}
CF	< 0.22	$0.46^{+0.11}_{-0.09}$	$0.87^{+0.06}_{-0.11}$	$0.97^{+0.03}_{-0.13}$	$0.78^{+0.07}_{-0.12}$
$N_{\rm H}/10^{22}\,{\rm cm}^{-2}$	13 ± 5	13^{t}	13^{t}	13^{t}	13^{t}
$\log \xi$	$1.07^{+0.14}_{-0.04}$	1.07^{t}	1.07^{t}	1.07^{t}	1.07^{t}
$v_{\rm out}/{\rm c}$	$-0.24^{+0.12}_{-0.03}$	-0.24^{t}	-0.24^{t}	-0.24^{t}	-0.24^{t}
χ^2/ν	131/114	91/105	111/107	106/104	107/93
H_0	0.14	0.84	0.38	0.42	0.16

Table 5.4: The parameters of the best fit model while μ is kept constant while the velocity shift is parameterised by f_v and the column by $\dot{M}$. The total χ^2/ν is 545/551 and the Null probability is 0.56.
Key:
^{t}: tied to the previous 2007 observation.
^{b}: the parameter hits the edge of the grid.
H_0 refers to the Null probability.

seen that the fixed μ moves to 0.57 ± 0.01, which is at the middle of the μ variation in the fit with μ and $\dot{M}$ left free to vary. Now that μ is not varying the column density $\dot{M}$ must change to compensate. However, the values and range actually decrease showing that the changes in μ were inflating $\dot{M}$. The general trend of larger values of $\dot{M}$ with decreasing flux is still consistent. The ratios to these two fits can be seen in the end column of Fig. 5.5.

The *Suzaku* observations show variability in $\dot{M}$ and some form of velocity shift due to μ and/or f_v. It is unclear from these datasets whether there are structural changes or the wind is just responding to radiative driving (of course, radiative driving could also cause structural changes within the wind). It is hard to distinguish between these two scenarios.

Fortunately for calculations of $L_{\rm kin}$ this does not seem to make much difference to the required mass outflow rate (except for the extreme case of 2013c), which means the dominant uncertainty is the outflow velocity. Because the observed velocity will be lower

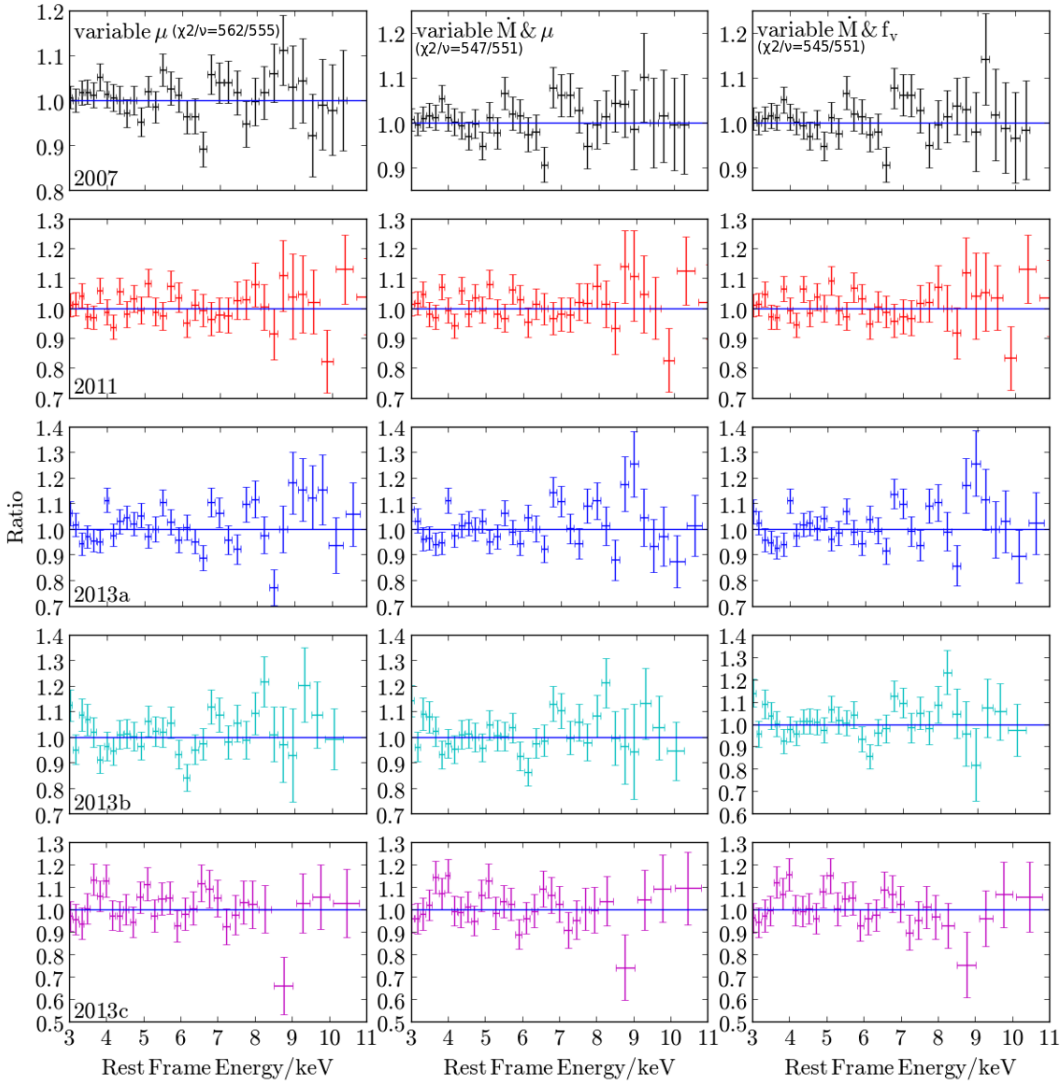

Figure 5.5: The ratio of the *Suzaku* datasets to the variable μ, $\dot{M}$ & μ and $\dot{M}$ & f_v models. Note the strong residuals in the 2013a row for all columns. However, both of the models which allow $\dot{M}$ to vary reduces the feature at $\sim 8.5\,\mathrm{keV}$ – despite being too broad so not removing the feature.

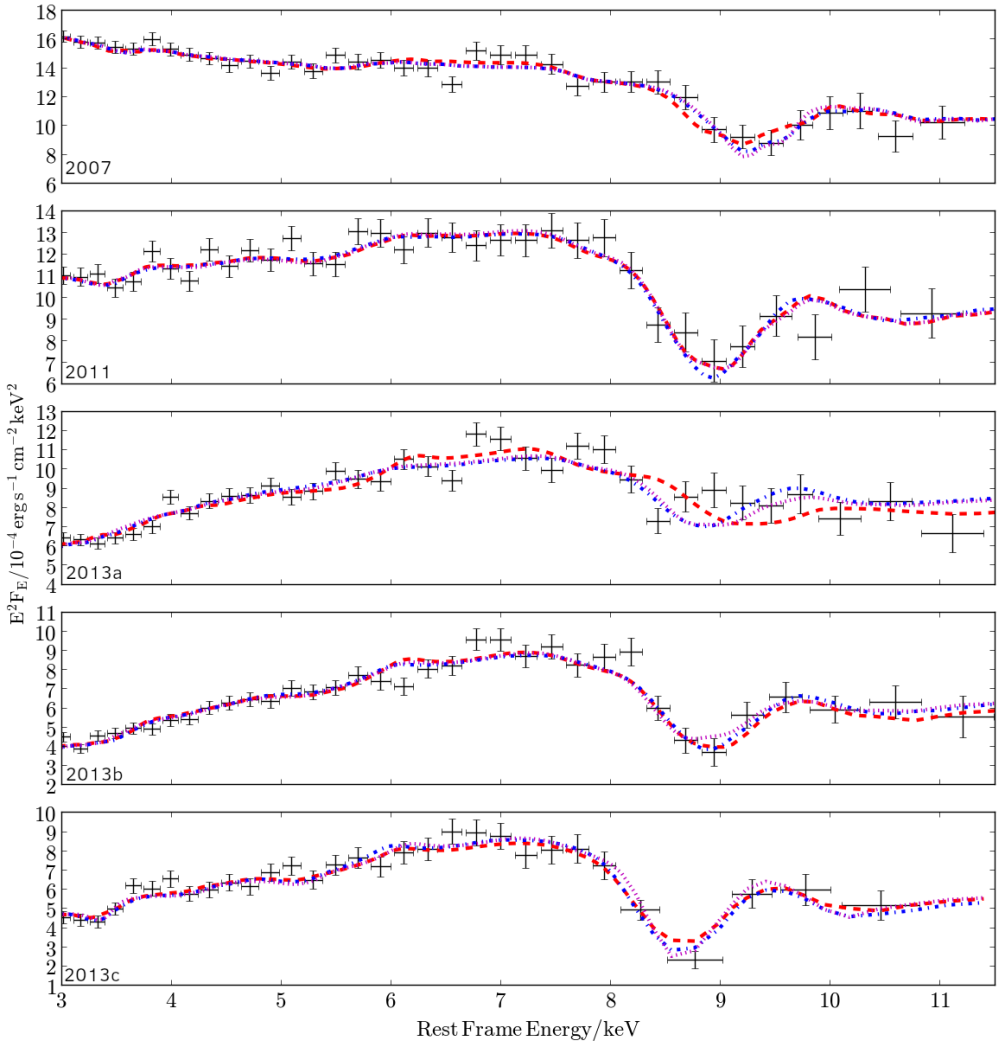

Figure 5.6: The spectra and models of the *Suzaku* datasets, with the disk wind models superimposed. The red dashed line shows the μ variable model, the blue dash-dot line represents the μ & $\dot{M}$ model and lastly the magenta dotted lines stand for the $\dot{M}$ & f_v model. 2013a clearly shows the slowing for both of the $\dot{M}$ variable models although the feature is far too broad. 2007 also shows a shift in velocity, this time to higher velocity.

than the actual radial velocity (due to the projection into the LOS) $L_{\rm kin}$ will always be an underestimate. Using f_v and the launch velocities of the wind, I can infer the value for the radial outflow velocity. However this does assume that μ is accurate, so should be treated with caution.

Assuming an outflow velocity of 0.25c the $\dot{M}$ values in table 5.4 result in $L_{\rm kin}/L_{\rm bol}$ values between 5–10 %. If $v_{\rm out} = 0.225 f_v$c as a rough estimate for the radial outflow velocity instead then the inferred $L_{\rm kin}/L_{\rm bol}$ range is 8–27 %, which is comparable to the value obtained by Nardini et al. (2015). Even in the conservative case using $v_{\rm out} = 0.25$c the kinetic power exceeds the theoretical threshold of 0.5–5% (Hopkins & Elvis 2010; Di Matteo et al. 2005).

5.2 *XMM-Newton–NuSTAR* spectra

Moving on to the *XMM-Newton–NuSTAR* datasets in an attempt to understand the wind variability in the higher flux state the same phenomenological model with only $L_{2-10\,\rm keV}$ variations is applied. However, unlike in the *Suzaku* observations, the simultaneous *NuSTAR* observations provide high-energy information allowing for Γ to be found independently for each observation. This provides a slight over-fit of $\chi^2/\nu = 2531/2572$.

The Γ parameter, which can be found in table 5.5, comes up against the upper bound ($\Gamma = 2.4$) excluding observation A ($\Gamma = 2.24 \pm 0.04$). The value of Γ is close to the value expected from the previous chapter so the grid was not extended further — as it is computationally expensive and a reasonable fit was found with the current grid. Future work may look to extend the range in Γ to gain a more detailed insight into the wind parameters.

Obs B is the softest observed spectrum. This can be seen in Fig. 4.1 of the previous chapter. Because of this the covering fraction reduces from 0.30 ± 0.04 in observation A to $0.09^{+0.10}_{-0.08}$ in observation B before returning to $0.47^{+0.03}_{-0.04}$ in observation C. $L_{2-10\,\rm keV}$ once again follows the flux and varies from $0.448 \pm 0.012\, L_{\rm edd}$ in observation A to a low of $0.185^{+0.005}_{-0.006}\, L_{\rm edd}$ in observation E. The column density of the partial covering is larger (14^{+4}_{-2})

Obs	A	B	C	D	E
Γ	2.24 ± 0.04	$2.33^{b}_{-0.05}$	$2.40^{b}_{-0.02}$	$2.37^{b}_{-0.05}$	$2.40^{b}_{-0.04}$
$\dot{M}/\dot{M}_{\rm edd}$	$0.14^{+0.01}_{-0.02}$	0.14^{t}	0.14^{t}	0.14^{t}	0.14^{t}
$\%L_{2-10\,\rm keV}/L_{\rm edd}$	0.448 ± 0.012	$0.195^{+0.005}_{-0.006}$	$0.243^{+0.006}_{-0.007}$	$0.266^{+0.007}_{-0.008}$	$0.185^{+0.005}_{-0.006}$
f_v	$1.39^{+0.02}_{-0.03}$	1.39^{t}	1.39^{t}	1.39^{t}	1.39^{t}
μ	0.60 ± 0.01	0.60^{t}	0.60^{t}	0.60^{t}	0.60^{t}
`CF`	0.30 ± 0.04	$0.09^{+0.10}_{-0.08}$	0.45 ± 0.02	$0.47^{+0.03}_{-0.04}$	$0.38^{+0.02}_{-0.04}$
$N_{\rm H}/10^{22}\,{\rm cm}^{-2}$	14^{+3}_{-2}	14^{t}	14^{t}	14^{t}	14^{t}
$\log \xi$	3.1 ± 0.2	3.1^{t}	3.1^{t}	3.1^{t}	3.1^{t}
$v_{\rm out}/{\rm c}$	$-0.31^{+0.17}_{-0.12}$	-0.31^{t}	-0.31^{t}	-0.31^{t}	-0.31^{t}
FPMA offset	1.03 ± 0.02	1.02 ± 0.04	1.07 ± 0.03	1.01 ± 0.03	1.00 ± 0.03
FPMB offset	$1.02^{+0.03}_{-0.02}$	1.03 ± 0.04	$1.05^{+0.04}_{-0.03}$	1.00 ± 0.03	1.06 ± 0.03
χ^2/ν	629/610	425/371	471/469	421/475	402/414
H_0	0.29	0.03	0.46	0.96	0.66

Table 5.5: Best fit parameters for the disk wind model applied to the *XMM-Newton–NuSTAR* datasets allowing Γ and $L_{2-10\,\rm keV}$ variations. The value of Γ in all but observation A hits the upper bound of the parameter space. The total χ^2/ν is 2531/2571 and the Null probability is 0.71.
Key:
^{t}: tied to the value of observation A.
^{b}: the parameter hits the edge of the grid where $\Gamma = 2.4$.
H_0 refers to the Null probability.

and the $\log \xi$ is much larger (3.1 ± 0.2) than the *Suzaku* values; while the outflow velocity ($-0.31^{+0.17}_{-0.12}$c) is once again in the range expected from previous fits.

Fig. 5.7 shows ratios where: the wind is unfit (first column); the disk wind model is applied and only $L_{2-10\,\rm keV}$ is variable (middle column) and a fit allowing both $L_{2-10\,\rm keV}$ and f_v to vary (end column). The changes between the first and second columns show the features the disk wind model fits. The red line in Fig. 5.8 shows the $L_{2-10\,\rm keV}$ only model. It can be seen that ionisation changes do a reasonable job of explaining the changes in the line profile, though some of the features are slightly misplaced – for instance in observation B the model is over-predicting the velocity of the wind. This is not rectified by allowing f_v to

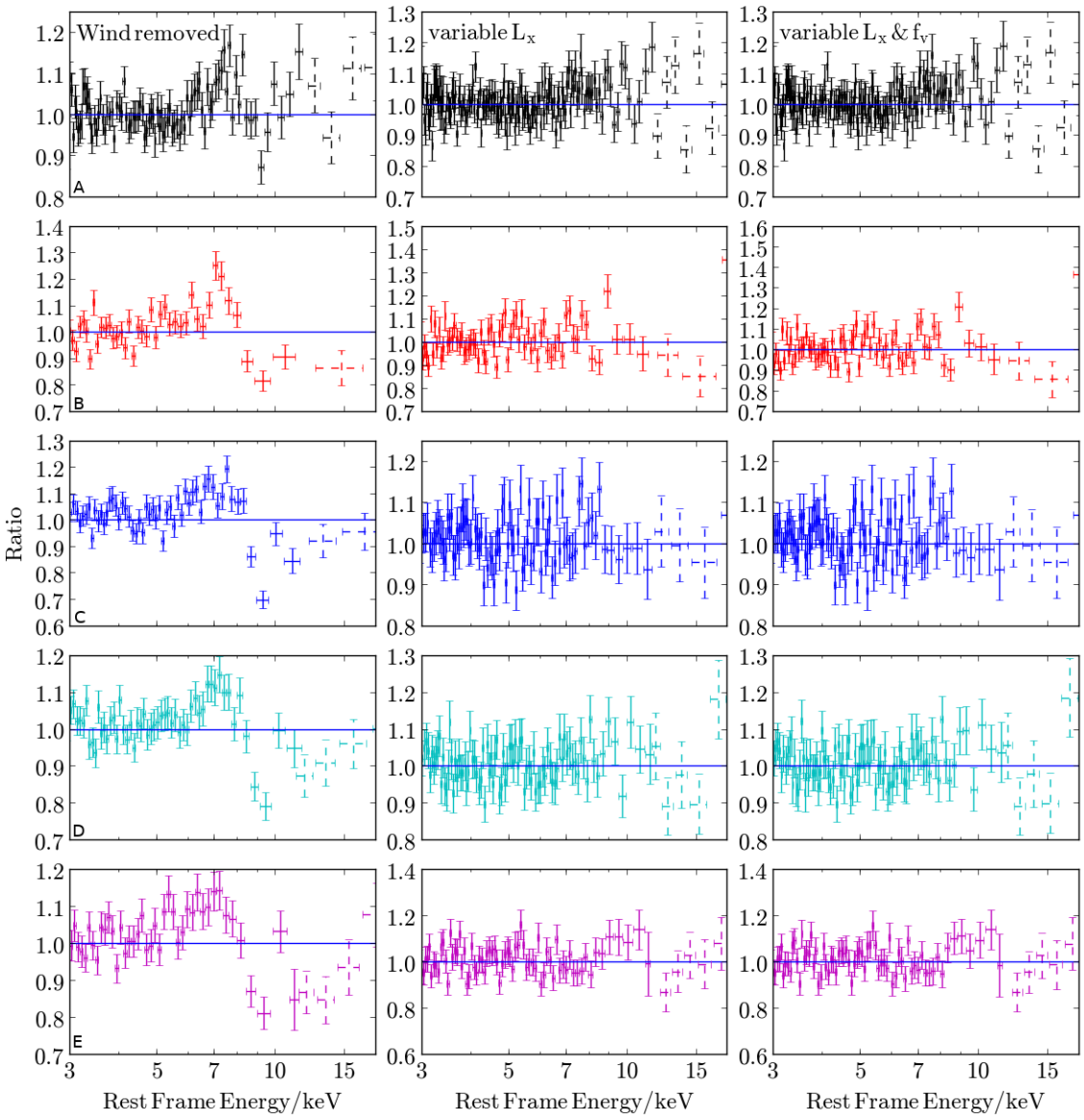

Figure 5.7: The ratios of the *XMM-Newton* (solid) and *NuSTAR* (dashed) datasets to a model with the disk wind removed & the continuum shifted (Wind removed) and a model with the disk wind intact (variable $L_{2-10\,\mathrm{keV}}$). They are shown side by side to show the influence of the wind in both emission and absorption. *NuSTAR* date are plotted only above 11 keV for clarity. While the fit is generally good, there is evidence for a second feature in observation E: the model appears to be overcompensating around 9 keV to compensate for the residuals around 12 keV.

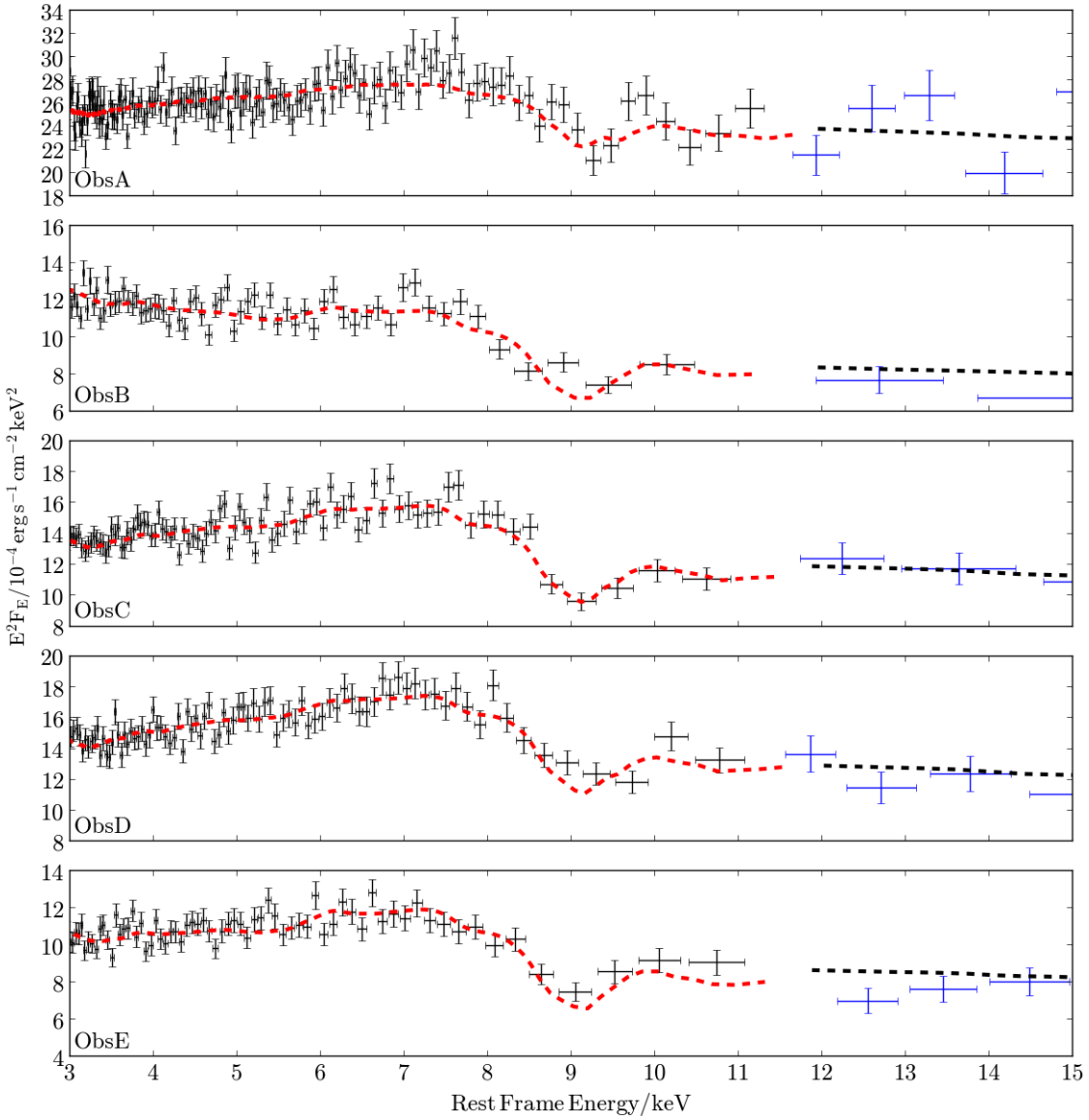

Figure 5.8: The unfolded data for *XMM-Newton* (black) & *NuSTAR* (blue) which is only shown above 11 keV, along with the unfolded models are red dashed (*XMM-Newton*) and black dashed (*NuSTAR*). It is obvious that observation B has fine structure and observation D has an asymmetric shape skewed to higher energies.

vary as can been seen in the end column of Fig. 5.7 where the middle and end columns look almost identical. From this it can be seen that variations in $L_{2-10\,\mathrm{keV}}$ and Γ do a satisfactory job of explaining the observed disk wind variability. This is similar to what was seen in the previous chapter, where it was inferred that the source variability was the dominant factor. Once again the modelling allows the calculation of $L_{\mathrm{kin}}/L_{\mathrm{bol}} = 7\%$ for $v_{\mathrm{out}} = 0.25\mathrm{c}$ and 11% using $v_{\mathrm{out}} = 0.225 f_v \mathrm{c}$ which is slightly lower than the value presented in Nardini et al. (2015) but still over the $L_{\mathrm{kin}}/L_{\mathrm{bol}} = 0.5$–5%.

5.3 Simultaneous fit of all observations

Taking the information from fitting the disk winds to the *Suzaku* and *XMM-Newton–NuSTAR* datasets individually, a model is constructed to fit all the datasets (including the archival *XMM-Newton*) simultaneously. The advantage to the simultaneous fit is it can be constructed to test the correlation in section 4.7. Varying f_v and $L_{2-10\,\mathrm{keV}}$ is analogous to measuring v_{out} and the observed flux respectively, but with several advantages. $L_{2-10\,\mathrm{keV}}$ accounts for the flux absorbed by the wind so is a better measure of the driving radiation. As μ is degenerate with f_v it is kept constant for all observations. Γ is not allowed to vary between observations for the *Suzaku* and archival *XMM-Newton* (due to a lack of data above 10 keV). $\dot{M}$ is allowed to vary between the groups and within the *Suzaku* observations where it was previously required. The partial coverer $\log \xi$ is allowed to vary between the three data groups (archival *XMM-Newton*, *Suzaku* and *XMM-Newton–NuSTAR*) but not within them. Column density (N_{H}) is kept constant as varying both $N_{\mathrm{H}}$and $\log \xi$ would be degenerate. `CF` is allowed to vary to account for the changes in curvature for all observations.

Fitting the disk wind model as described above produces $\chi^2/\nu = 4986/5049$ (see table 5.6). Typically all the datasets are well fit by varying the luminosity ($L_{2-10\,\mathrm{keV}}$). A decrease in luminosity produces deeper profiles as ionisation decreases. However modest changes in the mass outflow rates (between 10–20% $\dot{M}_{\mathrm{edd}}$) along with changes in the wind velocity

(via the f_v parameter from 1.25–1.94) are required. The parameters of the partial covering are comparable to the previous fits. `CF` varies from $0.10^{+0.08}_{-0.07}$ to 0.46 ± 0.02 between two observations (observation B and observation C) which are separated by only 8 days. The *Suzaku* observations show the extremes in covering fraction of < 0.06 in 2007 and 0.83 ± 0.03 in 2013b. $\log \xi = 0.66^{+0.06}_{-0.05}$, 2.86 ± 0.13 and $2.61^{+0.16}_{-0.15}$ for the archival *XMM-Newton*, *Suzaku* and *XMM-Newton–NuSTAR* observations; this does not correlate with flux state. The low ionisation for the archival *XMM-Newton* data group is likely driven by the 2001 observation which despite its high flux has a lot of continuum curvature.

Note that in the *XMM-Newton* 2007 observations the f_v value is shifted to larger values than *XMM-Newton–NuSTAR* observation A which is comparable in flux. The feature produced by the model seems to be too broad, therefore the weak narrow features of the 2007 *XMM-Newton* observations are not well fit as seen in Fig. 5.1. This suggests a change in the wind structure – perhaps a narrowing of the outflow as the observed energy shift is not particularly high (therefore not just an increase in μ). This causes the model to fit a dip at higher energies (see Fig. 5.1); these features likely contribute more to χ than the narrow lower energy features forcing the f_v to larger values. Therefore the *XMM-Newton* 2007 observations are excluded from the regression analysis. These secondary features could be another part of the wind moving at a larger velocity; this should be investigated further.

Obs	X 2001	X 2007a	X 2007b	S 2007	S 2011	S 2013a	S 2013b	S 2013c
Γ	$2.27^{+0.04}_{-0.02}$	2.27^{t}	2.27^{t}	$2.31^{b}_{-0.12}$	2.31^{t}	2.31^{t}	2.31^{t}	2.31^{t}
$\dot{M}/\dot{M}_{\rm edd}$	0.17 ± 0.02	0.17^{t}	0.17^{t}	0.14 ± 0.03	0.18 ± 0.04	0.10 ± 0.03	$0.14^{+0.06}_{-0.03}$	$0.19^{+0.08}_{-0.04}$
$\%L_{2-10\,\rm keV}/L_{\rm edd}$	$0.505^{+0.015}_{-0.013}$	$0.410^{+0.010}_{-0.009}$	$0.233^{+0.008}_{-0.006}$	$0.256^{+0.008}_{-0.009}$	$0.217^{+0.014}_{-0.010}$	0.143 ± 0.006	$0.112^{+0.011}_{-0.005}$	$0.124^{+0.019}_{-0.009}$
f_v	1.62 ± 0.09	$1.94^{b}_{-0.08}$	1.62 ± 0.05	$1.46^{+0.10}_{-0.05}$	1.36 ± 0.04	1.37 ± 0.06	1.33 ± 0.05	$1.25^{+0.02}_{-0.04}$
μ	0.58 ± 0.01	0.58^{t}	0.58^{t}	0.58^{t}	0.58^{t}	0.58^{t}	0.58^{t}	0.58^{t}
$\%c_{\rm f}$	79^{+11}_{-15}	34^{+12}_{-13}	23^{+13}_{-7}	< 6	37 ± 4	74^{+3}_{-6}	83 ± 3	68 ± 4
$N_{\rm H}/10^{22}\,{\rm cm}^{-2}$	$10.8^{+0.8}_{-0.7}$	10.8^{t}	10.8^{t}	10.8^{t}	10.8^{t}	10.8^{t}	10.8^{t}	10.8^{t}
$\log \xi$	$0.66^{+0.06}_{-0.05}$	0.66^{t}	0.66^{t}	2.86 ± 0.13	2.86^{t}	2.86^{t}	2.86^{t}	2.86^{t}
$v_{\rm out}/{\rm c}$	$-0.31^{+0.16}_{-0.14}$	-0.31^{t}	-0.31^{t}	-0.31^{t}	-0.31^{t}	-0.31^{t}	-0.31^{t}	-0.31^{t}
χ^2/ν	277/245	445/397	273/261	131/114	96/107	117/111	109/108	117/97
H_0	0.08	0.05	0.29	0.14	0.76	0.34	0.46	0.09

Obs	XN A	XN B	XN C	XN D	XN E
Γ	$2.25^{+0.04}_{-0.03}$	$2.34^{b}_{-0.05}$	$2.40^{b}_{-0.02}$	$2.38^{b}_{-0.04}$	$2.40^{b}_{-0.04}$
$\dot{M}/\dot{M}_{\rm edd}$	0.13 ± 0.01	0.13^{t}	0.13^{t}	0.13^{t}	0.13^{t}
$\%L_{2-10\,\rm keV}/L_{\rm edd}$	0.455 ± 0.008	$0.199^{+0.003}_{-0.004}$	0.247 ± 0.004	0.270 ± 0.005	0.189 ± 0.004
f_v	1.42 ± 0.06	1.40 ± 0.04	1.41 ± 0.03	1.42 ± 0.03	1.36 ± 0.03
μ	0.58^{t}	0.58^{t}	0.58^{t}	0.58^{t}	0.58^{t}
$\%\,\mathtt{C_f}$	31^{+4}_{-3}	10^{+8}_{-7}	46 ± 2	47 ± 3	39^{+2}_{-4}
$N_{\rm H}/10^{22}\,{\rm cm}^{-2}$	10.8^{t}	10.8^{t}	10.8^{t}	10.8^{t}	10.8^{t}
$\log \xi$	$2.61^{+0.16}_{-0.15}$	2.61^{t}	2.61^{t}	2.61^{t}	2.61^{t}
$v_{\rm out}/{\rm c}$	-0.31^{t}	-0.31^{t}	-0.31^{t}	-0.31^{t}	-0.31^{t}
offset^{a}	1.02 ± 0.02	0.99 ± 0.04	1.04 ± 0.03	0.99 ± 0.03	0.98 ± 0.03
offset^{b}	1.01 ± 0.02	1.01 ± 0.04	1.02 ± 0.03	0.98 ± 0.03	1.05 ± 0.03
χ^2/ν	763/748	582/540	647/664	602/682	598/632
$\rm H_0$	0.34	0.10	0.67	0.99	0.83

Table 5.6: Best fit model parameters for the model of $L_{2-10\,\rm keV}$ and f_v variations for all PDS 456 datasets. The f_v of the 2007 datasets is shifted to higher values; it appears that the curvature at the end of the band pass is being fit instead of the absorption feature. The total $\chi^2/\nu = 4985/5049$ and Null probability $\rm H_0 = 0.74$. When simultaneously fit some spectra are not as well fit as compared to the individual fits (such as 2013c) while others are fit better (observation D). This is not surprising due to the pressure of parameters such as μ which are kept constant forcing the model in different parts of the parameter space. The total χ^2/ν is 5095/5049 and the Null probability $\rm H_0 = 0.32$. Here, ^{t} refers to parameters which are tied to the value of observation A and ^{b} denotes the parameter hits the edge of the grid.

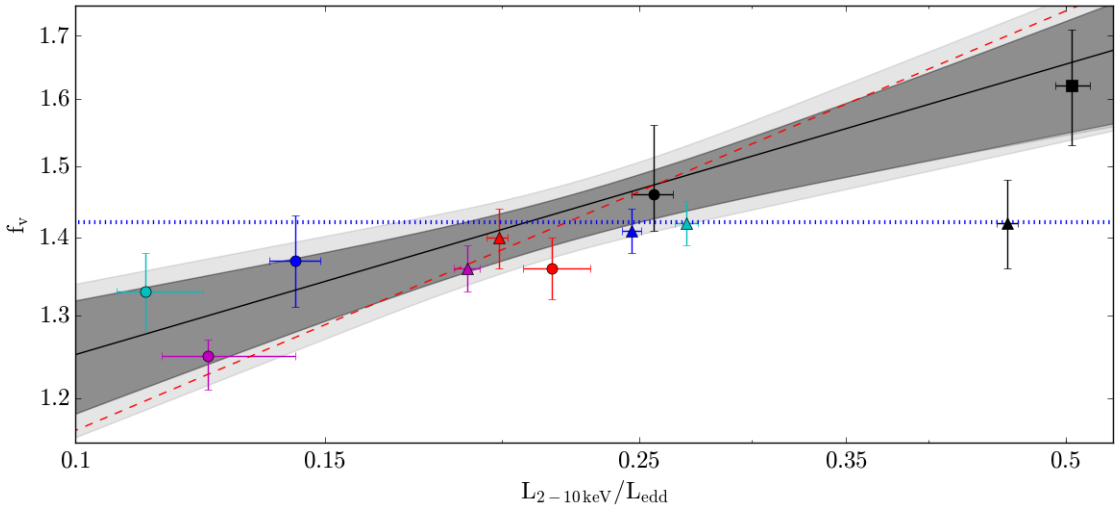

Figure 5.9: The regression line (black) of f_v (a proxy for outflow velocity) and $L_{2-10\,\mathrm{keV}}$. Triangle, circle and square markers represent the archival *XMM-Newton*, *Suzaku* and *XMM-Newton–NuSTAR* data respectively, with the colours corresponding to those of Fig 5.1; the dark and light shaded areas give 1 and 3σ errors. The blue dotted line represents the best fit for a constant f_v ($= 1.45$). The red dashed line has the equation $f_v \propto L^{0.25}$ while the regression line has the equation $f_v \propto L^{0.17\pm0.06}$. The positive slope is a clear indication of the radiative driving, as a magnetic flow would have a $L^{-0.25}$, as the velocity depends on the launch radius ($v \propto R^{-0.5}$) and the only dependence on luminosity comes from its ionising effects ($R \propto L^{0.5}$).

The correlation between $L_{2-10\,\mathrm{keV}}$ and outflow velocity can be seen in Fig. 5.9 with several regression lines superimposed. The blue dotted line corresponds to a constant ($f_v = 1.45 \pm 0.01$). The red dashed line represents the power law with a fixed slope of 0.25 which is predicted for a radiatively driven outflow modulated by ionisation changes (as explained in section 4.7) and the black line is a power law with a best-fit slope of 0.17 ± 0.06. The dark (1σ) and light (3σ) shaded areas correspond to the confidence intervals on the black regression line. It can be seen from the plot, but also from the slope values, that the slope found in this work is flatter (meaning the wind is likely more complex than assumed in the derivation in section 4.7) than 0.25 although still in agreement at the 3σ level.

Using the self-consistent disk wind model better accounts for the reduced observed luminosity due to absorption within the wind. Therefore, $L_{2-10\,\mathrm{keV}}$ gives a better measure of the intrinsic luminosity. As $L_{2-10\,\mathrm{keV}}$ will also affect the ionisation it will also change the inferred range of f_v. Therefore, it is important that this correlation is still found when using the disk wind model. To investigate the effect that variable ionisation (controlled by the $L_{2-10\,\mathrm{keV}}$ and Γ parameters) has on the $L_{2-10\,\mathrm{keV}}$ vs f_v correlation, f_v was set to one for all observations; the resulting shift observed in the line energy is due to changes in ionisation. This line energy produces a $\sim 10\%$ reduction in the range of the f_v parameter.

Despite the discrepancy between the observed and predicted values this is still strong evidence for a radiative flow. The predicted velocity structure of a magnetically driven flow has an outflow velocity with a fixed dependence on launch radius ($v \propto \sqrt{R}$) without radiative driving the wind will only respond to a increase in luminosity by over-ionising the inner edge, moving the visible edge outward. Combining these two effects produces $v \propto (L^{0.5})^{-0.5} \propto L^{-0.25}$. As the observed slope is positive ($f_v \propto L^{0.17\pm0.06}$) with a null hypothesis of 6×10^{-9} compared to 2×10^{-17} for a constant $f_v = 1.45 \pm 0.01$. This is strong evidence against a purely magnetic wind.

The slope of the regression may be driven predominantly by the *Suzaku* observations and the 2001 *XMM-Newton* datasets as the *XMM-Newton–NuSTAR* observations were well fit with a constant f_v. This may suggest that the outflow is more sensitive to the radiative driving when the wind is optically thicker (as these are the observations with deeper absorption profiles) as to be expected for a radiatively driven flow.

5.4 Conclusion

From this study of the disk wind present in the PDS 456 datasets, it appears that in the high state represented by the *XMM-Newton–NuSTAR* observations the variability of the wind profile can be explained by change in the $L_{2-10\,\mathrm{keV}}$ and Γ (the parameters of the source

illuminating the disk wind). The lower luminosity observations in the *Suzaku* campaign require changes to the mass outflow rate, such as in 2013c which has a higher mass outflow rate to account for the deep absorption profile that is observed. This is co-incident with increased covering fraction. As Matzeu et al. (2016) already showed (and is confirmed in the previous chapter with an extended dataset), the partial coverer is preferred when it is outflowing at velocities comparable to the wind. It also appears that both the velocity and strength of the partial coverer and of the highly ionised Fe K absorption are generally correlated (*XMM-Newton* 2001 and *Suzaku* 2013a being two notable exceptions).

Slightly lower mass outflow rates were derived ($\dot{M}$ = 5–7 $M_{\odot}$ yr^{-1}) for the *Suzaku* data when compared to Hagino et al. (2015) ($\dot{M}$ = 7–10 $M_{\odot}$ yr^{-1}). The main difference between this work and Hagino et al. (2015) is that the atomic database is large in the Sim et al. (2010) model. This shows that ionisation is important for the measurement of $\dot{M}$ and therefore $L_{\rm kin}$. $L_{\rm kin}/L_{\rm edd}$ is found to be: 0.5–5% assuming $v_{\rm out}$ = 0.25c or 8–27% if $v_{\rm out} = 0.225 f_v$c is used.

The current generation of models alongside XSTAR grids produces a reasonable fit to the data allowing for a better understanding of the physical changes within the flow. Future models should incorporate clumps within the wind to self-consistently include the partial covering. In summary:

- On the whole, most of the variations in the outflow can be explained by variation in the ionisation, linked to the ionising 2–10 keV luminosity and photon index. This is clearly the case for the *XMM-Newton–NuSTAR* observations.
- Thus, generally the deeper profiles occur in the less luminous states (lower $L_{2-10\,\rm keV}$), when the wind opacity is higher.
- However, in some of the *Suzaku* datasets in particular, additional wind variability is required. This may be in the form of variations either in the flow structure (through varying the μ parameter) or through a combination of variations in $\dot{M}$ and the outflow velocity.

- Overall, the trend for the wind velocity (parameterised here through the f_v parameter) to increase with ionising luminosity is confirmed, as per the Matzeu et al. (2017) study and is consistent with a radiatively driven wind. It was important to verify with a model that takes into account the suppression of the observed luminosity by the wind.

- I find values of the outflow kinetic power of $L_{\rm kin}$ = 5–10% of $L_{\rm edd}$ when conservatively assuming an outflow velocity of 0.25c; slightly below the value of 15% found by Nardini et al. (2015). However when factoring in f_v assuming a mean launch velocity of 0.225c, the range of $L_{\rm kin}/L_{\rm edd}$ moves to 8–27%; as mentioned this value assumes that the value of μ is accurate.

- In the future, variations in the lower ionisation partial covering absorber may be accounted for by adapting the wind models – accounting for clumps within the flow.

6 The disk winds of other AGN

In this chapter I will model the disk winds of two other noteworthy AGN. This small sample allows me to explore the parameter space of the disk wind model. Firstly I will be studying PG1211 + 143, an archetypal fast disk wind which shows absorption variability loosely correlated with the flux, whereby the high-flux observations show weaker absorption features. Secondly 1H 0707 − 495 is an extreme NLS1 which shows fast large amplitude flux variability and a powerful outflow. Both objects have been well studied so have a wealth of data and powerful outflows making them good candidates for study with a disk wind.

6.1 PG1211 + 143

PG1211 + 143 was the first detection of a UFO in a non-BAL AGN, with an observed velocity of 0.15 ± 0.01c (Pounds et al. 2003; Pounds & Page 2006), a redshift $z = 0.0809$ and a nominal 2–10 keV flux of $\sim 3 \times 10^{-12}$ erg s^{-1} cm^{-2}. By combining 2001, 2004 and 2007 *XMM-Newton* broad-band spectra, Pounds & Reeves (2009) noted a possible second (slower) velocity stream. However, the continuum curvature made the outflow velocity poorly constrained. To further explore the outflow a further seven orbits of *XMM-Newton* data were taken. Pounds et al. (2016) used this long campaign to confirm the second velocity stream, with the two components having velocities of $v_{\rm out,1} = 0.066 \pm 0.003$c and $v_{\rm out,2} = 0.129 \pm 0.002$c in the highly ionised outflow.

Pounds et al. (2016b) studied the stacked RGS spectra of the 2014 campaign and found the lower ionisation counterpart of the Fe K features in the soft X-ray spectrum from He-like and H-like ions of elements such as O, Ne and Fe with velocities between 0.061–0.188c (comparable to velocities obtained from fitting the Fe K outflow). However, Reeves et al. (2018) studied the individual RGS spectra in the 2014 campaign and found that the two soft X-ray absorption components show only a small velocity difference ($\Delta v = 0.003$c) and

different ionisations, with the observed variability between the 2014 spectra reproduced by varying the ionisation state or the column density. In either scenario, the lowest flux observation represents the most absorbed state, while the brightest state is almost completely unabsorbed (Reeves et al. 2018).

Lobban et al. (2016) showed that *XMM-Newton* spectra during the 2014 campaign are highly variable on the time scale of days. This is dominated by a rapidly variable absorber — both low ionisation as seen in the RGS and the highly ionised Fe K flow (this can be seen in the RMS spectra in Lobban et al. 2016). The timescales (of days) require it to be compact ($\sim 10 - 100\,R_{\rm g}$). This size scale agrees with the RGS study (Reeves et al. 2018).

As mentioned in sections 1.3.4 and 4.6, the type of soft X-ray absorbers seen in PDS 456 and PG1211 + 143 are not the typical warm absorbers observed in type 1 Seyferts, as evidenced by their fast outflow velocity (0.061 ± 0.001c) and rapid variability (~ 2 days). Instead, these absorbers are likely to originate from the disk wind and, depending on their filling factor, may carry significant kinetic energy relative to $L_{\rm edd}$. Reeves et al. (2018) estimated an outflow rate of $\sim 2\,M_{\odot}$ yr^{-1}, which is comparable to that of the Fe K outflow.

From an analysis using only the *NuSTAR* observation in table 6.1 — which was simultaneous with observation G of the 2014 campaign — Zoghbi et al. (2015) claimed that a relativistically blurred disk reflection model could account for the Fe K profile and hard excess. Zoghbi et al. (2015) claimed that no fast outflow was detected. However, *NuSTAR* alone is not generally sufficient for this kind of study due to its broad detector response; even in PDS 456 the wind cannot be constrained only using *NuSTAR*. It therefore can only be used for winds with extremely broad features. Pounds et al. (2016) found, in an analysis of the higher resolution *XMM-Newton* spectra for observation G, that the fast outflow is indeed present. It is relevant to note that the absorption feature in observation G is comparatively weak having an EW of -72^{+39}_{-89} eV compared to observation E that has an equivalent width of -133^{+114}_{-64} eV.

Performing a joint analysis of the *XMM-Newton* and *NuSTAR* data, Lobban et al. (2016) found that while a blurred reflection model can account for some of the Fe Kα emission

and the continuum above 10 keV, it does not account for the absorption which is clearly present in both Fe K and soft X-ray bands in the much higher resolution *XMM-Newton* spectra.

The disk wind model described in chapter 3 includes the Compton reflection from the wind and the emission profile over the Fe K region, therefore a full treatment of the wind should be done before inferring blurred reflection in objects known to have a disk wind.

A key question is what is the cause of the rapid absorption changes and how does it respond to the continuum changes in PG1211 + 143? From modelling the spectra across different epochs I will be able to determine whether the absorption variability is due to a direct response of the gas to the photo-ionising continuum variations, or whether the absorption variability is due to the inhomogeneous nature of the outflow.

6.1.1 Observations

The observations used in this study of PG1211 + 143 come from two epochs in 2001 and 2014 both using *XMM-Newton*. The two epochs of this study are in different states of obscuration, with 2001 being more absorbed in both the continuum and at Fe K. The 2001 observation was taken on 15$^{\text{th}}$ June with a net exposure of 49.6 ks with an observed flux of $F_{2-10\,\text{keV}} = 3.11 \times 10^{-12}$ erg s^{-1} cm^{-2}. Seven orbits of *XMM-Newton* were taken 13 years later between 2$^{\text{nd}}$ June 2014 and 7$^{\text{th}}$ July 2014 with a total duration of 645.8 ks with a mean observed flux of $F_{2-10\,\text{keV}} = 3.72 \times 10^{-12}$ erg s^{-1} cm^{-2}. For details on the observations see table 6.1.

The 2001 data were reduced using a circular region of radius 30″ for both the background and source. The 2014 observations were reduced as per Lobban et al. (2016) with source events extracted from a circular region with radius of 20″ and a square background region ~ 38 times the area of the source region. In both cases periods of high background were removed to prevent this from distorting the spectra.

During the five weeks of the 2014 campaign a varying degree of obscuration is observed.

However, as noted by Lobban et al. (2016), most of the variability observed is in the soft part of the spectrum. This allows the use of the mean spectrum above 2 keV, giving a higher signal to noise (S/N) for the analysis of the disk wind. The mean Fe K band spectrum from 2014 (Figure 6.1) illustrates the high quality data of the new observations, where multiple absorption lines are revealed at Fe K (Pounds et al. 2016).

The 2001 and 2014 mean spectra are presented in Fig. 6.1. The 2001 plot shows a hard spectrum with a strong Fe K absorption feature. While the 2014 mean spectrum appears comparatively flat, there is still a strong broad emission feature and absorption features above 7 keV.

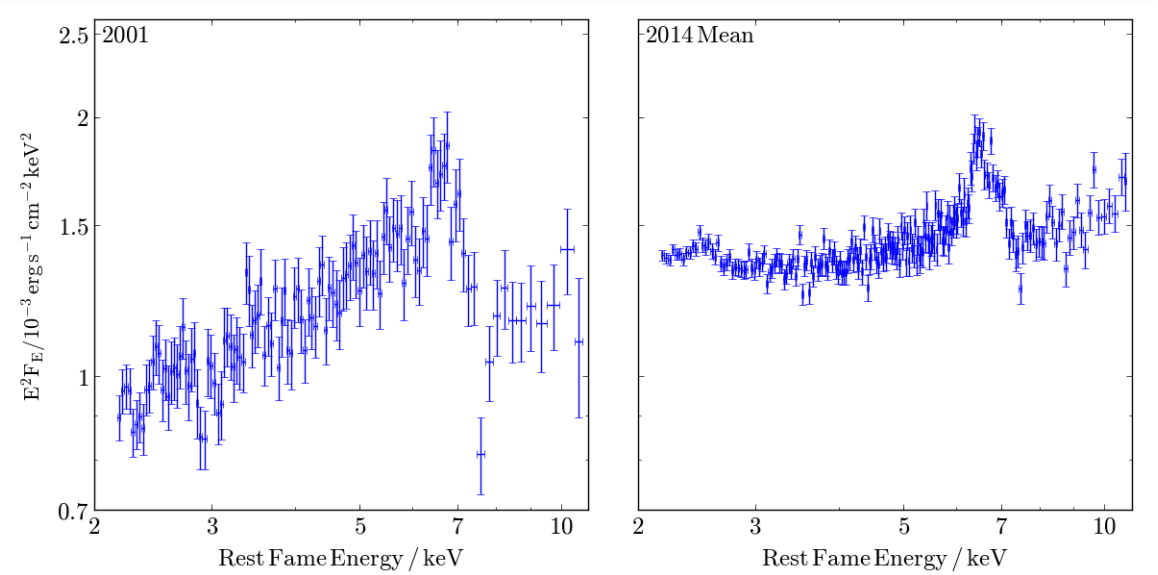

Figure 6.1: The spectra of PG1211 + 143 used in this study. The variability is seen most drastically between 2–5 keV where there is a flattening of the spectrum going from 2001 to the 2014 mean spectrum.

Obs	Satellite	Obs ID	Date^d	Net Exposure^n/s	Flux^f / erg s^{-1} cm^{-2}
2001	*XMM-Newton*	0112610101	2001-06-15	49.6	3.11
A	*XMM-Newton*	0745110101	2014-06-02	78.2	3.80
B	*XMM-Newton*	0745110201	2014-06-15	93.2	3.49
C	*XMM-Newton*	0745110301	2014-06-19	89.5	3.63
D	*XMM-Newton*	0745110401	2014-06-23	88.3	3.76
E	*XMM-Newton*	0745110501	2014-06-25	51.2	4.29
F	*XMM-Newton*	0745110601	2014-06-29	89.3	3.77
G	*XMM-Newton*	0745110701	2014-07-07	86.0	3.42
2014 mean	*XMM-Newton*	-	-	542.5	3.72

Table 6.1: The details of observations used in this study of PG1211 + 143. The 2014 mean spectrum represents the combination of observations A to G.
Key:
^{n} : the net exposure of the observation in the PN camera after filtering for background flares and correcting for dead time.
^{f}: the 2–10 keV flux from modelling the spectra with a two-power law continuum and Gaussians for emission and absorption features.
^{d}: the start date of the observation.

6.1.2 The disk wind model

Disk wind models have previously been applied to PG1211 + 143. Fukumura et al. (2015) presented an MHD wind model to explain the absorption feature in the 2001 dataset. They found the column to be $N_H = 1.21 \times 10^{23}\,cm^{-2}$ and $1.67 \times 10^{23}\,cm^{-2}$. Sim et al. (2010) also modelled the stacked PN data from Pounds & Reeves (2009) (2001, 2004 and 2007 observations) with a single grid model which reproduced the overall Fe K line profile; this can be seen in Fig. 6.2. The Sim et al. (2010) model gives a mass outflow rate of $0.5\,M_\odot$ yr^{-1}. The ionising luminosity was fixed at $2.5 \times 10^{43}\,erg\,s^{-1}$ with an inclination (μ) of 0.575 and $f_v = 0.5$. The parameters used for the disk wind grid and the model applied in this work to PG1211 + 143 can be found in table 6.2. Therefore the absorption features in PG1211 + 143 have been fit with both MHD and radiative disk wind models in previous work. However, neither of the aforementioned models were fitted to multiple observations in order to investigate how well they explain the spectral variability.

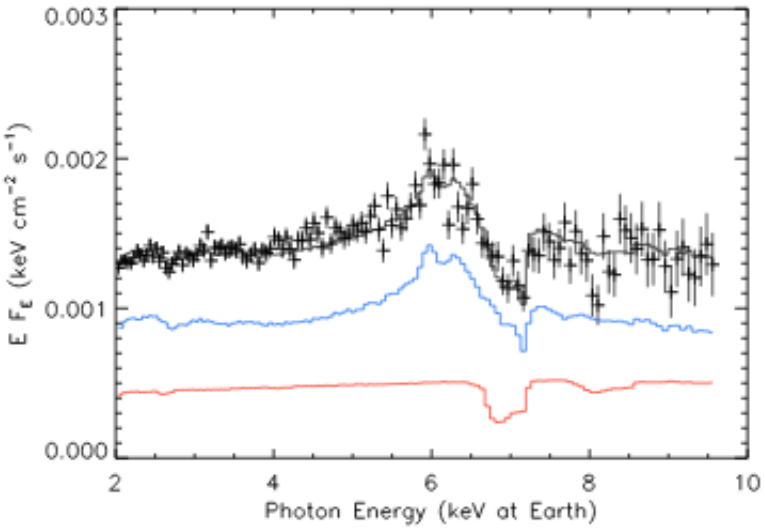

Figure 6.2: Taken from Sim et al. (2010), which shows thedisk wind model fit to the stacked PN spectra of PG1211 + 143 presented in Pounds & Reeves (2009). Even though the model fits well there are hints of another feature around 8 keV.

6.1.3 Fitting the PG1211 + 143 data

Due to the soft nature of the observed spectra, coupled with the detector response, there are many times more counts (7×) below 2 keV than above it. This would bias the fit statistic towards features in the soft spectrum if the full 0.5–10 keV band was used. While these features are probably linked to the disk wind (Reeves et al. 2018), being clumps within the wind, these clumps are not present in the Sim et al. (2010) model. Therefore, the focus will be on the spectra above 2 keV.

To fit these two spectra the continuum model prescribed by Pounds & Reeves (2009); Pounds et al. (2016) of two power laws (one harder $\texttt{po}_\texttt{h}$ than the other $\texttt{po}_\texttt{s}$) is used and a partial coverer to allow for the transition to the absorbed state and along with a distant reflector outside of the wind. This yields a phenomenological model of:

Parameter	Sim et. al. 2010	This work
$M_{\rm BH}$	$10^7\,M_\odot$	$5\times10^7\,M_\odot$
$\dot{M}_{\rm edd}$	$0.37\,M_\odot\ {\rm yr}^{-1}$	$1.85\,M_\odot\ {\rm yr}^{-1}$
$L_{\rm edd}$	$1.3\times10^{45}\ {\rm erg\,s}^{-1}$	$6.3\times10^{45}\ {\rm erg\,s}^{-1}$
$\dot{M}$	$1.5\,\dot{M}_{\rm edd}$	0.2–20 $\dot{M}_{\rm edd}$
$L_{\rm bol}$	$0.8\,L_{\rm edd}$	$0.2\,L_{\rm edd}$
$L_{2-10\,{\rm keV}}$	$2\%\,L_{\rm edd}$	0.5-7.5% $L_{\rm edd}$
Γ	1.9	1.8
$R_{\rm min}$	$50\,R_{\rm g}$	$64\,R_{\rm g}$
$R_{\rm max}$	$3\,R_{\rm min}$	$1.5\,R_{\rm min}$
d	$R_{\rm min}$	$R_{\rm min}$
$R_{\rm v}$	$8\,R_{\rm min}$	$R_{\rm max}$
f_v	0.5	0.5, 1, 2
μ	0.575	0.025–0.975

Table 6.2: The input parameters of the disk wind model applied to the stacked data (Sim et al. 2010) and the observations from 2001 and 2014 (this work). The main difference between the model parameters is $R_{\rm v}$ which is reduced to $1.5\,R_{\rm min}$ in this work as the skew of the profile it produces (from the wind accelerating) is an artefact of the stacking.

$$F = (\texttt{po}_s + \texttt{po}_h) * \texttt{pc} * \texttt{dw} + \texttt{reflector}. \tag{6.1}$$

Because a narrow distant reflector would come from an extended structure, the LOS would only pass through a column density so low that it will not have a noticeable effect. The photon index of the reflector's input spectrum is tied to that of the harder power law and the abundance of iron is fixed to solar. The inclination is fixed at 45°, which is consistent with the value found by Lobban et al. (2016). The high energy cut-off is fixed at 300 keV as this has little effect below 10 keV. The ionisation and normalisation of the reflector are free to vary but kept the same between both observations. Once again the observed flux and $L_{2-10\,\mathrm{keV}}$ are linked and $L_{2-10\,\mathrm{keV}}$ is allowed to vary between observations. For $f_v =$ 0.5, 1 and 2, this yields fits of $\chi^2 = 1682$, 1674 and 1735 with $\nu = 1589$ degrees of freedom. Allowing the normalisation of the reflector to vary does not produce a significant change in χ^2 ($\Delta\chi^2/\Delta\nu < 1/1$) so it is kept constant.

Scenarios with varying column densities ($\dot{M}$ and μ) are tested; both produce improved fits compared to varying $L_{2-10\,\mathrm{keV}}$ alone. Varying $\dot{M}$ produces $\chi^2\,(f_v) = 1641$ (0.5), 1672 (1) and 1676 (2) for $\nu = 1588$ giving a confidence interval of $> 6\sigma$ for $f_v = 1$ and 2 but only a 95% confidence for $f_v = 1$. Allowing μ to vary produces $\chi^2\,(f_v) = 1637$ (0.5), 1664 (1) and 1672 (2) for $\nu = 1588$. While varying both $\dot{M}$ and μ at the same time does not produce a statistically significant change in χ^2, it does allow the $L_{2-10\,\mathrm{keV}}$ to take on more sensible parameters as seen in table 6.3 where two representative sets of parameters are presented.

As Pounds et al. (2016) found evidence for a second velocity stream-line, therefore a second grid is added, offset from the first in f_v with all parameters tied. Various combinations of values for f_v were tested to find the best fit for 2014 and 2001.

An initial fit constraining $L_{2-10\,\mathrm{keV}}$ with the observed flux (the constrained model) provides a statistically worse fit to the data than the previous single grid model. Fig. 6.3 shows the ratios to the constrained model in black for both datasets, the absorption feature is clearly still present in the constrained model for 2001 (top panel, black ratio).

It can be seen in table 6.4 (presented for the 2001 constrained model; 2001^C) that

Parameter	2014 mean	2001	2014 mean	2001
$\dot{M}/\dot{M}_{\rm edd}$	$0.70^{+0.11}_{-0.01}$	$1.37^{+0.32}_{-0.42}$	$0.83^{+0.20}_{-0.09}$	$1.36^{+1.00}_{-0.30}$
% $L_{2-10\,\rm keV}/L_{\rm edd}$	$3.52^{+0.06}_{-0.36}$	$7.32^{b}_{-1.95}$	$5.70^{+0.88}_{-0.81}$	$2.23^{+2.42}_{-0.39}$
$\rm f_v$	0.50^{f}	0.50^{f}	0.50^{f}	0.50^{f}
μ	$0.60^{+0.02}_{-0.01}$	0.60^{t}	$0.58^{+0.01}_{-0.02}$	$0.67^{+0.01}_{-0.03}$
$N_{\rm H}/{\rm cm}^{-2}$	$10.61^{+1.44}_{-1.61}$	10.61^{t}	$9.73^{+1.53}_{-1.50}$	9.73^{t}
`CF`	$0.13^{+0.04}_{-0.05}$	0.67 ± 0.02	0.13 ± 0.05	0.67 ± 0.02
$\log({\rm Flux}_{2-10})$	-10.90^{c}	-10.59^{c}	-10.69^{c}	-11.10^{c}
Γ_h	$1.80^{+0.03}_{-0.04}$	1.80^{t}	1.79 ± 0.04	1.79^{t}
Γ_s	3.00^{f}	3.00^{f}	3.00^{f}	3.00^{f}
ratio	0.79^{f}	0.14^{f}	0.79^{f}	0.14^{f}
$\log \xi$	$2.35^{+0.07}_{-0.04}$	2.35^{t}	$2.35^{+0.07}_{-0.04}$	2.35^{t}
${\rm Norm}/10^{-8}$	$1.52^{+0.34}_{-0.32}$	1.52^{t}	1.56 ± 0.36	1.56^{t}
χ^2/ν	1063/1009	578/573	1059/1009	574/573
H_0	0.11	0.43	0.13	0.48

Table 6.3: Model parameters for a single disk wind grid fit to the mean 2014 and 2011 PG1211+143 spectra. $L_{2-10\,\rm keV}$ drastically decreases between 2014 and 2001, whereas the mass outflow rate is not as affected despite the changes in $L_{2-10\,\rm keV}$. Tied parameters are treated as free when calculating individual spectra statistics and $\rm H_0$ refers to the Null probability.
Key:
^{b}: hits upper bound of $L_{2-10\,\rm keV} = 7.5\%\ L_{\rm edd}$.
^{f}: parameter value is fixed.
^{c}: value is calculated from $L_{2-10\,\rm keV}$.
^{t}: value has been fixed between models.

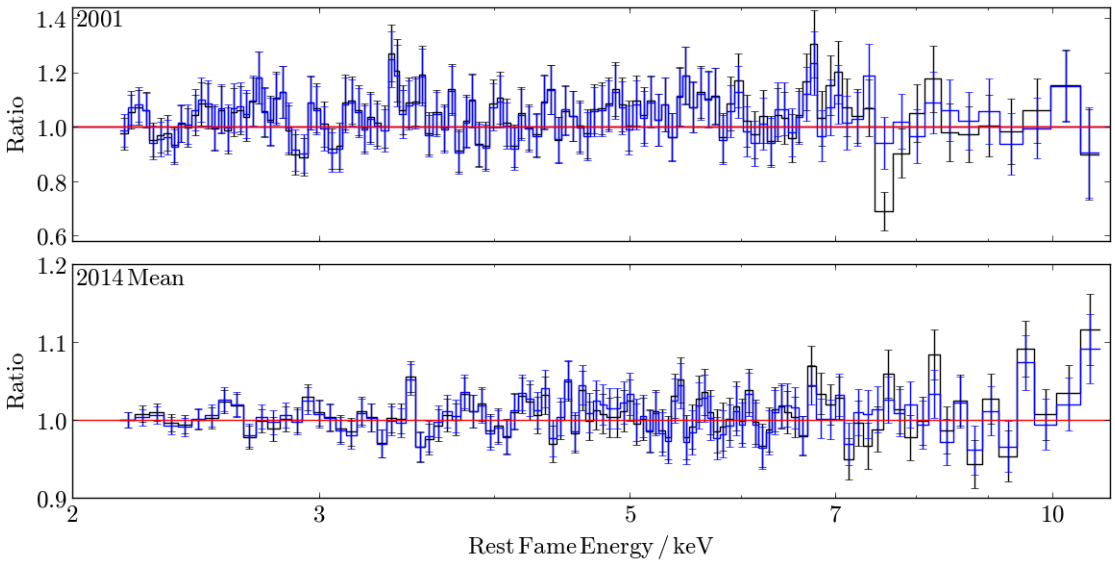

Figure 6.3: The ratio of the 2001 and mean 2014 spectra of PG1211 + 143 to the disk wind models; the black model is the constrained model whereas the blue is unconstrained. The most notable change is in the $\sim 7.8\,\mathrm{keV}$ feature.

there has been runaway competition between $L_{2-10\,\mathrm{keV}}$ and $\dot{M}$ whereby the mass outflow rate suppresses the observed flux requiring $L_{2-10\,\mathrm{keV}}$ to compensate. This produces inflated values for both $L_{2-10\,\mathrm{keV}}$ ($7.35^{b}_{-4.55}$; where ^{b} stands for the upper bound of the grid) and $\dot{M}$ ($1.99^{+0.69}_{-1.59}$) which are both poorly constrained.

Decoupling the observed flux and ionising luminosity (the unconstrained models) produces a fit of $\chi^2/\nu = 1600/1585$. The parameters can be seen in table 6.4. The decoupling allows $L_{2-10\,\mathrm{keV}}$ and $\dot{M}$ to assume more sensible values of $0.67^{+0.35}_{b}$ and $0.37^{+0.23}_{-0.11}$. Going from the constrained (observed flux and $L_{2-10\,\mathrm{keV}}$ linked) to unconstrained (observed flux and $L_{2-10\,\mathrm{keV}}$ decoupled)models for both the 2014 mean and 2001 data gives a significant improvement in the fit: $\Delta\chi^2/\Delta\nu = 26/1$ (for 2014 mean) and $\Delta\chi^2/\Delta\nu = 34/1$ (for 2001), both of which give a greater than 99.9% confidence.

The decomposition of the two grids can be seen in Fig. 6.4. The top panel shows

Parameter	2014 mean^C	2001^C	2014 mean	2001
$\dot{M}/\dot{M}_{\rm edd}$	$0.43^{+0.07}_{-0.06}$	$1.99^{+0.69}_{-1.59}$	$0.78^{+0.09}_{-0.10}$	$0.37^{+0.23}_{-0.11}$
% $L_{2-10\,\rm keV}/L_{\rm edd}$	$2.17^{+0.03}_{-0.19}$	$7.35^{b}_{-4.55}$	$4.72^{+0.53}_{-0.48}$	$0.67^{+0.35}_{b}$
$\rm f_{v1}$	0.50^{t}	1.00^{t}	0.50^{t}	1.00^{t}
$\rm f_{v2}$	1.00^{t}	2.00^{t}	1.00^{t}	2.00^{t}
μ	0.64 ± 0.01	$0.62^{+0.01}_{-0.04}$	$0.54^{+0.02}_{-0.03}$	$0.43^{+0.03}_{-0.02}$
$N_{\rm H}/{\rm cm}^{-2}$	$11.2^{+1.4}_{-1.5}$	11.2^{t}	10.3 ± 1.6	10.3^{t}
Covering Faction	$0.18^{+0.03}_{-0.05}$	$0.67^{+0.03}_{-0.05}$	0.07 ± 0.06	0.64 ± 0.02
$\log({\rm Flux}_{2-10})$	-11.11^{t}	-10.58^{t}	$-10.06^{+0.10}_{-0.13}$	$-10.72^{+0.23}_{-0.15}$
Γ_h	$1.84^{+0.04}_{-0.03}$	1.84^{t}	$1.75^{+0.05}_{-0.03}$	1.75^{t}
Γ_s	3.00^{t}	3.00^{t}	3.00^{t}	3.00^{t}
ratio	0.79^{f}	0.14^{f}	0.79^{f}	0.14^{f}
ξ	$2.34^{+0.06}_{-0.05}$	2.34^{t}	$2.34^{+0.08}_{-0.09}$	2.34^{t}
${\rm Norm}/10^{-8}$	$1.56^{+0.43}_{-0.29}$	1.56^{t}	$1.42^{+0.37}_{-0.38}$	1.42^{t}
χ^2/ν	1070/1009	591/574	1044/1008	557/573
$\rm H_0$	0.09	0.30	0.21	0.68

Table 6.4: The models of PG1211 + 143 with two disk wind grids. The ratio parameter is the ratio of the two power-law normalisations; this is found by fitting the model and allowing the normalisations to vary, the ratio is then fixed and a flux offset is applied so that the spectral shape is maintained. Here, $\rm H_0$ refers to the Null probability.
Key:
^{b}: the parameter hits the bound of the grid.
^{c}: the parameter is calculated based on another parameter.
^{C}: the model has the ionising luminosity ($L_{2-10\,\rm keV}$) constrained by the observed flux ${\rm Flux}_{2-10\,\rm keV}$.

the unfolded mean 2014 spectra with three models: the total (red), the "slow" grid (with $f_v = 0.5$) and the "fast" grid (with $f_v = 1$); below the unfolded spectra are the ratios of the data to the three models. The "slow" grid removes the strongest line ($\sim 7.5\,\mathrm{keV}$) whereas "fast" grid can be seen to remove the features at $\sim 8\,\mathrm{keV}$.

The required break in the $L_{2-10\,\mathrm{keV}}$-flux constraint means that the ionisation state of the wind is lower than would be expected for the observed flux. One way to understand this is that less flux than expected is incident on the wind. This could occur due to an absorber between the source and outflow structure. An alternative is that the wind becomes denser. To do this the wind's structure must change, reducing the volume of the outflow. This could be done by changing the ratio of $R_{\mathrm{in}}/R_{\mathrm{out}}$. Both of these scenarios are visualised in Fig. 6.5. Due to the long timescale (~ 13 years) of this change the overall change in the structure of the outflow cannot be ruled out. However, the lower ionisation lines seen in the RGS spectra would suggest that the wind is clumpy and variable, therefore the clumps are the preferred explanation.

Thus, although PDS 456 does not require an unconstrained model, a similar picture emerges across both PDS 456 and PG1211 + 143 whereby the winds have clumpy structures within them. In both objects the Fe K absorption represents the highest ionisation phase of the wind, with the lower ionisation matter being due to denser parts within the outflow. In PG1211 + 143 these dense clouds (the low ionisation absorber) appear to shield the higher ionisation part of the flow, whereas in PDS 456 this does not seem to be happening which is something that should be studied.

Finally, the point of modelling the disk wind is to calculate the kinetic power taking the simple approach that $L_{\mathrm{kin}}/L_{\mathrm{bol}} = 12$–$25\%$ for a v_{out} of 0.129c, however taking the same approach (as with PDS 456) produces $L_{\mathrm{kin}}/L_{\mathrm{bol}} = 20$–$38\%$ for $v_{\mathrm{out}} = 0.158 f_v$c. Once again, even the most conservative value is above the $L_{\mathrm{kin}}/L_{\mathrm{bol}} = 5\%$ threshold.

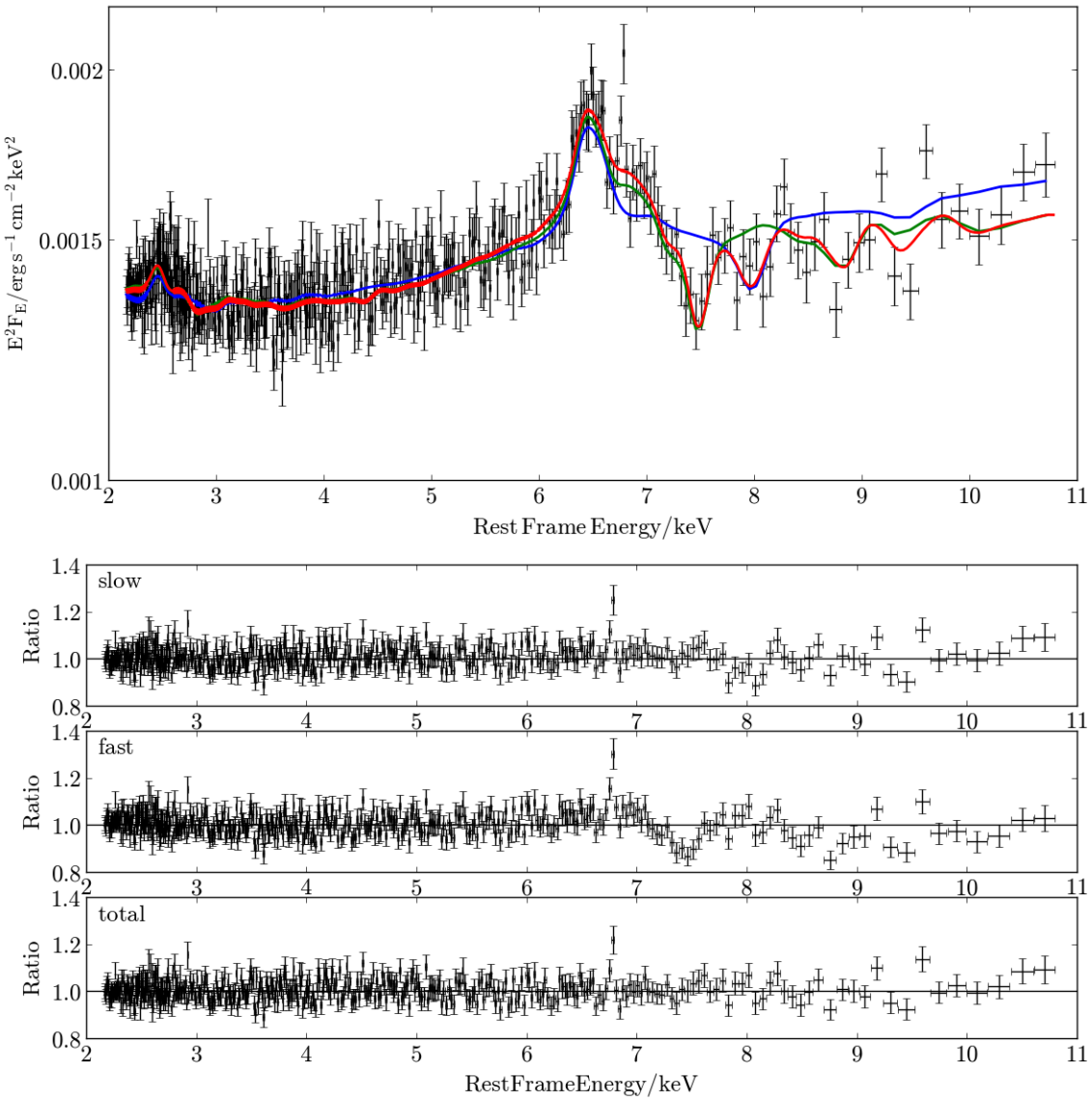

Figure 6.4: The top panel shows a decomposition of the "slow" ($f_v = 0.5$) and "fast" ($f_v = 1$) grids shown in green and blue respectively, with the total in red. Below are the ratios to each of the models. A comparison between "slow" and "fast" ratios in the three lower panels show the features in the spectra which the two grids fit; the strong $\sim 7.5\,\mathrm{keV}$ feature in the "fast" ratio being the most noticeable difference.

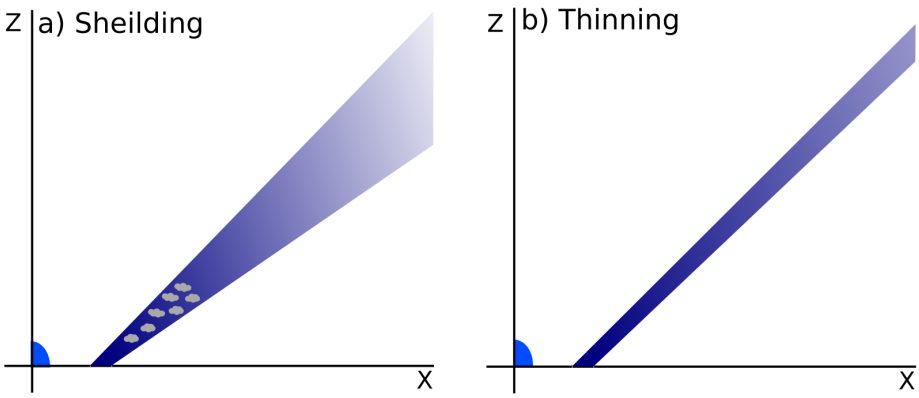

Figure 6.5: The proposed structure of the two scenarios for explaining the flux/ionisation deviation observed in fitting the 2001 spectrum. The "Shielding" scenario in panel a shows clumps within the flow that will reduce the flux seen within the wind. These clumps could be embedded within the flow as shown, or between the flow and the source (this is called shielding). Panel b shows the structural changes that could produce a change in density without a change in the mass outflow rate, which would also increase the scattering, lowering the observed flux and thus leading to the runaway scenario we encountered before.

6.2 1H 0707 − 495

1H 0707 − 495, as with other complex NLS1s, is characterised by rapid and high amplitude flux variability (which can be seen in Fig. 6.6), which also translates into spectral variability. Done & Jin (2016) found evidence that 1H 0707 − 495 is accreting at a super-Eddington rate. This led Hagino et al. (2016) to suggest that continuum driving could be the dominant driving mechanism for the outflow.

Above 2 keV at least, PDS 456 and 1H 0707 − 495 have remarkably similar spectra — as noted by Hagino et al. (2016). Due to a difference in their black hole masses the combination of 1H 0707 − 495 and PDS 456 allows the study of powerful outflows on different time scales. PDS 456 allows more temporal resolution, while 1H 0707 − 495 offers a comparatively much longer baseline.

Due to its variability 1H 0707 − 495 is well studied using both spectral and timing-based techniques. Despite this wealth of data there is much controversy about the nature of the variability, whether it is due to inner disk reflection (Fabian et al. 2004; Zoghbi et al. 2010; Kara et al. 2013, 2015; Dauser et al. 2012) or absorption (Gardner & Done 2015; Mizumoto et al. 2014). Kara et al. (2013) presented a study of the time lags observed in a dataset with 1.3 Ms exposure including observations from 2000 to 2010, attributing the lags to the light travel delay coming from reflection off the inner disk. Gardner & Done (2015), on the other hand, presented an absorption-based model where occulting clouds reproduce the variability observed in complex NLS1s in general. Both of these models produce both observable effects in the spectral and temporal domains — although Kara et al. (2013) are the only one to currently explain the energy dependence observed in the time lags.

However, inner disk lags are difficult to interpret in systems containing disk winds, as Compton scattering within the structure of the wind complicates the observed lags even in a smooth structure. As already seen with PDS 456 and PG1211 + 143, these winds do not seem to be a simple smooth flow and instead likely contain clumpy substructure which will further complicate the already complex lags. In the Gardner & Done (2015) model it is

variations in the clumps crossing the line of sight that are used to explain the lags.

In Kara et al. (2013) the X-ray emitting corona is required to be very small ($< 3\,R_{\rm g}$). However, Dovčiak & Done (2016) showed that, to explain the observed X-ray flux using inverse Compton scattering, the corona (sitting above the black hole, extended along the rotation axis) must be $> 20\,R_{\rm g}$ to intercept enough seed photons from the accretion disk. Also note that the observed flux will be reduced compared to the intrinsic luminosity due to suppression from the wind, meaning that the lower bound on the corona size is probably even larger.

Kara et al. (2015) presented a fit to three *NuSTAR* observations where they explain the sharp drop at 6–7 keV (observed) as seen in Fig. 6.7 as the blue wing of the emission from a broadened ionised reflector with an Fe abundance > 7.2 times the solar abundance. However, Hagino et al. (2016) studied 16 observations from 2000 to 2011 using the previously mentioned MONACO code, producing a fit which does not require strong gravitational effects or large over-abundance of iron ($\mathrm{A_{Fe.}} = 7$–20) as per the reflection models such as in Fabian et al. (2004, 2009, 2012); Zoghbi et al. (2010); Kara et al. (2013).

6.2.1 Observations

To better understand the nature of the wind variability in 1H 0707 − 495, a small sample of observations have been analysed. The first set of observations were the long *XMM-Newton* campaigns in 2008 and 2010, with a flux range of 3.7×10^{-13} to 1.9×10^{-12} erg s^{-1} cm^{-2}. When extracting the data products the regions used are circular with radii of 30″ for the source and 1′ for the background; throughout the *XMM-Newton*'s PN spectra will be used.

Due to 1H 0707 − 495's rapid variability (as seen in Fig. 6.6) it is not possible to extract spectra of individual flares. Therefore, the 2–10 keV light curves are used to produce three flux-bins with roughly equal exposure for each of the 2008 and 2010 campaigns; the separations can be seen in Fig. 6.6. For 2008, count rates of 0.06cts/s and 0.11cts/s are used. For 2010, count rates of 0.04cts/s and 0.08cts/s are used.

Obs	Obs ID	Start Date	Exposure/ks
2008A	0511580101	2008-01-29	124
2008B	0511580201	2008-01-31	124
2008C	0511580301	2008-02-02	123
2008D	0511580401	2008-02-04	122
2010A	0653510301	2010-09-13	117
2010B	0653510401	2010-09-15	128
2010C	0653510501	2010-09-17	128
2010D	0653510601	2010-09-19	129
2011	0554710801	2011-01-12	98
Obs 1^N	60001102002	2015-05-23	144
Obs 3^N	60001102006	2015-05-24	47

Table 6.5: The details of the observations used in this study of 1H 0707 − 495. ^{N}is used to denote observations using *NuSTAR* as opposed to *XMM-Newton* for the other observations.

In addition to the long campaigns another *XMM-Newton* observation was taken in 2011 which occurred in a low flux state ($F_{2-10\mathrm{keV}} = 2.8 \times 10^{-13}$ erg s^{-1} cm^{-2}); the same regions were used as with the higher flux states. Finally, the two higher flux ($F_{2-10\mathrm{keV}} = 7.5 \times 10^{-13}$ erg s^{-1} cm^{-2}) *NuSTAR* observations presented by Kara et al. (2015) are also used. The lower flux ($F_{2-10\mathrm{keV}} = 4.2 \times 10^{-13}$ erg s^{-1} cm^{-2}) *NuSTAR* observation did not have the S/N required to fit the absorption profile, so was not used. To extract the spectra, a source region of 40″ and background region of 1′.4 were fed into the NuSTARDAS software package. The spectra are then combined to get better S/N.

A representative sample of spectra can be seen in Fig. 6.7. The red and pink spectra represent the extremes of the 2008 and 2010 flux-binned spectra, along with the low state 2011 (in black) and averaged *NuSTAR* spectra (in blue). The change in spectral shape between the "high" and "low" flux states can clearly be seen when comparing the pink and black spectra between 2–4 keV.

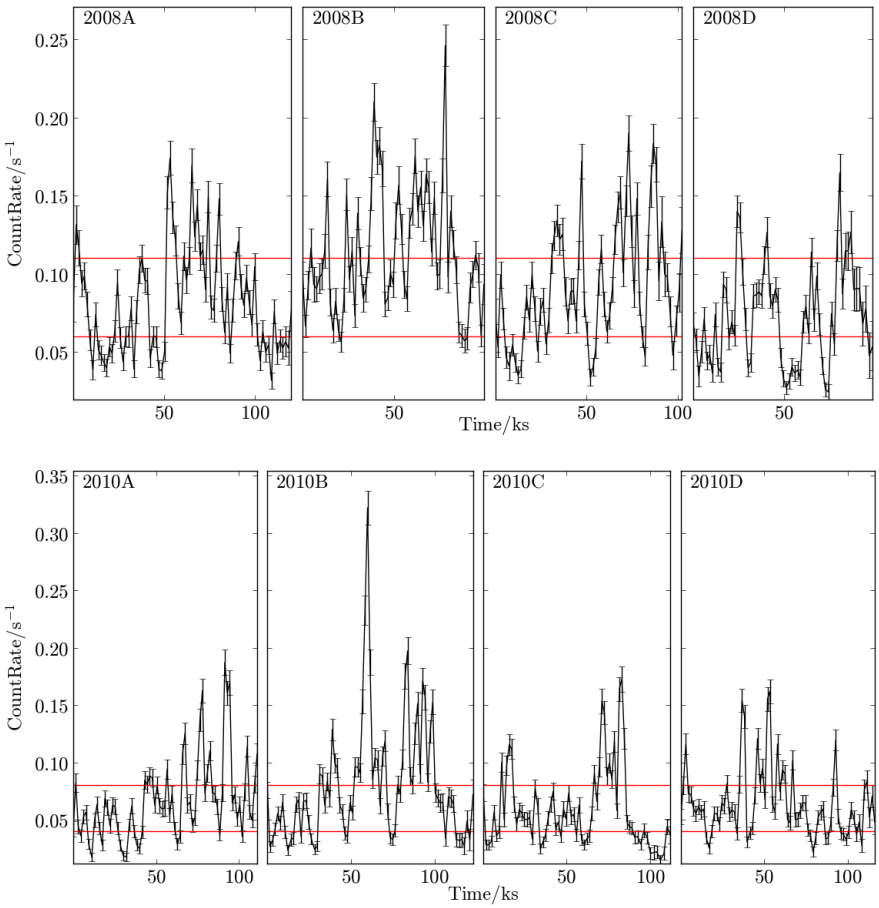

Figure 6.6: The light curves of 2008 and 2010 of 1H 0707 − 495 with the separations of 0.06cts/s and 0.11cts/s for 2008; for separating 2010 the count rates are 0.04cts/s and 0.08cts/s. Note the rapid variations do not allow isolation of individual flares.

6.2.1.1 Flux selected spectra in 2008 and 2010

The 2008 campaign has a generally higher count rate as seen in Fig. 6.6. In both the 2008 and 2010 datasets the Fe K absorption feature increases in strength as the flux decreases, while the Fe K emission feature appears to be strongest in the intermediate spectra. Fig. 6.8 shows the high, mid and low spectra for 2008 and 2010 campaign campaigns.

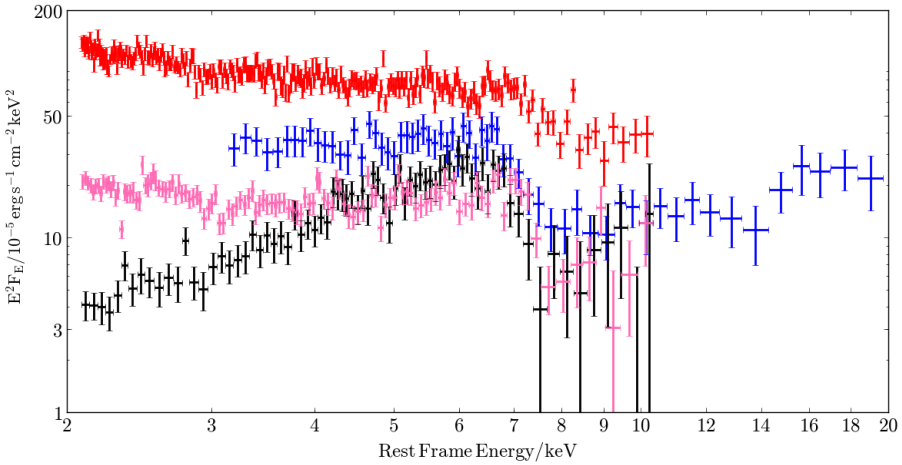

Figure 6.7: A representative sample of spectra of 1H 0707 − 495. The red and pink spectra represent the extremes of the 2008 and 2010 flux-binned spectra, along with the low state 2011 (black) and averaged *NuSTAR* (blue) spectra.

6.2.2 The model

The model used is a power law (`po`) continuum modified by a disk wind (`dw`) producing the phenomenological model of `po` ∗ `dw`. Above 2 keV these components appear to be sufficient for the high state above 2 keV, whereas a partial coverer is required to fit the hard spectra of the low state in 2011. There is no requirement for a distant reflector due to the lack of a narrow Fe K feature, as can be seen in Fig. 6.8. To fit the datasets, a disk wind grid is produced using parameters based on previous fits to 1H 0707 − 495. These parameters can be found in table 6.6. A particular value of interest in this model is $R_{\rm max} = 3\,R_{\rm min}$ as described previously in section 3.2.9 resulting in a broader profile than in the grid models for PDS 456 and PG1211 + 143. Once again to constrain the ionisation the observed flux is calculated from the $L_{2-10\,\rm keV}$ parameter.

6.2.3 2008 data

When fitting the 2008 data, initially only $L_{2-10\,\mathrm{keV}}$ is allowed to vary between observations. This produces a fit of $\chi^2/\nu = 1727/1707$; the parameters are presented in the top section

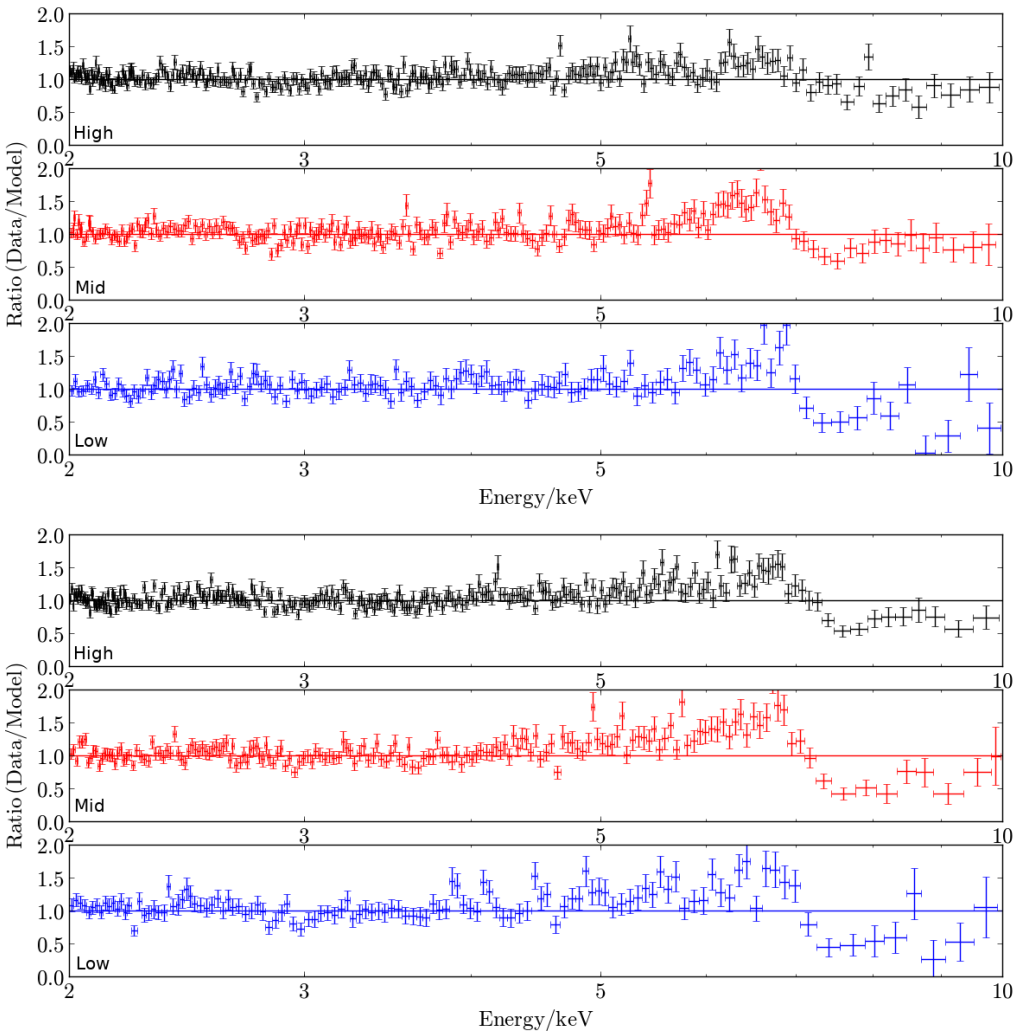

Figure 6.8: The flux-binned spectra of 1H 0707 − 495 used in this study compared to a power law with a variable photon index in the 2–10 keV band. The upper plot shows the 2008 spectra while the lower plot shows the 2010 spectra.

Parameter	Value
$M_{\rm BH}$	$2 \times 10^6\,M_\odot$
$\dot{M}_{\rm edd}$	$0.074\,M_\odot\ {\rm yr}^{-1}$
$L_{\rm edd}$	$2.5 \times 10^{44}\ {\rm erg\,s}^{-1}$
$\dot{M}$	0.145–11 $\dot{M}_{\rm edd}$
$L_{\rm bol}$	$\sim L_{\rm edd}$
$L_{2-10\,{\rm keV}}$	0.04–40% $L_{\rm edd}$
Γ	2.4
$R_{\rm min}$	$32\,R_{\rm g}$
$R_{\rm max}$	$3\,R_{\rm min}$
d	$R_{\rm min}$
$R_{\rm v}$	$R_{\rm max}$
f_v	0.5–1.25
μ	0.025–0.975

Table 6.6: The parameters used to produce the 1H 0707 − 495 disk wind model.

of table 6.7. As the model does not include partial covering higher energy X-rays are not required to determine Γ. The fit is improved ($\Delta\chi^2/\Delta\nu = 21/2$) when Γ is allowed to vary between observations. This is not surprising as the second component of the principal component analysis presented by Parker et al. (2015) matched a pivoting power law. The photon index seems to follow the high-soft/low-hard relation which is generally seen in AGN, varying from 2.61 ± 0.03 in the high flux spectra to $2.48^{+0.06}_{-0.05}$ in the low flux state spectra. The fit is further improved by allowing μ to vary ($\Delta\chi^2/\Delta\nu = 29/2$) producing a slight over-fit. As seen in table 6.7 this allows the Γ of mid flux spectra to move to a more intermediate value while the extremes also become more extreme producing a smoother transition. It also seems that the lower spectra were dominant in deciding the inclination of the wind, as it stays at $\mu = 0.48$ whereas μ for the mid and high flux spectra move to larger inclinations (lower μ) where scattering dominates. This is probably to allow for the stronger emission in those spectra as seen in Fig. 6.8.

$L_{2-10\,\mathrm{keV}}$ variable							
Level	$\dot{M}/\dot{M}_{\mathrm{edd}}$	% $L_{2-10\,\mathrm{keV}}/L_{\mathrm{edd}}$	f_v	μ	Γ	χ^2/ν	H_0
High	$0.92^{+0.04}_{-0.06}$	2.79 ± 0.03	$0.80^{+0.04}_{-0.03}$	$0.48^{+0.01}_{-0.03}$	$2.56^{+0.03}_{-0.02}$	706/665	0.13
Mid	0.92^{t}	1.61 ± 0.02	0.80^{t}	0.48^{t}	2.56^{t}	592/600	0.58
Low	0.92^{t}	$0.84^{+0.02}_{-0.01}$	0.80^{t}	0.48^{t}	2.56^{t}	429/434	0.56
$L_{2-10\,\mathrm{keV}}$ & Γ variable							
High	$0.92^{+0.04}_{-0.08}$	2.76 ± 0.04	$0.81^{+0.03}_{-0.04}$	0.48 ± 0.02	2.61 ± 0.03	698/665	0.18
Mid	0.92^{t}	1.64 ± 0.03	0.81^{t}	0.48^{t}	2.49 ± 0.04	588/600	0.63
Low	0.92^{t}	0.85 ± 0.02	0.81^{t}	0.48^{t}	$2.48^{+0.06}_{-0.05}$	420/434	0.68
$L_{2-10\,\mathrm{keV}}$, Γ & μ variable							
High	$0.71^{+0.08}_{-0.04}$	$2.74^{+0.04}_{-0.03}$	$0.86^{+0.07}_{-0.04}$	$0.32^{+0.02}_{-0.04}$	2.64 ± 0.03	686/665	0.28
Mid	0.71^{t}	1.63 ± 0.02	0.86^{t}	$0.31^{+0.11}_{-0.03}$	$2.55^{+0.05}_{-0.06}$	585/600	0.67
Low	0.71^{t}	0.86 ± 0.02	0.86^{t}	0.48 ± 0.04	$2.41^{+0.06}_{-0.05}$	406/434	0.83

Table 6.7: The models fitted to the 2008 campaign; all models have the observed flux linked to the $L_{2-10\,\mathrm{keV}}$. The value for χ^2/ν in individual spectra tied parameters are treated as free.
The total χ^2/ν are as follows:
$L_{2-10\,\mathrm{keV}}$ variable (χ^2/ν): 1727/1707
$L_{2-10\,\mathrm{keV}}$ & Γ variable (χ^2/ν): 1706/1705
$L_{2-10\,\mathrm{keV}}$, Γ & μ variable (χ^2/ν): 1677/1703

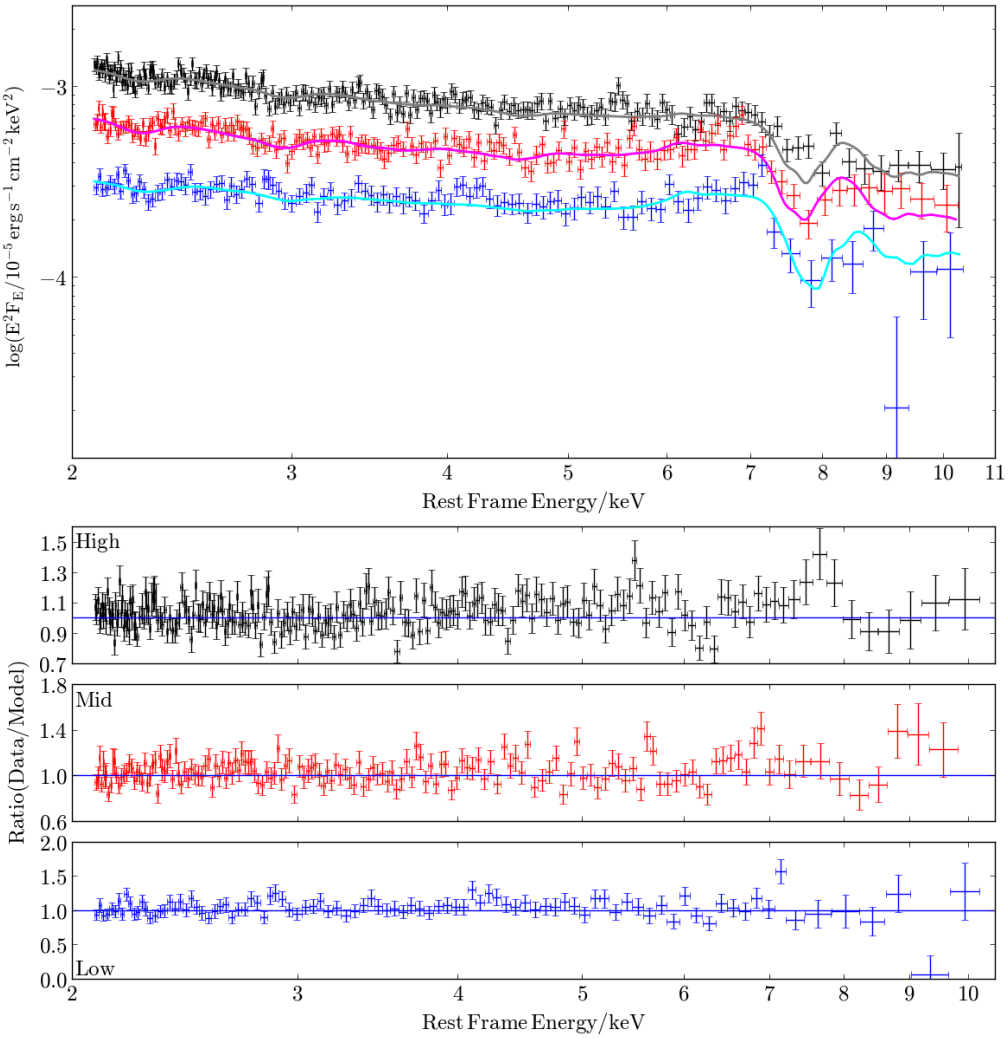

Figure 6.9: The unfolded flux-binned spectra of the 2008 1H 0707 − 495 campaign and best-fit (the variable $L_{2-10\,\mathrm{keV}}, \Gamma$ & μ) models along with the ratios to the aforementioned best-fit model. The model for the high flux spectra (seen in black) appears to over-predict the absorption whereas the other two spectra seem to be reasonably well fit.

6.2.4 2010 data

Once again only $L_{2-10\,\mathrm{keV}}$ was allowed to vary between observations. This yields $\chi^2/\nu = 1640/1530$; the parameters can be seen in table 6.8. Compared to the 2008 campaign f_v is

larger ($1.10^{+0.04}_{-0.03}$) while μ is lower at $0.37^{+0.01}_{-0.03}$. The interplay between these seems to make the observed absorption feature broader with a similar centroid energy to the 2008 spectra. Varying Γ improves the fit ($\Delta\chi^2/\Delta\nu = 39/2$) and a further increase can be found by varying $\dot{M}$, producing a fit of $\chi^2/\nu = 1567/1526$ ($\Delta\chi^2/\Delta\nu = 34/2$). This produces the trend in Γ seen when fitting the 2008 spectra, however, when comparing the similar slices from the aforementioned spectra the photon index is generally softer despite the flux being lower as seen in the count rate in the light curves.

$L_{2-10\,\mathrm{keV}}$ variable							
Level	$\dot{M}/\dot{M}_{\mathrm{edd}}$	% $L_{2-10\,\mathrm{keV}}/L_{\mathrm{edd}}$	f_v	μ	Γ	χ^2/ν	H_0
High	$0.79^{+0.05}_{-0.06}$	2.36 ± 0.03	$1.10^{+0.04}_{-0.03}$	$0.37^{+0.01}_{-0.03}$	$2.61^{+0.03}_{-0.02}$	686/652	0.17
Mid	0.79^{t}	1.10 ± 0.02	1.10^{t}	0.37^{t}	2.61^{t}	572/506	0.02
Low	0.79^{t}	0.55 ± 0.01	1.10^{t}	0.37^{t}	2.61^{t}	382/364	0.24
$L_{2-10\,\mathrm{keV}}$ & Γ variable							
High	$0.78^{+0.04}_{-0.07}$	2.33 ± 0.03	$1.11^{+0.04}_{-0.03}$	$0.37^{+0.01}_{-0.03}$	2.66 ± 0.03	679/652	0.22
Mid	0.78^{t}	1.14 ± 0.02	1.11^{t}	0.37^{t}	$2.48^{+0.04}_{-0.05}$	544/506	0.12
Low	0.78^{t}	0.54 ± 0.01	1.11^{t}	0.37^{t}	2.67 ± 0.08	377/364	0.30
$L_{2-10\,\mathrm{keV}}, \Gamma$ & $\dot{M}$ variable							
High	$1.03^{+0.13}_{-0.15}$	2.33 ± 0.03	$1.10^{+0.05}_{-0.03}$	$0.37^{+0.01}_{-0.03}$	2.70 ± 0.04	670/652	0.31
Mid	$0.81^{+0.08}_{-0.07}$	1.14 ± 0.02	1.10^{t}	0.37^{t}	2.49 ± 0.05	544/506	0.12
Low	$0.56^{+0.08}_{-0.09}$	0.54 ± 0.01	1.10^{t}	0.37^{t}	2.45 ± 0.09	364/364	0.49

Table 6.8: The models fitted to the 2010 campaign; all models have the observed flux linked to $L_{2-10\,\mathrm{keV}}$. When calculating the value for χ^2/ν in individual spectra tied parameters are treated as free.
The total χ^2/ν are as follows:
$L_{2-10\,\mathrm{keV}}$ variable (χ^2/ν): 1640/1530
$L_{2-10\,\mathrm{keV}}$ & Γ variable (χ^2/ν): 1601/1528
$L_{2-10\,\mathrm{keV}}, \Gamma$ & $\dot{M}$ variable (χ^2/ν): 1569/1526

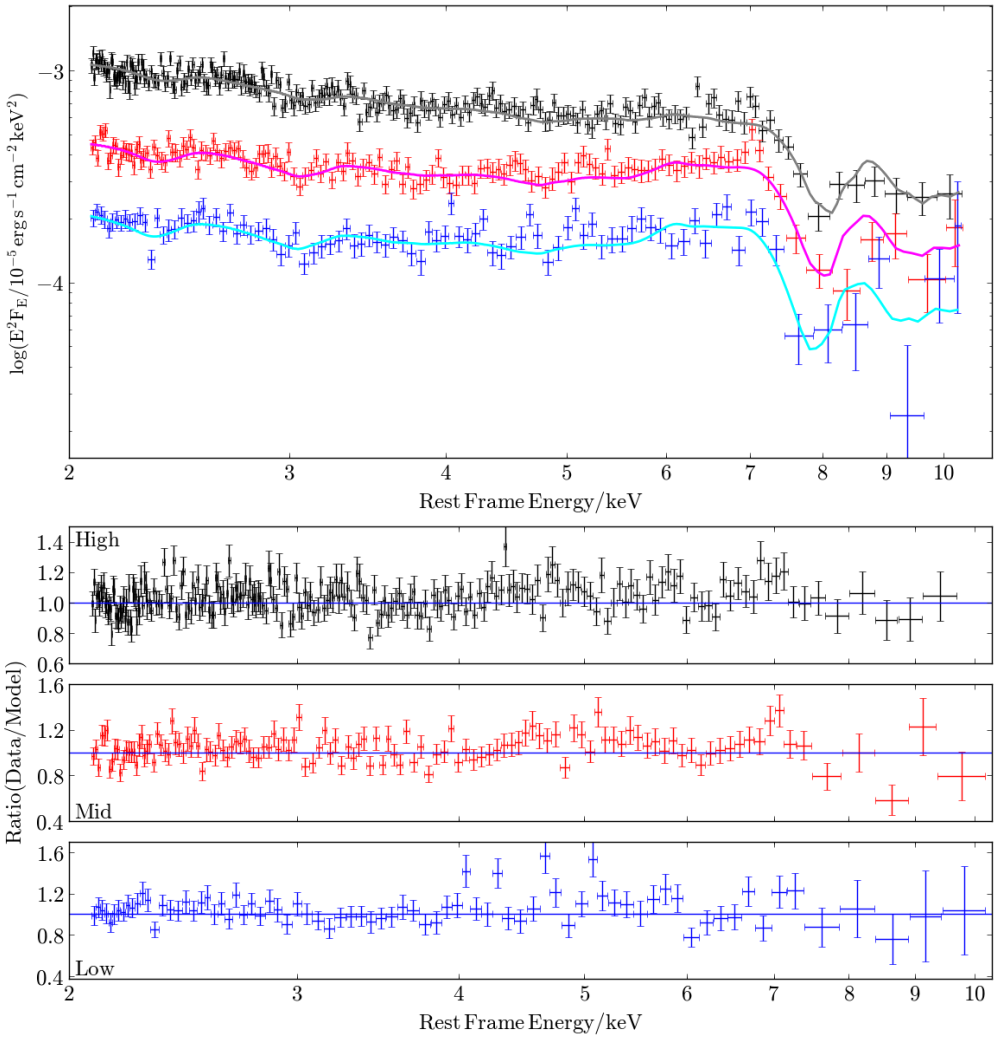

Figure 6.10: The unfolded spectra and the $L_{2-10\,\mathrm{keV}}, \Gamma$ & $\dot{M}$ model. The high and low flux spectra are well fit, however the mid flux spectrum shows residuals between 4 and 7 keV.

Fig 6.10 shows the unfolded spectra and the $L_{2-10\,\mathrm{keV}}, \Gamma$ & $\dot{M}$ model along with ratios to the model. The high flux spectrum shows a strong absorption feature (unlike the high flux spectra in 2008). The mid flux spectrum still shows features between 4 and 7 keV and the absorption feature appears skewed (as seen in the unfolded spectra). The low flux spectra

are well fit, as in 2008.

6.2.5 2011 and *NuSTAR* data

The analysis extends to the observation in 2011 (which is in the low state) and the high state *NuSTAR* observations. Both of these offer interesting insights into the variability of the disk wind in 1H 0707 − 495. Both datasets require slight variations on the initial `po` ∗ `dw` model.

First the low state is fit by adding a neutral partial coverer to the previous model resulting in a model of:

$$\texttt{pc} * \texttt{po} * \texttt{dw}. \tag{6.2}$$

When fitting the model to the 2011 data a partial cover is required and as there is no contemporaneous higher-energy data the photon index is fixed to 2.5. The disk wind parameters $\dot{M}$, $L_{2-10\,\mathrm{keV}}$, μ and f_v are all variable producing a fit of $\chi^2/\nu = 156/151$; the parameters can be seen in table 6.9 (the Constrained column). However, as observed in PG1211 + 143, $\dot{M}$ and $L_{2-10\,\mathrm{keV}}$ have adopted unrealistic values of $6.31^{+0.41}_{-2.20}\,\dot{M}_{\mathrm{edd}}$ and $39.70^{b}_{-7.44}\%\,L_{\mathrm{edd}}$ respectively. While it is an extreme object these values are not reasonable even for 1H 0707 − 495. Therefore the observed flux is allowed to vary free from $L_{2-10\,\mathrm{keV}}$. This unconstrained model yields $\chi^2/\nu = 135/150$, with the model parameters more in line with expected values of $\dot{M}/\dot{M}_{\mathrm{edd}} \leq 0.82$ and $L_{2-10\,\mathrm{keV}}/L_{\mathrm{edd}} = 1.85^{+0.68}_{-1.25}$ which – while still not well constrained – are at least feasible. The f_v increases in the unconstrained model; this is likely driven by the breadth of the profile which can be seen in Fig. 6.11 – which shows the unfolded spectra, constrained (red) and unconstrained (blue) models, along with the ratios to the models. It can be seen in the residuals between 7–9 keV, that the unconstrained fit better represents the absorption feature.

Finally, the *NuSTAR* observations presented by Kara et al. (2015) are modelled. Like Kara et al. (2015), the 1$^{\mathrm{st}}$ and 3$^{\mathrm{rd}}$ spectra are combined so that the data were high enough in quality that a feature could be fit. A model of `constant` ∗ `po` ∗ `dw` is used. The constant is a multiplicative factor to account for cross-calibration between the two detectors.

Model	Constrained	Unconstrained
$\dot{M}/\dot{M}_{\rm edd}$	$6.31^{+0.41}_{-2.20}$	< 0.82
% $L_{2-10\,\rm keV}/L_{\rm edd}$	$39.70^{b}_{-7.44}$	$1.85^{+0.68}_{-1.25}$
$\rm f_{\it v}$	$0.61^{+0.16}_{-0.09}$	$0.81^{b}_{-0.17}$
μ	$0.35^{+0.04}_{-0.05}$	$0.36^{+0.07}_{-0.06}$
$N_{\rm H}/10^{-22}{\rm cm}^{-2}$	$13.77^{+2.84}_{-2.24}$	$13.48^{+2.35}_{-2.29}$
Covering Fraction	0.89 ± 0.02	0.89 ± 0.02
Γ	2.50^{f}	2.50^{f}
$\log(F/\,{\rm erg\,s^{-1}\,cm^{-2}}\,)$	-10.56^{c}	-11.29 ± 0.27
χ^2/ν	156/151	135/150
$\rm H_0$	0.37	0.80

Table 6.9: The constrained and unconstrained models for the 2011 1H 0707 − 495 spectra. It is clear that the breaking of the constraint between $L_{2-10\,\rm keV}$ and the Flux shows a large reduction in $\dot{M}$ and $L_{2-10\,\rm keV}$. Here, $\rm H_0$ refers to the Null probability.
Key:
^{b}: hits upper bound of $40\%L_{\rm edd}$.
^{f}: parameter value is fixed.
^{c}: value is calculated.

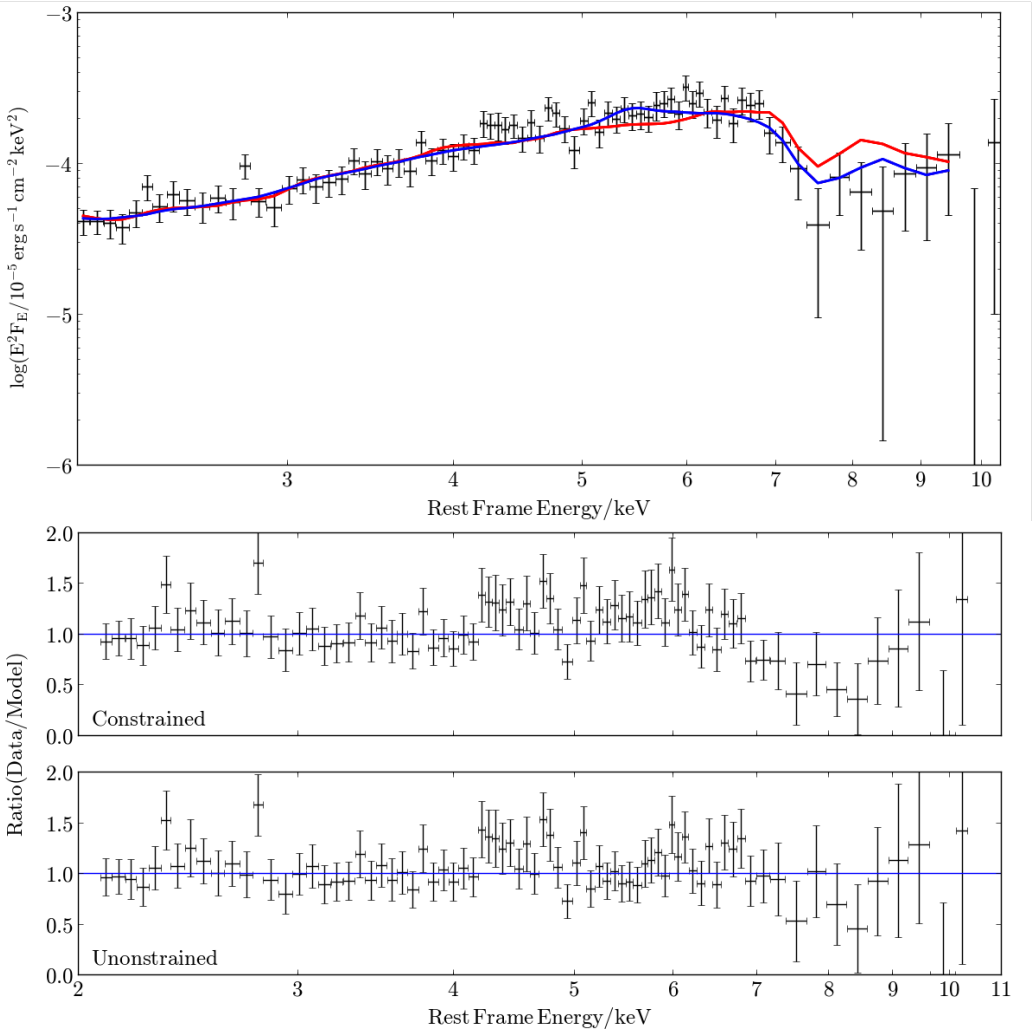

Figure 6.11: The unfolded data and best-fit models for low state 2011 along with the ratios to each model. The ratio of the constrained model clearly shows residuals between ~ 7 and 9 keV with the increase in depth between the two models (with constrained in red and unconstrained in blue) in the unfolded (upper) plot.

Once again, as an initial fit the $L_{2-10\,\mathrm{keV}}$ is used to combine the flux, while the other disk wind parameters are allowed to vary. This produces $\chi^2/\nu = 172/120$; the parameters are presented in table 6.10. However, as in the 2011 fit, the values of $\dot{M}$ and $L_{2-10\,\mathrm{keV}}$ become

Model	Constrained	Unconstrained
$\dot{M}/\dot{M}_{\rm edd}$	$9.03^{+0.50}_{-0.89}$	$0.27^{+0.11}_{-0.03}$
% $L_{2-10\,\rm keV}/L_{\rm edd}$	$39.79^{b}_{-3.44}$	$0.21^{+0.21}_{-0.04}$
$\rm f_v$	$0.61^{+0.08}_{-0.06}$	$1.25^{b}_{-0.12}$
μ	$0.41^{+0.02}_{-0.01}$	$0.29^{+0.03}_{-0.04}$
Γ	$2.61^{+0.09}_{-0.10}$	2.69 ± 0.10
$\log(F/\,\rm erg\,s^{-1}\,cm^{-2}\,)$	-10.56^{c}	$-11.50^{+0.06}_{-0.09}$
FPMB offset^{a}	$1.10^{+0.08}_{-0.07}$	1.09 ± 0.07
χ^2/ν	172/120	129/119
$\rm H_0$	0.14	0.25

Table 6.10: The constrained and unconstrained models for the *NuSTAR* dataset. The parameters such as $\dot{M}$ and $L_{2-10\,\rm keV}$ decrease to more sensible values in the unconstrained models. An interplay between f_v and μ also broadens the profile. $\rm H_0$ refers to the Null probability.
Key:
^{b}: hits upper bound of $L_{2-10\,\rm keV} = 40\%\,L_{\rm edd}$.
^{f}: parameter value is fixed.
^{c}: value is calculated.
^{a}: the multiplicative offset between the *NuSTAR* detectors.

extreme: $\dot{M} = 9.03^{+0.50}_{-0.89}\,\dot{M}_{\rm edd}$ and $L_{2-10\,\rm keV} = 39.79^{b}_{-3.44}\,L_{\rm edd}$ (where ^{b} is the upper bound of the grid). Therefore, the flux is allowed to vary freely, producing a large improvement to the fit: $\Delta\chi^2/\Delta\nu = 43/1$. The values of $L_{2-10\,\rm keV}$ and $\dot{M}$ reduce to more reasonable values: $\dot{M}$ $= 0.27^{+0.11}_{-0.03}\,\dot{M}_{\rm edd}$ and $L_{2-10\,\rm keV} = 0.21^{+0.21}_{-0.04}\%\,L_{\rm edd}$. The breadth of the feature in the *NuSTAR* spectra may be driving the f_v to larger values, which forces μ to larger inclinations to reduce the observed velocity so that the feature remains in the correct part of the spectrum. This could reduce the measured $\dot{M}$, though a larger $R_{\rm max}/R_{\rm min}$ ratio could alleviate this. However, the current database of atomic transitions does not currently extend to low enough ionisation states to make this accurate. The improvement between the constrained (red) and unconstrained (blue) models can be seen in Fig. 6.12 which shows the unfolded spectra, models and the ratios between them.

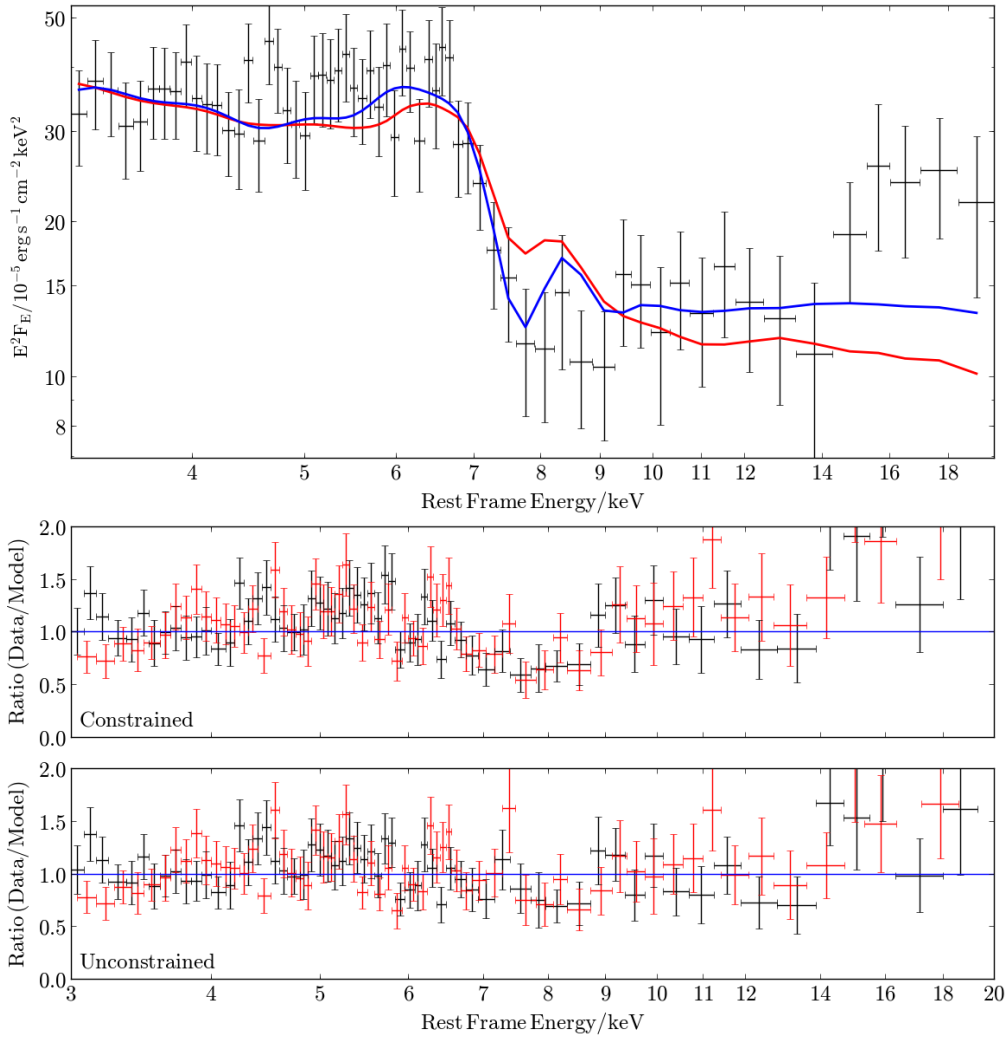

Figure 6.12: The unfolded data of the *NuSTAR* data and best-fit model. The average of the FPMA and FPMB detectors is used for plotting purposes only. In the ratios both are shown, FPMA in black and FPMB in red.
The ratio to the constrained model clearly shows residuals between 7 and 9 keV which is corrected in the ratio to the unconstrained model. As with 2011 spectra, the increase in depth between the two models (with constrained in red and unconstrained in blue) can be seen in the unfolded (upper) plot.

6.2.6 Conclusions

In conclusion, 1H 0707 − 495 requires a broad wind ($R_{\rm min}/R_{\rm max} = 3$; maybe even higher, suggesting continuum driving), meaning its mass outflow rate must be high given its column density. Using the mass outflow rates found in the modelling $L_{\rm kin}/L_{\rm bol} = 10$–$35\%$ assuming an outflow rate of 0.2c. Assuming the disk wind geometry used is reasonable the more realistic velocity $v_{\rm out} = 0.177 f_v$c (where $[v(R_{\rm min}) + v(R_{\rm max})]/2 = 0.177$c) is attained, which in turn produces $L_{\rm kin}/L_{\rm bol} = 5$–$33\%$. Even in the conservative case the theoretical threshold of 5% is exceeded.

In the 2008 and 2010 high state observations the flux selected spectra show variations in both $L_{2-10\,\rm keV}$ and Γ, with a loose correlation between the two (with softer spectra being higher in flux). The 2008 and 2010 campaigns also show variation in the observed column through μ or $\dot{M}$. In 2010 flux selected spectra $\dot{M}$ shows a correlation with flux; this is to be expected if the wind is radiatively driven. Future work should attempt to fit more flux states to see if this can be quantified. However when comparing high flux spectra of the 2008 and the 2010 datasets, the absorption feature is clearly different. This suggests that the wind is not correlated just with flux on longer time scales.

The photon index varies between $2.41^{+0.06}_{-0.05}$–2.65 ± 0.03 for 2008 and 2.45 ± 0.09–2.70 ± 0.04 for 2010. A variable photon index is to be expected as it appears in the principal components of Parker et al. (2015) for 1H 0707 − 495. The change in photon index would correspond to a change in energy of the coronal electrons of $\Delta k_b T_e \sim 31\,\rm keV$ assuming the corona's optical depth is $\tau_e = 0.44$ (Wilkins & Gallo 2015). This could easily be achieved by the difference in $L_{2-10\,\rm keV} \sim 1\%\, L_{\rm edd}$ seen in the model parameters even in the short time of the observed flares.

In both the high flux *NuSTAR* and the low flux 2011 *XMM-Newton* spectra fits require the breaking of the $L_{2-10\,\rm keV}$ flux constraint. The interpretation would be the two same scenarios as in PG1211 + 143: a change in the volume of the wind or a change in shielding/clumping. Once again neither can be ruled out. However, as PDS 456 and

PG1211 + 143 show evidence for clumpy winds and clumps can be used to match the timing properties observed in 1H 0707 − 495 (Gardner & Done 2015), the clumpy scenario is preferred.

7 Conclusions and future work

7.1 Conclusions

The mass of the black holes powering AGN ($M_{\rm BH} = 10^6$–$10^9\,M_\odot$) is known to correlate with some parameters of their host galaxies (such as $M_{\rm bulge}$, $L_{\rm bulge}$ and σ_*). This implies a co-evolution between the two. However, the black hole's gravitational sphere of influence is far too small to cause these correlations directly. Therefore, a feedback mechanism is required to link these size scales. The discovery of extremely energetic outflows from the black holes powering luminous quasars (Pounds et al. 2003; Reeves et al. 2003; Chartas et al. 2002) provides a possible source of feedback. The possible energy output of these winds could exceed the binding energy of their host's bulge by several orders of magnitude (King & Pounds 2003). They are also quite common, being observed in 35–40% of AGN (Tombesi et al. 2010; Gofford et al. 2013). These winds could provide the mechanical feedback that controls both the formation of stellar bulges and simultaneously regulates black hole's growth. Some form of feedback is also required in simulations of galaxy formation as galaxies without feedback become much larger than observed (Bower et al. 2006). This suggests that all galaxies were active at some point in the past.

In section 1.4.1 it was shown that the disk wind in PDS 456 (using conservative values presented in Nardini et al. 2015) has an energy output which is more than an order of magnitude larger than the binding energy of the host galaxy's bulge. Tombesi et al. (2011) and Gofford et al. (2015) calculated $L_{\rm kin}$ for their respective samples. Gofford et al. (2015) found that 85% of AGN in the sample exceeded $L_{\rm kin}/L_{\rm bol}$ of 0.5% (Hopkins & Elvis 2010) and 45% exceed$L_{\rm kin}/L_{\rm bol} = 5\%$ (Di Matteo et al. 2005), where 0.5% and 5% are theoretically predicted thresholds for unbinding the host bulge. However, a limit of the modelling in these studies is the use of ad hoc absorption models for the outflow. Many features, such as the breadth, outflow velocity and ionisation are not linked to physical properties of the outflow

and therefore are not constrained by one another. Furthermore, the wind's emission was not calculated self-consistently, hence the scattering and line emission from the wind is poorly constrained. This will have the effect of possibly under-predicting the amount of absorption. These issues can be improved upon by using a disk wind model; a sample has been selected for future work (see section 7.2.1). This sample would provide better quality measurements for the correlations seen in Gofford et al. (2015) (such as $v_{\rm out}$ vs $L_{2-10\,\rm keV}/L_{\rm edd}$ or $\dot{M}/\dot{M}_{\rm edd}$ vs $L_{2-10\,\rm keV}/L_{\rm edd}$), allowing for a better understanding of the scaling relations of outflows.

Before applying the disk wind model to the sample, the model's behaviour must be tested with respect to the large variance in observed absorption features exhibited by some prototypical outflows. On this basis, three objects (PDS 456, PG1211 + 143 and 1H 0707 − 495) known to host powerful and variable outflows were selected; in addition, these objects cover almost the full range of black hole masses observed in AGN.

The first object, PDS 456, is an AGN which closely resembles objects from the quasar epoch ($z = 2$–3). PDS 456 appears to have two main spectral states: high and low flux, which are characterised by soft and hard X-ray spectra respectively. A transition between these two states was observed in *Suzaku* data. In 2007, PDS 456 was caught in the high-flux state. In 2013 PDS 456 transitioned to the lowest flux and hardest spectra observed to date — with the 2011 spectra being in an intermediate state. By fitting all the spectra it was seen that an increase in absorption causes the observed transition, by adding continuum curvature (by removing soft flux from the spectra) and increasing the depths of the absorption feature at Fe K. This is seen when modelling with either a simplistic model of neutral partial covering with Gaussian emission/absorption lines (equation 4.1), or with more complex models of photon-ionised gas in both emission and absorption (equation 4.2). Matzeu et al. (2016) found that in the 2013 observations the partial covering absorbers were outflowing with a velocity comparable to the wind. This is also seen in chapter 4, when extending to the *Suzaku* 2007 and 2011 observations which increases the range in observed outflow velocity.

The same phenomenological model (equation 4.3) is found to be an adequate explanation for the spectra of the subsequent *XMM-Newton–NuSTAR* campaign. However, the continuum

variability requires a change in photon index which was not allowed when fitting the *Suzaku* data due to the lack of high-energy data. This model is also comparable to that of Nardini et al. (2015). Overall, PDS 456 displays two modes of variability. In the high state changes are dominated by the intrinsic continuum, whereas the transition to the low flux state is dominated by an increase in obscuration.

The Sim et al. (2010) disk wind model (as presented in chapter 3) was applied to the PDS 456 data in chapter 5. Linking $L_{2-10\,\mathrm{keV}}$ to the observed flux produces a strong constraint on the ionising luminosity and, therefore, the mass outflow rate (as they are degenerate to some degree). When fitting the *Suzaku* dataset similar trends to the phenomenological model are seen in the disk wind parameters where the $L_{2-10\,\mathrm{keV}}$ alone could not describe the change in the disk wind. The changes in the absorption feature require an increase in the mass outflow rate ($\dot{M}$) between each observation (excluding 2013a), along with a velocity modifier (in the form of f_v or μ). On the other hand in the high flux state datasets of *XMM-Newton–NuSTAR* and archival *XMM-Newton* the $L_{2-10\,\mathrm{keV}}$ parameter (along with the photon index in the *XMM-Newton–NuSTAR* campaign) is found to be capable of explaining the variability in the observed line profile. Therefore the transition to the low state is not a more extreme version of the normal intrinsic variability but is instead an absorption event.

The correlation between v_{out} and $L_{2-10\,\mathrm{keV}}$, observed in Matzeu et al. (2017), is replicated when comparing $L_{2-10\,\mathrm{keV}}$ and f_v parameters of the disk wind model obtained when fitting all of the PDS 456 spectra simultaneously. The measured correlation of $f_v \propto {L_{2-10\,\mathrm{keV}}}^{0.17\pm0.06}$ is flatter than the expected value of $f_v \propto L_x^{0.25}$ for a radiatively driven flow which is modulated by ionisation, but is consistent within the 2σ confidence interval. This correlation suggests that the $L_{2-10\,\mathrm{keV}}$ flux is accelerating the outflow. This requires the wind to be Compton thick, as the $L_{2-10\,\mathrm{keV}}$ luminosity is substantially sub-Eddington. As the wind is not directly observed to be Compton thick, it must be out of the line of sight. One thing this correlation does rule out is a purely magnetically driven outflow, as the expected dependence of velocity on $L_{2-10\,\mathrm{keV}}$ in that case is predicted to be $f_v \propto L_x^{-0.25}$. However, this does not prevent magnetic fields playing a critical role in the launching mechanism of the wind, as suggested

by Matzeu et al. (2016). Combining these two arguments shows that, at least in PDS 456, the outflow could be launched by magnetic fields and then radiation pressure could help accelerate the outflow up to terminal velocity.

All of the objects studied here have powerful winds. This can be seen when calculating their $L_{\rm kin}/L_{\rm bol}$. As explained before $L_{\rm kin}/L_{\rm bol}$ is a useful measure when trying to understand how an outflow will affect its host galaxy. In PDS 456 taking a conservative outflow velocity of $v_{\rm out} = 0.25$c produces $L_{\rm kin}/L_{\rm bol} = 5$–$10\%$, which is slightly lower than the $L_{\rm kin}/L_{\rm bol} \sim 15\%$ measured by Nardini et al. (2015). However, the value measured is an underestimate by definition (because $v_{\rm out,obs} \leq v_{\rm out,wind}$). The disk wind model provides a better estimate (assuming the geometry is realistic), by taking the launch velocity of $[v_{\rm launch}(R_{\rm max}) + v_{\rm launch}(R_{\rm min})]/2$ and multiplying it by f_v ($v_{\rm out} = 0.225 f_v$c), producing $L_{\rm kin}/L_{\rm bol} = 8$–$27\%$. For PG1211 + 143, $L_{\rm kin}/L_{\rm bol} = 12$–$25\%$ using the reported $v_{\rm out}$ of 0.129c (Pounds et al. 2016a). Once again assuming the geometry is correct, an outflow velocity of $v_{\rm out} = 0.158 f_v$c can be estimated, yielding $L_{\rm kin}/L_{\rm bol} = 20$–$38\%$. Finally, using the same method for 1H 0707 − 495 we find $L_{\rm kin}/L_{\rm bol} = 10$–$35\%$ for $v_{\rm out} = 0.2$c (as per Hagino et al. 2016) and $L_{\rm kin}/L_{\rm bol} = 5$–$33\%$ when using $v_{\rm out} = 0.177 f_v$c. Therefore, even the lowest estimates are equal to or exceed the more conservative $L_{\rm kin}/L_{\rm bol} = 5\%$ (Di Matteo et al. 2005) in all these objects and in some cases the kinetic power could exceed that value by a factor six. This results in a large amount of energy/momentum to be deposited into the host's bulges even over conservative duty cycles.

During the fitting of both PG1211 + 143 and 1H 0707 − 495 it was found that linking the intrinsic $L_{2-10\,\rm keV}$ and the observed flux caused $L_{2-10\,\rm keV}$ and $\dot{M}$ to compete with each other, in an attempt to find a better fit to the absorption feature. This leads to inflated values in both parameters. Thus breaking this constraint allows the $L_{2-10\,\rm keV}$ and $\dot{M}$ parameters to adopt more sensible values. This effectively means that the ionisation of the outflow is lower than expected for $L_{2-10\,\rm keV}$. Hence one of two scenarios is required: a change in volume or a decrease in the flux incident on the wind — likely via clouds, in the intervening space or embedded within the wind. The Sim et al. (2010) model assumes a smooth flow, therefore it

does not take into account any clumps embedded within the wind, which is perceived in all of these objects. These clumps affect the ionisation state of the wind. Therefore, if not accounted for the measured $\dot{M}$ will be less accurate. Furthermore, the clumps will boost the mass outflow rate themselves (depending on their filling factor), producing a larger value of $L_{\rm kin}$. Further work is required to address this issue if the energy output from winds is to be quantified.

There are two main shortcomings in this work which should be addressed in future work. The first is the small number of objects studied. This limits the conclusions which can be drawn on the overall population of AGN winds. Secondly, although the assumption of a smooth flow is convenient when modelling the disk wind, there is observational evidence that the wind is inhomogeneous.

7.2 Future work

7.2.1 Extending the modelling to the wider archive

Nardini et al. (2015) showed the presence of a fast ($v_{\rm out} \sim 0.3$c), wide-angle ($\Omega \geq 2\pi$) accretion disk wind in the luminous quasar PDS 456, through the detection of a broad P-Cygni profile in X-rays at iron K. With a kinetic luminosity of 10^{46} erg s^{-1} the disk wind will impart a significant feedback on larger scales. Such outflows almost certainly play a fundamental role in galaxy evolution, therefore the quantification of this phenomenon is essential for understanding the development of galaxies over cosmic time. Tombesi et al. (2015) and Feruglio et al. (2015) showed a link between some small scale outflows (seen in the X-rays) and large (kpc) scale molecular outflows. Thus the fast accretion disk winds may be the initial stage of the process that eventually leads to the molecular mass losses of hundreds to thousands $M_{\odot}$ yr^{-1} on the scales of the AGN host galaxy. Therefore, it is crucial to study the best examples of fast outflows, with the highest quality data in order to establish their potential significance in terms of galaxy feedback. The usage of disk wind

models for PDS 456, PG1211 + 143 and 1H 0707 − 495 has been demonstrated and extending this analysis to a larger sample based on the available archival data from NASA/HEASARC is needed to better understand AGN disk winds.

The sample of 15 radio-quiet type 1 AGN, shown in table 7.1, consists of objects that Tombesi et al. (2010) and/or Gofford et al. (2013) found to have strong blue-shifted Fe Kα absorption features. These objects have both *XMM-Newton* and *NuSTAR* archival data[1] rest frame coverage up to 40 keV in *XMM-Newton* and *Suzaku*. Two recently discovered objects with fast winds, IRAS F11119+3257 (Tombesi et al. 2015) and IRAS 13224−3809 (Parker et al. 2017) have also been added. This AGN sample has extensive X-ray coverage in the archives with *XMM-Newton*, *Suzaku* and *NuSTAR*, in many cases exceeding 1 Ms of total exposure time over the last decade. This would ensure not just high S/N spectra, but also allow wind variability to be probed and how it responds to the ionising continuum. Using the Sim et al. (2010) model to fit the objects with the strongest iron K absorption profiles, over a wide range in parameter space, would allow the exploration of the disk wind properties across a variety of AGN with different conditions, such as wind speed, luminosity, mass outflow rate and black hole mass. The sample spans from 0.01c to 0.3c in outflow velocity, from 10^{43}–10^{47} erg s^{-1} in luminosity and black hole masses of 10^{6}–10^{9} $M_{\odot}$. The accretion rate also varies from a few percent of $L_{\rm edd}$ in the lower luminosity Seyfert 1s, up to $L_{\rm edd}$ and beyond in the extreme NLS1 IRAS 13224−3809. AGN with modest mass outflow rates are included, such as in the lower luminosity Seyferts, Mrk 766, NGC 4051, NGC 1365 and MCG −6−30−15, where the outflow velocities are $<$ 10,000 km s^{-1}. At the other extreme is the powerful high redshift (z = 3.9) BAL QSO, APM 08279+5255 (Chartas et al. 2002), and the luminous ULIRG/QSO IRAS F11119+3257 (z = 0.189), both having fast X-ray winds. A large-scale molecular outflow has been observed in IRAS F11119+3257 (Tombesi et al. 2015) and APM 08279+5255 (Feruglio et al. 2017). Mrk 766 (z = 0.0129) has two clear blue-shifted absorption lines in its *Suzaku* spectrum, from He and H-like iron,

[1] APM 08279+5255 is the exception due to its high redshift (z = 3.9): it has

AGN	Velocity[a]	Exp (ks)[b]	Redshift
APM 08279+5255[1,2]	0.285 ± 0.011	630	3.9
ESO 103−G035[2]	0.056 ± 0.025	130	0.0133
IRAS F11119+3257[7]	0.255 ± 0.011	350	0.189
IRAS 13224−3809[3]	0.236 ± 0.006	3100	0.0658
IC 4329A[6]	0.105 ± 0.005	560	0.0161
MCG −5−23−16[6]	0.118 ± 0.005	1200	0.0085
MCG −6−30−15[2]	0.007 ± 0.002	1300	0.0077
MR 2251−178[2]	0.137 ± 0.008	830	0.064
Mrk 766[2]	0.017 ± 0.004	1000	0.0129
NGC 1365[2]	0.008 ± 0.001	2000	0.0055
NGC 3516[2]	0.004 ± 0.002	1500	0.0088
NGC 4051[2]	0.018 ± 0.001	1400	0.0023
NGC 4151[2]	0.055 ± 0.023	1300	0.0033
NGC 5506[2]	0.246 ± 0.006	640	0.0062
Swift J127.4+5654[2]	0.231 ± 0.006	790	0.0144

Table 7.1: A sample of AGN in the *HEASARC* archive which have strong absorption features to which the Sim et al. (2010) disk wind code could be applied.
Key:
[a] Outflow velocity in units of c measured from iron K profile.
[b] Total accumulated exposure of archival data from *XMM-Newton*, *Suzaku* and *NuSTAR* in ksec.
References: [1] Chartas et al. (2002), [2] Gofford et al. (2013), [3] Parker et al. (2017), [4] Pounds et al. (2003), [5] Reeves et al. (2009), [6] Tombesi et al. (2010) and [7] Tombesi et al. (2015)

but with a modest outflow velocity of 0.02–0.03c. This AGN was fitted with a disk wind model by Sim et al. (2008), with a wind launch radius of $R_{\rm min} \sim 400\,R_{\rm g}$ and a mass outflow rate of 0.4 $M_{\odot}$ yr^{-1}. Thus the Sim et al. (2010) model can be extend to the wider archive to explore of disk winds over the full range of AGN accretion behaviour.

7.2.2 The future of the Sim et al. (2010) radiative transfer code

As mentioned previously in this chapter, the work within this thesis has outlined improvements which need to be applied to the Sim et al. (2010) code. These improvements could also lead into future studies in addition to the disk wind sample. These can be broken up into roughly three areas: firstly, the addition of density perturbations (or "clumps") within the smooth flow as required by the mounting evidence (presented in this thesis and the literature) that winds have a multiphase structure; secondly, the recent hydrodynamical simulations of Dyda & Proga (2018a) where azimuthal symmetry was broken (similar to the work in Sim et al. (2010) performed on output from the Proga & Kallman (2004) simulations); and finally, the timing properties of these winds (Mizumoto et al. 2019).

7.2.2.1 Clumps

The requirement for the introduction of density perturbations within outflows is clear: both PDS 456 and PG1211 + 143 show evidence for soft absorbers with outflow velocities comparable to the highly ionised Fe Kα wind. To model these within a flow, lower-ionisation material must be present. Naively, these density perturbations can be easily inserted into the computational structure. This poses several problems for getting physically meaningful results as there are many "parameters" which we do not necessarily know a priori, such as the filling factor, the density of these clumps and their radial distribution. To fit these parameters could be computationally expensive or highly degenerate. However, some of these can be found (or at least inferred) through the use of large monitoring campaigns (from which the frequency of absorbed states and hence the filling factor can be estimated) and high resolution spectra (providing the density) such as those of PDS 456 or PG1211 + 143. Therefore only objects which fulfill these requirements can be studied in this way until the parameter space is well studied.

Furthermore, the low ionisation state of the features which have been observed requires

the database of atomic transitions used by the code to be extended. This is also required so that the code maintains its relevance for future missions. In particular for missions with micro-calorimeters (X-ray detectors which measure the temperature change caused by an incoming photon, which provides high spectral resolution) such as the X-ray Imaging and Spectroscopy Mission (XRISM) and the Advanced Telescope for High-ENergy Astrophysics (ATHENA).

As the optical depth of a cloud increases it will self-shield, producing ionisation gradients. At small radii (where the computational structure has a higher resolution) this is not an issue. However, at larger radii where a cloud is the size of a single computational cell it is not possible to have a gradient. Therefore, the cell structure for simulations is required to be finer (smaller grid cells), which would drastically increase the computing resources required. A possible solution is to increase the complexity of cell structure, however the changes to the code required are non-trivial.

7.2.2.2 Breaking of azimuthal symmetry

The work in Dyda & Proga (2018a) presents a recent set of hydrodynamic simulations where the disk wind is non-azimuthally symmetric. By emulating the method used in Sim et al. (2010), the spectra that would be produced by the Dyda & Proga (2018a) disk wind could be investigated. Breaking the azimuthal symmetry of the wind, more complex structures can be formed. Therefore, changing the inclination angle and azimuthal rotation of the observer will produce substantially different spectra where the emission (extended) and absorption (line of sight) are partially decoupled. As there is no guarantee that disk winds are azimuthally symmetric, a more realistic set of spectra can be produced.

7.2.2.3 Timing

In section 6.2 on 1H 0707 − 495 it was mentioned that the time lags detected in systems with disk winds are not likely to be caused by simple reverberation off an accretion disk. This is because the wind itself is a scattering medium. When reverberation within the disk wind is combined with recombination rates this will introduce its own characteristic lag signature — even without including line of sight variability of the wind as presented in the Gardner & Done (2014) model. The ability of the Sim et al. (2010) code to extract spectra at defined time intervals could be used to construct the transfer function of the wind, which is a vital ingredient when using timing methods to study outflows. This could then be used to compute lag-energy spectra which could be compared to observational data. This may be more relevant for future high through-put telescopes such as ATHENA.

Publications

1. *"Variability of the High-velocity Outflow in the Quasar PDS 456"*; Reeves, J. N., Braito, V., Gofford, J., Sim, S. A., Behar, E., **Costa, M.**, Kaspi, S., Matzeu, G., Miller, L., O'Brien, P., Turner, T. J., Ward, M., 2014, ApJ, 780, 45

2. *"Revealing the Location, Structure of the Accretion Disk Wind in PDS 456"*; Gofford, J., Reeves, J. N., Braito, V., Nardini, E., **Costa, M. T.**, Matzeu, G. A., O'Brien, P., Ward, M., Turner, T. J., Miller, L., 2014, ApJ, 784, 77

3. *"Black hole feedback in the luminous quasar PDS 456"*; Nardini, E., Reeves, J. N., Gofford, J., Harrison, F. A., Risaliti, G., Braito, V., **Costa, M. T.**, Matzeu, G. A., Walton, D. J., Behar, E., Boggs, S. E., Christensen, F. E., Craig, W. W., Hailey, C. J., Matt, G., Miller, J. M., O'Brien, P. T., Stern, D., Turner, T. J., Ward, M. J. 2015, Sci, 347, 860

4. *"The Chandra/HETG view of NGC 1365 in a Compton-thick state"*; Nardini, E., Gofford, J., Reeves, J. N., Braito, V., Risaliti, G., **Costa, M.**, 2015, MNRAS, 453, 2558

5. *"Broadband short term X-ray variability of the quasar PDS 456"*; Matzeu, G. A., Reeves, J. N., Nardini, E., Braito, V., **Costa, M. T.**, Tombesi, F., Gofford, J., 2016, AN, 337, 495

6. *"Discovery of Broad Soft X-ray Absorption Lines from the Quasar Wind in PDS 456"*; Reeves, J. N., Braito, V., Nardini, E., Behar, E., O'Brien, P. T., Tombesi, F., Turner, T. J., **Costa, M. T**, 2016 ApJ, 824, 20

7. *"Imprints of a high-velocity wind on the soft X-ray spectrum of PG1211+143"*; Pounds, K. A., Lobban, A., Reeves, J. N., Vaughan, S., **Costa, M.**, 2016, MNRAS, 459, 4389

8. *"X-ray flaring in PDS 456 observed in a high-flux state"*; Matzeu, G. A., Reeves, J. N., Nardini, E., Braito, V., Turner, T. J., **Costa, M. T.**, 2017, MNRAS, 465, 2804

9. *"Evidence for a radiatively driven disc-wind in PDS 456?"*; Matzeu,G. A., Reeves,J. N., Braito V., Nardini E., McLaughlin D. E., Lobban A. P., Tombesi F., **Costa M. T.**, 2017, MNRAS, 472, L15

Bibliography

Aller M. C., Richstone D. O., 2007, ApJ, 665, 120

Antonucci R., 1993, Annu. Rev. Astron. Astrophys., 31, 473

Balbus S. A., Hawley J. F., 1998, Reviews of Modern Physics, 70, 1

Bautista M. A., Kallman T. R., 2001, ApJS, 134, 139

Beckmann V., Shrader C. R., 2012, Active Galactic Nuclei. Wiley-VCH

Bennert V. N., Auger M. W., Treu T., Woo J.-H., Malkan M. A., 2011, ApJ, 726, 59

Blandford R. D., Payne D. G., 1982, MNRAS, 199, 883

Blustin A. J., Page M. J., Fuerst S. V., Branduardi-Raymont G., Ashton C. E., 2005, A&A, 431, 111

Boissay R., Ricci C., Paltani S., 2016, A&A, 588, A70

Boller T., Brandt W. N., Fink H., 1996, A&A, 305, 53

Bottorff M., Korista K. T., Shlosman I., Blandford R. D., 1997, ApJ, 479, 200

Bower R. G., Benson A. J., Malbon R., Helly J. C., Frenk C. S., Baugh C. M., Cole S., Lacey C. G., 2006, MNRAS, 370, 645

Castor J. I., Abbott D. C., Klein R. I., 1975, ApJ, 195, 157

Chartas G., Brandt W. N., Gallagher S. C., Garmire G. P., 2002, ApJ, 579, 169

Chartas G. et al., 2016, Astronomische Nachrichten, 337, 356

Collin S., Kawaguchi T., 2004, A&A, 426, 797

Contopoulos J., Lovelace R. V. E., 1994, ApJ, 429, 139

Cowie L. L., Barger A. J., Bautz M. W., Brandt W. N., Garmire G. P., 2003, ApJ, 584, L57

Crenshaw D. M., Kraemer S. B., 2007, ApJ, 659, 250

Croom S. M., Smith R. J., Boyle B. J., Shanks T., Miller L., Outram P. J., Loaring N. S., 2004, MNRAS, 349, 1397

Crummy J., Fabian A. C., Gallo L., Ross R. R., 2006, MNRAS, 365, 1067

Czerny B., Nikołajuk M., Różańska A., Dumont A.-M., Loska Z., Zycki P. T., 2003, A&A, 412, 317

Dauser T., García J., Parker M. L., Fabian A. C., Wilms J., 2014, MNRAS, 444, L100

Dauser T. et al., 2012, MNRAS, 422, 1914

den Herder J. W. et al., 2001, A&A, 365, L7

Di Matteo T., Springel V., Hernquist L., 2005, Nature, 433, 604

Done C., Davis S. W., Jin C., Blaes O., Ward M., 2012, MNRAS, 420, 1848

Done C., Jin C., 2016, MNRAS, 460, 1716

Dovčiak M., Done C., 2016, Astronomische Nachrichten, 337, 441

Dyda S., Proga D., 2018a, MNRAS, 475, 3786

Dyda S., Proga D., 2018b, MNRAS, 481, 5263

Elitzur M., 2012, ApJL, 747, L33

Emmering R. T., Blandford R. D., Shlosman I., 1992, ApJ, 385, 460

Everett J. E., 2005, ApJ, 631, 689

Fabian A. C., Ballantyne D. R., Merloni A., Vaughan S., Iwasawa K., Boller T., 2002, MNRAS, 331, L35

Fabian A. C., Miniutti G., Gallo L., Boller T., Tanaka Y., Vaughan S., Ross R. R., 2004, MNRAS, 353, 1071

Fabian A. C. et al., 2009, Nature, 459, 540

Fabian A. C. et al., 2012, MNRAS, 419, 116

Ferland G. J., Rees M. J., 1988, ApJ, 332, 141

Ferrarese L., Ford H., 2005, SSRv, 116, 523

Ferrarese L., Merritt D., 2000, ApJL, 539, L9

Feruglio C. et al., 2017, A&A, 608, A30

Feruglio C. et al., 2015, A&A, 583, A99

Francis P. J., Hewett P. C., Foltz C. B., Chaffee F. H., Weymann R. J., Morris S. L., 1991, ApJ, 373, 465

Fukumura K., Tombesi F., Kazanas D., Shrader C., Behar E., Contopoulos I., 2015, ApJ, 805, 17

García J. et al., 2014, ApJ, 782, 76

García J., Kallman T. R., 2010, ApJ, 718, 695

Gardner E., Done C., 2014, MNRAS, 442, 2456

Gardner E., Done C., 2015, MNRAS, 448, 2245

Gebhardt K. et al., 2000, ApJL, 539, L13

George I. M., Fabian A. C., 1991, MNRAS, 249, 352

Gierliński M., Done C., 2004, MNRAS, 349, L7

Gillessen S., Eisenhauer F., Fritz T. K., Bartko H., Dodds-Eden K., Pfuhl O., Ott T., Genzel R., 2009, ApJ, 707, L114

Giustini M., Turner T. J., Reeves J. N., Miller L., Legg E., Kraemer S. B., George I. M., 2015, A&A, 577, A8

Gofford J., Reeves J. N., McLaughlin D. E., Braito V., Turner T. J., Tombesi F., Cappi M., 2015, MNRAS, 451, 4169

Gofford J., Reeves J. N., Tombesi F., Braito V., Turner T. J., Miller L., Cappi M., 2013, MNRAS, 430, 60

Guilbert P. W., Rees M. J., 1988, MNRAS, 233, 475

Gültekin K. et al., 2009, ApJ, 698, 198

Gupta A., Mathur S., Krongold Y., Nicastro F., 2013, ApJ, 772, 66

Haardt F., Maraschi L., 1991, ApJL, 380, L51

Haardt F., Maraschi L., 1993, ApJ, 413, 507

Hagino K., Done C., Odaka H., Watanabe S., Takahashi T., 2017, MNRAS, 468, 1442

Hagino K., Odaka H., Done C., Gandhi P., Watanabe S., Sako M., Takahashi T., 2015, MNRAS, 446, 663

Hagino K., Odaka H., Done C., Tomaru R., Watanabe S., Takahashi T., 2016, MNRAS, 461, 3954

Hamann F., Sabra B., 2004, in Richards G. T., Hall P. B., eds, Astronomical Society of the Pacific Conference Series Vol. 311, AGN Physics with the Sloan Digital Sky Survey. p. 203

Häring N., Rix H.-W., 2004, ApJL, 604, L89

Harrison F. A. et al., 2013, ApJ, 770, 103

Heckman T. M., Kauffmann G., Brinchmann J., Charlot S., Tremonti C., White S. D. M., 2004, ApJ, 613, 109

Hopkins P. F., Elvis M., 2010, MNRAS, 401, 7

Jansen F. et al., 2001, A&A, 365, L1

Kaastra J. S., Mewe R., Liedahl D. A., Komossa S., Brinkman A. C., 2000, A&A, 354, L83

Kara E., Fabian A. C., Cackett E. M., Steiner J. F., Uttley P., Wilkins D. R., Zoghbi A., 2013, MNRAS, 428, 2795

Kara E. et al., 2015, MNRAS, 449, 234

Kazanas D., Fukumura K., Behar E., Contopoulos I., Shrader C., 2012, The Astronomical Review, 7, 92

Keel W. C., 1983, ApJ, 269, 466

Kellermann K. I., Sramek R., Schmidt M., Shaffer D. B., Green R., 1989, AJ, 98, 1195

Kelley R. L. et al., 2007, PASJ, 59, 77

Kennicutt Jr. R. C., 1992, ApJS, 79, 255

King A., 2003, ApJL, 596, L27

King A., 2005, ApJL, 635, L121

King A. R., 2010, MNRAS, 402, 1516

King A. R., Pounds K. A., 2003, MNRAS, 345, 657

Kollatschny W., Zetzl M., 2013, A&A, 551, L6

Komossa S., Voges W., Xu D., Mathur S., Adorf H.-M., Lemson G., Duschl W. J., Grupe D., 2006, AJ, 132, 531

Konigl A., Kartje J. F., 1994, ApJ, 434, 446

Kormendy J., Ho L. C., 2013, Annu. Rev. Astron. Astrophys., 51, 511

Kormendy J., Richstone D., 1995, Annu. Rev. Astron. Astrophys., 33, 581

Koyama K. et al., 2007, PASJ, 59, 23

Krause M. O., 1979, Journal of Physical and Chemical Reference Data, 8, 307

Laor A., Fiore F., Elvis M., Wilkes B. J., McDowell J. C., 1994, ApJ, 435, 611

Larkin A. C., McLaughlin D. E., 2016, MNRAS, 462, 1864

Lawrence C. R., Zucker J. R., Readhead A. C. S., Unwin S. C., Pearson T. J., Xu W., 1996, ApJS, 107, 541

Legg E., Miller L., Turner T. J., Giustini M., Reeves J. N., Kraemer S. B., 2012, ApJ, 760, 73

Lightman A. P., White T. R., 1988, ApJ, 335, 57

Lobban A. P., Pounds K., Vaughan S., Reeves J. N., 2016, ApJ, 831, 201

Lobban A. P., Reeves J. N., Miller L., Turner T. J., Braito V., Kraemer S. B., Crenshaw D. M., 2011, MNRAS, 414, 1965

Lobban A. P., Vaughan S., Pounds K., Reeves J. N., 2016, MNRAS, 457, 38

Longinotti A. L. et al., 2013, ApJ, 766, 104

Lucy L. B., 2002, A&A, 384, 725

Lucy L. B., 2003, A&A, 403, 261

Lusso E. et al., 2010, A&A, 512, A34

Lynden-Bell D., 1969, Nature, 223, 690

Magdziarz P., Zdziarski A. A., 1995, MNRAS, 273, 837

Magorrian J. et al., 1998, AJ, 115, 2285

Marconi A., Hunt L. K., 2003, ApJL, 589, L21

Marconi A., Risaliti G., Gilli R., Hunt L. K., Maiolino R., Salvati M., 2004, MNRAS, 351, 169

Marinucci A., Tortosa A., NuSTAR AGN Physics Working Group 2016, Astronomische Nachrichten, 337, 490

Martínez-Sansigre A., Rawlings S., Lacy M., Fadda D., Jarvis M. J., Marleau F. R., Simpson C., Willott C. J., 2006, MNRAS, 370, 1479

Mason K. O. et al., 2001, A&A, 365, L36

Matzeu G. A., Reeves J. N., Braito V., Nardini E., McLaughlin D. E., Lobban A. P., Tombesi F., Costa M. T., 2017, MNRAS, 472, L15

Matzeu G. A., Reeves J. N., Nardini E., Braito V., Costa M. T., Tombesi F., Gofford J., 2016, MNRAS, 458, 1311

Matzeu G. A., Reeves J. N., Nardini E., Braito V., Turner T. J., Costa M. T., 2017, MNRAS, 465, 2804

McKernan B., Yaqoob T., Reynolds C. S., 2007, MNRAS, 379, 1359

Merloni A., 2004, MNRAS, 353, 1035

Merritt D., Ferrarese L., 2001, ApJ, 547, 140

Mizumoto M., Ebisawa K., Sameshima H., 2014, PASJ, 66, 122

Mizumoto M., Ebisawa K., Tsujimoto M., Done C., Hagino K., Odaka H., 2019, MNRAS, 482, 5316

Murphy K. D., Yaqoob T., 2009, MNRAS, 397, 1549

Nandra K., Pounds K. A., 1994, MNRAS, 268, 405

Nardini E., Fabian A. C., Reis R. C., Walton D. J., 2011, MNRAS, 410, 1251

Nardini E., Fabian A. C., Walton D. J., 2012, MNRAS, 423, 3299

Nardini E. et al., 2015, Science, 347, 860

Nomura M., Ohsuga K., Takahashi H. R., Wada K., Yoshida T., 2016, PASJ, 68, 16

Norman C. et al., 2002, ApJ, 571, 218

Ohsuga K., Mineshige S., 2011, ApJ, 736, 2

Ohsuga K., Mineshige S., Mori M., Kato Y., 2009, PASJ, 61, L7

Osterbrock D. E., 1981, ApJ, 249, 462

Osterbrock D. E., Pogge R. W., 1985, ApJ, 297, 166

Owen F. N., O'Dea C. P., Keel W. C., 1990, ApJ, 352, 44

Parker M. L. et al., 2015, MNRAS, 447, 72

Parker M. L. et al., 2017, Nature, 543, 83

Peterson B. M., 1997, An Introduction to Active Galactic Nuclei. Cambridge University Press

Porquet D. et al., 2018, A&A, 609, A42

Porquet D., Reeves J. N., O'Brien P., Brinkmann W., 2004, A&A, 422, 85

Pounds K., Lobban A., Reeves J., Vaughan S., 2016, MNRAS, 457, 2951

Pounds K. A., Lobban A., Reeves J. N., Vaughan S., Costa M., 2016a, MNRAS, 459, 4389

Pounds K. A., Lobban A., Reeves J. N., Vaughan S., Costa M., 2016b, MNRAS, 459, 4389

Pounds K. A., Page K. L., 2006, MNRAS, 372, 1275

Pounds K. A., Reeves J. N., 2009, MNRAS, 397, 249

Pounds K. A., Reeves J. N., King A. R., Page K. L., O'Brien P. T., Turner M. J. L., 2003, MNRAS, 345, 705

Proga D., Kallman T. R., 2004, ApJ, 616, 688

Proga D., Stone J. M., Kallman T. R., 2000, ApJ, 543, 686

Rees M. J., 1984, Annu. Rev. Astron. Astrophys., 22, 471

Reeves J. N. et al., 2014, ApJ, 780, 45

Reeves J. N., Braito V., Nardini E., Behar E., O'Brien P. T., Tombesi F., Turner T. J., Costa M. T., 2016, ApJ, 824, 20

Reeves J. N., Lobban A., Pounds K. A., 2018, ApJ, 854, 28

Reeves J. N. et al., 2009, ApJ, 701, 493

Reeves J. N., O'Brien P. T., Vaughan S., Law-Green D., Ward M., Simpson C., Pounds K. A., Edelson R., 2000, MNRAS, 312, L17

Reeves J. N., O'Brien P. T., Ward M. J., 2003, ApJL, 593, L65

Reeves J. N., Porquet D., Braito V., Nardini E., Lobban A., Turner T. J., 2016, ApJ, 828, 98

Reeves J. N., Turner M. J. L., 2000, MNRAS, 316, 234

Reines A. E., Volonteri M., 2015, ApJ, 813, 82

Risaliti G., Elvis M., Fabbiano G., Baldi A., Zezas A., 2005, ApJL, 623, L93

Salpeter E. E., 1964, ApJ, 140, 796

Schmidt M., 1963, Nature, 197, 1040

Schmidt M., Green R. F., 1983, ApJ, 269, 352

Scott A. E., Stewart G. C., 2014, MNRAS, 438, 2253

Serlemitsos P. J. et al., 2007, PASJ, 59, S9

Severgnini P. et al., 2006, A&A, 451, 859

Seyfert C. K., 1943, ApJ, 97, 28

Shakura N. I., Sunyaev R. A., 1973a, A&A, 24, 337

Shakura N. I., Sunyaev R. A., 1973b, A&A, 24, 337

Sim S. A., Long K. S., Miller L., Turner T. J., 2008, MNRAS, 388, 611

Sim S. A., Miller L., Long K. S., Turner T. J., Reeves J. N., 2010, MNRAS, 404, 1369

Sim S. A., Proga D., Miller L., Long K. S., Turner T. J., 2010, MNRAS, 408, 1396

Simpson C., Ward M., O'Brien P., Reeves J., 1999, MNRAS, 303, L23

Singh K. P., Garmire G. P., Nousek J., 1985, ApJ, 297, 633

Stern D. et al., 2002, ApJ, 568, 71

Strüder L. et al., 2001, A&A, 365, L18

Tadhunter C., 2008, New Astron. Rev., 52, 227

Takahashi T. et al., 2007, PASJ, 59, 35

Tarter C. B., Salpeter E. E., 1969, ApJ, 156, 953

Tatum M. M., Turner T. J., Miller L., Reeves J. N., DiLiello J., Gofford J., Patrick A., Clayton M., 2016, ApJ, 818, 12

Tatum M. M., Turner T. J., Sim S. A., Miller L., Reeves J. N., Patrick A. R., Long K. S., 2012, ApJ, 752, 94

Thorne K. S., 1974, ApJ, 191, 507

Tombesi F., Cappi M., Reeves J. N., Nemmen R. S., Braito V., Gaspari M., Reynolds C. S., 2013, MNRAS, 430, 1102

Tombesi F., Cappi M., Reeves J. N., Palumbo G. G. C., Braito V., Dadina M., 2011, ApJ, 742, 44

Tombesi F., Cappi M., Reeves J. N., Palumbo G. G. C., Yaqoob T., Braito V., Dadina M., 2010, A&A, 521, A57

Tombesi F., Meléndez M., Veilleux S., Reeves J. N., González-Alfonso E., Reynolds C. S., 2015, Nature, 519, 436

Turner M. J. L. et al., 2001, A&A, 365, L27

Turner T. J., Pounds K. A., 1988, MNRAS, 232, 463

Vaughan S., Reeves J., Warwick R., Edelson R., 1999, MNRAS, 309, 113

Vaughan S., Uttley P., Pounds K. A., Nandra K., Strohmayer T. E., 2011, MNRAS, 413, 2489

Walter R., Fink H. H., 1993, A&A, 274, 105

Warren S. J., Hewett P. C., Osmer P. S., 1994, ApJ, 421, 412

Waters T., Proga D., Dannen R., Kallman T. R., 2017, MNRAS, 467, 3160

Watson M. G. et al., 2009, A&A, 493, 339

Wilkins D. R., Gallo L. C., 2015, MNRAS, 448, 703

Wilms J., Allen A., McCray R., 2000, ApJ, 542, 914

Woo J.-H., Urry C. M., 2002, ApJ, 579, 530

Yun M. S., Reddy N. A., Scoville N. Z., Frayer D. T., Robson E. I., Tilanus R. P. J., 2004, ApJ, 601, 723

Zoghbi A., Fabian A. C., Uttley P., Miniutti G., Gallo L. C., Reynolds C. S., Miller J. M., Ponti G., 2010, MNRAS, 401, 2419

Zoghbi A. et al., 2015, ApJL, 799, L24